



ScuDo

Scuola di Dottorato ~ Doctoral School

WHAT YOU ARE, TAKES YOU FAR



Doctoral Dissertation  
Doctoral Program in Chemical Engineering (31<sup>st</sup> Cycle)

# High-energy sustainable Lithium Sulfur batteries for electrical vehicles and renewable energy applications

Development of innovative electrodes

**Usman Zubair**

\* \* \* \* \*

**Supervisor**

Prof. Nerino Penazzi

**Doctoral Examination Committee:**

Prof. Robert Dominko, Referee, Kemijski inštitut, Ljubljana (Slovenia)

Prof. Catia Arbizzani, Referee, Università di Bologna (Italy)

Prof. Stefania Specchia, Politecnico di Torino (Italy)

Prof. Francesco Trotta, Università degli Studi di Torino (Italy)

Prof. Silvia Bodoardo, Politecnico di Torino (Italy)

Politecnico di Torino

October 31, 2018



This thesis is licensed under a Creative Commons License, Attribution-Noncommercial - NoDerivative Works 4.0 International: see [www.creativecommons.org](http://www.creativecommons.org). The text may be reproduced for non-commercial purposes, provided that credit is given to the original author.

I hereby declare that the contents and organization of this dissertation constitute my own original work and does not compromise in any way the rights of third parties, including those relating to the security of personal data.



.....  
Usman Zubair  
Turin, October 31, 2018



# Summary

It will not be overstated if it is admitted that Li-ion batteries are one of the greatest achievements of the modern industrialized world. Li-ion batteries are everywhere in gadgets, laptops and almost in every portable consumer electronics. But, future energy storage demand for electrical mobility and smart grid asking for much higher energy density, sustainable and cheaper solutions. Lithium-sulfur (Li/S) technology has emerged as one of the promising solutions to such demands as it can offer five times high energy density than that of state of art Li-ion technology. Li/S system can be potentially regarded as a sustainable and cheaper technology owing to abundance and benignity of sulfur. However, the insulating nature of sulfur and  $\text{Li}_2\text{S}$ , free solubility of lithium polysulfides (LiPS) in the electrolyte, shuttling of LiPS across separator and use of metallic lithium as anode challenge the scientific community to offer some practical solutions for its commercialization. The effort has to be done in various dimensions to realize stable and long-life Li/S batteries.

In this dissertation, first the focus is given to design cathode materials that can effectively host sulfur and its redox species. In addition to synthesizing effective host materials that can efficiently interact with LiPS, the emphasis is also maintained on practicability and industrial viability of the procedures. Literature carries various reports in which highly sophisticated materials and complex methodologies have been opted to show the longevity of sulfur cathodes using lithium metal as the anode. However, these approaches have been questioned for their industrial feasibility. So, in this dissertation, we have put forth multiple approaches to realize efficient and long-life sulfur cathodes keeping in view industrial viability. In the very first part of the thesis, a strong literature review has been presented to better understand the present state of research in Li/S technology. In the next three chapters, diverse strategies have been exploited to reach stable

sulfur cathodes. In the next chapter, two practical approaches have been established to accomplish silicon anodes. In the last section, sulfur cathodes and silicon anodes have been integrated in full cell configuration to accomplish lithium metal free sulfur cells.

In the second chapter, two strategies have been put forth to produce microporous and hierarchical porous carbon matrices. The microporous carbon has been achieved by carbonization of  $\beta$ -cyclodextrin nanosponges. This preliminary work lays the foundation to understand Li/S system. In the second strategy, elemental doped high surface area hierarchical porous carbons have been realized by KOH activation and carbonization of polypyrrole and polythiophene. Using these nitrogen or sulfur-doped hierarchical porous carbons, the sulfur cathode has delivered highly stable capacities for more than 300 cycles. In the third chapter, three approaches have been proposed to prepare inorganic moieties decorated carbon structures. In one strategy, Magnèli phase  $\text{TiO}_x$  decorated carbon has been synthesized by simultaneous carbothermal reduction and carbonization from commercial  $\text{TiO}_2$  powder. In another approach, electrochemically  $\text{MnO}_x$  deposited carbon structures have been exploited for high sulfur loading freestanding electrodes. In the last approach, VN decorated nitrogen-doped carbon has been achieved by a simultaneous in-situ ammonization and carbonization from commercial  $\text{V}_2\text{O}_5$  powder. All three strategies exhibited promising stable cycling and rate capabilities performances with reduced capacity decay rate. In each case, as-synthesized materials have been physiochemically characterized for their distinct properties and ability to interact with LiPS.

In the fourth chapter, electroactive polymer covered carbon/sulfur composite has been suggested. In this section, a practical inadequacy of previous reports has been addressed where chloride-ion doped polyaniline had been proposed to limit LiPS solubility. We offered an alternative and trivial solution by accomplishing formate-ion doped polyaniline wrapped carbon/sulfur composite by in-situ oxidative polymerization. The as-prepared cathodes exhibited very stable performance around  $800 \text{ mAh g}^{-1}$  for more than 500 cycles at  $0.2\text{C}$ . In the fifth chapter, Si@void@CNF have been integrated with elemental doped hierarchical porous carbon/sulfur to reach lithium metal free Li/S full cells. For the purpose, Si anode has been lithiated and balanced in areal density to the sulfur cathode. The as-assembled full cell has shown the promising capacity of  $800 \text{ mAh g}^{-1}$  with 50% stabilized capacity retention for than 100 cycles at  $0.15\text{C}$ . So, the rational design of porous carbon matrices has enabled to realize full Li/S cell.

# Acknowledgment

I would like to pay gratitude to my mentors, Prof. Nerino Penazzi and Prof. Silvia Bodoardo, for providing me the opportunity to steer my research in an autonomous fashion. Your mentorship and discussions guide me a lot in accomplishing this piece of work. Silvia's original ideas always inspire you, but Ph.D. limits you to a certain topic. These all equipped me to achieve the next levels as an independent researcher. How can I forget my electrochemistry group mates!!! Carlotta Francia, Julia Amici, Daniele Versaci and Mojtaba Alidoost. Your support was not less than an opportunity to accomplish this dissertation. Carlotta Francia I am thankful to you for your unwavering support throughout my Ph.D. You enabled me to conclude my dissertation by keeping platforms available for various characterizations.

I would like to acknowledge the contributions of Leitat Technological Center guys Dr. Christoph Aucher, Dr. Sandra Crespiera, and Dr. Raquel Tejada. Christoph Aucher, project manager ALISE, for giving me an opportunity to work at Leitat technological centers located in Barcelona and Terrassa. Sandra for your guidance and Raquel for your help throughout my stay at Leitat. And I would like to acknowledge Prof. Robert Dominko and Dr. Alen Vižintin for providing me an opportunity to work at National Institute of Chemistry, Ljubljana, Slovenia. I have learned a lot in those few days.

In the end, I would like to thank my family and friends to oblige me keeping a balance in life. My life partner Nausheen Irshad thanks a lot for tolerating tough schedules of me during my Ph.D. days. I want to give a credit of compiling this dissertation to you on continuously inspecting the status of write up. Who always keep me alive to take care of my very own research stuff? My little son Muhammad Umer for sure it is you, dear. I want to thank Amjad Rafique, Tanveer Ahmad, Yair Akram, and other friends for their support. In very last, I want to thank my mother Rizwana Zubair who nurtured me to spend a confident life.



*I would like to dedicate  
this thesis to my loving  
mother and my family*



# Contents

1	Introduction: State of the art .....	1
1.1	Introduction to Li-ion battery (LIB) technologies .....	1
1.2	Introduction to Li/S technology .....	3
1.2.1	Operational mechanism of Li/S batteries .....	3
1.2.2	Challenges to Li/S battery system .....	5
1.3	Approaches to improve Li/S battery technology – A critical review	7
1.3.1	Cathode configurations .....	8
1.3.2	Induction of interlayers .....	16
1.3.3	Separators modifications .....	16
1.3.4	Towards low PS solubility electrolytes and additives .....	18
1.3.5	Inactive binder to interactive matrices .....	19
1.3.6	Lithium anode protection .....	20
1.3.7	Alternative anodes .....	21
1.4	Characterization Methodologies opted to study Li/S cathode materials and cells .....	23
1.5	Concluding Remarks .....	26
2	Development of novel carbon host materials for sulfur cathodes .....	27
2.1	Ultra-microporous carbon (MPC) from hyper crosslinked $\beta$ - cyclodextrin nanosponges as sulfur host .....	28
2.1.1	Development of MPC based on cyclodextrin nanosponges and MPC based sulfur cathode .....	28
2.1.2	Physiochemical Characterization .....	30
2.1.3	Electrochemical Testing .....	35

2.2	Highly porous hierarchical heteroatom doped carbons/sulfur cathodes	39
2.2.1	Development of nitrogen/sulfur doped carbon cathodes	39
2.2.2	Physiochemical Characterization	41
2.2.3	Electrochemical Testing	45
2.3	Conclusion	47
3	Development of metal compound decorated carbon/sulfur cathodes	49
3.1	Nanoscale Magnéli phase $Ti_nO_{2n-1}$ embedded carbon matrices	49
3.1.1	Development of Magnéli phase $Ti_nO_{2n-1}$ embedded carbon, its sulfur composite and cathode	50
3.1.2	Physiochemical Characterization	52
3.1.3	Electrochemical Testing	58
3.2	Electrochemically $MnO_x$ deposited carbon fiber (CF) substrates as freestanding sulfur cathodes	61
3.2.1	Development of $MnO_x$ deposited CF freestanding sulfur cathode	61
3.2.2	Physiochemical Characterization	63
3.2.3	Electrochemical Testing	69
3.3	Vanadium Nitride (VN) decorated Nitrogen doped carbon-graphene/Sulfur Cathodes	72
3.3.1	Development of VN decorated N-doped carbon-rGO / sulfur composite cathode	72
3.3.2	Physiochemical Characterization	74
3.3.3	Electrochemical Testing	77
3.4	Conclusion	79
4	Development of functional polymers coated sulfur cathodes	81
4.1	Formate-ion doped Polyaniline (PANi-COOH) enveloped mesoporous Carbon/Sulfur Composite	82
4.1.1	Development of Formate-ion doped PANi enveloped C/S composite and cathodes	83
4.1.2	Physiochemical Characterization	85

4.1.3	Electrochemical Testing.....	87
4.2	Conclusion .....	90
5	Development of Si based anodes for Li/S batteries.....	91
5.1	Silicon nanoparticles (SiNP) incorporated carbon nanofibers (CNF) based anodes.....	92
5.1.1	Development of SiNP@SiO <sub>2</sub> @CNF and SiNP@void@CNF composite materials and anodes .....	92
5.1.2	Physiochemical characterization.....	94
5.1.3	Electrochemical Testing.....	98
5.2	Electroactive polymers based Si/CNT and Si/rGO anodes .....	101
5.2.1	Development of Si anodes using PEDOT:PSS as binder with various carbon additives .....	102
5.2.2	Physiochemical characterization.....	103
5.2.3	Electrochemical Testing.....	104
5.3	Conclusion .....	106
6	Towards Li metal free sulfur batteries .....	109
6.1	All carbon based Lithiated Silicon Sulfur full cell .....	109
6.1.1	Balancing of anode and cathode .....	110
6.1.2	Electrochemical Performance .....	110
6.2	Conclusion .....	112
7	Conclusion and Prospects .....	113
	References.....	117
	Appendix A.....	131



# List of Tables

Table 1. 1: Representative LIB cathode materials; their crystal structures, capacities, and median working potentials .....	2
Table 1. 2: Representative Li/S cathode materials; their architecture, sulfur content, and loading, and cycling performance .....	14
Table 1. 3: Representative interlayer strategies; interlayers compositions, corresponding sulfur content, and loading, and cycling performance .....	17
Table 1. 4: Representative binder for Li/S cathodes; type of polymer as binder, sulfur content and loading, and cycling performance .....	20
Table 1. 5: Representative Silicon anodes; anode material and architecture, Si content and loading, and cycling performance .....	22
Table 2. 1: Elemental analysis of MPC and C/S composites.....	33
Table 2. 2: Discharge capacities of CS composites reported for different cycles with different C-rate.....	38
Table 2. 3: Yield and textural properties polypyrrole-derived activated carbons .	43
Table 3. 1: Relative percentage of each of the Mn species present in the samples .....	68
Table 3. 2: Results of XPS of Binding Energy and energy separations for the 3s orbital of Mn. ....	68
Table 5. 1: ICP analysis of SSCNF.....	97
Table 5. 2: Various compositions and thicknesses of nSi and PEDOT:PSS with and without conductive agents .....	103
Table 7. 1: Performance matrix of as-prepared S cathodes architecture, sulfur content and loading, and cycling performance .....	116
Table 7. 2 : Performance matrix of as-prepared Si anodes architecture, sulfur content and loading, and cycling performance .....	116
Table 7. 3 : Performance matrix of Li metal free full cell realized using carbon matrices.....	116



# List of Figures

Figure 1.1: Specific capacities and operating potentials of different kind of cathode and anode materials for present and future Li-ion battery technologies.....	3
Figure 1. 2: Schematic illustration of the working mechanism and limitations associated with Li/S system.....	4
Figure 1. 3: a) Typical charge and discharge voltage profile of Li/S system b) illustration of different discharging events occurring at different voltages at the cathode.....	4
Figure 1. 4: a) Energy diagram of Li/S cell (sulfur as cathode and Li as an anode) with events of charging and discharging, b) typical cyclic voltammetry profile of Li/S cell.....	5
Figure 1. 5: A roadmap opted for the development of positive sulfur electrodes for Li/S system .....	8
Figure 1. 6: Graphic illustration of various cathode configuration approaches to suppress LiPS at the cathode .....	10
Figure 2. 1: Schematic depiction of the opted strategy to prepare rGO wrapped MPC/S composites.....	28
Figure 2. 2: Schematic illustration of the production steps to prepare rGO@MPC/S composites .....	29
Figure 2. 3: FESEM images of MPC prepared from $\beta$ -cyclodextrin nanosponge.....	31
Figure 2. 4: FESEM images of a) SI_CS b) MI_CS c) rGO@MI_CS (images are at a different scale to observe the typical structures present in the composites) ...	31
Figure 2. 5: FESEM images of a, c) bare MI_CS particles and b, d) rGO-wrapped MI_CS particles .....	31
Figure 2. 6: Secondary image and back-scattered contrast FESEM imaging of C/S composites a) SI_CS b) MI_CS c) rGO@MI_CS .....	32
Figure 2. 7: Sulphur mapping in C/S composites using EDS analysis for a) SI_CS b) MI_CS c) rGO@MI_CS.....	32
Figure 2. 8: Isotherms from BET analysis of a) MPC b) SI_CS c) MI_CS d) rGO@MI_CS.....	33
Figure 2. 9: a) XRD analysis of sulfur, carbon, and carbon sulfur composite b) illustration of sulfur distribution in rGO wrapped microporous carbon from the characteristics EDS, XRD and BET results.....	34
Figure 2. 10: Charge and discharge capacity of a) SI_CS b) MI_CS c) rGO@MI_CS with GF d) rGO@MI_CS with CFP for the first two cycles at 0.1C.....	36
Figure 2. 11: Long-term Galvanostatic cycling at 0.2C and Coulombic efficiencies of a) SI_CS b) MI_CS c) rGO@MI_CS with GF d) rGO@MI_CS with CFP .....	37

Figure 2. 12: Rate capability of the rGO@MI_CS composite with CFP as an interlayer .....	39
Figure 2. 13: Schematic illustration of the synthesis of N-doped and S-doped activated carbons from polypyrrole and polythiophene using KOH as an activating agent.....	40
Figure 2. 14: FESEM images of polypyrrole (PPyr) (a) and polythiophene (PThio) (d), PPyr based activated carbon (b), PThio-based activated carbon (e), sulfur-infused PPyr_C (c) and sulfur-infused PThio_C (f) .....	41
Figure 2. 15: EDS elemental mapping of S/PPyr_C composite .....	42
Figure 2. 16: EDS elemental mapping of S/PThio_C composite .....	42
Figure 2. 17: Nitrogen sorption isotherms (a) and pore size distribution (PSD) curves (b) of polypyrrole and polythiophene-based activated carbons .....	43
Figure 2. 18: High-resolution XPS spectra of PPyr based carbon, C 1s (a) and N 1s (b) and PThio based carbon C 1s (c) and S 2p (d).....	44
Figure 2. 19: XRD diffraction patterns (a) and Raman spectra (b) of elemental sulfur, PPyr_C/S and PThio_C/S composites.....	45
Figure 2. 20: TGA analysis of PPyr_C/S and PThio_C/S composites and their first order derivative to assess the quantity of sulfur .....	45
Figure 2. 21: a) cyclic performance (squares: specific capacity, stars: Coulombic efficiency) of S/C_PPyr and S/C_PThio composite, (b, c) voltage profile vs. specific capacity of S/C_PPyr (b) and S/C_PThio (c).....	47
Figure 3. 1: Schematic illustration of the synthesis strategy for carbothermal reduction of TiO <sub>2</sub> nanotubes to Magnéli phase TiO <sub>2n-1</sub> nanoparticle-embedded carbon host matrices (TiO <sub>2n-1</sub> NP@C). .....	51
Figure 3. 2: FESEM images of (a) TiO <sub>2</sub> NT (b) TiO <sub>2n-1</sub> @C, (c) TiO <sub>2n-1</sub> @C (secondary electron image), (d) TiO <sub>2n-1</sub> @C (back-scattered electron image), (e) Sulfur-infused TiO <sub>2n-1</sub> @C/S, and (f) Sulfur-infused TiO <sub>2n-1</sub> NP@C/S (SE) .....	52
Figure 3. 3: TEM images of (a) TiO <sub>2</sub> NTs, (b) TiO <sub>2n-1</sub> @C matrices and (c) TiO <sub>2n-1</sub> @C/S composites. HRTEM images of (d) TiO <sub>2</sub> NTs, (e) TiO <sub>2n-1</sub> @C matrices and (f) TiO <sub>2n-1</sub> @C/S composites taken at a magnification of 300 kx. SAED patterns of (h) TiO <sub>2</sub> NTs, (i) TiO <sub>2n-1</sub> @C matrices and (j) TiO <sub>2n-1</sub> @C/S composites acquired from the areas shown the inset images. The scale bar in the inset corresponds to 50 nm. (Blue corresponds to rutile TiO <sub>2</sub> , green corresponds to Ti <sub>9</sub> O <sub>17</sub> and red corresponds to elemental S).....	54
Figure 3. 4: EDS elemental mapping of sulfur-infused TiO <sub>2n-1</sub> @C/S matrix composite. ....	54
Figure 3. 5: (a) Nitrogen adsorption-desorption isotherms for TiO <sub>2n-1</sub> @C and TiO <sub>2n-1</sub> @C/S. (Inset) corresponding pore size measurements. (b)	

Thermogravimetric analysis of as prepared sulfur-infused $\text{TiO}_2\text{n-1@C/S}$ matrix. ....	55
Figure 3. 6: (a) XRD analysis of $\text{TiO}_2\text{n-1@C}$ and $\text{TiO}_2\text{n-1@C/S}$ composite (b) Experimental illustration of LiPS adsorption onto Magnéli phases $\text{TiO}_2\text{n-1}$ NPs loaded in a carbon matrix, in solution (c) XPS Ti 2p core-level photoemission spectra of $\text{TiO}_2$ NT, $\text{TiO}_2\text{n-1@C/S}$ and (d) S 2p core-level photoemission from charged and discharged $\text{TiO}_2\text{n-1@C/S}$ cathodes. ....	57
Figure 3. 7: (a) Cycling performance of $\text{TiO}_2\text{n-1@C/S}$ NP composite Li-S cathode electrodes at C-rates from 0.2C to 1C. (b) Corresponding discharge-charge profiles for each C-rate test. (c) Rate response of the $\text{TiO}_2\text{n-1@C/S}$ NP composite at 0.1C, 0.2, and 1C. (d) Corresponding discharge-charge profiles at 0.2 C up to 500 cycles. (e) 500 cycle performance and Coulombic efficiency and (f) Long term cycling behavior at a high C-rate of 1C for 1000 cycles. ....	59
Figure 3. 8: (a) First 3 cycles by the CV of Sulfur infused $\text{TiO}_2\text{n-1 NP@C/S}$ matrix cathode. ....	60
Figure 3. 9: (a-c) FESEM investigation of the surface of Sulfur infused $\text{TiO}_2\text{n-1 NP@C/S}$ cathode after 300 cycles. (d) EDX maps of the exhausted cycled $\text{TiO}_2\text{n-1 NP@C/S}$ cathode material confirming a similar elemental distribution compared to pristine as-synthesized material prior to galvanostatic cycling. ....	61
Figure 3. 10: Typical Voltage-time profile for electrochemical deposition of $\text{MnOOH}$ through anodic chronopotentiometry.....	62
Figure 3. 11: SEM images of electrodeposited $\text{MnOx}$ films on CCC treated at various temperatures and atmospheric conditions; a,b) 100 °C in air, c,d) 300 °C in air, e,f) 400 °C in air, g,h) 400 °C in argon i, j) 450 °C in air k,l) FESEM 300 °C in air .....	64
Figure 3. 12: HRTEM images of various deposited $\text{MnOx}$ films; a,b,c) 100 °C air d,e,f) 400 °C air g,h,f) 400 °C argon .....	65
Figure 3. 13: XRD diffraction patterns of various as-deposited $\text{MnOx}$ films .....	66
Figure 3. 14: a) Mn K edge XANES spectra for Mn reference compounds, energy edge position change with increasing valence value. b) Mn K edge XANES spectra for measured samples.....	66
Figure 3. 15: The calibration curve and the obtained valence state for the four measured samples. ....	66
Figure 3. 16: XPS spectra Mn 2p <sub>3/2</sub> of $\text{MnOx}$ samples. ....	67
Figure 3. 17: XPS spectra Mn 2p <sub>3/2</sub> of $\text{MnOx}$ samples that had different thermal treatments in the air.....	67
Figure 3. 18: Long-term Galvanostatic charge-discharge cycling performance of freestanding $\text{MnOx}$ deposited carbon fiber paper as a sulfur cathode.....	69

Figure 3. 19: Charge and discharge profiles of various synthesized freestanding MnOx deposited carbon fiber paper as a sulfur cathode a) MnOx_400°C_Ar b) MnOx_400°C_Air c) MnOx_300°C_Air d) MnOx_250°C_H2+Ar.....	70
Figure 3. 20: Long-term Galvanostatic charge-discharge cycling performance of freestanding MnOx deposited carbonized cellulose cloth as a sulfur cathode .....	71
Figure 3. 21: Charge and discharge profiles of various synthesized freestanding MnOx deposited carbonized cellulose cloth as a sulfur cathode a) MnOx-400°C_Ar b) MnOx-300°C_Air c) MnOx-450°C_Air d) MnOx-400°C_Air e) w/o MnOx deposition.....	72
Figure 3. 22: a,b) SEM images of VN/N doped carbon-graphene matrix; c,d) sulfur-infused VN/N doped carbon-graphene composite.....	74
Figure 3. 23: a) Thermogravimetric analysis of as prepared sulfur-infused VN/N doped carbon-graphene matrix .....	75
Figure 3. 24: a) XRD pattern of intermediate VOx/rGO complex, VN/N doped carbon-graphene matrix, sulfur-infused VN/N doped carbon-graphene composite b) Raman spectroscopy of VN/N doped carbon-graphene matrix, sulfur-infused VN/N doped carbon-graphene composite.....	75
Figure 3. 25: a) Experimental demonstration of LiPS adsorption capability of VN-N doped carbon composite b) XPS analysis of VN/N doped carbon-graphene matrix and LiPS adsorbed VN/N doped carbon-graphene matrix. ....	76
Figure 3. 26: (a) Cycling performance of VNNC/S composite Li-S cathode electrodes at C-rates from 0.2 C to 1 C. (b) Corresponding discharge-charge profiles at 0.2 C up to 500 cycles. (c) Rate response of the VNNC/S composite at 0.1C, 0.2, 1C and 2C. (d) Corresponding discharge-charge profiles for each C-rate test. and (e) Long term cycling behavior at a high C-rate of 1 C for 850 cycles with Coulombic efficiency.....	78
Figure 3. 27: First 3 cycles by the CV of VNNC/S cathode.....	79
Figure 4. 1: Chemical structures of different redox forms of polyaniline [179] ...	82
Figure 4. 2: Backside of HCl doped PANi@C/S composite coated Aluminum foils a) 3 times DI water and 3 times alcohol washed b) extensively washed with the bulk of DI water .....	83
Figure 4. 3: Scheme for the preparation of PANi wrapped KJBC/S composite....	84
Figure 4. 4: FESEM micrographs of a, c) KJBC/S b, d) PANi@KJBC/S .....	86
Figure 4. 5: TGA and DTG of a) KJBC/S composite, b) PANi@KJBC/S composite .....	86
Figure 4. 6: X-ray diffraction patterns of Ketjen Black Carbon (KJBC), Formate-ion doped PANi, KJBC/S composite, and PANi@KJBC/S composite.....	86

Figure 4. 7: XPS spectra of corroded Al coated with PANi-Cl composite and PANi-HCOOH composite.....	87
Figure 4. 8: Long-term Galvanostatic cycling performance (squares: specific capacity, stars: Coulombic efficiency) a) comparison of cycling performances of PANi@KJBC/S, S80/KJBC and S70/KJBC for 300 cycles, b) cycling performance of PANi@KJBC/S cathodes for 500 cycles.....	88
Figure 4. 9: Voltage capacity profiles of all three electrodes during long-term cycling test a) S80/KJBC b) S70/KJBC and c) PANi@KJBC/S.....	89
Figure 4. 10: C-rate capability test of S70/KJBC and PANi@KJBC/S composites a) Galvanostatic cycling performance and corresponding Coulombic efficiency at various current rates b) Voltage capacity profiles of charge and discharge at various currents.....	89
Figure 4. 11: first cycle of PANi@KJBC/S composite cathode by CV.....	90
Figure 5. 1: Schematic representation of as-configured Si anodes with all designs integrated strategy (i.e. Si nanoparticles with void spaces in CNF (SVCNF) and cross-linked alginate binder) and proposed a functioning mechanism.....	93
Figure 5. 2: FESEM images of as-spun SSCNF anode sheet (a,b) and just washed SVCNF anode composite (c,d) .....	95
Figure 5. 3: TEM imaging of SSCNF (a,b,c) and SVCNF (d,e,f) revealing the structural and morphological elements of the Si anode composites.....	95
Figure 5. 4: EDS mapping of SSCNF material to identify the composition of various localities in composite .....	96
Figure 5. 5: EDS mapping of SVCNF to confirm the presence of pure Si hosted in the void .....	97
Figure 5. 6: a) TGA analysis of SSCNF and SVSNF composites b) FTIR spectra of pristine alginate and CA crosslinked alginate.....	97
Figure 5. 7: a) XRD pattern of SSCNF and SVCNF b) Raman spectra of CNF, SSCNF, and SVSNF .....	98
Figure 5. 8: a) Cyclic performance (squares: specific capacity, stars: Coulombic efficiency) of nSi, SSCNF, and SVCNF anodes vs. lithium foil on basis of silicon contribution, b) half-cell performance of CNF, SSCNF, and SVCNF on the basis active material loading, voltage profile of c) SSCNF anode, d) SVCNF anode with nominal contribution of first cycle SEI formation.....	99
Figure 5. 9: a) a comparison of Galvanostatic performance of SVCNF anodes constructed using pristine alginate and CA crosslinked alginate b) long term cycling performance of SVCNF anode at current rate 1786 mA g <sup>-1</sup> in comparison to cycling performance SSCNF and nSi anode at current rate 716 mA g <sup>-1</sup> .....	101
Figure 5. 11: Molecular structure of PEDOT:PSS .....	102

Figure 5. 12: Snapshots of the anodes acquired by doctor blade coating with 50 $\mu\text{m}$ clearance on Cu foils for a) nSi/PEDOT:PSS b) nSi/rGO/PEDOT:PSS c) nSi/CNT/PEDOT:PSS .....	104
Figure 5. 13: SEM images of various as prepared Si anode a,b) nSi/PEDOT:PSS; c,d) nSi/rGO/PEDOT:PSS; e,f) nSi/CNT/PEDOT:PSS .....	104
Figure 5. 14: Galvanostatic cycling performance of nSi/PEDOT:PSS anodes a) effect of conductive additives b) effect of coating thickness using various doctor blade clearances c) effect of separator d) effect of electrolyte on cycling performance .....	105
Figure 5. 15: a) Long-term cycling performance of nSi/CNT/PEDOT:PSS electrodes; b,c) CV and EIS of nSi/CNT/PEDOT:PSS anodes using ALISE electrolyte; d,e) CV and EIS of nSi/CNT/PEDOT:PSS anodes using ILS electrolyte .....	106
Figure 6. 1: Balancing of lithiated SVCNF anodes vs. PPyr_C/S and PThio_C/S cathodes in terms of areal capacity and estimation of cut-off voltage for full cells .....	110
Figure 6. 2: a, c) Galvanostatic cycling performance and voltage vs. capacity profile of PPyr_C/S cathode against lithiated SVCNF anode, b, d) Galvanostatic cycling performance and voltage vs. capacity profile of PThio_C/S cathode against lithiated SVCNF anode .....	111

# List of Abbreviations

LIB	Lithium ion batteries
Li/S	Lithium sulfur technology
LiPS	Lithium polysulfides
C/S, CS	Carbon sulfur
SEI	Solid electrolyte interface
CV	Cyclic voltammetry
EIS	Electrochemical impedance spectroscopy
DME	1, 2-dimethoxyethane
DIOX	1, 3-dioxolane
LiTFSI	Lithium bis(trifluoromethanesulfonyl)imide
MPC	Microporous carbon
CF	Carbon fiber
CNF	Carbon nanofibers
GDL	Gas diffusion layer
CFP	Carbon fiber paper
CCC	Carbonized cellulose cloth/fabric
VNNC	Vanadium nitride/ nitrogen doped carbon
PPyr	Polypyrrole
PThio	Polythiophene
PANi	Polyaniline
PAN	Polyacrylonitrile
PP	Polypropylene

MWCNT	Multiwall carbon nanotubes
KJBC	Ketjen black carbon
NMP	N-methyl-2-pyrrolidone
PVDF	Polyvinylidene fluoride
EDX	Energy-dispersive X-ray spectroscopy
FE-SEM	Field emission scanning electron microscopy
HR-TEM	High-resolution transmission electron microscopy
XRD	X-ray diffraction
XPS	X-ray photoelectron spectroscopy
TGA	Thermogravimetric analysis
NP	Nanoparticles
NT	Nanotubes
rGO	reduced Graphene oxide
PEDOT:PSS	Poly(3,4-ethylenedioxythiophene) polystyrene sulfonate
ICP-MS	Inductively coupled plasma – mass spectroscopy
BET	Brunauer–Emmett–Teller
XANES	X-ray absorption near edge structure
CA	Citric acid
OCP	Open circuit potential
SSCNF	nano Silicon@ silica@ carbon nanofibers
SVCNF	nano Silicon@ void@ carbon nanofibers

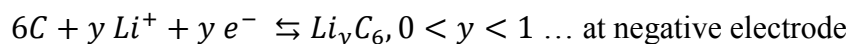
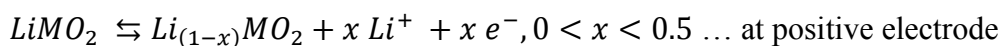
# Chapter 1

## Introduction: State of the art

### 1.1 Introduction to Li-ion battery (LIB) technologies

Continuous depletion of fossil fuels' resources and ever-increasing environmental concerns have challenged humanity to look for an alternative, sustainable and clean energy solutions. The scientific community has been since then involved in the problem, and vigorously explored solar, wind and wave energies to provide clean alternatives to society. Researchers started successfully harvesting these energy sources for both stand-alone facilities and national grids. But, powering the vehicles and power tools directly from these sources is not possible to date, unless researchers come up with the solution to store energy from these clean sources directly or indirectly. Li-ion batteries (LIBs), owing to high energy and power density, have materialized as an ultimate electrochemical energy storage choice for portable devices, power tools, electrical vehicles, and smart grid applications [1].

Typically, LIBs are comprised of an intercalating positive electrode (cathode) made of layered transition metal oxide ( $\text{LiMO}_2$ ) and a negative electrode (anode) made of carbon graphite separated by a polyolefin separator soaked in an electrolyte that is a mixture of alkyl carbonate organic solvents (ethylene carbonate-dimethyl carbonate (EC-DMC)) and a lithium salt ( $\text{LiPF}_6$ ). The reversible electrochemical reactions at both electrodes are as follows:



The LIB cathode materials are lithium containing transition metal oxides, where Li ions can be diffused freely through the crystal structure. These oxides can be categorized as one, two or three-dimensional based on crystal structures that are also determinant of number of intercalation dimension. Various LIB cathode materials are reported in Table 1.1 with their specific and volumetric capacities. LIB anode materials are majorly dominated by graphite and hard carbon. Graphite

is the most dominant anode material that is characterized by flat discharging profile. Among graphite, modified natural graphite is leading followed by mesophase and synthetic graphite. The theoretical gravimetric capacity of carbon anode materials is limited to some 372 mAh g<sup>-1</sup> [2]. Another anode material is lithium titanium dioxide Li<sub>4</sub>Ti<sub>5</sub>O<sub>12</sub> (LTO) with a lower capacity of 170 mAh g<sup>-1</sup>, yet it is a commercial choice because of the zero-strain intercalation mechanism [3]. Silicon and tin-based anode materials are in rigorous research because of their high theoretical capacities (i.e. 3579 and 994 mAh g<sup>-1</sup> respectively) [2]. The gravimetric or volumetric energy density (Wh kg<sup>-1</sup> or Wh L<sup>-1</sup>) is one of the most important criteria to evaluate the battery's performance along with power density. LIB has successfully revolutionized the era of portable devices. LIB based electrical vehicles (EVs) also started diffusing into the market with some impact. Yet, there are always debates about the sustainability, safety, and efficiency of the proposed solution. LIBs impose a practical limit to the mileage of these vehicles on a single charge. The energy density of LIBs is practically limited to 250-300 Wh kg<sup>-1</sup> at pack level [4]. Secondly, LIB are always questioned for their safety and cost (300 \$ kW h<sup>-1</sup>), mainly because of cobalt [5, 6].

**Table 1. 1:** Representative LIB cathode materials; their crystal structures, capacities, and median working potentials

Crystal structure	Compound	Specific capacity (theoretical/experimental) (mAh g <sup>-1</sup> )	Volumetric capacity (theoretical/practical) (mAh cm <sup>-3</sup> )	Median voltage (V)
<b>Layered (2D) structures</b>	LiCoO <sub>2</sub> (LCO)	274/148	1363/550	3.8
	LiNiO <sub>2</sub>	275/150	1280	3.8
	LiMnO <sub>2</sub>	285/140	1148	3.3
	LiNi <sub>0.5</sub> Mn <sub>0.5</sub> O <sub>2</sub>	280/170	-	3.6
	LiNi <sub>0.33</sub> Mn <sub>0.33</sub> Co <sub>0.33</sub> O <sub>2</sub> (NMC)	280/160	1333/600	3.7
	LiNi <sub>0.8</sub> Co <sub>0.15</sub> Al <sub>0.05</sub> O <sub>2</sub> (NCA)	279/199	1284/700	3.7
	Li <sub>2</sub> MnO <sub>3</sub>	458/180	1708	3.8
<b>Spinel (3D) structures</b>	LiMn <sub>2</sub> O <sub>4</sub> (LMO)	148/120	596	4.1
	LiCo <sub>2</sub> O <sub>4</sub>	142/84	704	4.0
<b>Olivine (1D) structures</b>	LiFePO <sub>4</sub> (LFP)	170/165	589	3.4
	LiMnPO <sub>4</sub>	171/168	567	3.8
	LiCoPO <sub>4</sub>	167/125	510	4.2

## 1.2 Introduction to Li/S technology

As highlighted, typical Li-ion technologies cannot meet the high-energy demands for systems such as smart grids and electrical transportation, as their energy density is practically limited to  $300 \text{ W h kg}^{-1}$ . Li-S batteries emerged as a prospective solution to the issue due to their remarkably high specific energy value ( $2600 \text{ W h kg}^{-1}$  or  $2800 \text{ W h L}^{-1}$ ) that is  $> 5$  times to the available Li-ion technology [7, 8]. The reversible electrochemical conversion of sulfur ( $\text{S}_8$ ) into  $\text{Li}_2\text{S}$  through a series of lithium polysulfides (LiPS) derives the high-energy Li-S system. Natural abundance of elemental sulfur in the Earth's crust makes Li-S technology an attractive low cost alternative to Li-ion batteries. Sulfur cathode exhibits conversion chemistry and stands prominent in the matrix of both insertion and conversion type cathode materials because of high specific capacity ( $1672 \text{ mAh g}^{-1}$ ).

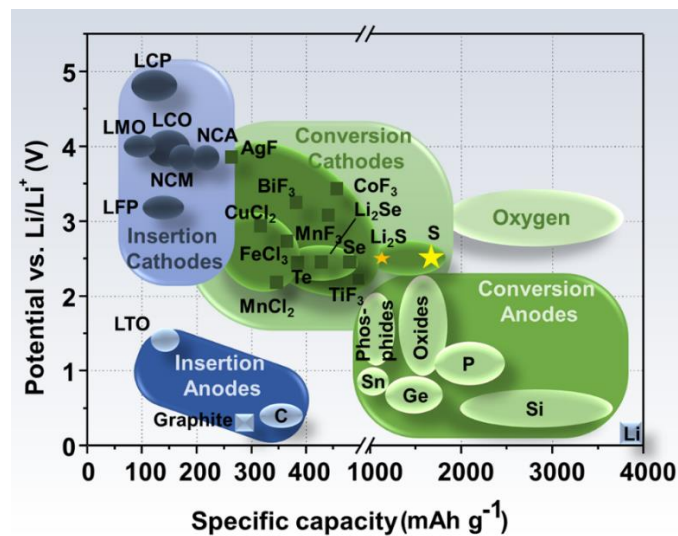


**Figure 1.1:** Specific capacities and operating potentials of different kind of cathode and anode materials for present and future Li-ion battery technologies

### 1.2.1 Operational mechanism of Li/S batteries

A conventional Li/S cell is composed of a carbon/sulfur cathode, a Li or lithiated anode and a liquid electrolyte placed in between two electrodes parted by a separator. Discharging involves both electrochemical and chemical (disproportionation) reactions. The sulfur ( $\text{S}_8$ )-containing cathode typically discharges in two plateaus; the first plateau (relatively smaller) appears at a voltage around 2.3 V vs.  $\text{Li}^+/\text{Li}$ , corresponding to  $\text{S}_8$  reduction to  $\text{Li}_2\text{S}_8$  to  $\text{Li}_2\text{S}_6$ . Then, there is a transition between 2.3 and 2.1 V, which is associated to the conversion of long chain PS ( $\text{Li}_2\text{S}_n$ ,  $n > 4$ ) to medium chain PS ( $\text{Li}_2\text{S}_n$ ,  $n \leq 4$ ). A second long plateau occurs at 2.1 V vs.  $\text{Li}^+/\text{Li}$  linked to the transformation of  $\text{Li}_2\text{S}_4$  to  $\text{Li}_2\text{S}_2$  and finally  $\text{Li}_2\text{S}$  [9, 10]. The whole process is depicted in figure 3. Charging of sulfur cathode takes place at 2.3 and 2.4 V to shift back to  $\text{S}_8$  from  $\text{Li}_2\text{S}$  again through a series of LiPS. The reactions at the two electrodes can be simply represented as follows:



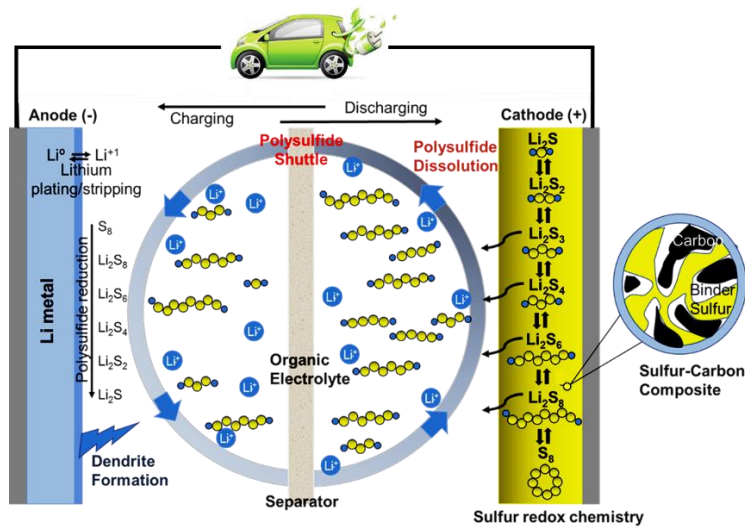
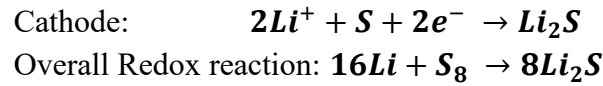


**Figure 1. 2:** Schematic illustration of the working mechanism and limitations associated with Li/S system

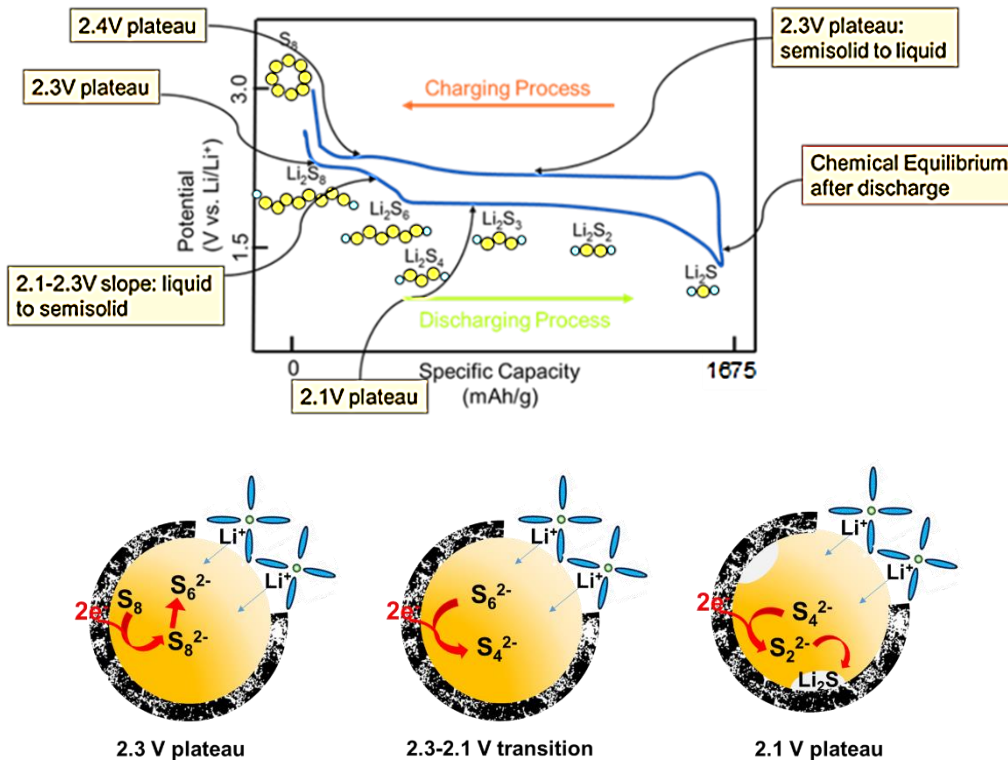


**Figure 1. 3:** a) Typical charge and discharge voltage profile of Li/S system b) illustration of different discharging events occurring at different voltages at the cathode

At open circuit potential (OCP,  $\Phi_{oc}$ ), the potential difference arises from the electrochemical potentials of lithium anode ( $\Phi_a$ ) and  $S_8$  cathode ( $\Phi_c$ ) (figure 1.4a). On discharging,  $S_8$  shows two reductions peaks in cyclic voltammetry to transform into  $Li_2S$ . Discharging brings sulfur cathode at lower electrochemical potential. On

charging, oxidation of  $\text{Li}_2\text{S}$  to  $\text{S}_8$  happens with a broad oxidation peak with a shoulder around 2.4 V and battery is again at  $\varnothing_{oc}$  (Figure 1.4b).

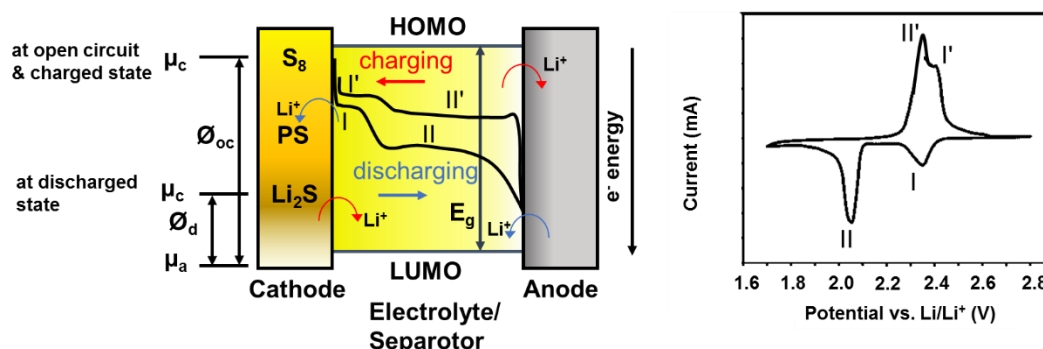


**Figure 1. 4:** a) Energy diagram of Li/S cell (sulfur as cathode and Li as an anode) with events of charging and discharging, b) typical cyclic voltammetry profile of Li/S cell

## 1.2.2 Challenges to Li/S battery system

Li/S battery technology is presently facing several setbacks that result in poor cycle life. Some of the drawbacks in Li/S technology include (i) low degree of sulfur utilization, (ii) fast capacity fading, (iii) poor rate capability and (iv) low Coulombic efficiency [10]. These limitations arise from all three active components (i.e. sulfur cathode, a lithium anode, and electrolyte) of Li/S cell.

### Limitations from the sulfur cathode

The terminus products of Li/S cell (i.e.  $\text{S}_8$  and  $\text{Li}_2\text{S}$ ) are very insulating in nature. The literature reported conductivities are  $5 \times 10^{-18} \text{ S cm}^{-1}$  and  $10^{-15} \text{ S cm}^{-1}$  for  $\text{S}_8$  and  $\text{Li}_2\text{S}$  respectively. This makes essential the use of some conductive structures to ensure electronic conduction pathways. Free solubility of intermediate LiPS ( $\text{Li}_2\text{S}_n$ ,  $n = 4-8$ ) in liquid electrolyte causes the elimination of active material from the electrode surface. Dissolution of LiPS also causes the shuttle of sulfur species to the anode where they chemically reduce to  $\text{Li}_2\text{S}$  (figure 1.2) and result in progressive decay of cathodic and anodic active materials [11]. There is an increase in the volume of the cathode active material that causes morphological disruption. If the volume change is not buffered, then there will be a lack of morphological restoration and result in loss of active materials. This limitation obliges the use of highly porous matrices that in turn demand a high amount of electrolyte for correct operation [8, 10].

### Limitations originated from the anode

At present, the non-availability of high capacity negative electrodes directs the use of lithium (Li) metal as a counter electrode. Li can be considered as an ideal anode material for high-energy storage system because of its exceptionally high theoretical specific capacity ( $3860 \text{ mAh g}^{-1}$ ), low density ( $0.534 \text{ g cm}^{-3}$ ) and the lowest negative electrochemical potential ( $-3.040 \text{ V vs. SHE}$ ). Nevertheless, Li anodes are subjected to uncontrolled dendritic growth and poor Coulombic efficiency (C-efficiency) [12]. Dendritic growth on the surface of Li results in short

circuits and consequently, a big safety hazard is entitled. On the other side, this dendritic growth also results in dead Li whose outcome is short cycle life. Poor C-efficiency in such a system arises electrolyte degradation due to interaction with active Li surface [12-14]. These issues either can be resolved by protecting the Li surface, hindering the dendritic growth as well as preventing the electrolyte from coming in direct contact with Li surface, or by developing new high capacity anodes like silicon (Si) or SnO<sub>2</sub>. Si anode theoretically exhibits very high theoretical capacity (4200 mAh g<sup>-1</sup>) but the process of alloying into Li<sub>4.2</sub>Si and de-alloying results in abrupt morphological changes, thus quick loss of active material from the electrode surface. SnO<sub>2</sub> based electrodes also show the reasonably high specific capacity of 782 mAh g<sup>-1</sup> but these anode materials also require rigorous synthesis and are subjected to fast decay as Si [13].

### **Limitations associated with the electrolyte system**

Sulfur and its redox species one way or another are soluble in the electrolyte system, thus resulting in undesirable products that constrain the correct operation of the battery. So, the selection of electrolyte and additives plays a critical role in the final performance of the device. Currently, the combination of binary organic solvents with some lithium salt has been widely opted as an electrolyte to discern the performance of Li/S batteries. The most relevant properties of electrolyte solvent are their dielectric constant, viscosity, electrochemical stability, and donor number; those, in turn, determine the LiPS solubility, mobility, and dissociation. So, the most relevant solvent for Li/S should be with high donor number, low dielectric constant to lithium salts and LiPS, stable towards the nucleophilic attack of LiPS and highly viscous to reduce the LiPS solubility. Ether-based solvents fulfill these criteria significantly. So, the most commonly employed electrolyte system is a combination of linear and/or cyclic ethers such as 1,2-dimethoxyethane (DME), diethylene glycol dimethyl ether (diglyme, DEGDME), tetraethylene glycol dimethyl ether (tetraglyme, TEGDME), polyethylene glycol dimethyl ether (PEGDME) and 1,3-dioxolane (DOL) etc with some Li salt such as LiTFSI or LiClO<sub>4</sub> [15-18]. LiClO<sub>4</sub> was not able to make its ways because of safety hazards. In addition to these, LiNO<sub>3</sub> is also part of most electrolyte systems as an additive. LiNO<sub>3</sub> somehow is considered a solid electrolyte interface (SEI) promoter on solid lithium surface to suppress the LiPS reactivity and inhibit the moss-like growth on Li surface [19, 20]. The major drawback arises from this system is the solubility of LiPS in it. LiPS are freely soluble in present-day electrolyte system, thus, they can shuttle to across the system and results in the fast capacity fade. Shuttling of LiPS give rise to continuous loss of active material at the anode as Li<sub>2</sub>S. The shuttle phenomenon arises from concentration gradient within a cell that can be observed as prolonged charging due to recurring redox reactions, thus effect in low Coulombic efficiency [11, 21]. Poor rate capability performance also originates from the electrolyte system, as soluble LiPS alters the electrolyte ionic conductivity and impedes the mass transport. In addition to LiPS, there is the presence of radical species, such as S<sub>3</sub><sup>•-</sup>, that can reportedly react with carbonates based solvents irreversibly [22], whilst reaction is not happening in solid state [17, 23]. Different

electrolytes altogether exhibit different solubility towards sulfur and LiPS, hence there is a noteworthy change in working behavior of the system. Ether-based electrolytes are most widely accepted and preferred over other solvents sulfolanes [18, 24] and tetrahydrofuran (THF) [25]. In dimethyl sulfoxide, sulfur can only be reduced to  $S_4^{2-}$  species that results in poor efficiency, while THF with 100% efficiency exhibit thermodynamic instability towards bare Li metal. The composition of different electrolyte systems will be discussed in the coming section. Electrolyte to the sulfur ratio (E/S) is also one of the critical determinants of Li/S cell performance [26]. High E/S greatly contributes towards the initial high capacity values due to better solubility of LiPS but results in low energy density and may cause faster capacity decay initially. On another hand, low E/S promotes a stable performance but causes low sulfur utilization

### 1.3 Approaches to improve Li/S battery technology – A critical review

Several methodologies are proposed to make  $S_8$ ,  $Li_2S$  [27] and LiPS accessible for electrochemical reactions. Most of the research work is dedicated to designing the cathode materials for Li-S system, where sulfur is typically embedded into conductive (ionic and electronic) matrices. There exist two main strategies to improve the performance of sulfur cathodes; the first involves the physical confinement of sulfur, and the second is associated with chemical binding of LiPS. Porous carbon matrices are studied as effective scaffold materials to entrap sulfur and its species owing to their higher specific surface area, lightweight and conductivity. The most frequently reported carbon matrices are microporous, mesoporous carbons, carbon nanotubes, carbon nanofibers, and graphene. Nevertheless, the non-polar character of carbon limits the chemical immobilization of LiPS at the cathode. Other confinement methods involve the wrapping of sulfur/carbon or sulfur nanoparticles in conductive polymers such as polyaniline, polypyrrole, polyacrylonitrile. Here, LiPS are also physically immobilized to alleviate the shuttling effect. However, in certain cases, sulfur is covalently bonded to polymer structures. The recent investigations involve the use of sulfiphilic frameworks such as metal oxides, metal chalcogenides, metal nitrides, metal carbides, MXene,  $C_3N_4$  [28] where the LiPS are chemically immobilized to the positive electrode. Metal structures such as  $TiO_x$ ,  $SiO_2$ ,  $Al_2O_3$ ,  $MnO_x$ ,  $MgO$ ,  $V_2O_5$ ,  $MoS_2$ ,  $TiN$  are considered as effective media to adsorb sulfur and its species owing to intrinsic polar hydrophilic surfaces. Such metallic compounds can interact with LiPS via chemisorption or can exhibit acid-base interactions and/or form a surface-bound active redox mediator [29, 30]. Other methodologies involve the induction of interlayers, coating and/or modification of separators and selection of electrolyte systems to lower LiPS solubility. Modified separators and interlayers proved significantly effective in trapping and blocking LiPS to reduce the parasitic reactions at the anode. Altering the chemistry of inactive binders, as previously reported, could turn them into interactive matrices where LiPS can be detained

through electrostatic interactions. Lastly, the protection of Li anode surface or construction of a new type of anodes is pivotal in realizing the safe and long life Li/S batteries.

### 1.3.1 Cathode configurations

Sulfur-based cathodes can be obtained using three different forms of active materials including the allotropic forms of sulfur,  $\text{Li}_2\text{S}$  or polysulfides. Various strategies and configurations are opted to assemble sulfur cathodes include porous structures, sponges, foams or aerogels, sandwiched, layered or stacked structures, hollow spherical structures, core-shell/yolk-shell nanostructures, metal as electrocatalyst or integrated strategies. Figure 1.5 shows the roadmap for d Li/S cathode development along the course of research.

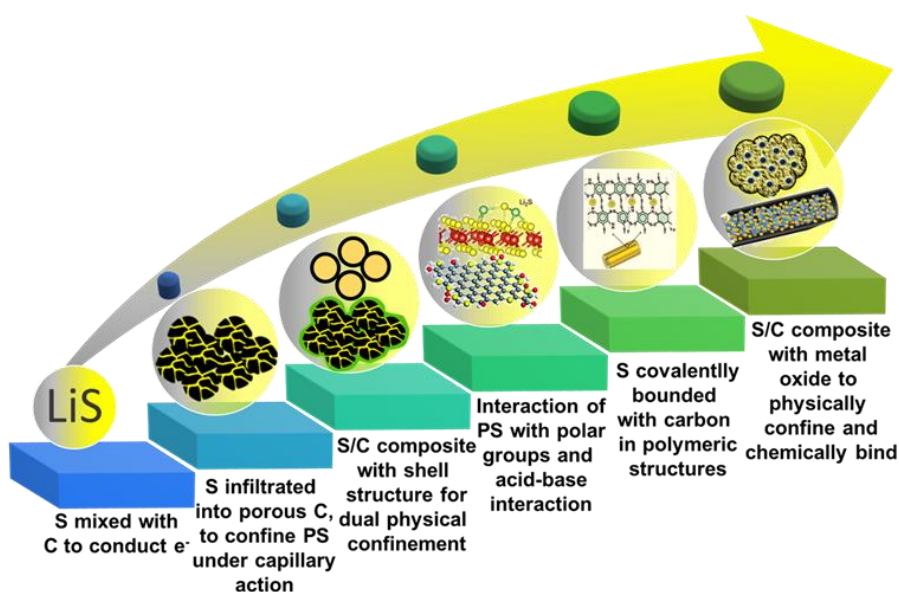


**Figure 1. 5:** A roadmap opted for the development of positive sulfur electrodes for Li/S system

### Carbon-based assemblies

Carbon materials unarguably are the most employed structures as host materials for sulfur cathodes owing to their intrinsic conductivity and design flexibility. Carbons can physically host sulfur and its species in their porous structures, and provide electronically conductive pathways to realize the electrochemistry of insulating sulfur. Carbons have been exploited as sulfur cathodes with reference to dimension possibilities, form and amount of porosity, kind and degree of functionality and level of graphitization as illustrated in Figure 1.6 [31]. Sulfur cathodes have been realized with zero-dimensional solid or hollow carbon spheres, one dimensional (1D) carbon nanotubes (CNT) and nanofiber, two dimensional (2D) graphene or three-dimensional (3D) carbon aerogels and sponge structures. Poor electronic conductivity of sulfur inevitably urges the use of conductive carbon particles such as carbon black or acetylene black to pursue the reversible electrochemical reaction of sulfur. Carbon in such form will not directly lessen LiPS dissolution and shuttling

at any level. However, the use of high surface area porous carbons can do the trick by accommodating the sulfur and its species into the pores analogous to micro-reactors thus effectively contribute towards lower LiPS dissolution, leading to the suppression of shuttling phenomena. A pioneer work was done by Nazar group in which they successfully cycled the sulfur cathode prepared by melt infusing sulfur into CMK-3 highly order mesoporous carbon [32]. Mesoporous carbons have been considered ideal because of their small dimensions that allow the physical confinement of elemental sulfur and its species. Xiao and co-workers have demonstrated that pore structure and volume have a little contribution to cathode performance. This has been attributed to the fact that mainly the electrochemical reactions take place at the interface between carbon and sulfur as shown in Figure 1.3b [33]. So, the large surface area appears the most decisive factor owing to higher kinetics and intimate contact. However, microporous carbons are also considered effective because of their very small dimension as sulfur can only be accommodated in smaller sulfur allotropic forms such as  $S_2$ ,  $S_3$ ,  $S_4$  [34]. Hierarchically porous carbons offer the advantages of all dimension confinement capabilities synergistically [35]. Level of graphitization determines the conduction proficiency of carbon, hence ensures better sulfur utilization and high rate capability by diminishing polarization. Carbon materials are characterized as a non-polar class of materials, hence carbon surface shows no chemical interaction towards LiPS. Carbon surfaces can be polarized by introducing heteroatoms such as O, N, S, and B to realize the LiPS interactions. Introduction of oxygen poses a detrimental effect because it reduces the conductivity and promotes side reactions with sulfur species. However, nitrogen doped carbons have shown promising contribution towards the enhancement of battery performance because of polar interactions with LiPS [36]. 1D-carbon materials include carbon nanofibers (CNFs) [37-39] and CNTs [40-42] have been surveyed as a host material for the sulfur cathode. These structures offer a larger surface area, high conductivity, and mechanical strength. Hollow, porous and surface modified CNFs structures were among studied materials while in the case of CNTs defected and surface doped tubes have been examined. 2D graphene and graphene oxide (GO) carbon structures have also been investigated by design of various architectures. Although these 2D structures offer high plane conductivity and larger surface area, yet they are not suitable as it is to contain LiPS unless architected with spatial symmetry. Some of the examples are core-shell graphene or GO/ sulfur composite [43, 44], unstacked double-layer templated graphene [45] etc. GO offers the possibility of chemically interacting with LiPS, but on another hand, it reduces the conductivity linked to graphene. Nitrogen-doped graphene showed a greater potential as a host material for sulfur cathode [46]. 3D carbon scaffolds also emerged as a prospective candidate to host sulfur. Such frameworks are usually assembled using 1D and/or 2D carbon structures [47, 48]. Hybrid/composite approaches such as rGO/CNT, graphene/CNF have also been considered with remarkable performance [39, 49, 50].

## Conducting polymers confinements

Conductive polymers such as polyaniline (PANI) [51, 52], polypyrrole (PPyr) [51, 53-55], poly(3,4-ethylenedioxythiophene) PEDOT [51, 56, 57], polythiophene (PThio) [58], and polyacrylonitrile (PAN) [59] have also been investigated as host materials for sulfur cathodes owing to their conductivity, physical confinement capability and possibly chemical interactions originate from polar bonds. Various reports have addressed the wrapping of carbon/sulfur composites with such conductive polymers to take advantage from the synergy between them [54, 56], while some others opted the coating of such polymers around bare sulfur nanoparticles [51, 55]. Earlier investigations related to this group of cathodes were limited to a small number of cycles mainly because of aggregation and dissolution of elemental sulfur. However, recent reports have shown remarkable cycling performance by designing the molecular level composite [60]. This is achieved by decreasing the particle size to nano-dimension and consistent wrapping of those that in turn suppress the LiPS shuttling. For example, Ma et al. have reported PANi/S composites that were prepared by vapor phase infusion of sulfur into hollow PANi sphere. They have successfully displayed 1000 charging and discharging cycles with capacity retention of 602 mAh g<sup>-1</sup> at 0.5C [61]. It can be deduced that conductive polymers have not superseded their carbon or inorganic counterparts in performance, but their scalable and moderate synthesis conditions have favored their exploration.

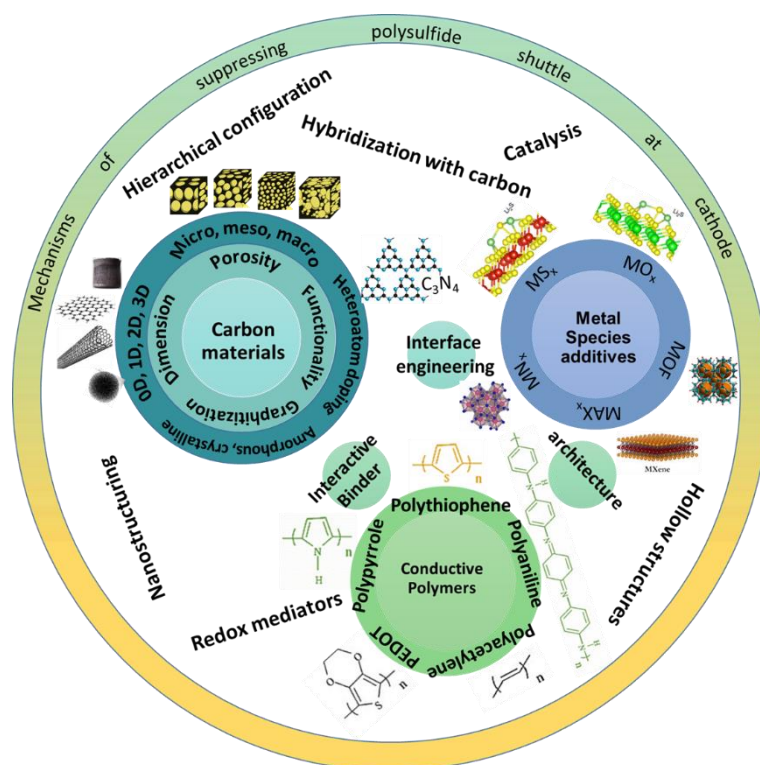
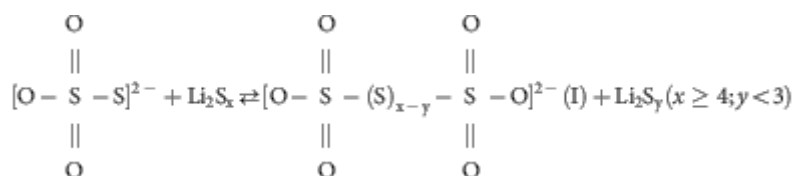


**Figure 1. 6:** Graphic illustration of various cathode configuration approaches to suppress LiPS at the cathode

### Inorganic formulations: Metal compounds

Metal compounds have been studied intensively in last three years as promising candidates to host sulfur in lithium-sulfur batteries. It is believed that these materials bear sulfiphilic surfaces and contribute to surface enhanced redox chemistry or capability to spatially locate  $\text{Li}_2\text{S}$ . These compounds open the horizon for new strategies to trap LiPS. Metal oxides such as  $\text{TiO}_x$ ,  $\text{SiO}_2$ ,  $\text{Al}_2\text{O}_3$ ,  $\text{MnO}_x$ ,  $\text{VO}_x$ ,  $\text{NiO}$ ,  $\text{Cu}_2\text{O}$ ,  $\text{FeO}_x$ ,  $\text{CoO}_x$ ,  $\text{MoO}_3$  are recognized as effective matrices to adsorb sulfur and its species owing to intrinsic polar hydrophilic surfaces of oxides. Morphologically these metal oxides occur as 2D materials but still show good cyclic performance in Li/S batteries as sulfur species can be chemisorbed, exhibit acid-base interactions and/or form a surface-bound active redox mediator. In various studies, optimized Li/S cells using metal oxides show a very low capacity degradation (i.e. less than 0.05% per cycle). Various interactions between metal oxides and polysulfides have been pointed out in the literature using the “Goldilocks” principle [30]. According to this principle, metal oxides or similar materials such as graphene oxide that possess the redox potential above a threshold (i.e. 2.4 V) would oxidize polysulfides to thiosulfates or sulfates and those with redox potential less than 2.1 V have no redox interaction with polysulfides as indicated in Figure 7. For example, a number of metal oxides ( $\text{NiO}$ ,  $\text{Cu}_2\text{O}$ ,  $\text{CoO}$ ,  $\text{TiO}_2$ ,  $\text{Ti}_4\text{O}_7$ ,  $\text{Fe}_2\text{O}_3$ , and  $\text{Fe}_3\text{O}_4$ ) with redox potential lower than 1.5 V exhibits no chemical reaction with LiPS. These metal oxides with low redox potential can retain LiPS mostly with polar interactions. Nazar and coworkers reported two metal oxides  $\text{VO}_2$  and  $\text{CuO}$  with redox potential between 2.4 and 3 V that can selectively initiate the oxidation of polysulfides into thiosulfates ( $\text{S}_2\text{O}_3^{2-}$ ). Thiosulfates play a vital role in chemically trapping soluble LiPS by catenating them as polythionate complex as indicated in the following equation [30, 62]. These polythionates are reclaimed on oxidation and perform their role during charging. Oxides with redox potential above 3.4 V such as  $\text{V}_2\text{O}_5$  or  $\text{NiOOH}$  over-oxidizes the polysulfides into sulfates ( $\text{SO}_4^{2-}$ ), which has no role in trapping the polysulfides.  $\text{V}_2\text{O}_5$  can also be used as metal oxide with only polar interaction by running the cell at lower voltage window and avoiding the accumulation of inactive sulfates. Although  $\text{V}_2\text{O}_3$  has lower redox potential, yet it can trigger thiosulfate formation because it is unstable in an oxidation environment and possess 4+ or 5+ oxidation states of vanadium on the surface [30].



Liang et al studied three different graphene metal oxides composite materials to host sulfur for Li/S cells.  $\text{Co}_2\text{O}_3$ -graphene exhibited the fast capacity decay (i.e. 0.34% per cycle over 250 cycles) due to the polarization of oxide. Whilst  $\text{V}_2\text{O}_5$ -graphene and  $\text{VO}_2$ -graphene Li/S cells show competitive performance for the initial 150 cycles with capacity retention of 76% and 74%. Afterward, their performance

falls apart due to the utilization of polysulfides into sulfates by  $V_2O_5$  as mention in the previous argument. On another hand, VO<sub>2</sub>-graphene Li/S cell continued cycling for 1000 cycles with capacity decay of 0.058% per cycle. However, by tuning the voltage window for  $V_2O_5$  spheres based S cathode from 1.8-3.0 V to 1.8-2.5 V, it became possible to cycle the cell for 300 cycles with a capacity decay 0.048% per cycle by avoiding the over-oxidation problem as shown in the figure [30]. In a study, it has also been demonstrated that  $\delta$ -MnO<sub>2</sub> nanosheets loaded with 75% sulfur exhibited the specific capacity of 1300 mAh g<sup>-1</sup> and fades at 0.036% per cycle over 2000 cycles. This milestone performance from MnO<sub>2</sub> cannot be referred to chemisorption, instead, it is understood that MnO<sub>2</sub> interacts with LiPS to produce intermediates such as thiosulfates. As discussed earlier, these thiosulfates species anchor the high order polysulfides by catenating to give rise to surface-bound polythionate complexes, and a further reduction to Li<sub>2</sub>S and lower polysulfide is achieved through disproportionation. This mechanism prevents the polysulfide dissolution and shuttling for stable and long term cycling [62].

Surface coordination greatly influences the polysulfide binding to metal oxides. Yi Cui et al revealed that conductive Magnéli phases  $Ti_nO_{2n-1}$  ( $3 < n < 10$ ) such as  $Ti_4O_7$  has good binding capability for sulfur species at low coordinated Ti centers in contrast to  $TiO_2$  termed as Sulfiphilic. Magnéli demonstrated that the structure of  $Ti_nO_{2n-1}$  is analogous to that of edge-shared  $TiO_6$  octahedra in rutile except the sharing of every nth octahedron due to the Ti reduction and the resulting oxygen vacancies as shown in the figure. In  $Ti_4O_7$ , Ti atoms at surface show coordination of 4, 5 and 6, where only 37.5% of atoms are coordinated to six (saturated bonding) remaining 62.5% are bonded chemically in unsaturated mode. Secondly, Ti with coordination number 5 in  $Ti_4O_7$  is easily available for interaction as they lie in step sites in contrast  $TiO_2$  where they are on terrace sites. Thus, reduction of  $TiO_2$  imparts the electrical conductivity and provides the structure for strong interaction of sulfur based species because of oxygen like valence characteristics. The initial discharge capacity of  $TiO_2$ -S,  $Ti_6O_{11}$ -S, and  $Ti_4O_7$ -S were reported 701, 713, and 1044 mAh g<sup>-1</sup>, respectively at 0.1C with C efficiency 96%. The capacity retention for  $Ti_6O_{11}$  and  $Ti_4O_7$  was reported 89% and 99% respectively in comparison to  $TiO_2$  with retention lower than 58% for 100 cycles [63].

Transition metal sulfides such as  $TiS_2$ ,  $ZrS_2$ ,  $VS_2$ ,  $FeS_2$ ,  $NbS_2$ ,  $MoS_2$ ,  $SnS_2$  were also investigated as host materials for the sulfur cathode in Li/S batteries [64]. Metal sulfides exhibit higher conductivity than that of metal oxides, even carries metallic and half metallic phases. Seh et al. have reported 2D transition metal disulfides such as  $TiS_2$ ,  $VS_2$ , and  $ZrS_2$  as effective host materials for  $Li_2S$ . In particular, they have reported very good performance for  $TiS_2$  encapsulated  $Li_2S$  showing the specific capacity of 503 mAh g<sup>-1</sup>  $Li_2S$  under 4C with capacity decay less than 0.058% per cycle and high areal capacity of 3.0 mAh cm<sup>-2</sup> under high mass-loading conditions (5.3 mg $Li_2S$  cm<sup>-2</sup>).  $TiS_2$  good performance as a host material for sulfur is attributed to high conductivity and polar Ti-S bonds that can potentially interact strongly with LiPS and  $Li_2S$ . The results of the ab initio simulations point out strong

Li–S as well as strong S–S interaction. The binding energy between  $\text{Li}_2\text{S}$  and a single layer of  $\text{TiS}_2$  was estimated 2.99 eV that is 10 folds higher than that between  $\text{Li}_2\text{S}$  and a single layer of graphene (0.29 eV).  $\text{Li}_2\text{S}@Zr\text{S}_2$  and  $\text{Li}_2\text{S}@V\text{S}_2$  core-shell structures also exhibited high initial specific capacities of 777 and 747mAh/g  $\text{Li}_2\text{S}$  at 0.2C with capacity retentions of 85% and 86% respectively after 100 cycles, which are much higher than bare  $\text{Li}_2\text{S}$  cathodes (66% after 100 cycles) [65].

Pang et al exhibited a metallic cobalt sulfide  $\text{Co}_9\text{S}_8$  as a host material with a graphene-like interconnecting nanosheet architecture. The cathodes assembled using  $\text{Co}_9\text{S}_8$  showed excellent electrochemical performance with an initial discharge capacity of 890 mAh  $\text{g}^{-1}$  with a fading rate of 0.045% per cycle over 1500 cycles at C/2. This performance is delegated to metallic conductivity ( $290 \text{ S cm}^{-1}$ ) due to the existence of peritectic phase in the Co–S phase diagram, and hierarchal porosity of 3D structured  $\text{Co}_9\text{S}_8$  nanosheets that imparts superior adsorptivity for LiPS. The absorptivity of LiPS with  $\text{Co}_9\text{S}_8$  is far superior to that of commercial Super P and Vulcan carbon and twice to either of meso  $\text{TiO}_2$  and  $\text{Ti}_4\text{O}_7$ . The anchoring of LiPS was confirmed studying the binding energy on  $\text{Co}_9\text{S}_8$  surfaces via a combination of first-principles calculations and XPS studies [66].  $\text{MoS}_{2-x}/\text{rGO}$  has also been investigated with promising electrochemical performance. It has been demonstrated that sulfur deficient sites greatly contribute towards LiPS conversion and catalyze LiPS conversion kinetics. Because of higher participation in reaction chemistry, a very low quantity of  $\text{MoS}_{2-x}/\text{rGO}$  has a greater influence on electrochemical performance [67].

MXenes, a new class of 2D materials reported in 2011, are the stacks of 2D transition metal carbides and carbonitrides of general formula  $\text{M}_{n+1}\text{X}_n\text{T}_x$ , where M stands for metal atom, X stands for C and/or N,  $n = 1, 2, \text{ or } 3$ , and  $\text{T}_x$  represents various surface terminations (OH, O, and/or F groups) [15]. These 2D structures are intrinsically highly conductive and bear the chemically active surfaces to interact with polysulfides by metal-sulfur interaction. Nazar et al demonstrated MXene phase  $\text{Ti}_2\text{C}$  with 70% sulfur loading as an effective host for Li/S batteries without high surface area and well-ordered pores structure as required by other host materials. It is reported that sulfur and its lithium species are strongly held at metallic sites of highly conductive MXene phase  $\text{Ti}_2\text{C}$ . 70 wt% S/ $\text{Ti}_2\text{C}$  composite cathodes show excellent cycling performance with specific capacity 1200 mAh/g at C/5 and capacity retention of 80% is achieved over 400 cycles at C/2 current rate because of the strong interaction of the polysulfide species with the surface Ti atoms [68]. In a subsequent study, the same researchers claimed long term cycling performance up to 1200 cycles with capacity retention of 450mAh/g and decay rate of 0.043% for CNT- $\text{Ti}_2\text{C}$ , CNT- $\text{Ti}_3\text{C}_2$  and CNT- $\text{Ti}_3\text{CN}$  host material [69].

Recently, transition metal nitrides and phosphides also exhibited note-worthy electrochemical performances when integrated into sulfur cathodes. Hao et al. reported electronic conductive TiN as efficient LiPS immobilizer via chemisorption for high sulfur utilization and excellent rate performance [70]. In another

investigation, VN/graphene composite has been realized for its strong LiPS anchoring performance with low polarization and faster conversion kinetics [71]. Transition metal phosphides Ni<sub>2</sub>P, Co<sub>2</sub>P, and Fe<sub>2</sub>P based sulfur cathodes showed the higher sulfur utility and better cycling performance. It is illustrated that metal phosphides not only can interact with LiPS but also catalyze the Li<sub>2</sub>S decomposition [72]. Zhong et al. have revealed cobalt phosphide interaction mechanism with LiPS that how surface oxidation greatly contributes towards strong LiPS adsorption [73].

Non-conductive metal-organic frameworks with superior polysulfides absorptivity have been investigated to host sulfur directly or in synergy with other matrices. [74]

**Table 1. 2:** Representative Li/S cathode materials; their architecture, sulfur content, and loading, and cycling performance

Category of cathode	Cathode Material and architecture	Sulfur content (wt%) / sulfur loading	Cycling performance	Ref.
<b>Carbon based matrices</b>	Amphiphilic Hollow Carbon nanofibers	-/ 1	838/670 (0.5C, 300)	[38]
	Carbon nanotubes	90/ 1.6	575/350 (0.5C, 80)	[42]
	Graphene oxide coated S particles	50/ -	890/800 (0.2C, 1000)	[44]
	Unstacked double-layer templated graphene	64/0.8	1084/701 (1C, 200)	[45]
	Ordered microporous carbon	40/>1	1000/600 (C/4, 500)	[34]
	Hierarchical porous carbon	50/-	1193/ 883 (0.1C, 50)	[35]
	3D aerogel	27/-	2368/822 (0.06C, 50)	[48]
	rGO/CNT	68/1	1191/933.3 (1C, 500)	[50]
	CNF coaxially wrapped with Graphene	33/2-3	1047/694 (0.1C, 50)	[39]
		Polyaniline	62/-	1392/602 (0.5C, 1000)

<b>Conductive polymer confinements</b>	Polypyrrole	70/1.5	1320/675 (0.125C, 150)	[53]
	Polypyrrole	65/2.5-3	1102/712 (0.5C, 300)	[75]
	Polythiophene	72/-	1193/830 (0.05C, 80)	[58]
	PEDOT:PSS	78/1.5	1165/780 (0.5C, 500)	[51]
<b>Inorganic moieties/ metal compounds</b>	TiO <sub>2</sub> impregnated hollow CNF	67/0.4 (Li <sub>2</sub> S)	458/371 (2C, 340)	[76]
	Ti <sub>4</sub> O <sub>7</sub> nanoparticles	48/ 1.5-1.8	850/595 (2C, 500)	[77]
	MnO <sub>2</sub> nanoflakes in hollow CNF	71/ 3.5	890/662 (0.5C, 300)	[78]
	Nb <sub>2</sub> O <sub>5</sub> nanocrystals	48/ 1.5	1289/913 (0.5C, 200)	[79]
	V <sub>2</sub> O <sub>3</sub> in hierarchical porous carbon	55/1.5	1286/912 (0.2C, 250)	[80]
	Co <sub>9</sub> S <sub>8</sub> /C hollow nanopolyhedra	62/ 1.5 & 3	840/680 (0.5C, 300) 3 mg cm <sup>-2</sup>	[66]
	TiS <sub>2</sub> core-shell	51/1 (Li <sub>2</sub> S)	956/736 (0.5C, 400)	[65]
	MoS <sub>2-x</sub> /rGO	75/ 1.5	1160/628 (0.5C, 600)	[67]
	TiN nanoparticles	70/ 1.5	1012/660 (0.5C, 200)	[70]
	VN/ rGO composite	56/ 3	1128/917 (1C, 200)	[71]
	Ni <sub>2</sub> P with N, P doped carbon	76/3.4	840/ 758 (0.5C, 400)	[72]
	CoP	- /3	850/ 835 (1C, 200)	[73]
	Ti <sub>2</sub> C nanosheets	70/1	1200/960 (0.5C, 400)	[68]
	Ti <sub>3</sub> CN nanosheet/ CNT	83/1.5	890/450 (0.5C, 1200)	[69]
	Cu-MOF / Cu-TDPAT	50/1.2	820/745 (1C, 500)	[74]

### 1.3.2 Introduction of interlayers

As demonstrated in the previous section, sulfur cathodes are essentially porous, so the loss of active material in the form of LiPS towards the anode is inevitable due to chemical potential and concentration gradients. Manthiram group came up with an idea of introducing additional traps for LiPS to limit the LiPs at the cathode as much as possible. They termed these additional trapping layers between separator and cathode as “interlayers” [81]. Interlayers are introduced either as a flexible freestanding layer or as a coating on the polymeric substrate. Later approach was opted to engineer the surface of the separator to reduce the weight of freestanding interlayers and excess requirement of electrolyte, hence increase the energy density of the cell that will be discussed in a subsequent section. In literature, the reported materials as interlayers include MWCNTs, electrospun carbon nanofibers, carbonized commercial papers, and micro and meso porous carbon papers. Manthiram et al are the first to introduce an approach using free-standing MWCNT thin film and microporous carbon paper as a reservoir for LiPS in 2012 [82, 83]. Manthiram and co-workers used a number of interlayer strategies that can both physically and/or chemically contain LiPS at the cathode side. For example, in a study electrospun meso-microporous carbon nanofiber freestanding interlayer was investigated to mitigate LiPS migration [84], in another they used the activated carbon paper bearing functional groups as an effective interlayer [85]. Wang et al have demonstrated electroactive cellulose-supported graphene oxide as an effective bifunctional interlayer [86]. Ma et al. have demonstrated free-standing polypyrrole nanotubes film [75] and carbon paper anchored polypyrrole [87] as effective bifunctional interlay to limit LiPS at the cathode. Han et al. reported Al<sub>2</sub>O<sub>3</sub> atomic layer deposited nanoporous carbon cloth that can both physically trap and chemically interact with soluble LiPS [88]. Ultrafine TiO<sub>2</sub> decorated CNF sheet was also reported as an effective interlayer to suppress LiPS shuttle [89]. The strategies previously investigated are reasonably effective because of their ability to reactive dead sulfur.

### 1.3.3 Separators modifications

Separator modification is advantageous from an industrial point of view, as it will reduce the number of layers to assemble and reduce the requirement of the electrolyte. However, modifications require relatively better engineering approaches to achieve uniformly thick and well-distributed interlayer on solvophobic separator surfaces. In this context, the studied carbon materials include nanocarbon, MWCNT, graphene, graphene oxide and micro mesoporous carbon [90]. Yao et al introduced a physical barrier to block LiPS by coating Ketjen black carbon on PP separator [90]. Functional doped mesoporous carbon and graphene were also considered as a coating material to chemically engage LiPS in electrolyte solution because of their affinity with the heteroatomic system [91, 92]. Lu et al. reported sulfonated reduced graphene oxide coated separator as ion selective interlayer that can physically trap LiPS and chemically anchor LiPS with an

electronegative sulfonic group [93]. Chung et al. studied boron doped CNTs coated on a separator as an effective LiPS trapping interface [94]. Graphitic carbon nitride ( $g\text{-C}_3\text{N}_4$ ) are endowed with LiPS adsorption pyridinic-N sites and imparts mechanical stability to a separator to stand with long cycling [95]. Ion selective and electrically conductive polymers such as Nafion, lithiated Nafion, polydopamine coated separators were explored to block LiPS at the cathode side. Recently, polymers with intrinsic microporosity were also evaluated for their LiPS blocking capabilities. Metal oxides such as  $\text{Al}_2\text{O}_3$  [96] and  $\text{V}_2\text{O}_5$  [97] were also considered as interlayer by coating them on the conventional separator. Additionally, a number of interlayer strategies were also investigated synergistically, for instance, Fan et al proposed a novel interlayer material comprises of functionalized boron nitride nanosheets and graphene [98]. Zhuang et al. proposed a rational design for a ternary layer separator with polypropylene, graphene oxide, and Nafion to impede LiPS shuttle [99]. Song et al. combined graphene and  $\text{Al}_2\text{O}_3$  onto a PP separator, and proposed a graphene/ $\text{Al}_2\text{O}_3$ /PP trilayer separator [96]. Although this approach effectively stop the LiPS at the cathode side, yet it does not fully reactivate the sulfur products for electrochemical reactions at the cathode.

**Table 1. 3:** Representative interlayer strategies; interlayers compositions, corresponding sulfur content, and loading, and cycling performance

Class of interlayer	Interlayer Material composition	Sulfur content (wt%) / sulfur loading	Cycling performance [initial/final (mAh g <sup>-1</sup> ) (C-rate, cycles)]	Ref.
Free-standing interlayers	Free-standing MWCNTs interlayer	70	1446/962 (C/5, 50)	[83]
	Bifunctional microporous carbon interlayer	70	1367/1000 (1C, 100)	[82]
	Electrospun micro and mesoporous CNF interlayer	70/ 1	988/485 (1C, 300)	[84]
	Electroactive cellulose supported GO interlayer	63 / 1-1.5	920/600 (0.1C, 100)	[86]
	Polypyrrole nanotube film	80/2.5-3	1102/712 (0.5C, 300)	[75]
	Polypyrrole anchored carbon paper	70	939/555 (0.5C, 200)	[87]
	ALD $\text{Al}_2\text{O}_3$ carbon cloth	59 / 12	1136/766 (40 mA g <sup>-1</sup> , 40)	[88]

	TiO <sub>2</sub> decorated CNF sheet	60/ 0.8	935/694 (1C, 500)	[89]
<b>Separator coatings</b>	Ketjen balck coated spearator	70/1.5-2	1350/740 (C/2, 500)	[90]
	N and P dual doped graphene	70	1158/638 (1C, 500)	[92]
	sulphonated rGO coated separator	67/1.2-1.5	1300/802 (0.5C, 250)	[93]
	Boron doped CNTs coated separator	70/2.4-2.5	849/509 (1C, 500)	[94]
	g-C <sub>3</sub> N <sub>4</sub> coated separator	54/ 1.7 & 5	1100/733 (1C, 400)	[100]
	V <sub>2</sub> O <sub>5</sub> layered separator	61.8/ 1.25	890/800 (C/15, 250)	[97]
	Boron nitiride nanosheets/graphene coated separptor	60	1100/558 (3C, 1000)	[98]
	GO and Nafion coated PP separator	60/1.2 & 4	1057/700 (.5C, 200)	[99]
	Graphene/Al <sub>2</sub> O <sub>3</sub> /PP trilayer separator	60/ 0.75	1068/804 (0.2C, 100)	[96]

### 1.3.4 Towards low PS solubility electrolytes and additives

As it is stated earlier that LiPS are freely soluble in a liquid electrolyte that not only facilitates the electrochemical reactions but also causes shuttle mechanism. Therefore, other electrolyte systems such as ionic liquids, liquid electrolytes with poor solvation effect for LiPS, electrolytes with common ion effect, gel polymer electrolytes and solid-state electrolytes are under exploration to mitigate the LiPS shuttle effect. Sun et al. came up with an approach of using high carbon/oxygen ratio ethers such as methyl tert-butyl ether and diisopropyl ether as cosolvents in conventional electrolyte compositions [87]. They have demonstrated better electrochemical performance than that of conventional electrolyte due to poor solvation towards LiPS by these high C/O ratio ethers, maintaining the lithium salt solubility. Dominko and his co-workers replaced TGDME with a fluorinated ether 1,2-(1,1,2,2-tetrafluoroethoxy)ethane maintaining DIOX as a co-solvent with one molar LiTFSI, exhibited a better discharge profile and higher C-efficiency. They attributed better performance to reduced LiPS solubility arising from poor Li<sup>+</sup> solvation [101]. Chen et al. instead used another fluorinated ether bis(2,2,2-trifluoroethyl) ether to realize better performance in full Li/S cell [102]. In another study, the Dominko group used an ionic liquid (N,N-diethyl-N-methyl-N-(2-methoxyethyl)ammonium bis(trifluoromethanesulfonyl)imide) [DEME][TFSI] along with DIOX and 1M LiTFSI to achieve low LiPS solubility system [103]. The solubility of long-chain LiPS can be limited by selecting another type of electrolyte

salt such as lithium trifluoromethyl-4,5-dicyanoimidazole (LiTDI). Replacing LiTFSI in conventional electrolyte system with LiTDI lowers the  $\text{Li}_2\text{S}_8$  solubility by 83%, improve long term cycling and enabled to achieve higher C-efficiency [104]. Some reports used LiPS catholyte or LiPS as co-salt to enhance the performance of sulfur cathode [105], while Chen et al. achieved promising outcomes using organosulfide electrolyte (dimethyl disulfide, DMDS) as cosolvent. DMDS induce alternative reaction pathway by forming dimethyl polysulfides and contribute greatly towards capacity and sulfur utilization [106]. This strategy is still corrosive towards metallic Li anode similar to LiPS. Nazar and her coworkers have proposed a combination of solvent-salt complex acetonitrile(ACN)<sub>2</sub>-LiTFSI and hydrofluorinated ether [107]. This system can redirect Li/S reaction pathways due to sparingly solvation capability, in contrast, to fully solvation system. It is demonstrated that this system effectively promotes the formation of medium and short chain LiPS prior to the formation of crystalline  $\text{Li}_2\text{S}$  because of disproportionation reactions and avoid long chain LiPS. Hence, the cell comprises of this electrolyte system exhibit lower overpotential and higher sulfur utilization at 50 °C [108]. Yet, in another study, a novel combination of hydrophobic sulfonamide solvent (N,N-dimethyl triflamide (DMT) or N,N-dipropyl triflamide (DPT)) and a low ion-pairing salt (lithium salt of fluorinated alkoxy aluminates) has been evaluated. This system acts as non-solvent at ambient but transforms to sparingly solvating electrolyte at a higher temperature. Consequently, this combination showed higher C-efficiency with  $\text{LiNO}_3$ , low LiPS solubility and relatively good rate performance [109].  $\text{Li}^+$  ion conducting solid-state electrolyte can be promising as it can effectively separate metallic lithium surface from LiPS and can enable the use of metal Li as an anode.  $\text{P}_2\text{S}_5$  has been effectively used as an additive in the solid-state electrolyte and it can effectively passivate Li surface by forming  $\text{Li}_3\text{PS}_4$  [110]. Xu et al. have reported superionically conductive  $\text{Li}_7\text{P}_{2.9}\text{Mn}_{0.1}\text{S}_{10.7}\text{I}_{0.3}$  as an optimal choice for all solid-state Li/S battery [111].

### 1.3.5 Inactive binder to interactive matrices

Conventional fluoropolymer binders such as poly (tetrafluoroethylene) PTFE or poly (vinylidene fluoride) PVDF are regarded as an inactive ingredient of the slurry. Although they are compatible and chemically stable, yet they are unable to withstand huge volume changes because of structural rigidity and do not contribute towards LiPS interactions. As polar and functional polymers can interact with LiPS, so they can contribute towards the stability of cathode by binding LiPS in the vicinity of the electrode surface. Such polymers that also bear high adhesion capability can be utilized effectively as binders. A number of functional binders such as polyethylene oxide (PEO) [112], polyvinyl alcohol (PVA), polyacrylic acid (PAA) [113], polyethylenimine [114], poly(ethylene glycol) PEG formulations [115] and cationic polyelectrolytes [116-118] have been explored with some impact. Recently, an aqueous inorganic polymer binder with flame retardant properties ammonium polyphosphate (APP) has also been reported. It has been demonstrated that APP surpasses PVDF in a number of functional properties like

strong LiPS affinity, high binding energy, high swell ratio, low polarization, flame retardancy and water-based processability [119].

**Table 1. 4:** Representative binder for Li/S cathodes; type of polymer as binder, sulfur content and loading, and cycling performance

	Type of polymer used as binder	Sulfur content (wt%) / sulfur loading (mg cm <sup>-2</sup> )	Cycling performance [initial/final (mAh g <sup>-1</sup> ) (C-rate, cycles)]	Ref.
<b>Organic polymers</b>	Polyethylene oxide (PEO)	62/1.5	933/380 (0.1C, 400)	[112]
	Polyacrylic acid (PAA)	60/1.5	804/325 (C/5, 50)	[113]
	Polyethylenimine (PEI)	60 / 8.6	1126/744 (0.05C, 50)	[114]
	Poly(ethylene glycol) diglycidyl ether with polyethylenimine	60/1.2-1.5	600/430 (1.5C, 400)	[115]
<b>Natural polymers</b>	Carboxymethyl cellulose (CMC) with sulfurized PAN	23/1	900/938 (0.9C, 500)	[120]
	Chitosan	63/1-1.5	1145/680 (C/2, 100)	[121]
	Gelatin	63	1137/642 (0.4 mA cm <sup>-2</sup> , 30)	[122]
<b>Inorganic Polymer</b>	Ammonium polyphosphate	60/2-3	753/640 (0.5C, 400)	[119]
<b>Poly electrolyte binder</b>	poly[(N,N-diallyl-N,N-dimethylammonium) bis(trifluoromethane sulfonyl)imide]	70/4-8	1244/731 (C/5, 250)	[117]
	Core-shell polyelectrolyte binder	50/1	1400/1008 (100, 0.125 C)	[118]

In addition to synthetics, a number of natural polymers like chitosan [121], gelatine [122], alginate [123], carboxymethylcellulose (CMC) [120] and other carbohydrates etc, are worth investigating because of their abundance in functional

groups. A number of reports already indicated better performance of electrodes with functional binders in contrast to conventional PVDF or PTFE [124].

### 1.3.6 Lithium anode protection

As pointed earlier, Li metal anode strongly hampers the commercialization of Li/S technology because of its high reactivity drawing to the decomposition of the electrolyte. Secondly, irregular stripping and plating on Li metal surface give birth to dendritic Li growth that causing short circuit and continuous loss of active material. Hence, Li anode contributes greatly towards the poor cyclability and urges the use of excess electrolyte to realize reasonable cycling performance. Use of unprotected Li metal as an anode in prototype cells is also a safety hazard and can result in unexpected unpleasant events.

Lithium anodes protection is enabled by several strategies. For examples, the use of electrolyte additives such as CsPF<sub>4</sub>, LiF etc. that can effectively play their roles in suppressing the dendrite growth by inducing passivation layer. In former Cs<sup>+</sup> cation is considered self-healing towards lithium tips by impeding the deposition of Li<sup>+</sup> on outgrowth [125], while LiF plays the trick by lowering diffusion barrier at the lithium-electrolyte interface. Other strategies involve the use 3D porous hosts for lithium deposition, for example; use of 3D copper foil with sub-micron skeleton [126], manufacture of rGO-Li composite by diffusion of melted Li [127, 128], deposition of a graphene layer on top of lithium foil [129]. These approaches lower the effective local current density owing to high surface area, impose more uniform charge distribution that is less favorable for dendrite formation, and accommodate Li deposits into void space. Li anode can also be realized in future energy storage devices by designing all-solid-state Li/S cells.

### 1.3.7 Alternative anodes

Regretfully, alternative anode strategies significantly lack in attaining the researcher's attention in Li/S full cell configuration. Yet, there are some mention-worthy investigations conducted by some researchers. In the current scenario, silicon surfaced as an optimal choice mainly because of its highest lithium storage capacity on lithiation Li<sub>15</sub>Si<sub>4</sub> among an existing lot of anode materials. But, Si anode is subjected to an unfavorable increase in volume that is around 400% of the initial on alloying. On reciprocating, dealloying of Li<sub>15</sub>Si<sub>4</sub> leaves a huge quantity of active material inaccessible for further lithiation. So, the pulverization and loss of electrical contact of anode active material from the current collector result in low C-efficiency and fast capacity fading. Secondly, the mechanical stresses arose from volume changes give rise to cracks and SEI disruption, which result in continuous depletion of the electrolyte. Thus, there is a dire need to design an anode architecture that can absorb these volume changes without compromising on active material and electrolyte. Several forms of nanostructured silicon such as nanoparticles [130, 131], nanotubes, nanowires [132], nanoporous hollow silicon [133, 134] have been employed to encounter with these volume changes. In

addition, various conductive matrices have also been investigated including carbon, graphite and conducting polymers [135, 136] to uphold the electronic contact in form of various architectures such as core-shell [137, 138], yolk shell [139-142], pomegranate [133, 143], sponges or hybrids. Various researchers have demonstrated that architectures with free volume or void structures greatly contribute towards the stability of Si anode by standing the volume changes. This strategy also safeguards the stable SEI on carbon shell, thus contributes towards low electrolyte depletion. Additionally, binders play a critical role to achieve better electrochemical performance by keeping the structure intact both mechanically and electrically. Various binding systems such as CMC/citric acid, crosslinked chitosan, CMC crosslinked with poly(acrylic acid) have been proposed to target stable electrochemical performance [144, 145]. Several mechanisms have been proposed to comprehend this binder particle interaction but this interaction alone is not enough to stand with these volume changes. Tin (Sn) has also been registered as possible alternative anode material for Li/S batteries [146], as tin can alloy with 4.4 atoms of Li per atom of Sn providing relatively high specific capacity (i.e. 994 mAh g<sup>-1</sup>). However, these Sn-based anodes are also subjected to higher volume changes. These structural changes are usually buffered using carbon matrices. Other approaches involve the use of lithium alloys to produce anodes.

**Table 1. 5:** Representative Silicon anodes; anode material and architecture, Si content and loading, and cycling performance

Category of Silicon anodes	Si Anode Materials and architecture	Si loading (mg cm <sup>-2</sup> )	Cycling performance	Ref.
<b>Carbons</b>	Electrospun core-shell nanoSi-fibers	0.6	721 (5 A g <sup>-1</sup> , 300)	[137]
	Double-shelled yolk structured silicon	1-1.2	720 (5 A g <sup>-1</sup> , 1000)	[140]
	Raspberry-like hollow nanospheres with carbon shells	0.7	517 (2 A g <sup>-1</sup> , 500)	[147]
<b>Polymers</b>	PANi cross-linked network	0.3-0.4	1200 (1 A g <sup>-1</sup> , 1000)	[135]
	PEDOT:PSS Conducting Polymer	0.4-1.5	1927 (2 A g <sup>-1</sup> , 100)	[136]
<b>Metal</b>	hollow Si-Cu alloy nanotubes		1010 (3.4 A g <sup>-1</sup> , 1000)	[148]
<b>Metal oxides</b>	Si@TiO <sub>2</sub> core-shell nanospheres	0.621	804 (0.1C, 100)	[149]

## 1.4 Characterization Methodologies opted to study Li/S cathode materials and cells

Technique	Principle	Application
<b>Thermogravimetry (TGA)</b>	A thermal analysis technique involves the recording of mass changes as a function of temperature and time	<ul style="list-style-type: none"> <li>estimation of active material (i.e. S and Si)</li> </ul>
<b>BET Analysis</b>	Basis on physical adsorption of gas molecules upon the solid surface to estimate specific surface area and porosity	<ul style="list-style-type: none"> <li>specify the surface area, type of porosity and pore volume of porous matrices</li> </ul>
<b>Transmission Electron Microscopy (TEM)</b>	Beam of highly accelerated electrons is directed onto the specimen, and then scattered and lost electrons were collected to image the morphology of the specimen.	<ul style="list-style-type: none"> <li>Investigate the morphology of composite material</li> </ul>
<b>Field Emission Scanning Electron Microscopy (FESEM)</b>	A beam of highly accelerated electrons is directed onto the specimen, then backscattered and secondary electrons were imaged to view the topology of the sample.	<ul style="list-style-type: none"> <li>Investigate the morphology of composite material</li> </ul>
<b>Energy Dispersive X-ray Spectroscopy (EDS)</b>	An elemental analysis technique involves the exposure of accelerated electron beam on a sample that causes the emission of X-rays specific to atomic structure.	<ul style="list-style-type: none"> <li>To discern the elemental composition of the materials</li> <li>To verify the distribution of elements through elemental mapping</li> </ul>
<b>X-ray photon spectroscopy (XPS)</b>	Surface chemical characterization technique in which surface of the specimen	<ul style="list-style-type: none"> <li>To investigate the bonds and atomic composition of the surfaces</li> </ul>

	is irradiated with X-rays, and then surface emitted photoelectrons were collected for assessing their binding energy and count, that is linked to electronic configuration under ultra-high vacuum.	<ul style="list-style-type: none"> <li>▪ To determine the chemical interactions among various elements of the composite</li> </ul>
<b>Fourier-transform Infrared Spectroscopy (FTIR)</b>	A chemical analysis technique that involves the adsorption of infrared radiations explicitly corresponds to bonds present in the molecules.	<ul style="list-style-type: none"> <li>▪ To determine the bonds and interactions among organic molecules</li> </ul>
<b>X-ray Diffraction (XRD)</b>	An analytical technique in which X-rays are directed to crystalline structures and then diffracted radiations were detected. The diffraction of radiations relates to lattice spacing.	<ul style="list-style-type: none"> <li>▪ To evaluate the crystalline structure of materials</li> <li>▪ To determine the phase composition of materials</li> </ul>
<b>Selected Area Electron Diffraction (SAED)</b>	An analytical technique in which electron wave-particle duality exploited, ordered atoms in the path of electron beam act as a diffraction grating. The diffracted electrons are detected to assess the crystal structure.	<ul style="list-style-type: none"> <li>▪ To confirm the crystalline phases and composition of the materials</li> </ul>
<b>Inductive Coupled Plasma- Mass spectroscopy (ICP-MS)</b>	A mass spectroscopic technique that involves the ionization of sample through the inductively coupled plasma, then ions were separated and quantified using mass spectrometer. It can detect various elements	<ul style="list-style-type: none"> <li>▪ To determine the right composition of elements to ppm levels</li> </ul>

	at part per quadrillion concentration.	
<b>Mass spectroscopy Gas chromatography (MS-GC)</b>	A mass spectroscopic technique that involves the heating of specimen to separate the individual elements and then quantification through a mass spectrometer.	<ul style="list-style-type: none"> <li>▪ To find out the elemental composition of materials</li> </ul>
<b>Raman Spectroscopy</b>	A scattering technique in which specimen is illuminated with a monochromatic laser beam, the interacted and scattered beam that bears different frequency owing to inelastic interaction, is recorded to construct Raman spectra	<ul style="list-style-type: none"> <li>▪ To discern the level of graphitization of carbons</li> <li>▪ To confirm the phase composition of amorphous and crystalline material</li> </ul>

Technique	Principle	Application
<b>Galvanostatic charging/discharging (GC)</b>	An electroanalytical technique in which steady electronic current is extracted from, and added to an electrochemical system. The value of steady current (C-rate) is estimated from theoretical capacity. 1C means 1 h requires fully charging or discharging system to the theoretical value.	<ul style="list-style-type: none"> <li>▪ To investigate the charging and discharging behavior of electrode materials</li> <li>▪ To determine the cycle life of electrode materials and capacity fading rate</li> <li>▪ To investigate the C-rate capability of electrode material</li> </ul>
<b>Cyclic Voltammetry (CV)</b>	A potentiodynamic technique where working electrode potential is ramped linearly versus time to	<ul style="list-style-type: none"> <li>▪ To discern the oxidation and reduction reactions</li> <li>▪ To examine the reversibility of the</li> </ul>

	study oxidation and reduction of species.	lithiation and delithiation processes
<b>Electrochemical Impedance Spectroscopy (EIS)</b>	An electroscopic technique in which a small amplitude AC signal is applied to record AC frequency dependent resistance measurement.	<ul style="list-style-type: none"> <li>▪ To point out the series, polarization and charge transfer resistances, and Warburg impedance of the system</li> </ul>

## 1.5 Concluding Remarks

Although Li/S system is considered one of the most promising technologies to be commercialized in the near future, yet the system inadequacies have not been fully addressed. The scientific community is now fully involved in taking the research in Li/S to the next level. The number of publications, examining the Li/S system, has enormously increased from the last 5 years with appreciable success. Most of the early research work is related to sulfur cathodes where very high capacities have been realized with appreciable capacity retention. The proposed studies involve the complex and sophisticated synthesis of materials, which are comparatively difficult to scale up and industrialize. Initial studies were also not focused on higher sulfur loadings, so the purpose of high-energy Li/S system had not been met. Secondly, the anode was ignored in previous studies, and almost all of the studies involve the use of metallic lithium as the anode. Similarly, other constituents of the cell such as electrolyte, separator were also overlooked. However, the commercialization of Li/S technology has pushed the scientific community to offer simple and practical solutions focusing on every aspect of the system. Additionally, there is also significant progress in discerning the working mechanism of Li/S system applying the advanced in-operando techniques. Irrespective of this progress, there is a big margin to improve the technology to commercialization level. This is the reason that European Union H2020 team had approved a project named ALISE (Advanced Lithium Sulfur batteries for xEV) NMP-17-2014 under financial grant GA 666157. The project is about to build Li/S technology that can deliver specific energy of 500 Wh kg<sup>-1</sup> at the pack level.

In this project, the electrochemistry group at Polito is focused to offer simple and feasible solutions to realize cathodes, electrolyte, and anodes. In this particular, piece of work, the major focus is to come up with simple and practical approaches to prepare sulfur cathodes and silicon anodes. Next three chapters are dedicated to sulfur cathode materials where the novel materials have been synthesized and have been physiochemically and electrochemically characterized. In the very next chapter, the strategies have put forth to realize stable silicon anodes. In chapter 6, it is attempted to realize the lithium metal-free Li/S technology.

## Chapter 2

# Development of novel carbon host materials for sulfur cathodes

In literature, various synthetic routes have been listed to produce porous carbon matrices. They involve in one way or other; a) physical or/and chemical activation, b) catalytical activation using either metal salt or organometal complexes, c) carbonization of carbonizable and pyrolyzable polymer mixtures, d) carbonization of aerogel matrices produced under supercritical drying conditions and e) pyrolysis of biomass [150]. Most of these approaches bring about mesoporous materials. As per IUPAC endorsements, porous carbon can be categorized into three classes; 1) microporous materials with pores diameter  $< 2$  nm, 2) mesoporous materials with pores size in the range of 2-50 nm and 3) macroporous materials with pore diameter  $> 50$  nm [151]. To realize microporous carbon materials, either templating approaches or biomass pyrolysis have been employed. Presence of templates such as metal-organic frameworks requires their removal and subsequent washing. While the pyrolysis of biomass is quite subjective to the origin and topography of biomass sources. Secondly, the development of sulfur cathodes using carbon matrices involves low active mass loadings and short cycle life.

In the first part of this chapter, it has been successfully demonstrated that microporous carbons can be realized without templating, and the variations of biomass sources can be eliminated. Ultra-microporous carbons have been achieved by simple carbonization of cyclodextrin nanosponges. It has been demonstrated that sulfur and LiPS can be dually confined by physical trapping in the micropores of carbon and hampering their diffusion by the wrapping of rGO. In the second argument, high surface area nitrogen and sulfur-doped hierarchical porous carbons have been synthesized. Long term cycling points out towards the efficacy of doped hierarchical carbons in physical housing and chemical binding of LiPS. For both carbons, practical cathode loading (i.e. sulfur  $\sim 2$  mg cm<sup>-2</sup>) has opted, and simple electrode fabrication techniques on aluminum foil have been adopted

## 2.1 Ultra-microporous carbon (MPC) from hyper crosslinked $\beta$ -cyclodextrin nanosponges as sulfur host

A novel approach has been proposed to synthesize ultra-microporous carbon (MPC) with pores diameter ranges from 5-11 Å from hyper-crosslinked polymer  $\beta$ -cyclodextrin ( $\beta$ -CD) nanosponges. After sulfur infiltration into MPC, the C/S composite was wrapped by rGO to offer conductive pathways to access sulfur in the micropores and hamper the leaching of LiPS. This preliminary effort to realize stable sulfur cathodes has already been published in “Journal of Solid State Electrochemistry” [152].

### 2.1.1 Development of MPC based on cyclodextrin nanosponges and MPC based sulfur cathode

As stated, MPC was obtained from  $\beta$ -CD nanosponges and then sulfur was infiltrated by solution impregnation and melt infusion method. Afterward, the composite particles were covered with rGO to access and dually protect the sulfur in the micropores of the carbon. Schematic of the implemented strategy has been illustrated in Figure 2.1.

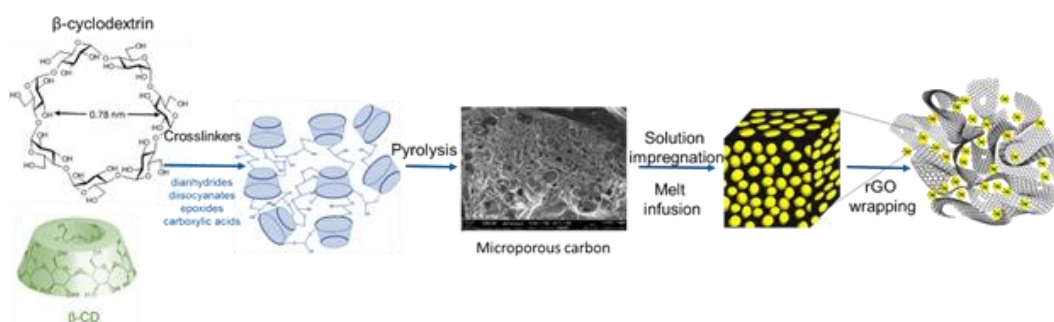


**Figure 2. 1:** Schematic depiction of the opted strategy to prepare rGO wrapped MPC/S composites.

### Synthesis of MPC and MPC/S

Polymer  $\beta$ -CD also labeled as  $\beta$ -CD nanosponges were synthesized by a crosslinking reaction using pyromellitic dianhydride (PY) following a methodology previously reported [153]. The cross-linked nanosponges were produced by reacting  $\beta$ -CD with PY in a molar ratio of 1:4. For the purpose, 2.7 mL of trimethylamine (19.4 mmol) (Sigma Aldrich) was dispersed into 100 mL of dimethyl sulfoxide (DMSO) (Fluka). Then, 11.35 g of anhydrous  $\beta$ -CD (10.0 mmol) (Roquette Italia SpA) and 17.45 g of PY (80.0 mmol) (Sigma Aldrich) were added into the mixture solution. All the reactants were dissolved, and the mixture was kept for 3 h to carry out the reaction at room temperature. Once the reaction was finished, the solid product was separated and grounded in a mortar. The solid mixture was Soxhlet extracted with acetone for 24 h. As obtained, PY  $\beta$ -CD nanosponges were then pyrolyzed in a tubular furnace at 800 °C with a heating rate

of 10 °C/min under nitrogen gas flux for 2 hours to obtain MPC as shown in Figure 2.2.

To obtain MPC/S composite, first sulfur (Sigma Aldrich) 1.5 g was dissolved in DMSO at 90 °C. Then, 1 g of MPC was dispersed in the solution mixture under continuous heating. The mixture was continuously heated for 6 h under magnetic stirring to ensure MPC impregnation with sulfur. The temperature of the solution was decreased to room temperature, which results in crystallization of sulfur into macropores of carbon. The solid mixture was separated by centrifugation and was washed with absolute ethanol. As attained, the carbon-sulfur composite is labeled as (SI\_CS). In order to obtain melt infusion of small sulfur allotropes ( $S_2$ ,  $S_3$ ,  $S_4$ ) into the micropores, SI\_CS composite was subjected to a heating profile under Argon stream in a tubular furnace. Initially, composite was subjected to 115 °C for 6 hours to melt the sulfur ( $S_8$ ), then temperature raises to 155 °C and holds for 12 h. At 155 °C, sulfur exhibit the lowest viscosity at which sulfur can break up into linear small chain allotropes and adsorbed by micropores The melt infused MPC/S composite (MI\_CS) was crushed into powder using pestle and mortar.

Graphene oxide (GO, Graphenea Inc.) 0.14 g was reduced at 700 °C for 2 h under  $H_2/Ar$  atmosphere. The obtained 0.06 g rGO was well dispersed in absolute ethanol under sonication. 1 g of MI\_CS composite was also dispersed in rGO ethanol dispersion under magnetic stirring for 5 hours. On removing the mechanical energy, the whole dispersion settles down quickly, which demonstrates that rGO adheres to the surfaces of MI\_CS composite particles through electrostatic interactions. Ethanol was spewed out from the top to acquire rGO wrapped MI\_CS composite (rGO@MI\_CS). rGO@MI\_CS composite was vacuum dried at 60 °C for 2 hours.

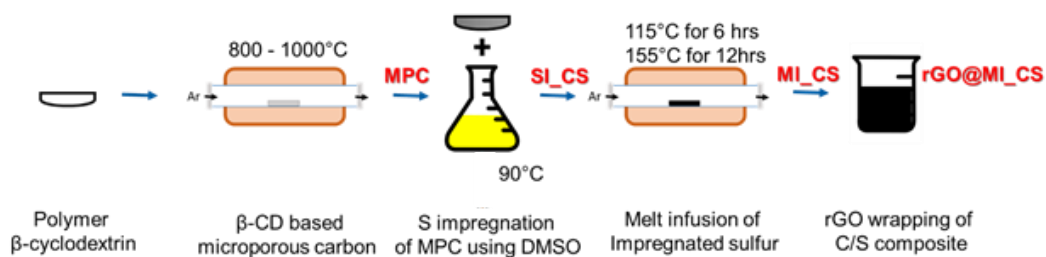


**Figure 2. 2:** Schematic illustration of the production steps to prepare rGO@MPC/S composites

### Construction of rGO wrapped MPC/sulfur cathodes and cells

Cathodes were prepared by mixing 80% MPC/S composites, 10% Shawinigan BlackAB50 carbon (CSW) and 10% polyvinylidene difluoride (PVDF). Slurries were obtained by 12 h mechanical mixing in N-methyl-2-pyrrolidone (NMP). Slurries were cast on clean aluminum foils on automatic film applicator using doctor blade thickness of 200  $\mu$ m. Cells were assembled in Ar-filled dry glove box (Mbraun Labstar) using an ECC-STD electrochemical cell configuration (EL-Cell, GmbH). The geometric area of the electrodes was 2.54  $cm^2$ . The cathodes had sulfur loading about 2  $mg\ cm^{-2}$ . A lithium disc (18 x 0.2 mm, Chemetall s.r.l.) was used

as the anode. A Celgard EH2010 (trilayer PP/PE/PP) and glass fiber 18 mm x 0.65 mm saturated in the electrolyte was used as the separator. In other cell configuration, glass fiber separator is replaced by carbon fiber paper (GDL, SIGRACET GDL24BC, SGL Technologies) to adsorb catholyte. The electrolyte consisted of 1,2-dimethoxyethane (DME) and 1,3-dioxolane (DIOX) 1:1 (v/v) with 1 M lithium bis(trifluoromethanesulfonyl)imide ( $\text{CF}_3\text{SO}_2\text{NLiSO}_2\text{CF}_3$ , LiTFSI) and 0.25 M  $\text{LiNO}_3$ . Cells were galvanostatically charged and discharged by an Arbin BT2000 battery tester at room temperature. Cycling tests were performed for 1st 5 cycles at C/10 with the end of discharge at 1.8 V and end of charge at 2.6 V. Onward cycling was carried out between 1.8 V and 2.6 V at C/5. The C-Rate is calculated using a theoretical capacity of  $1672 \text{ mAh g}^{-1}$ . All capacities are based on the mass of sulfur in the cathode.

### 2.1.2 Physicochemical Characterization

The morphology of as-synthesized  $\beta$ -cyclodextrin MPC and its sulfur composites were examined using field-emission scanning electron microscopy (FESEM, JEOL-JSM-6700F). Figure 2.3 reveals the structural and textural properties of MPC from  $\beta$ -CD nanosponge. MPC exhibits a spongy structure that makes it absorptive for sulfur. Sulfur shows a strong adsorbate-adsorbent interaction and can be chemisorbed in microporous carbon at higher temperature [154]. Figure 2.4 illustrates the morphologies of SI\_CS, MI\_CS, and rGO@MI\_CS composites. FESEM of SI\_CS exhibits the homogenous distribution of sulfur (light grain) in the composite, but it appears in the form of big chunks, which are loosely retained on the surfaces. This can be explained based on the dimension of micropores with reference to the dimension of sulfur ( $\text{S}_8$ ) having a ring-like arrangement. Micropores do not admit the ring like sulfur ( $\text{S}_8$ ) molecules to accommodate because of larger dimension, but chain like small sulfur allotropes can reside into the micropores [155].  $\text{S}_8$  crystallizes either orthorhombic  $\alpha$ -sulfur form with sixteen  $\text{S}_8$  molecules within the unit cell or monoclinic  $\beta$ -sulfur with six  $\text{S}_8$  molecules are not confined into pores. FESEM micrograph of MI\_CS (Fig. 2.4b) indicates negligible sulfur presence on the surface. In fact, sulfur liquifies at  $115^\circ\text{C}$  but at a little higher temperature  $155^\circ\text{C}$  it demonstrates the minimum viscosity (0.066 poise) and starts reducing into lower molecular metastable allotropes such as  $\text{S}_6$ ,  $\text{S}_4$ ,  $\text{S}_3$ , and  $\text{S}_2$  [156]. It is believed that physical captivity of smaller sulfur species in micropores, let the smaller allotropes to exist in primitive form through various cycles of charging and discharging. rGO@MI\_CS (figure 2.4c) exhibits the morphology of the carbon/sulfur composite wrapped with rGO. The planar assemblies typical of graphene sheets can be observed being perpendicular to the plane, randomly crumpled and interconnected, forming a disordered solid. From figure 2.5, it can be observed that CS particles are very well enveloped by rGO. This was attained via through dispersion of rGO and MI\_CS in ethanol under sonication followed by mechanical stirring at temperature about  $80^\circ\text{C}$ . On removing the heat and agitation, there is literally a complete clearing out of dispersion. rGO solubility in ethanol is around  $0.91 \mu\text{g ml}^{-1}$  with stable dispersion

at room temperature [157], but an immediate vanishing of rGO from ethanol on removing heat and stirring points out towards its strong hydrophobic interaction with CS particles. Back-scattered FESEM imaging of rGO@MI\_CS (figure 2.6c) exhibits a lack of contrast that also indicates of rGO wrapping around CS particles. The absence of contrast from MI\_CS to rGO@MI\_CS points out the coverage of sulfur present on the surface of carbon by rGO.

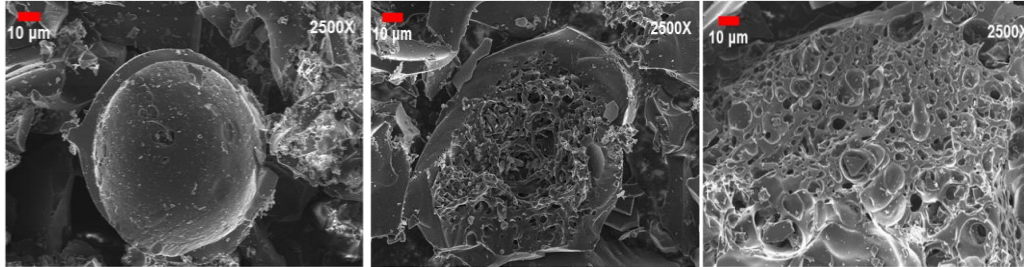


**Figure 2. 3:** FESEM images of MPC prepared from  $\beta$ -cyclodextrin nanosponge

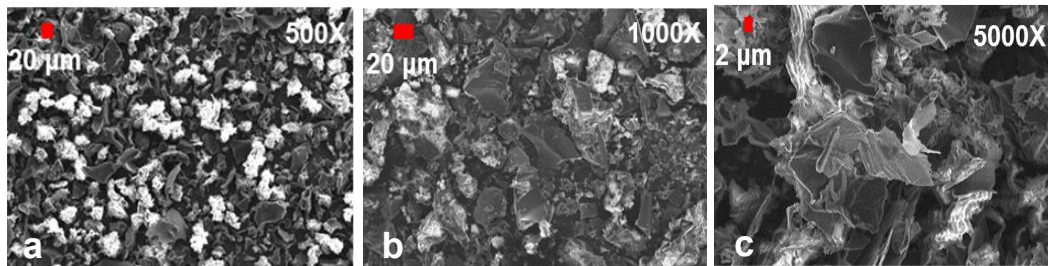


**Figure 2. 4:** FESEM images of a) SI\_CS b) MI\_CS c) rGO@MI\_CS (images are at a different scale to observe the typical structures present in the composites)

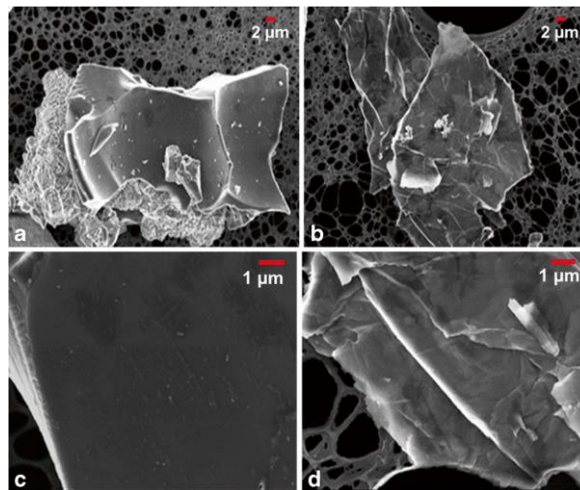


**Figure 2. 5:** FESEM images of a, c) bare MI\_CS particles and b, d) rGO-wrapped MI\_CS particles

Energy dispersive X-ray spectroscopy (EDX) of the composites was also executed on JEOL-JSM-6700F to examine the sulfur present in the structure of carbon matrices. Sulfur mapping is acquired by imaging X-ray signals from CS composites. In figure 2.7a, big sulfur chunks are present over or at the same level as carbon. In the case of MI\_CS (figure 2.7b) and rGO@MI\_CS (figure 2.7c)

composites, sulfur can be revealed as diffused in the matrices with a minor amount of sulfur inside the fractures of the surface. In rGO@MI\_CS, the carbon appears prevalent with sulfur diffused in the structure, which specifies that any sulfur at the CS surface is enveloped by rGO.

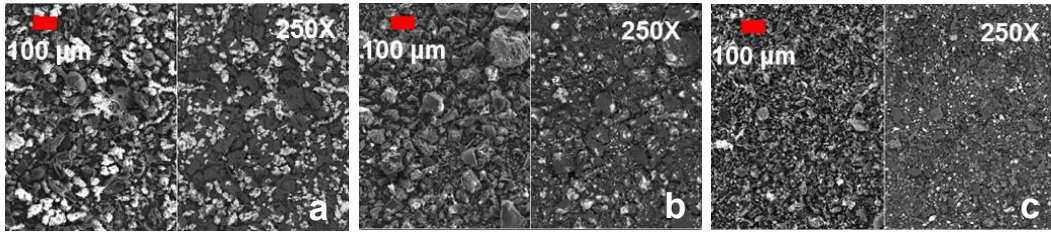


**Figure 2. 6:** Secondary image and back-scattered contrast FESEM imaging of C/S composites a) SI\_CS b) MI\_CS c) rGO@MI\_CS

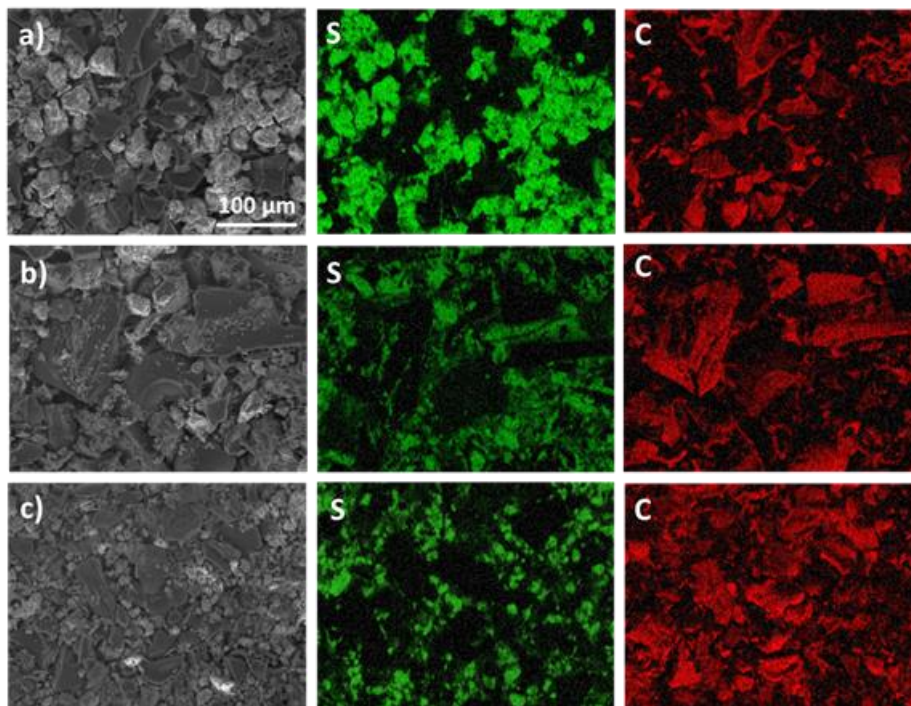


**Figure 2. 7:** Sulphur mapping in C/S composites using EDS analysis for a) SI\_CS b) MI\_CS c) rGO@MI\_CS

The elemental analysis was carried out using a Flash EA 1112 series CHNS/O Analyzer (Thermo Scientific). The samples were weighed in Tin capsules, placed inside the instrument, and then dropped into an oxidation/reduction reactor maintained at 900-1000 °C. All the organic and inorganic substances are converted into elemental gases that, after further, reduction are separated in a chromatographic column and finally detected. Elemental analysis of MPCs exhibited that the carbon content is about 78 wt. % with significant amounts of O 19.92 % and no traces of sulfur as presented in Table 2.1. Whereas the elemental analysis of C/S composites has revealed sulfur contents around 63 wt. %, 59 wt. % and 49 wt. % for SI\_CS, MI\_CS, and rGO@MI\_CS, respectively as shown in Table 2.1. The porosity of MPC and C/S composites was estimated by recording nitrogen adsorption

isotherms at 77 K by exposing at a series of precisely controlled relative pressures from 0 to 1 using an ASAP 2020 Micromeritics Instrument. Prior to the adsorption, the MPC and C/S composites were degassed at 150 °C and 50 °C (to avoid the sublimation of the sulfur) respectively under vacuum (10  $\mu\text{m Hg}$ ) for 12 h to remove the adsorbates and residual moisture, and then sample was cooled to nitrogen cryogenic temperature (77K). The specific surface area (SSA) of the samples was estimated by Brunauer–Emmett–Teller (BET) method using Langmuir model within the relative pressure range of 0.1 to 0.3, and the micropore volume and pore size distribution were estimated using density functional theory (DFT) assuming a slit geometry of the pores. The carbon obtained after the pyrolysis process was characterized by nitrogen adsorption-desorption isotherms. The result exhibited type I isotherm according to IUPAC classification that is the characteristic of microporous materials. MPC showed a specific surface area of 560  $\text{m}^2\text{g}^{-1}$ , with an average pore volume of 0.15  $\text{cm}^3\text{g}^{-1}$  and average pore diameter 5-13 Å as shown in figure 2.8. Contrary, the C/S composite showed very poor adsorption behavior, SI\_CS, MI\_CS, and rGO@MI\_CS exhibited the specific area 11.24  $\text{m}^2\text{g}^{-1}$ , 17.45  $\text{m}^2\text{g}^{-1}$  and 12.32  $\text{m}^2\text{g}^{-1}$  respectively.

**Table 2. 1:** Elemental analysis of MPC and C/S composites

Sample	% N	% C	% H	% S	%O evaluated
MPC	1.26	78.13	0.69	0.00	19.92
SI_CS	0.65	39.17	0.34	62.41	0.00
MI_CS	0.81	42.62	0.26	58.43	0.00
rGO@MI_CS	0.59	46.30	0.83	48.27	3.99

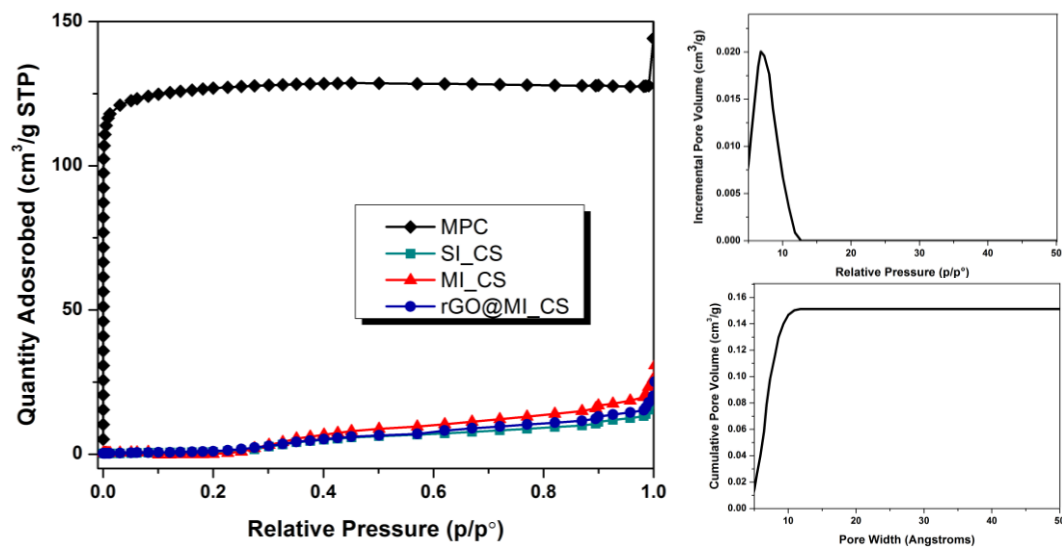


**Figure 2. 8:** Isotherms from BET analysis of a) MPC b) SI\_CS c) MI\_CS d) rGO@MI\_CS

Liang et al. have established in their study that sulfur can infiltrate into the micropores of activated mesoporous carbon via solution impregnation [158]. It is also revealed that micropore volume can be completely filled up even at lower sulfur loadings about 37 wt %. This finding is quite consistent with the FESEM images of SI\_CS (figure 2.4a and 2.6a) in our case, where a serious surface deposition and aggregation of sulfur can be observed over the carbon surfaces.

The XRD patterns were recorded on a Panalytical X'Pert PRO diffractometer with a PIXcel detector, using Cu Ka radiation, under the conditions of  $2\theta = 10-100^\circ$  and  $2\theta$  step size = 0.03, to witness the presence of sulfur. Figure 2.9a exhibits the XRD patterns of elemental sulfur, MPC and CS composites. The sharp diffraction peaks characterize that sulfur exists in a crystalline state, while the broad diffraction hump around  $24^\circ$  in the MPC diffractogram specifies the amorphous characteristic of carbon spheres. It appears that XRD pattern for SI\_CS closely resembles that of elemental sulfur without any diffraction hump from MPC. Whereas, MI\_CS and rGO@MI\_CS composites have shown the amorphous peak of MPC along with sulfur diffraction peaks that demonstrate that most of the sulfur has been concentrated into micro and macropores of the carbon. The infusion of sulfur into the porous carbon also ensure the improvement of electric conductivity of the composite.

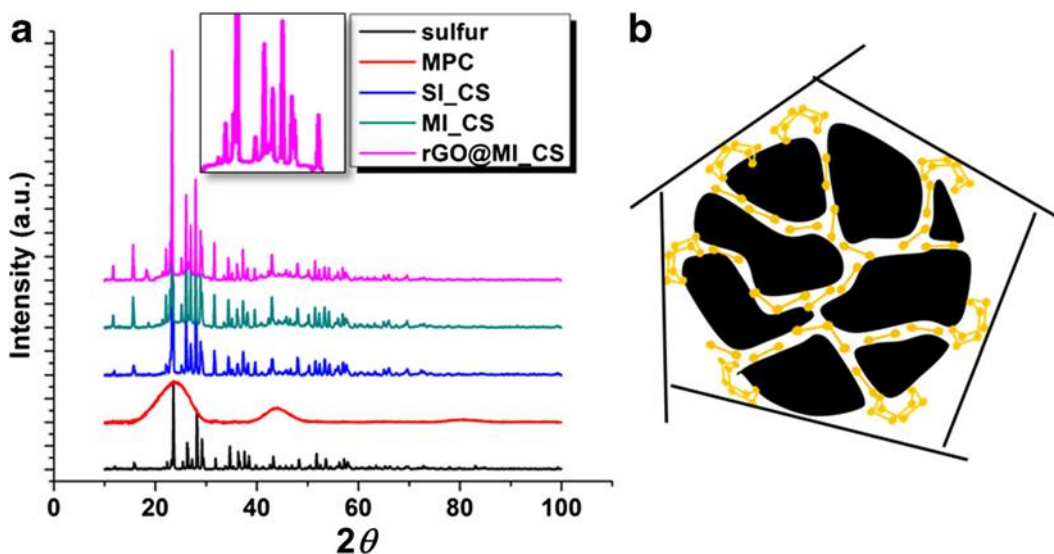


**Figure 2. 9:** a) XRD analysis of sulfur, carbon, and carbon-sulfur composite b) illustration of sulfur distribution in rGO wrapped microporous carbon from the characteristics EDS, XRD and BET results

Presence of shallow sulfur on the carbon surfaces inhibits the intimate electronic contact among carbon particles. For a comprehensive characterization of CS composite, a sketch of the MI\_CS with rGO synthesized material is provided in figure 2.9b, which illustrates the distribution of sulfur in the porous network. It is noteworthy that without performing any post-treatment after melt infusion, it is not possible to get rid of sulfur on the surfaces. Indeed, S melt infusion in a microporous carbon is generally accompanied by post thermal treatments to vaporize the

superfluous sulfur on the outer surface of carbon spheres. Here, the idea is to preserve such sulfur inside rGO to make it available for the electrochemical reaction and limiting its dissolution as much as possible during cell cycling. In this case, wrapping of MI\_CS with rGO can mask the sulfur present on the surfaces, thus provide the conductive pathways and hinder LiPS dissolution.

### 2.1.3 Electrochemical Testing

This part of my work was really carried out at the very start of my Ph.D. when I started working with this new system in my group. All electrochemical testing for this electrode material has been performed on EL-cell. This work leads to the conclusion that such an open electrochemical set up is not suitable for testing Li/S system majorly because of electrolyte migration and LiPS solubility. From figure 2.10a, it can be observed that the 1<sup>st</sup> cycle discharge capacity of SI\_CS cathode is about 510 mAh g<sup>-1</sup> at 0.1C. The characteristic two plateaus on discharge are not distinguishable, and the cathode retains only about 60% of the initial discharge capacity on second discharge. Such behavior can be attributed to shallow sulfur mainly present on the surface of MPC, which quickly dissolves into the electrolyte as LiPS. Whereas, two plateaus at 2.3 and 2.1 V are evident in the voltage profile of MI\_CS, figure 2.10b. The first voltage plateau is associated with the reaction of S<sub>8</sub> into S<sub>4</sub><sup>2-</sup>, which is mostly related to cyclo-S<sub>8</sub> localized on the carbon surface. The second voltage plateau arises from the conversion of allotropic sulfur S<sub>2-4</sub> that is restricted in the carbon micropores. Higher capacity retention is observed in this case, as the initial discharge capacity of MI\_CS is 842 mAh g<sup>-1</sup> and 610 mAh g<sup>-1</sup> at the 2<sup>nd</sup> discharge at 0.1C. Now, sulfur is well confined into the porous structure because of molecular captivity into the narrow micropores of carbon accomplished by thermal treatment. It is also observed that the potential plateau at 2.4 V vs. Li<sup>+</sup>/Li does not fully disappear after the first few cycles, further endorsing the effectiveness of melt infusion to better retain sulfur into the carbon. Additionally, it is believed that the electrochemical reaction of the sulfur cathode is constrained inside the narrow micropores of carbon and correspondingly higher capacity retention values can be attained. The rGO@MI\_CS, in which the composite material is wrapped by rGO, shows excellent electrochemical performances (figure 2.10c). In principle, a direct wrapping of S particles could lead to improved sulfur cathode material. Melt diffusion of S is widely used to prepare CS composite taking the advantage that the conductive network of graphene can contact sulfur particles in “plane-to-point” mode. However, LiPS formed during discharge can still readily diffuse out of graphene sheets with related “shuttle” effects. Thus, it is important to obtain sulfur particles well coated and confined. The sulfur dual confinement approach here proposed, with both MPC and rGO, helps minimize the dissolution and diffusion of LiPS, demotes shuttle effect and accommodates volume expansions during discharge. These factors have relevance on the performance of rGO@MI\_CS cathode, being the first discharge capacity of 1103 mAh g<sup>-1</sup> (figure 2.10c). On the second cycle, the discharge capacity decreases to 897 mAh g<sup>-1</sup> with

capacity retention of 81 % after SEI layer formation. S utilization is higher in rGO@MI\_CS compared to MI\_CS. At the 5<sup>th</sup> cycle at 0.1C the discharge capacity is still 760 mAh g<sup>-1</sup>.

Figure 2.10d highlights the recent progress in the architecture of cell design that is associated with the insertion of a carbon interlayer between the cathode and the separator. This strategy can effectively suppress LiPS shuttle and ensure proper functioning of cathode and anode simultaneously. As pointed out in the previous chapter, there are different carbon modified multifunctional separators able to act as interlayers to trap/block LiPS and limiting parasitic reactions. The positive effect of an interlayer is to curtail LiPS shuttle towards lithium anode by trapping LiPS between the interlayer and cathode, and even reversibly oxidized there into S<sub>8</sub>/Li<sub>2</sub>S. The interlayer has no adverse effect on the cathode but enhances the electrochemical stability of the cell. However, the interlayer boosts the inert weight of the cell, which should be lessened as much as possible considering the application and the need to increase the energy density. Thicker interlayers are preferred in case of cathodes with higher sulfur areal loading. Additionally, the application of interlayers requires easy fabrication, compatibility with cell assembly processes and low cost.

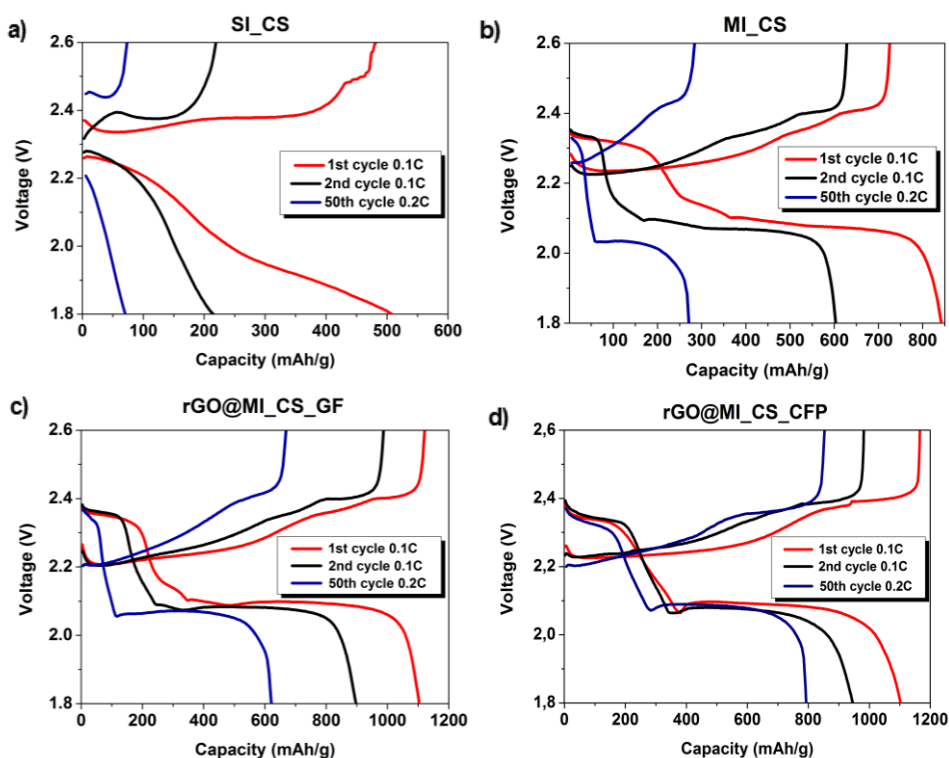


**Figure 2. 10:** Charge and discharge capacity of a) SI\_CS b) MI\_CS c) rGO@MI\_CS with GF d) rGO@MI\_CS with CFP for the first two cycles at 0.1C

Here, it is demonstrated that there is a major improvement in electrochemical performance of sulfur cathode using commercially available porous carbon papers as interlayers. The results are shown in Fig. 2.10d. In this case, the rGO@MI\_CS cathode is coupled with carbon fiber paper in place of glass fiber separator.

rGO@MI\_CS\_CFP exhibited excellent capacity retention with a first discharge capacity of 1108 mAh g<sup>-1</sup> that downgraded to 947 mAh g<sup>-1</sup> for the second cycle at 0.1C. This high capacity retention could be associated with suppression of LiPS from composite surfaces at the cathode by the carbon fiber separator. The benefits due to the use of the interlayer are evident by comparing the discharge capacities of the cathodes at two different C rates (Table 2.2). The comparison between rGO@MI\_CS\_GF and rGO@MI\_CS\_CFP shows that their initial performance is equivalent, demonstrating 1103 mAh g<sup>-1</sup> and 1108 mAh g<sup>-1</sup> at 0.1C, respectively. However, the discharge capacity after 100 cycles at 0.2C is significantly lower for rGO@MI\_CS\_GF resulting in 483 mAh g<sup>-1</sup> compared to 723 mAh g<sup>-1</sup> of rGO@MI\_CS\_CFP with the interlayer.

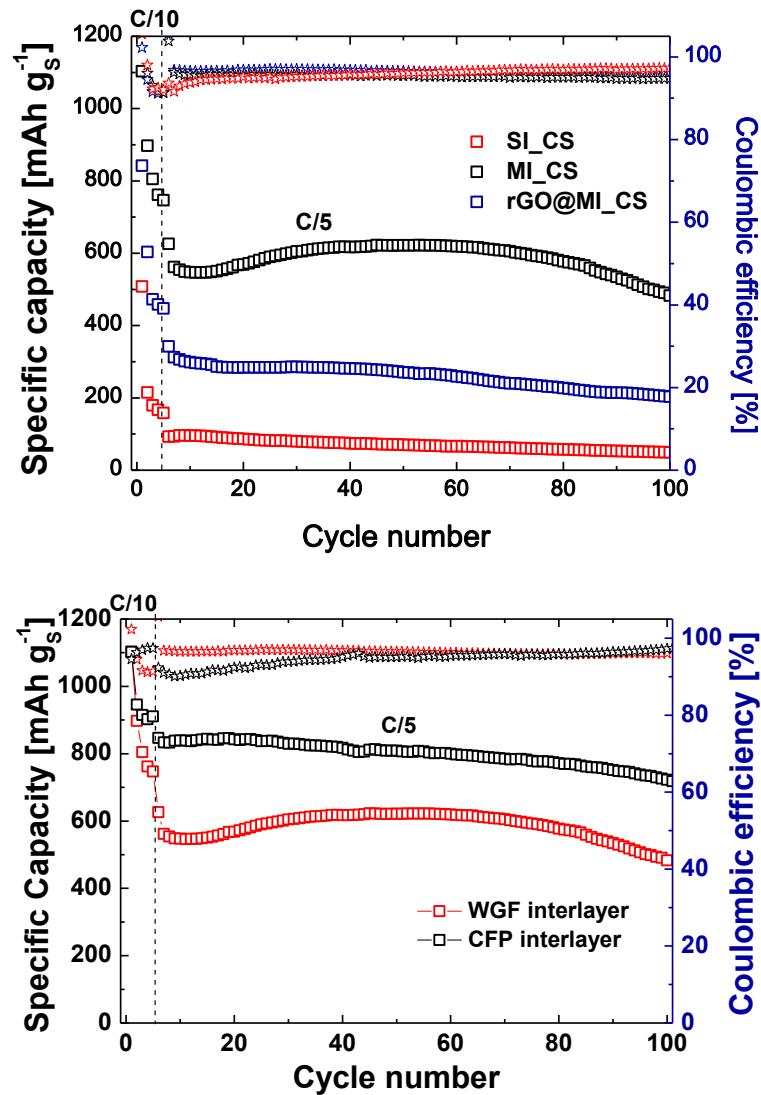


**Figure 2. 11:** Long-term Galvanostatic cycling at 0.2C and Coulombic efficiencies of a) SI\_CS b) MI\_CS c) rGO@MI\_CS with GF d) rGO@MI\_CS with CFP

Next, the cycling performance of the three Li/S cathodes was studied (figure 2.11). At 0.2C, an initial capacity of about 100 mAh g<sup>-1</sup> was measured for SI\_CS, followed by a decrease to the relatively stable capacity of 70 mAh g<sup>-1</sup> after 50

continuous cycles. Although 96% coulombic efficiency, within the next 50 cycles the capacity dropped to  $50 \text{ mAh g}^{-1}$  designating the poor performances of SI\_CS cathode. For the other two cathodes, relatively high capacities were observed. For MI\_CS, about 0.40 % decrease in the capacity from the first to the 100<sup>th</sup> cycle was noticed at 0.2C (figure 2.11a). At the end of the cycling test, the retained discharge capacity was about  $200 \text{ mAh g}^{-1}$ . As for rGO@MI\_CS cathode, better cycling performance was realized (figure 2.11b) with  $620 \text{ mAh g}^{-1}$  at 50<sup>th</sup> cycle. There is an increment in specific capacity for rGO@MI\_CS at 0.2 C that can be probably ascribed to the activation of active material. Similar capacity trends have already been observed and reported in the literature. Initial lower values of capacity can also be due to incomplete soaking of the S cathode by the electrolyte. Whereas, a rGO@MI\_CS cathode with carbon paper interlayer (figure 2.11d) showed excellent performance for prolonged cycling at 0.2C. A cell with this configuration showed  $850 \text{ mAh g}^{-1}$  capacity that is stable for more than 100 cycles with about 0.1 % capacity loss per cycle.

**Table 2. 2:** Discharge capacities of CS composites reported for different cycles with different C-rate

Discharge Capacity	SI_CS	MI_CS	rGO@MI_C S_GF	rGO@MI_C S_CFP
1 <sup>st</sup> cycle at C/10	508.25	841.89	1103.01	1108.10
2 <sup>nd</sup> cycle at C/10	214.72	603.09	897.04	946.95
5 <sup>th</sup> cycle at C/10	157.89	447.06	746.87	909.37
6 <sup>th</sup> cycle at C/5	92.90	342.24	626.05	846.82
10 <sup>th</sup> cycle at C/5	95.66	298.39	547.50	839.36
50 <sup>th</sup> cycle at C/5	70.11	271.01	621.48	808.61
100 <sup>th</sup> cycle at C/5	49.23	203.43	482.97	722.71

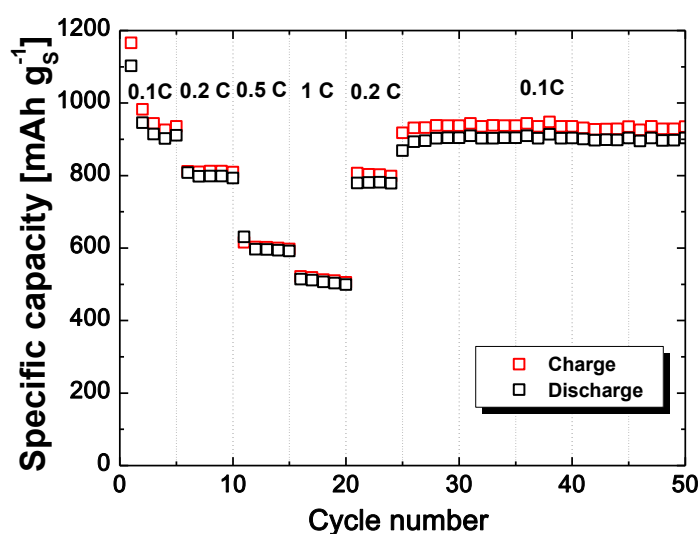


**Figure 2. 12:** Rate capability of the rGO@MI\_CS composite with CFP as an interlayer

rGO@MI\_CS cathode with carbon paper interlayer has exhibited superior rate capability with specific capacity more than 450 mAh g<sup>-1</sup> at 1C (figure 2.12). In addition, the electrode has demonstrated good capacity recovery when subjected to different C-rates (from about 800 mAh g<sup>-1</sup> at 0.2 C to 600 mAh g<sup>-1</sup> at 0.5 C and then back to 800 mAh g<sup>-1</sup>) that signifies system high reversibility. This substantiates the complexity of the Li/S system where the parallel efforts are required to design an efficient cathode in combination with other strategies to limit the shuttling of LiPS inside the cell.

## 2.2 Highly porous hierarchical heteroatom doped carbons/sulfur cathodes

It has been established that mainly electrochemical reactions take place at the interface between carbon and sulfur, so larger surface area is vital to achieving faster kinetics and higher sulfur utilization [33]. Hierarchical porosity offers better accessibility of electrolyte to sulfur but equally assists to limit bulk solubility of LiPS. However, the non-polar nature of carbon delimits the LiPS adsorption at the cathode. Doped carbon matrices provide enough bond polarity to interact with LiPS [36].

### 2.2.1 Development of nitrogen/sulfur-doped carbon cathodes

In this study, it is decided to produce all-design aspects integrated carbon to host sulfur. High surface area elemental doped hierarchical porous carbons have been synthesized via combining KOH activation and carbonization using polymers as precursor following previous reports [159, 160]. Here, nitrogen and sulfur-doped high surface area hierarchical porous carbons were produced by simultaneous activation and carbonization of polypyrrole and polythiophene respectively in a single stage. Both polypyrrole and polythiophene were synthesized with the aid of FeCl<sub>3</sub> as oxidant with approximately 100% yield. Polypyrrole and polythiophene were homogeneously mixed with KOH. Both mixtures were subjected to a temperature of 800°C to achieve simultaneously chemical activation and carbonization to obtain doped porous carbons as shown in figure 2.13.

### Synthesis of nitrogen/sulfur-doped carbons

PPyr and PThio were synthesized with the aid of FeCl<sub>3</sub> as an oxidant. In a typical synthesis of PPyr, a solution of FeCl<sub>3</sub> in water (0.5M) was prepared by mixing 16.2 g of FeCl<sub>3</sub> in 200 ml of DI water. Successively 3 g of pyrrole was added drop by drop to the solution under vigorous stirring. The solution was magnetically stirred for 2 h to attain PPyr. While, in the synthesis of PThio, 3 g of 2-thiophenemethanol in 20 ml of acetonitrile were added drop by drop, under vigorous stirring, to a solution of 28.9 g FeCl<sub>3</sub> in 100 ml acetonitrile. The resulting mixture was stirred for 15h at room temperature to achieve PThio. The obtained polymers were

separated by filtration on a fiberglass filter, washed with abundant DI water and then with acetone. Finally, they were dried individually in the oven, at 120 °C, overnight. The chemical activation and carbonization of PPyr and PThio were performed by heating (at a ramp rate of 2.5°C/min) a KOH/polymer mixture under nitrogen to a final temperature of 800 °C for 1h. In case of PPyr, KOH/PPyr weight ratio was kept 4. 1.6 g of PPyr was ground in a mortar with 6.4 g of KOH until obtaining a homogeneous mixture before proceeding to the activation in the tubular furnace. On the other hand in case of PThio, KOH/PThio weight ratio was retained 2. 1.39 g of PThio were ground in a mortar with 2.78 g of KOH until obtaining a homogeneous mixture before proceeding to the activation in the tubular furnace. In order to wash the activated samples, HCl solution was prepared by mixing 50.58 g of DI water with 5.62 g of HCl (37wt %). The samples were added to this solution and magnetically stirred for 30 min. Afterward, 5.62 g of HCl (37wt%) were added to the solutions which were stirred overnight. Successively, both solutions were filtered over a fiberglass filter and washed with DI water until reaching a neutral pH. Finally, the samples were dried in an oven, at 120 °C overnight. The as-obtained carbons were labeled as PPyr\_C and PThio\_C.

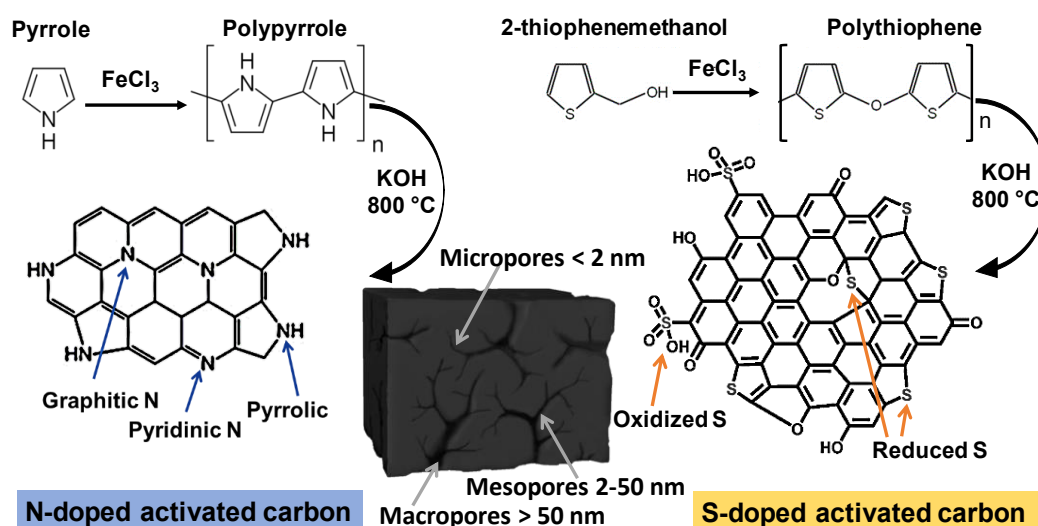


**Figure 2. 13:** Schematic illustration of the synthesis of N-doped and S-doped activated carbons from polypyrrole and polythiophene using KOH as an activating agent

### Construction of nitrogen/sulfur-doped carbon cathodes

PPyr\_C/S and PThio\_C/S cathodes were prepared by mixing 65% elemental sulfur and 35% of as prepared carbons. For the purpose, 1.05 g of sulfur (Sigma Aldrich) was dissolved in CS<sub>2</sub> at room temperature. 0.45 g of PPyr\_C or PThio\_C was added in the solution mixture. The solution mixture was magnetically stirred at room temperature to eliminate most of CS<sub>2</sub>. The wet mixture was further mixed up with pestle and mortar. Then, the as obtained dry powder was transferred to furnace tube under argon stream, where the composite was heated to 155 °C for 10 h by raising the temperature at rate of 1 °C min<sup>-1</sup>. The temperature was then raised to 250 °C to remove shallow sulfur. The slurry was prepared by mixing 80% active material, 10% carbon black (TIMCAL Super C45) and 10% polyvinylidene fluoride (PVDF)

in N-methyl-2-pyrrolidone (NMP). The homogenous mixing was attained by mixing with mixer mill (MM400, Retsch) at 20 Hz for 20 min. The slurry was cast onto aluminum foil using a doctor blade to acquire sulfur loading ( $2 \text{ mg cm}^{-2}$ ). Electrodes with diameter 15 mm were cut out of casted foils, and were dried at  $50^\circ\text{C}$  under vacuum for 6 h.

### 2.2.2 Physicochemical Characterization

The morphology of as-prepared polymers (PPyr, PThio), carbons (C\_PPyr, C\_PThio), sulfur-infused composites (S/C\_PPyr and S/C\_PThio) was examined using field-emission scanning electron microscopy (FESEM, JEOL-JSM-6700F) (figure 2.14). FESEM showed sponge-like construction for polypyrrole that is shaped by interconnected nanoparticles (diameter~200 nm), while polythiophene exhibited microspheres like morphology ranging from 0.2 to  $1.2 \mu\text{m}$ . These morphologies are highly advantageous for pores development in currently opted methodology, as they ensure large interfacial contact for the reaction between polymer precursors and an activating agent (KOH). After carbonization, the polypyrrole structure is fused and deteriorated into irregular porous carbon structures. While polythiophene showed collapsed structures of irregular carbon with large macropores with a little residue of carbon nanobeads. After sulfur infusion into the carbon structures, there is no alteration in carbon morphology and sulfur is not evident from imaging.

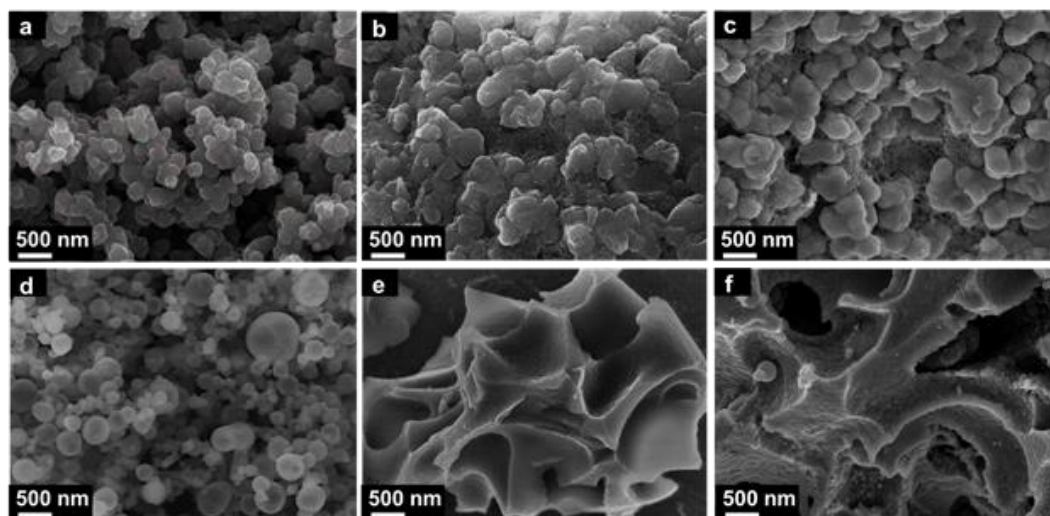


**Figure 2. 14:** FESEM images of polypyrrole (PPyr) (a) and polythiophene (PThio) (d), PPyr based activated carbon (b), PThio-based activated carbon (e), sulfur-infused PPyr\_C (c) and sulfur-infused PThio\_C (f)

To further probe the sulfur presence and uniform distribution in PPyr\_C/S and PThio\_C/S composites, EDS mapping was carried out (figure 2.15, 2.16). EDS of the S/C\_PPyr and S/C\_PThio was also performed using JEOL-JSM-6700F to investigate the sulfur distribution in the structure of the C matrix. Sulfur mapping is acquired under FESEM by imaging the X-ray signals from the composite surface. From EDS mapping of PPyr\_C/S composite, it can be observed that sulfur is well distributed with appreciable nitrogen signals coming from doped nitrogen of carbon

(figure 2.15). EDS mapping of PThio\_C/S composite also depicted the uniform distribution of elemental sulfur, the strength of signals is an indicator of doped sulfur presence at carbon sites (figure 2.16).

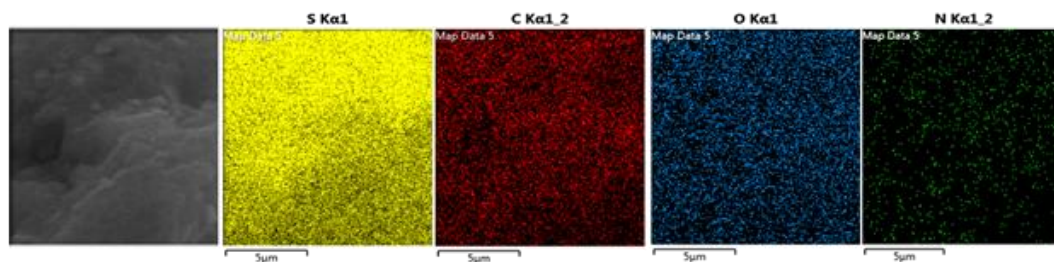


**Figure 2. 15:** EDS elemental mapping of S/PPyr\_C composite

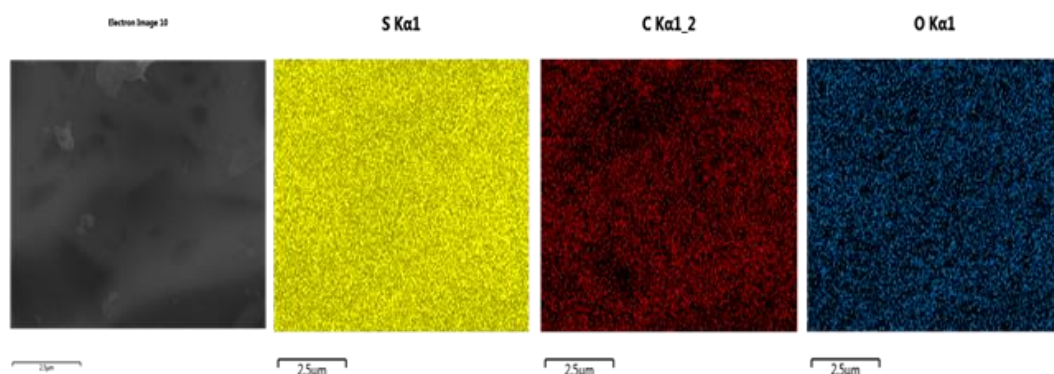


**Figure 2. 16:** EDS elemental mapping of S/PThio\_C composite

The microstructure and porosity of C\_PPyr and C\_PThio were analyzed by recording nitrogen adsorption isotherms at 77 K by exposing at a series of precisely controlled relative pressures from 0 to 1 with an ASAP 2020 Instrument (Micromeritics). Prior to the adsorption measurements, carbon matrices were degassed at 120 °C under vacuum (10 µm Hg) for 12 h to remove the adsorbates and residual moisture, and then the samples were cooled to nitrogen cryogenic temperature (77K). The specific surface area (SSA) of the samples was calculated by Brunauer–Emmett–Teller (BET) method using Langmuir model within the relative pressure range of 0 to 1 and the micropore volume and pore size distribution were estimated using Non-local density functional theory (NLDFT) assuming a slit geometry of the pores. The microstructure and porosity of PPyr\_C and PThio\_C were evaluated by nitrogen sorption isotherms (figure 2.17). The results obtained as well as the yield of synthesis is reported in Table 2.3. PPyr\_C exhibits significant adsorption at low relative pressure ( $<0.1 P/P_0$ ) indicating micropores followed by a nearly linear increase in adsorption in relative pressure range 0.1 to 0.4 representing mesopores. In fact, the PSD curve of PPyr\_C showed that the porosity is formed by two well-defined pore systems: uniform micropores ( $\approx 1.2$  nm) and small mesopores ( $\approx 2.3$  nm). Moreover, PPyr activated carbon showed a very high surface area ( $2903 \text{ m}^2 \text{ g}^{-1}$ ) calculated for relative pressure range 0.04 to 0.2 and pore volume  $3.456 \text{ cm}^3 \text{ g}^{-1}$ . PThio\_C instead gives type I isotherm according to IUPAC classification with large nitrogen uptake at lower relative pressure ( $<0.1 P/P_0$ )

characterizing to greater microporosity. However, a sheer slope can be observed between relative pressure range 0.1 to 0.3, representing very small dimension mesopores. PSD curve of PThio\_C reported in Figure 2.17b is showing a multimodal size distribution with three smaller peaks between 1 and 2 nm, and a smaller peak in the mesoporous region at about 2.2 nm. PThio activated carbon also showed the high surface area around  $3000 \text{ m}^2 \text{ g}^{-1}$  and pore volume  $3.5 \text{ cm}^3 \text{ g}^{-1}$ . Both carbons exhibit hierarchical porous carbon structures.

**Table 2. 3:** Yield and textural properties polypyrrole-derived activated carbons

	Yield	S <sub>BET</sub>	Pore Volume	Pore Size
<b>Sample</b>	%	m <sup>2</sup> g <sup>-1</sup>	cm <sup>3</sup> g <sup>-1</sup>	nm
<b>PPyr_C</b>	22	2903	3.456	1.2/2.3
<b>PThio_C</b>	28	3092	3.50	1.13/2.2

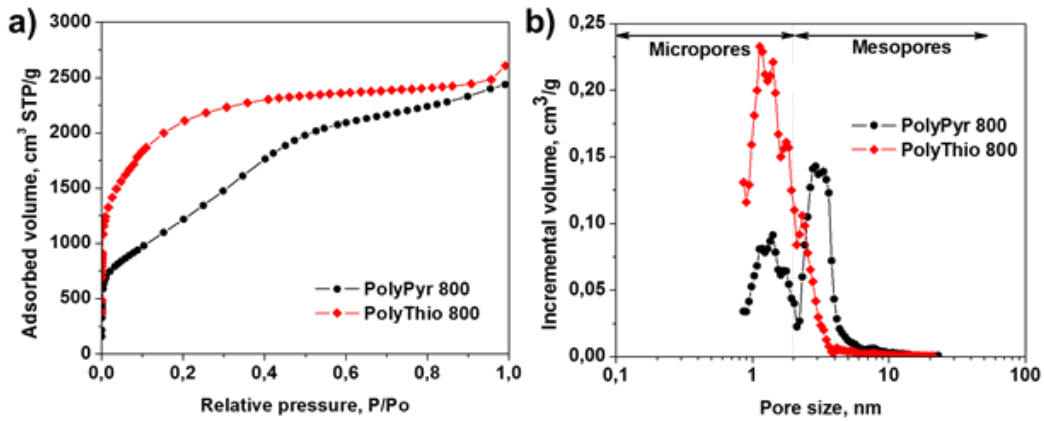


**Figure 2. 17:** Nitrogen sorption isotherms (a) and pore size distribution (PSD) curves (b) of polypyrrole and polythiophene-based activated carbons

XPS analysis has been performed to discern the presence of doping elements and their chemical bonds contribution towards the carbon. XPS measurements of C\_PPyr and C\_PThio were carried out using a Physical Electronics PHI5800 (USA) multi-technique ESCA system, with a monochromatic Al K $\alpha$  X-ray radiation. For testing, the samples were placed in an ultrahigh vacuum chamber at  $2 \times 10^{-10}$  Torr. XPS spectra have shown the contribution from N and S in addition to C and O respectively for polypyrrole and polythiophene-based carbons (figure 2.18). For PPyr\_C, XPS has exhibited 1.96% nitrogen content on atomic weight percentage that is contributing in the form of graphitic or quaternary N, pyridinic or pyrrolic N and pyridinic N at binding energies about 401.3 eV, 399.6 eV, and 396.6 eV. Graphitic N greatly contributes to the conductivity of the carbon matrix while pyridinic and pyrrolic N provide binding sites for polysulfides [161]. On another side, PThio\_C exhibited 4% sulfur content on atomic weight percentage as per XPS analysis, where sulfur exists both in directly bonded form with carbon (-C-S-) and bonded with carbon in oxidized form (-C-SOx) [159]. XPS spectra of carbon for both types of activated carbon showed the existence of carbonyl and carboxyl groups.

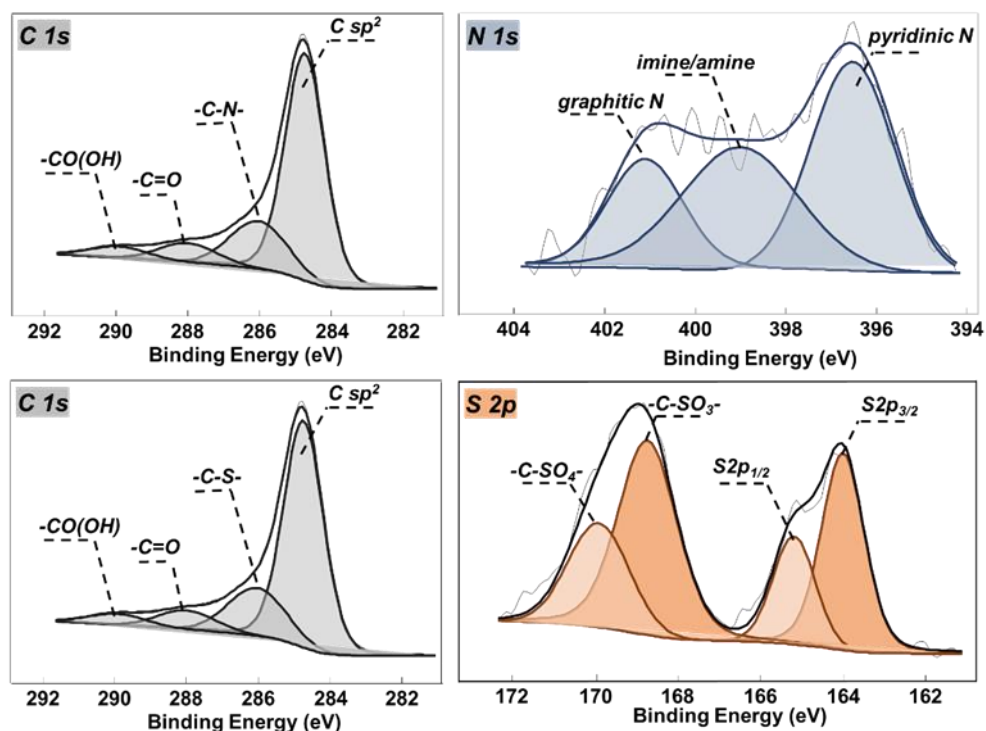


**Figure 2. 18:** High-resolution XPS spectra of PPy based carbon, C 1s (a) and N 1s (b) and PThio based carbon C 1s (c) and S 2p (d)

XRD patterns of elemental sulfur, PPy\_C/S and PThio\_C/S are given in Figure 2.19a. The XRD patterns of elemental sulfur, S/C\_PPy, and S/C\_PThio were recorded on a Panalytical X'Pert PRO diffractometer with a PIXcel detector, using Cu K $\alpha$  radiation, under the conditions of  $2\theta = 10-100^\circ$  and  $2\theta$  step size = 0.03, to observe the presence of crystalline S8 in the composite structure. Both PPy\_C/S and PThio\_C/S composites are not conferring any peak that signifies elemental crystalline sulfur, which in turn corroborating the assumption that sulfur is not existing out of porous carbon structures. Instead, XRD spectra of activated carbons exhibiting two wider peaks at  $24^\circ$  and  $44^\circ$ , demonstrating the graphitic features of the carbons. Raman spectroscopy has been performed for sulfur, PPy\_C/S and PThio\_C/S to evaluate the presence of sulfur in composite and level of graphitization of carbons (Figure 2.19b). Raman spectroscopy of PPy\_C/S and PThio\_C/S was carried out on Renishaw InVia micro-Raman spectrometer, with a laser excitation wavelength of 514.5 nm and a laser spot size of  $\sim 20 \mu\text{m}$ . Both PPy\_C and PThio\_C exhibited D- band and G-band of carbon at  $1350 \text{ cm}^{-1}$  and  $1580 \text{ cm}^{-1}$  respectively, characterizing the presence of graphitic structures. ID/IG value for both carbons averages around 0.9 representing the moderate degree of graphitization, hence conductivity. In Raman spectra of PPy\_C/S and PThio\_C/S, sulfur is not revealing its signal that is also signifying the fact that sulfur is infiltrated completely into the pores.

Thermogravimetric analyses (TGA) of S\_PPy and S\_PThio were carried out on a Mettler Toledo TGA/SDTA 851 instrument by heating the composite at  $10 \text{ }^\circ\text{C min}^{-1}$  from room temperature to  $800 \text{ }^\circ\text{C}$  under argon. TGA analyses reveal the presence

of 62% and 69% elemental sulfur for PPyr\_C/S and PThio\_C/S respectively (figure 2.20).

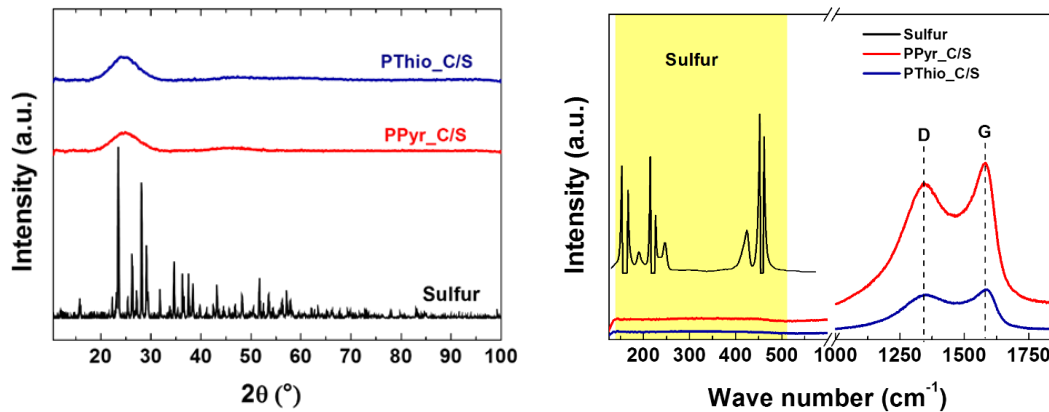


**Figure 2. 19:** XRD diffraction patterns (a) and Raman spectra (b) of elemental sulfur, PPyr\_C/S and PThio\_C/S composites

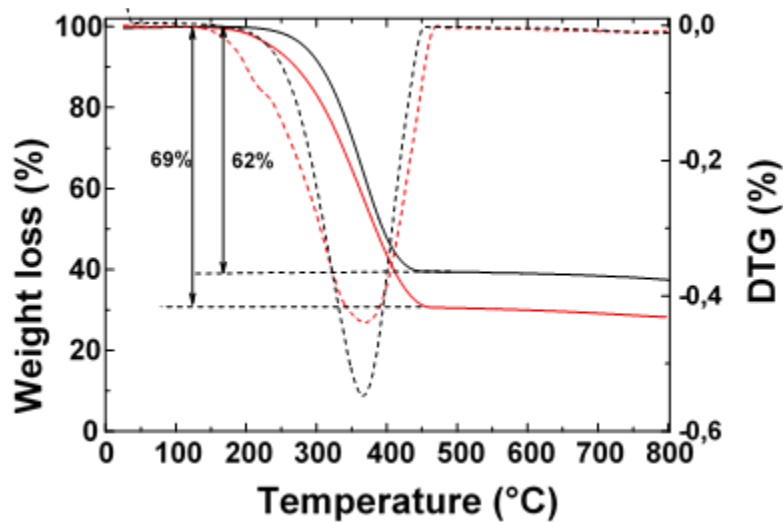


**Figure 2. 20:** TGA analysis of PPyr\_C/S and PThio\_C/S composites and their first order derivative to assess the quantity of sulfur

### 2.2.3 Electrochemical Testing

For the half-cell testing of as assembled S/PPyr\_C and S/PThio\_C cathodes, coin cells (CR2032 type) were assembled in Ar-filled dry glove box (Mbraun Labstar with  $\text{O}_2$  and  $\text{H}_2\text{O} < 0.1$  ppm) using lithium metal as the anode. The geometric area of the electrodes was  $1.76 \text{ cm}^2$ . A lithium disc ( $16 \times 0.2$  mm, Chemetall s.r.l.) was used as the anode. A Celgard EH2010 (trilayer PP/PE/PP)  $20 \text{ mm} \times 25 \mu\text{m}$  soaked with the electrolyte was used as the separator. The electrolyte consisted of 1,2-dimethoxyethane (DME) and 1,3-dioxolane (DIOX) 1:1 (v/v) with 1 M lithium bis(trifluoromethanesulfonyl)imide ( $\text{CF}_3\text{SO}_2\text{N}(\text{LiSO}_2\text{CF}_3)_2$ , LiTFSI) and 0.25 M  $\text{LiNO}_3$ . Each cell contains no more than 20  $\mu\text{L}$  of the electrolyte. Cells comprised of sulfur cathodes were galvanostatically discharged to 1.8 V and charged to 2.6 V

by an Arbin BT-2000 battery tester at room temperature. The C-rate is calculated using a theoretical capacity of sulfur (i.e.)  $1672 \text{ mAh g}^{-1}$ .

Both N and S doped hierarchical porous carbon/sulfur cathodes exhibited promising half-cell electrochemical performances vs. lithium anode (figure 2.21). Sulfur-infiltrated cathodes were subjected to a current density equivalent to 0.1C for the first cycle, and further cycling was performed at C-rate 0.2C (i.e.  $335 \text{ mA g}^{-1}$ ). At the first cycle, PPy<sub>r</sub>\_C/S cathode showed a discharge capacity of  $1448 \text{ mAh g}^{-1}$  very close to the theoretical capacity of sulfur ( $1672 \text{ mAh g}^{-1}$ ) with CE above 100% indicates the loss of lithium ion during discharging. While PThio\_C/S cathode exhibited  $1097 \text{ mAh g}^{-1}$  with a CE again higher than 100%. So, it can be inferred that doped hierarchical porous carbon consumes electrolyte in either SEI formation or lithiate a portion of the sulfur in micropores to solid state  $\text{Li}_2\text{S}$  through a direct electrochemical reaction. From 2nd cycle performed at 0.2C C-rate, both cathodes show a fall in specific capacities in part linked to the increase in current regime to  $993 \text{ mAh g}^{-1}$  in case of PPy<sub>r</sub>\_C/S and  $782 \text{ mAh g}^{-1}$  for PThio\_C/S cathode. From this cycle onwards, both cathodes reach a stabilized performance. In the case of PThio\_C/S, the specific capacity falls to  $631 \text{ mAh g}^{-1}$  for more than 250 cycles with CE around 96.6%. There is a capacity loss of 19.3% for more than 250 cycles for PThio\_C at 0.2C that corresponds 0.077% capacity loss per cycle. Whereas, in the case of PPy<sub>r</sub>\_C/S specific capacity values drops to  $762 \text{ mAh g}^{-1}$  after 250 cycles charging and discharging with CE of 99.5%. So, for PPy<sub>r</sub>\_C/S cathode specific capacity values are substantially higher than that of PThio\_C/S cathode with capacity decay 0.09% per cycle.

From the voltage profiles, it can be observed that both cathodes show a first discharge plateau at 2.3 V related to the formation of long-chain LiPS. After a transition between 2.3 and 2.1 V, a second long plateau appeared around 2.1 V. Insignificant overcharging points out the effective suppression of LiPS shuttle. Better electrochemical performance can be witnessed for N doped PPy<sub>r</sub>\_C than that of S doped PThio\_C, which can be attributed to higher conductivity, better pore size distribution and a more efficient LiPS retention owing to nitrogen polar groups. PPy<sub>r</sub>\_C/S cathode exhibits a flat lower plateau that indicates the uniform deposition of  $\text{Li}_2\text{S}$  and consequently higher sulfur utilization. A sloping plateau after 2 V can be observed in both sulfur composites especially in case of PPy<sub>r</sub>\_C/S that is particular to the microporous carbons. This behavior is linked to the adsorption of  $\text{Li}_2\text{S}_2$  on micropores [162]. However, after long term cycling, this behavior is diminished to the normal steep fall in voltage after 2.1 V. Hierarchical pores ensure better electrolyte access to infiltrated sulfur into carbon micropores, higher electronic and ionic activity and facilitated electron/ion transfer at carbon-electrolyte interface. N-doped carbon exhibited better sulfur utilization than that of S-doped carbon. While both types of carbons offer a satisfying electrochemical performance in terms of long-term stability attributable to elemental doping.

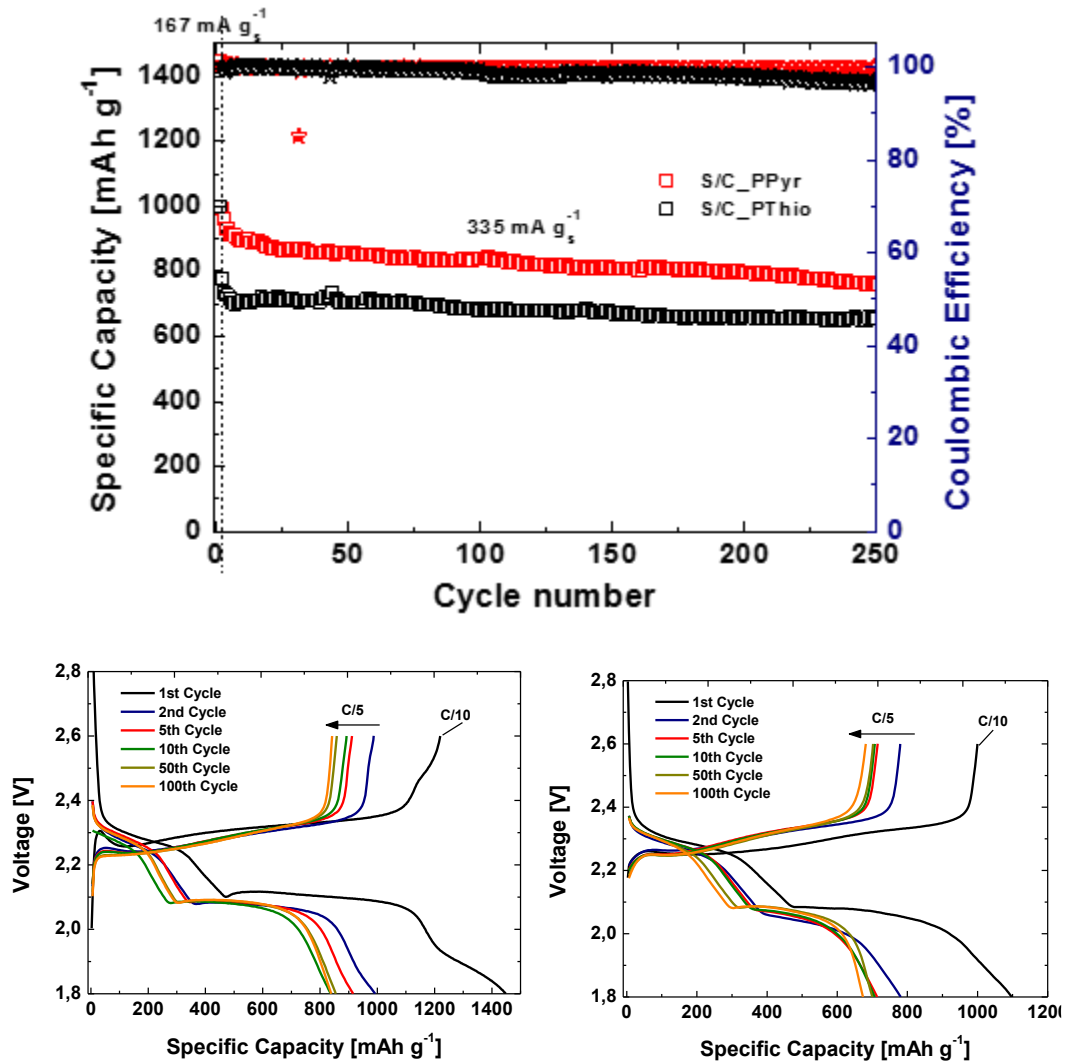


**Figure 2. 21:** a) cyclic performance (squares: specific capacity, stars: Coulombic efficiency) of S/C\_PPy and S/C\_PThio composite, (b, c) voltage profile vs. specific capacity of S/C\_PPy (b) and S/C\_PThio (c)

## 2.3 Conclusion

In summary, we have proposed a novel carbon matrix derived from bio-based material to host sulfur for Li-S battery application. For the first time, it was successfully demonstrated that microporous carbons can be obtained from pyrolysis of polymer  $\beta$ -cyclodextrin and exhibited a spongy structure that makes them absorptive for sulfur. We have shown that to make S and  $\text{Li}_2\text{S}$  available for the electrochemical process, it is necessary to provide a suitable conductive network by rGO wrapping the C/S composite. By using the proposed strategy, we are able to reach  $1108 \text{ mAh g}^{-1}$  at  $0.01\text{C}$  and  $626 \text{ mAh g}^{-1}$  at  $0.2\text{C}$  with a capacity loss of  $0.11\%$  per cycle for more than 100 cycles. In another cell configuration using carbon paper as an interlayer, discharge capacity raised to  $850 \text{ mA h g}^{-1}$  at  $0.2 \text{ C}$  and maintained it for 100 cycles with excellent rate capability and high Coulombic efficiency. Dual layer cathode protection strategy could prove a step forward towards commercial Li/S batteries for EVs using MPCs.

In the second strategy, elemental doped high surface area hierarchical porous carbons have been synthesized by the activation of polymers. As-prepared carbon with twice amount of infused sulfur exhibited remarkable electrochemical performance. Nitrogen-doped hierarchical porous carbon from polypyrrole showed the specific capacity of  $990 \text{ mAh g}^{-1}$  with capacity decay rate about 0.07% for more than 300 cycles at 0.2C. Whereas, sulfur-doped hierarchical porous carbon demonstrated the specific capacity of around  $800 \text{ mAh g}^{-1}$  with capacity decay rate 0.09% for more than 300 cycles at 0.02C. Such a high capacity stable cathodes were realized because of high surface area, hierarchical porosity, and elemental doping. Elemental doping provides enough polarity to the matrix to interact with LiPS.

## Chapter 3

# Development of metal compound decorated carbon/sulfur cathodes

In this chapter, we presented multiple designs-integrated strategies to realize highly stable sulfur cathodes. As highlighted earlier, metal oxides are considered as effective matrices to adsorb sulfur and LiPS because of intrinsic polar surfaces. Metal oxides can interact with LiPS via chemisorption or can exhibit acid-base interactions and/or form a surface-bound active redox mediator. As metal oxides are structurally 2D materials and exhibit limited specific surface area, so they have the negligible capability to physically stock sulfur and its species in comparison to carbon structures. So, carbon matrices decorated with metal oxide structures can effectively synergies the physical hosting of LiPS along with chemical interactions [163]. Here, three different strategies have been put forth to realize cathodes based on this approach. These synthesis strategies are facile, easy to industrialize and provide high loading sulfur cathodes.

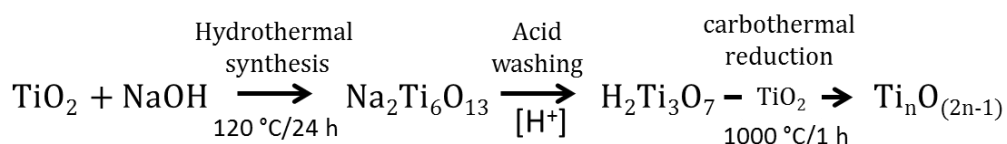
### 3.1 Nanoscale Magnéli phase $Ti_nO_{2n-1}$ embedded carbon matrices

Pure  $TiO_2$  has been investigated in various studies for its capability to chemically bind LiPS [164, 165]. Nazar et al. studied the effect of  $TiO_2$  presence in the carbon-sulfur cathode with significant improvement in discharge capacity retention [165]. Zhang et al. reported titanium dioxide loaded carbon fiber paper and  $TiO_2$ -anchored hollow carbon nanofiber structure as freestanding cathodes with the ability of physically/chemically trapped LiPS [164, 166]. In a recent study, double oxides structures were exploited in which  $SiO_2$  appears as a matrix to host sulfur and  $TiO_2$  shell create a physical and chemical barrier for LiPS to mitigate shuttle phenomena [167]. As the metal oxides are a poor conductor, they severely deter the coulombic efficiency and the high level of sulfur utilization. Stoichiometric  $TiO_2$  shows very low electrical conductivity (i.e.  $10^{-10} S m^{-1}$ ) [168].

But, sub-stoichiometric phases of  $\text{TiO}_2$ , chemical formula  $\text{Ti}_n\text{O}_{2n-1}$ , exhibit remarkable improvement in electrical conductance owing to planar defects and crystallographic shear planes [169-172]. These sub-stoichiometric oxides not only exhibit the conductivity comparable to carbon structures but are also stable in electrochemically oxidizing environments [173]. These Magnéli Phase  $\text{Ti}_n\text{O}_{2n-1}$  materials are already acknowledged for several applications including photovoltaics, photocatalysis, fuel cells, solar cells, and energy storage devices [173-175]. Previously, Cui et al. and Lin et al. had demonstrated  $\text{TiO}_2$  Magnéli phases as a host material for Li-S batteries with some results, but both of them involve complex and critical synthesis processes [176-178]. Moreover, they involve the use of pure hydrogen to achieve oxygen deficient phases of  $\text{TiO}_2$ . While Nazar et al. reported  $\text{Ti}_4\text{O}_7/\text{S}$  composite loaded on carbon fiber paper as positive electrode [179]. First, these approaches are not industrially viable as they involve pure hydrogen reduction environment, and require high reduction temperatures that promote the sintering of nanoparticles [180]. Secondly, organotitanium synthesis impedes the control on the shape of the Magneli phase nanoparticles as the shape of raw  $\text{TiO}_2$  is difficult to control [181]. Pure metal oxides cathodes are prone to pulverization, and cell assembled from these cathodes also have a need for high concentration of electrolyte to realize good performances that is not appropriate to aim high gravimetric capacities. These setbacks can be alleviated by integrating metal oxide nanoparticles into lightweight conductive carbon matrices.

### 3.1.1 Development of Carbon embedded Magnéli phase $\text{Ti}_n\text{O}_{2n-1}$ , its sulfur composite, and cathode

In this work, we targeted to attain multiple design strategies integrated into a single electrode. A cost-effective and sustainable approach has been opted to produce carbon matrices loaded with Magneli phase  $\text{Ti}_n\text{O}_{2n-1}$  nanoparticles as a host material for the sulfur cathode. Electrically conductive Magneli phase  $\text{Ti}_n\text{O}_{2n-1}$  nanoparticles loaded carbon matrices were synthesized by simple heat treatment of the mixture of  $\text{TiO}_2$  nanotubes and polyvinyl alcohol (PVA) at 1000 °C in the inert environment using Ti metal as an oxygen getter. Carbon from PVA helps to achieve the carbothermal reduction of  $\text{TiO}_2$  along with the suppression of sintering and grain growth in  $\text{TiO}_2$  nanoparticles. The Following scheme summarizes the reactions involved in the process.



As-built cathode material allows achieving high sulfur loading along with effective LiPS adsorption. Sulfur is introduced into the carbon matrix by simple thermal infusion process. The cells were effectively charged and discharged for hundreds of cycles at different C-rate. The post-operation analysis of 300 cycles discharged

cathode was carried out to rationalize the origin of good performances.

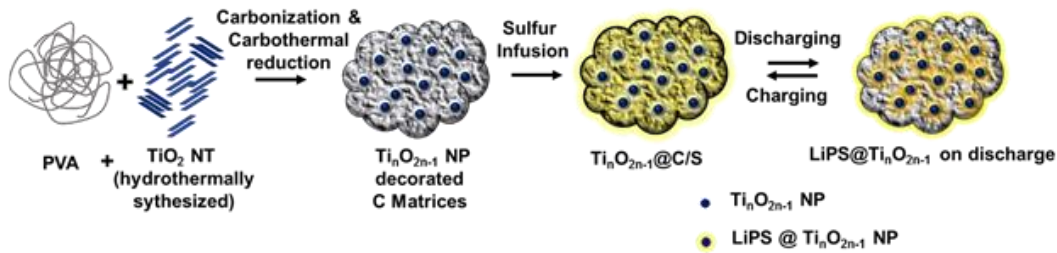


**Figure 3. 1:** Schematic illustration of the synthesis strategy for carbothermal reduction of  $TiO_2$  nanotubes to Magnéli phase  $Ti_nO_{2n-1}$  nanoparticle-embedded carbon host matrices ( $Ti_nO_{2n-1}$  NP@C).

### Facile Synthesis of Magnéli phase $Ti_nO_{2n-1}$ embedded carbon

1 g of commercial anatase  $TiO_2$  powder (Hombikat N100) is dispersed in 10 M NaOH solution (15 ml) under stirring. The mixture is transferred in Teflon lined autoclave (25 ml) for hydrothermal reaction. The hydrothermal reaction was carried out at 120 °C for 24 h. The mixture was separated and washed with distilled water five times. Collected mass was dipped in 0.1 M HCl solution for 12 h. Sample is washed again with abundance of distilled water. The weight of as prepared nanotubes was 1.076 gm. To perform carbothermal reduction and carbonization, 0.9 g of  $TiO_2$  nanotubes were dispersed in 100 ml of distilled water under sonication. In parallel, 2.3 g of PVA (molecular weight 146000-186000) from Sigma Aldrich is dissolved in 400 ml water with continuous stirring at 90 °C. The solutions were mixed together under stirring followed by heating to 90 °C for 12 h. The water is evaporated under heating to achieve a solid mixture of the two components. Carbonization and carbothermal reduction of PVA wrapped  $TiO_2$  nanotubes was carried out. Thermal synthesis involves the ramp temperature of 1000 °C for 1 hr at a heating rate 5 °C/min under an argon atmosphere with gas flow >50 ml/min in a tubular furnace using pure Ti metal as an oxygen getter. The weight of the composite was around 1.116 g and is black in color.

### Construction of $Ti_nO_{2n-1}$ embedded carbon /sulfur cathodes

0.6 g of carbon decorated  $Ti_nO_{2n-1}$  nanoparticles were mixed with 60% sulfur in pestle and mortar. The mixture was transferred in an autoclave under an argon atmosphere and sealed tight. Before putting inside the mixture was pressed into a disc under high pressure. The vessel is transferred into an oven for 4 h at 120°C and 12 h at 155°C. The sulfur infiltrated sample was collected. Coin cells 2032 were assembled in Ar-filled dry glove box (Mbraun Labstar). The geometric area of the electrodes was 2 cm<sup>2</sup>. The cathode contained the different S/C composite materials above described. A lithium disc (16 x 0.2 mm, Chemetall s.r.l.) was used as the anode. A Celgard EH2010 (trilayer PP/PE/PP) 19 mm x 0.65 mm soaked with the electrolyte was used as the separator. The electrolyte consisted of 1,2-dimethoxyethane (DME) and 1,3-dioxolane (DIOX) 1:1 (v/v) with 1 M LiTFSI and 0.25 M  $LiNO_3$ . The sulfur to electrolyte (E/S) was kept 5-6  $\mu L$   $mg^{-1}$  of sulfur. For the purpose of post mortem analysis, an ECC-STD electrochemical cell configuration (EL-Cell, Gmbh) was employed. Cells were galvanostatically

discharged to 1.8 V and charged to 2.6 V by an Arbin BT-2000 battery tester at room temperature. Cycling tests were performed at various C-rate. The C-Rate is calculated using a theoretical capacity of sulfur (i.e.)  $1672 \text{ mAh g}^{-1}$ . Cyclic voltammetry and electrochemical impedance spectroscopy measurements were performed on CH instrument electrochemical workstation using three electrodes configuration using  $\text{Li/Li}^+$  as a reference electrode.

### 3.1.2 Physicochemical Characterization

The morphology of  $\text{TiO}_2$  nanotubes,  $\text{C@Ti}_n\text{O}_{2n-1}$  matrix, and sulfur-infused Carbon@ $\text{Ti}_n\text{O}_{2n-1}$  composite was examined using field-emission scanning electron microscopy (FESEM, JEOL-JSM-6700F). Figure 3.2 elaborates the morphology of as-prepared  $\text{TiO}_2$  nanotubes ( $\text{TiO}_2$  NT), carbon matrices loaded with  $\text{Ti}_n\text{O}_{2n-1}$  nanoparticles ( $\text{Ti}_n\text{O}_{2n-1}$  NP@C), and sulfur-infused carbon matrices loaded with  $\text{Ti}_n\text{O}_{2n-1}$  nanoparticles ( $\text{Ti}_n\text{O}_{2n-1}$  NP@C/S) under FESEM. It can be observed that  $\text{TiO}_2$  NT exhibit the diameter around 10-15 nm with the lengths ranging 100-300 nm. FESEM images (Figure 3.2c, d) of  $\text{Ti}_n\text{O}_{2n-1}$  NP@C reveal that  $\text{Ti}_n\text{O}_{2n-1}$  nanoparticles are well embedded into the carbon matrices taken under secondary electrons (SE) and backscattered electron (BSE) acquiring mode. On carbothermal reduction, white  $\text{TiO}_2$  NT shifted their morphology to spherical black  $\text{Ti}_n\text{O}_{2n-1}$  nanoparticles with a diameter  $< 100$  nm. As pointed out earlier, this transformation of the morphology of oxides could be a result of oxygen extraction from lattice and high-energy treatment of nanotubes. Meanwhile, the carbonization of PVA provided the carbon matrices with  $\text{Ti}_n\text{O}_{2n-1}$  nanoparticles housing inside. It can be seen that the carbon matrix efficiently deter the sintering and grain growth of  $\text{TiO}_2$ , keeping the particles size  $< 100$  nm. There is no significant change in morphology after thermal infusion of sulfur into the composite (Figure 3.2e, f), which reflects the homogenous distribution of sulfur into and onto the  $\text{Ti}_n\text{O}_{2n-1}$  NP@C matrices.

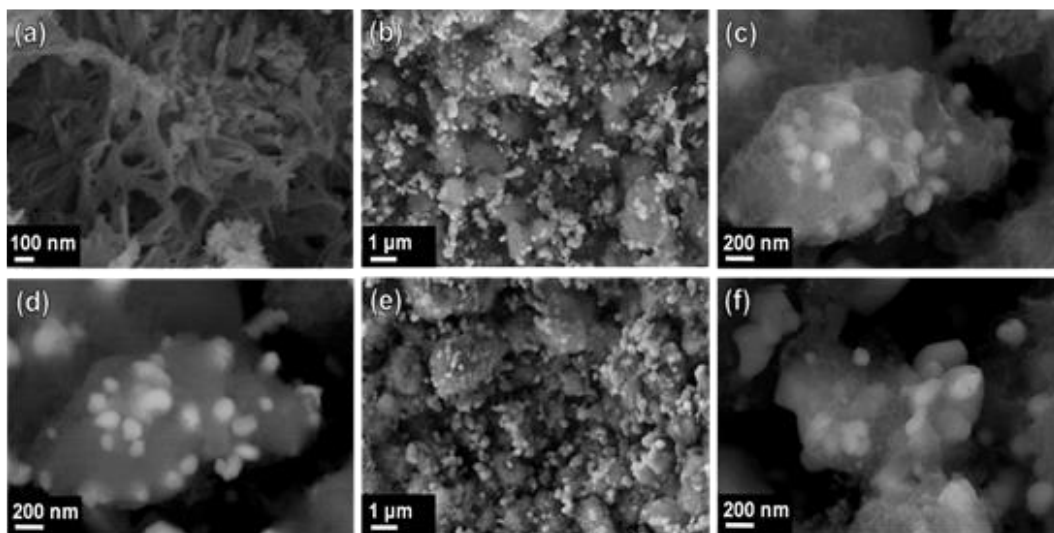


**Figure 3. 2:** FESEM images of (a)  $\text{TiO}_2$  NT (b)  $\text{Ti}_n\text{O}_{2n-1}$ @C, (c)  $\text{Ti}_n\text{O}_{2n-1}$ @C (secondary electron image), (d)  $\text{Ti}_n\text{O}_{2n-1}$ @C (back-scattered electron image), (e) Sulfur-infused  $\text{Ti}_n\text{O}_{2n-1}$ @C/S, and (f) Sulfur-infused  $\text{Ti}_n\text{O}_{2n-1}$  NP@C/S (SE)

High-resolution transmission electron microscopy (HRTEM) analysis of typical  $TiO_2$  NTs,  $Ti_nO_{2n-1}@C$  matrices and  $Ti_nO_{2n-1}@C/S$  composites are shown in Figure 3.3a-c, respectively. Bright field TEM imaging of  $TiO_2$  NTs confirms a multi-walled tube structure with an external diameter of  $\sim 10-15$  nm and an internal diameter of 5-8 nm. The NPs of  $Ti_nO_{2n-1}@C$  have a diameter of  $\sim 25-30$  nm, as shown in Figure 3b and e.  $Ti_nO_{2n-1}@C/S$  composites consist of  $Ti_nO_{2n-1}$  NPs embedded in the composite of C and S (Figure 3.3c). A high magnification TEM image of the C/S composite, illustrating its layered structure, is shown in Figure 3.3f. Selected area electron diffraction (SAED) patterns of  $TiO_2$  NTs,  $Ti_nO_{2n-1}@C$  matrices and  $Ti_nO_{2n-1}@C/S$  composites were acquired from the areas shown in the inset images in Figure 3.3h-j, respectively. The SAED pattern for a typical  $TiO_2$  NTs, shown in Figure 3.3h, indicates a polycrystalline structure of rutile phase  $TiO_2$  (JCPDS No. 21-1276). The SAED pattern for typical  $Ti_nO_{2n-1}@C$  matrices consists of a series of polycrystalline rings with d-spacings consistent with  $Ti_9O_{17}$  (JCPDS No. 50-0791). A series of polycrystalline rings with the same d-spacings were observed in the SAED pattern for the  $Ti_nO_{2n-1}@C/S$  composite, as shown in Figure 3j, indicating that the titanium oxide present in the NP@C matrices remains as  $Ti_9O_{17}$  during the preparation of the  $Ti_nO_{2n-1}@C/S$  composite. The additional diffraction spots present in the SAED pattern for the  $Ti_nO_{2n-1}@C/S$  composite, which is not found in the pattern for the  $Ti_nO_{2n-1}@C$  matrices, are due to the presence of elemental S. The d-spacings for these diffraction spots are consistent with orthorhombic S8 (JCPDS No. 08-0247).

Energy dispersive X-ray spectroscopy (EDS) of the composites and exhausted cathodes was also performed using JEOL-JSM-6700F to investigate the sulfur presence into the structure of  $C@Ti_nO_{2n-1}$  matrix. In this cathode material, the sulfur remained crystalline and stable under electron beam irradiation. EDS elemental mapping confirms that sulfur is homogeneously distributed throughout the composite microstructure (Figure 3.4). Mapping of Ti indicates that nanoparticles of  $Ti_nO_{2n-1}$  are well dispersed in the composite just underneath the carbon shell, as sharp boundaries cannot be defined. EDS signals for oxygen directly correspond to the position of  $Ti_nO_{2n-1}$  nanoparticles. Sulfur signals are comparatively weak over regions where Ti and O signals are quite strong, which highlights that sulfur is initially infiltrated into the carbon matrix and found as separate nanocrystallites, as determined by selected area electron diffraction. Thus, in order to observe the chemical interaction of LiPS with  $Ti_nO_{2n-1}$  nanoparticles, we obtained EDS analysis of cycled cathodes (vide infra, Figure 3.9). Thus, the pre-cycled composite is a carbon matrix loaded with individual  $Ti_nO_{2n-1}$  nanocrystals with segregated high areal loading of sulfur within the carbon matrix in close proximity.

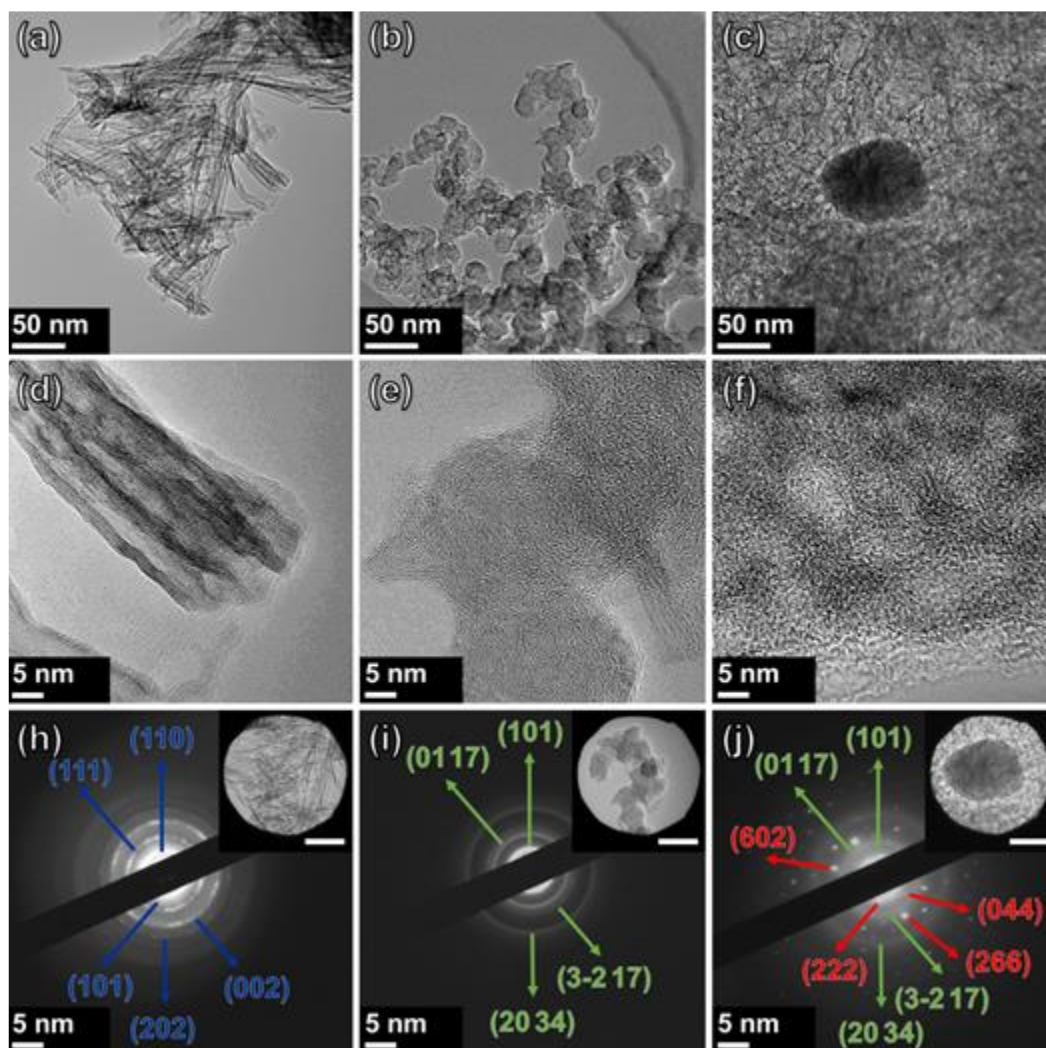


**Figure 3. 3:** TEM images of (a) TiO<sub>2</sub> NTs, (b) Ti<sub>n</sub>O<sub>2n-1</sub>@C matrices and (c) Ti<sub>n</sub>O<sub>2n-1</sub>@C/S composites. HRTEM images of (d) TiO<sub>2</sub> NTs, (e) Ti<sub>n</sub>O<sub>2n-1</sub>@C matrices and (f) Ti<sub>n</sub>O<sub>2n-1</sub>@C/S composites taken at a magnification of 300 kx. SAED patterns of (h) TiO<sub>2</sub> NTs, (i) Ti<sub>n</sub>O<sub>2n-1</sub>@C matrices and (j) Ti<sub>n</sub>O<sub>2n-1</sub>@C/S composites acquired from the areas shown the inset images. The scale bar in the inset corresponds to 50 nm. (Blue corresponds to rutile TiO<sub>2</sub>, green corresponds to Ti<sub>9</sub>O<sub>17</sub> and red corresponds to elemental S).

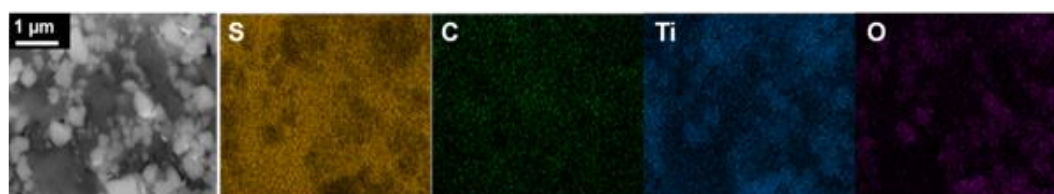


**Figure 3. 4:** EDS elemental mapping of sulfur-infused Ti<sub>n</sub>O<sub>2n-1</sub>@C/S matrix composite.

The microstructure and porosity of the Ti<sub>n</sub>O<sub>2n-1</sub>@C matrix and sulfur-infused Ti<sub>n</sub>O<sub>2n-1</sub>@C/S composite was quantitatively determined by nitrogen adsorption-desorption curves. The porous structures of C@Ti<sub>n</sub>O<sub>2n-1</sub> matrix and sulfur-infused Carbon@Ti<sub>n</sub>O<sub>2n-1</sub> composite were analyzed by recording nitrogen adsorption isotherms at 77 K by exposing at a series of precisely controlled pressures from 0 to 1 with an ASAP 2020 Instrument (Micromeritics). Prior to the adsorption measurements, the C@Ti<sub>n</sub>O<sub>2n-1</sub> matrix and sulfur-infused Carbon@Ti<sub>n</sub>O<sub>2n-1</sub>

composite were degassed at 150 °C and 50 °C (to avoid the sublimation of the sulfur) respectively under vacuum (10  $\mu\text{m Hg}$ ) for 12 h to remove the adsorbates and residual moisture, and then sample was cooled to nitrogen cryogenic temperature (77K). The specific surface area (SSA) of the samples was calculated by Brunauer–Emmett–Teller (BET) method using Langmuir model within the relative pressure range of 0 to 1 and the micropore volume and pore size distribution were estimated using density functional theory (DFT) assuming a slit geometry of the pores. Figure 3.5a demonstrates that the  $\text{Ti}_n\text{O}_{2n-1}@C$  matrix has a high surface area with a maximum pore size distribution at 5.0 nm. The isotherm in Fig. 3.5a shows a type IV hysteresis curve indicative of a mesoporous material. The hysteresis shape and the fact we observe no limiting adsorption at high  $P/P_0$  is a particular signature of a composite comprising slit-shaped pores [151]. This form of porosity in the host material is critical for suppressing shuttling phenomena for improved capacity retention. Moreover, the surface area is significantly reduced from 192  $\text{m}^2/\text{g}$  to 11.24  $\text{m}^2/\text{g}$  for sulfur-infused  $\text{Ti}_n\text{O}_{2n-1}@C/S$  composite. Importantly, this confirms that sulfur is properly and uniformly infused into pores of the  $\text{Ti}_n\text{O}_{2n-1}@C$  matrix. Thermogravimetric analysis was carried out on a Mettler Toledo TGA/SDTA 851 instrument by heating the composite at 10 °C  $\text{min}^{-1}$  from room temperature to 800 °C. Thermogravimetric analysis (TGA) from room temperature to 800 °C at 10 °C  $\text{min}^{-1}$  under nitrogen atmosphere confirmed that the sulfur loading is  $\sim 60\%$  (w/w) (figure 3.5b).

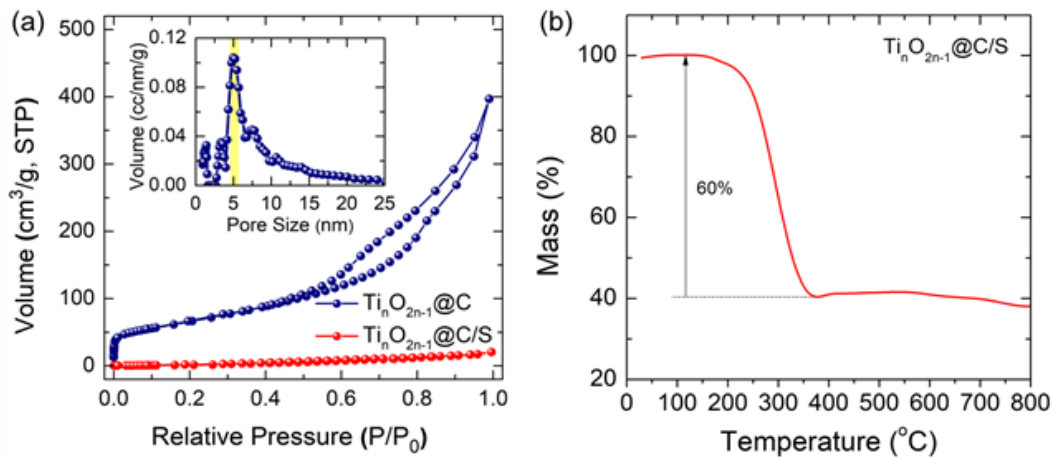


**Figure 3. 5:** (a) Nitrogen adsorption-desorption isotherms for  $\text{Ti}_n\text{O}_{2n-1}@C$  and  $\text{Ti}_n\text{O}_{2n-1}@C/S$ . (Inset) corresponding pore size measurements. (b) Thermogravimetric analysis of as prepared sulfur-infused  $\text{Ti}_n\text{O}_{2n-1}@C/S$  matrix.

The XRD patterns were recorded on a Panalytical X'Pert PRO diffractometer with a PIXcel detector, using Cu  $K\alpha$  radiation, under the conditions of  $2\theta = 10\text{-}100^{\circ}$  and  $2\theta$  step size = 0.03, to observe the presence of  $\text{TiO}_2$  sub-stoichiometric phases. Reduction of  $\text{TiO}_2$  into Magnéli phase  $\text{Ti}_n\text{O}_{2n-1}$  significantly enhanced the electrical conductivity from its rearrangement into the oxygen-deficient  $\text{Ti}_n\text{O}_{2n-1}$  phases (compared to anatase  $\text{TiO}_2$ ) and from an increase in  $\text{Ti}^{3+}$  species [169]. Maintaining electrical conductivity to rival graphitic carbon is one benefit of the Magnéli phases, whose surface chemistry also immobilizes LiPS during cycling. XRD data in Figure

3.6a did confirm that hydrothermal synthesis of TiO<sub>2</sub> NT incorporates rutile phases in pure commercial anatase Hombikat N100 TiO<sub>2</sub> powder, with typical diffraction patterns for nanostructured-layered materials. This polymorph of the material is reported as TiO<sub>2</sub>-B with an edge and corner-sharing TiO<sub>6</sub> subunits in the lattice and exhibits lower density than any of the pure phases of TiO<sub>2</sub> [182]. Broadening of the reflections in the diffraction pattern was also confirmed due to dimensional confinement. The carbothermal-reduced form of TiO<sub>2</sub> comprised several reflections corresponding to various Magnéli phases of TiO<sub>2</sub> by JCPDS indexing. The XRD pattern agreement showed ~70% coincidence of the reflections with Ti<sub>4</sub>O<sub>7</sub>, Ti<sub>5</sub>O<sub>9</sub> and Ti<sub>9</sub>O<sub>17</sub> compared with JCPDS files 50-0787, 51-0641 and 50-0791, respectively. The emergence of a characteristic peak for Ti<sub>4</sub>O<sub>7</sub> at 20.78° was observed in the XRD spectrum of Ti<sub>n</sub>O<sub>2n-1</sub>@C.

The interaction of LiPS with TiO<sub>2</sub> nanotubes and Ti<sub>n</sub>O<sub>2n-1</sub>@C matrix was investigated via a visual perception experiment under argon atmosphere. Solutions of different LiPS were prepared by reacting Li<sub>2</sub>S and S<sub>8</sub> into a mixture of DME and DIOX over a period of 72 h, under continuous stirring in argon. Figure 3.6b shows the particularly strong optical adsorption of LiPS onto Ti<sub>n</sub>O<sub>2n-1</sub>@C in contrast to solutions of pure TiO<sub>2</sub> NT samples. The LiPS solution containing TiO<sub>2</sub> NT showed a substantial discoloration confirming that TiO<sub>2</sub> also has certain adsorption capability for LiPS. This implies that the interaction of pure titania may not be adequate for higher sulfur loadings, and low electronic conductivity also limits long cycle life capability. On the contrary, we observe a strong discoloration of a concentrated mixture of LiPS in the first 12 h by adding Ti<sub>n</sub>O<sub>2n-1</sub>@C into the solution. The strong adsorption of LiPS by Ti<sub>n</sub>O<sub>2n-1</sub>@C can be attributed to physical adsorption by porous carbon and in the case of Magnéli Ti<sub>n</sub>O<sub>2n-1</sub> oxides, a strong polysulfide interaction that fixes LiPS to the oxide surface.

To further probe the electronic and chemical environment, XPS analysis of TiO<sub>2</sub> nanotubes, Ti<sub>n</sub>O<sub>2n-1</sub>@C/S composite, charged and discharged cathodes was performed. X-ray photoelectron spectroscopy (XPS) measurements were carried out using a Physical Electronics PHI5800 (USA) multi-technique ESCA system, with a monochromatic Al K $\alpha$  X-ray radiation. For testing, the samples were placed in an ultrahigh vacuum chamber at  $2 \times 10^{-10}$  Torr. Figure 5b show the Ti 2p core-level photoemission from TiO<sub>2</sub> NT and Ti<sub>n</sub>O<sub>2n-1</sub>@C/S composite. Both materials exhibited two hyperfine split photoemission of titanium oxide compounds at 459 eV and 464.6 eV from Ti<sup>4+</sup> 2p<sup>3/2-1/2</sup>. However, Ti<sub>n</sub>O<sub>2n-1</sub>@C/S shows two additional and well-differentiated lower intensity emissions at 461 eV and 457 eV from Ti<sup>+3</sup> 2p<sup>3/2</sup> and 2p<sup>1/2</sup> that correspond to a specific Ti-S bonding [172, 183]. In Magnéli phase Ti<sub>n</sub>O<sub>2n-1</sub>, surface Ti<sup>+3</sup> and oxygen vacant sites can interact with oxygen and oxides [184]. Likewise, as sulfur belongs to the same group, it also interacts with Magnéli phase Ti<sub>n</sub>O<sub>2n-1</sub> both in elemental and polysulfide form, which is what we detected within the Ti<sub>n</sub>O<sub>2n-1</sub>@C/S composite. The S2p photoelectron emission spectra of as-prepared cathodes and those after 300 charge-discharge cycles (Figure 3.6c). In our case, the spatially localized composite contains a large starting areal

sulfur loading ( $>2 \text{ mg cm}^{-2}$ ), and a high density of Magnéli oxide NPs dispersed throughout the voids and pores in the carbon matrix. The oxides at the electrode scale contain several oxides, all of which are conductive Magnéli oxides that enhance the chemical affinity for LiPS binding during the cycling process.

In both cases, the broad core-level emission between 164-172 eV was deconvoluted into two peaks centered at 170.2 eV and 167.7 eV, specifically associated with S-O ( $SO_2$ ) and S-O ( $SO_3$ ), respectively [21, 185]. This chemical state is often interpreted as electrolyte degradation, particularly associated with LiTFSI and  $LiNO_3$  electrolyte salts in the absence of  $TiO_2$ . According to Umebayashi et al. and Sayago et al. for adsorbed sulfur dioxide ( $SO_2$ ) molecules on a  $TiO_2$  surface, the typical photoemission from the S2p states are likewise located between 166 and 170 eV [186, 187]. In our case, this XPS signature related to surface-adsorbed  $SO_2$  /  $SO_3$  molecules from electrolyte decomposition through Ti-O-S binding at the surface of the Magnéli phase. This interaction is additional to the typical Ti-S bonding in which sulfur atoms have their S 2p peak between 160.7 and 163.7 eV. This might suggest that carbothermally reduced form of  $TiO_2$  can trap soluble LiPS by a mechanism similar to conversion to polythionate, previously described by Nazar et al which increases the adsorption efficiency [30]. However, pure phase  $Ti_4O_7$  is claimed to adsorb PS on its hydrophilic surface only through Ti-S interaction. Our measurements (Fig. 3.6c) shows that photoemission at  $\sim 163$  and 162 eV originate from S-S and Li-S bonding in LiPS and the peak at 160 eV corresponds to Ti-S bonding.

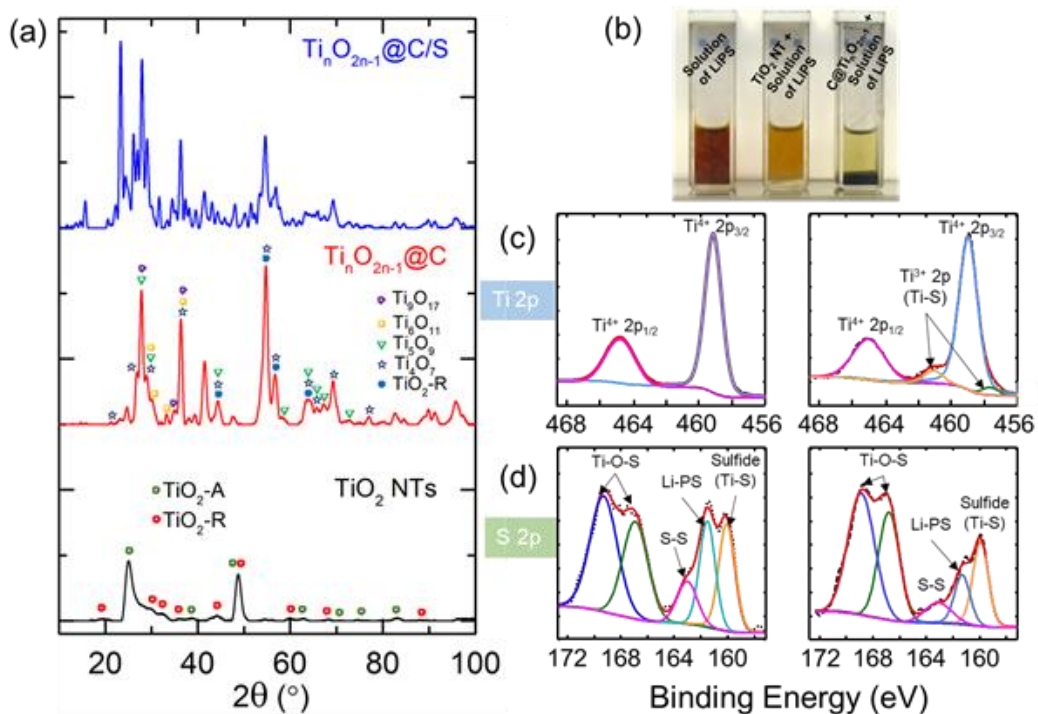


**Figure 3. 6:** (a) XRD analysis of  $Ti_nO_{2n-1}@C$  and  $Ti_nO_{2n-1}@C/S$  composite (b) Experimental illustration of LiPS adsorption onto Magnéli phases  $Ti_nO_{2n-1}$  NPs loaded in a carbon matrix, in solution (c) XPS Ti 2p core-level photoemission spectra of  $TiO_2$  NT,

Ti<sub>n</sub>O<sub>2n-1</sub>@C/S and (d) S 2p core-level photoemission from charged and discharged Ti<sub>n</sub>O<sub>2n-1</sub>@C/S cathodes.

Corresponding peaks derived from the Ti-S bond in the Ti 2p and S 2p spectrum after discharge demonstrated the ability of Ti to bond LiPS. We also examined the cathode by XPS after discharging and charging. As the ratio of relative peak intensities of polysulfides (S-S and Li-S) to Ti-O-S decreases in the charged cathode (Fig. 3.6c) compared to the discharged one, we deduce that low order polysulfides are oxidized during the charging process [188]. The Ti-S XPS spectra show that the photoemission intensity associated with strong polysulfide adsorption after charging (i.e. after a complete charge following 300 cycles) is reduced but still present. This suggests that sulfur species maintain interaction with several Magnéli phases of Ti<sub>2</sub>O<sub>2n-1</sub> that co-exist within the cathode in NP form for at least 300 cycles.

Post operation analysis of a cycled sample was performed in order to further probe the robustness of the sulfur-infused Ti<sub>n</sub>O<sub>2n-1</sub>@C/S cathode. The morphology of fully charged cathode after 300 cycles at 0.2C was investigated by FESEM and EDX analysis and confirms a pristine, intact microstructure and porosity of the original composite (Fig. 3.9), which reflects the ability of our cathode samples to mitigate any large morphological changes. Elemental mapping of the cycled cathode is quite similar to the elemental distribution shown for the as-prepared sulfur-infused Ti<sub>n</sub>O<sub>2n-1</sub>@C/S composite. There is an additional signal from fluorine comes from LiTFSI once SEI layer formation over the cathode is complete. There is sulfur distributed all over the surface, even at regions where the Ti signal is quite intense, conclusively showing a stable material system where sulfur interaction with conductive Magnéli phase Ti<sub>2</sub>O<sub>2n-1</sub> occurs.

### 3.1.3 Electrochemical Testing

To test the electrochemical performance of sulfur-infused Ti<sub>n</sub>O<sub>2n-1</sub>@C/S composite, CR2032-type coin cells were assembled. The as-prepared composite was cast on Al foil by mixing with PVDF and CSW carbon in a ratio of 8:1:1 with sulfur loading of 2-2.3 mg cm<sup>-2</sup>. The electrolyte to sulfur (E/S) ratio was kept 5-6 μL mg<sup>-1</sup>. Figure 3.7 shows the stable galvanostatic charging and discharging behavior of the cathodes at a specific current of 334 mA g<sup>-1</sup>, 836 mA g<sup>-1</sup>, and 1672 mA g<sup>-1</sup> (0.2C, 0.5C, and 1C, respectively) for 100 cycles. The initial discharge capacities of 1138 mA h g<sup>-1</sup>, 1100 mA h g<sup>-1</sup>, 956 mA h g<sup>-1</sup>, 801 mA h g<sup>-1</sup> and 700 mA h g<sup>-1</sup> were reached at specific currents 0.05C, 0.1C, 0.2C, 0.5C and 1C respectively. All discharge voltage profiles show two characteristic discharge plateau. The first, at 2.3 V, is linked to the reduction of sulfur to long chain LiPS, and the second at 2.1 V corresponds to the reduction into short-chain LiPS. Figure 3.7c demonstrates the rate capability of the composite cathode at various specific currents. Compared to sulfur-in-carbon electrodes, and the state of the art in conductive oxide host cathodes, we find a high initial capacity with excellent rate-dependent response and retention. Even at 1C, following consecutive 10-cycle tests, the cell retains a

capacity  $\sim 650 \text{ mAh g}^{-1}$  and retains the capacity at each rate, while completely recovering full capacity after switching back to the initial current rate.

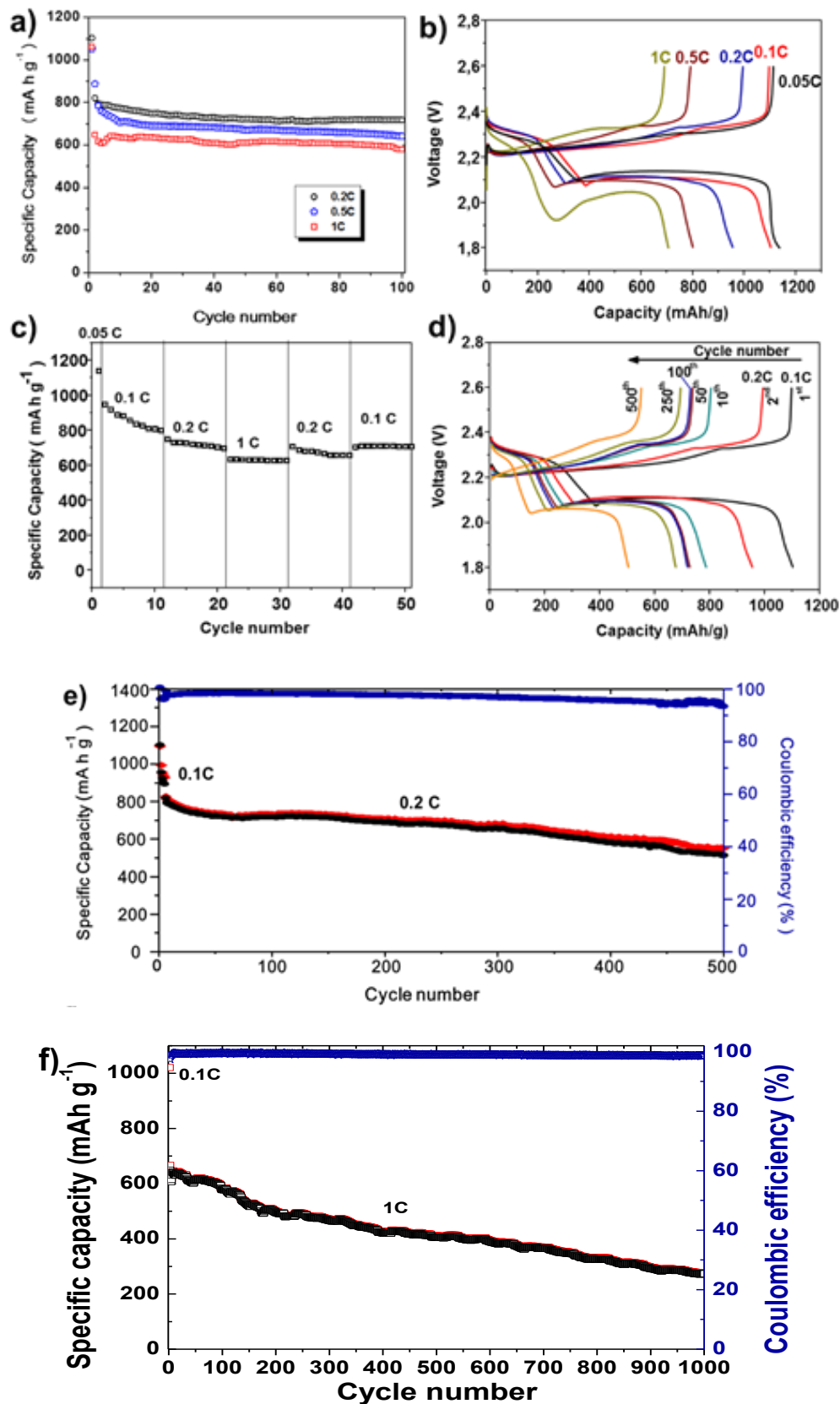


**Figure 3. 7:** (a) Cycling performance of  $\text{Ti}_n\text{O}_{2n-1}@C/S$  NP composite Li-S cathode electrodes at C-rates from 0.2C to 1C. (b) Corresponding discharge-charge profiles for each

C-rate test. (c) Rate response of the  $\text{Ti}_n\text{O}_{2n-1}@C/S$  NP composite at 0.1C, 0.2, and 1C. (d) Corresponding discharge-charge profiles at 0.2 C up to 500 cycles. (e) 500 cycle performance and Coulombic efficiency and (f) Long term cycling behavior at a high C-rate of 1C for 1000 cycles.

This indicates the robustness and efficiency of this cathode material even with an order of magnitude higher sulfur loading and low E/S ratio in comparison to previous oxide-based cathodes for Li-S batteries. We noted a small polarization effect at higher rates that is also suggestive of encapsulation of Magnéli phase  $\text{Ti}_n\text{O}_{2n-1}$  NPs by conductive carbon and structural porosity for quick access of electrolyte. Taking the advantages of higher electronic conductivity of Magnéli phase titania and carbon, and that of nanostructured oxide nanoparticles, the sulfur-infused  $\text{Ti}_n\text{O}_{2n-1}@C/S$  composite showed an initial specific capacity of 1050 mAh  $\text{g}^{-1}$  at 0.2 C with capacity retention of 65% over 500 cycles (Figure 3.7d, e). The long cycle performance of the cathode material was also evaluated at the higher rate of 1C for 1000 cycles as shown in Fig. 6f. At 1C, cathode material exhibited an initial capacity of 700 mAh  $\text{g}^{-1}$  with less than 0.06% capacity loss per cycle for 1000 cycles with Coulombic efficiency close to 99%. Thus, the cathode synthesis strategy is very efficient in suppressing LiPS dissolution and shuttling by trapping LiPS both physically and chemically and is capable of long cycle life stable operation with high capacity, and excellent response to faster rates.

The cathodes were also cycled voltammetrically (in the three-electrode configuration using Li<sup>+</sup>/Li as a reference electrode, Figure 3.8) at a voltage scan rate of 0.01  $\text{mV s}^{-1}$  between 1.5 and 3.0 V to examine the redox characteristics of the cycling process and material electrochemistry. Two distinctive and characteristic cathodic peaks can be observed at 2.35 V and 2.15 V while during oxidation a single large anodic peak appears at 2.45 V. The narrow linewidth of the current (reaction rate) peaks and their consistency confirm good electrical contact and insignificant overcharging behavior. Impedance spectroscopic data in Fig. S3 of the as-assembled cell at open circuit potential, and after five cycles of charging and discharging, also corroborate the CV and overall cell testing findings.

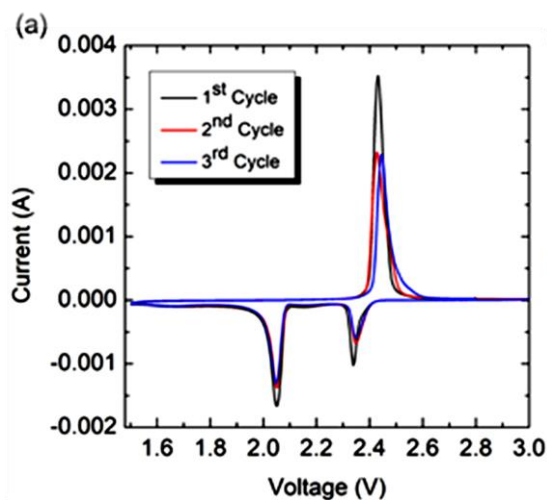


**Figure 3. 8:** (a) First 3 cycles by the CV of Sulfur infused  $\text{Ti}_n\text{O}_{2n-1}$  NP@C/S matrix cathode.

Solid-state  $Li^+$  ion diffusion is also enhanced on cycling due increase in active sites for interfacial electrochemical reaction. This determines the uniform distribution of sulfur, which is further confirmed by EDX mapping of exhausted electrodes, and faster  $Li^+$  ion transport into the electrode due to the stable SEI as pointed out in XPS analysis.

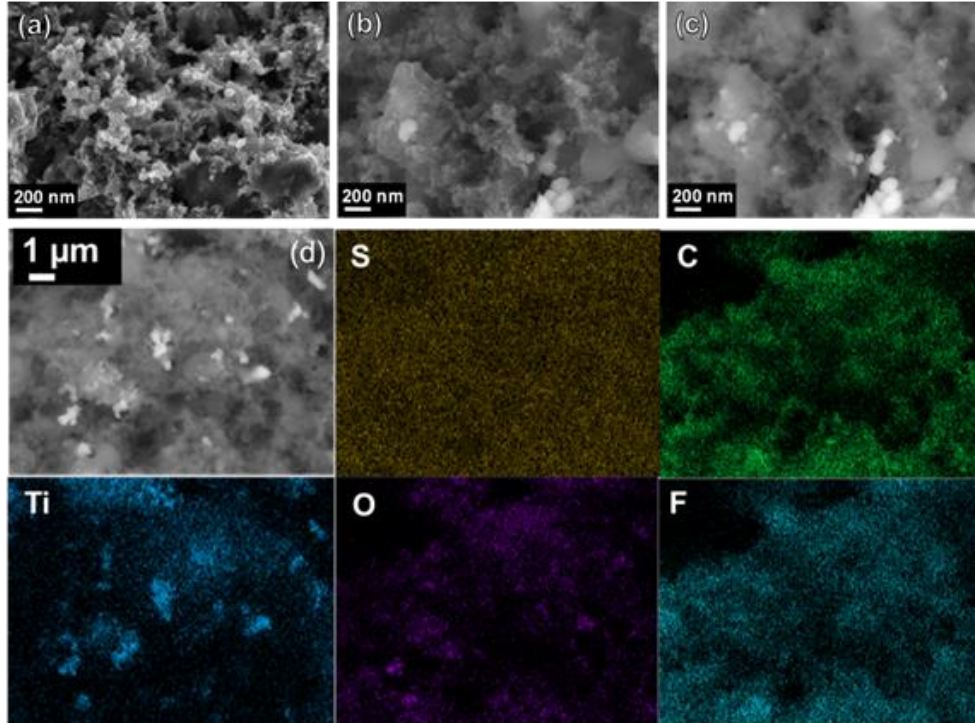


**Figure 3. 9:** (a-c) FESEM investigation of the surface of Sulfur infused  $Ti_nO_{2n-1}$  NP@C/S cathode after 300 cycles. (d) EDX maps of the exhausted cycled  $Ti_nO_{2n-1}$  NP@C/S cathode material confirming a similar elemental distribution compared to pristine as-synthesized material prior to galvanostatic cycling.

## 3.2 Electrochemically $MnO_x$ deposited carbon fiber (CF) substrates as freestanding sulfur cathodes

Various approaches have been proposed to realize stable sulfur cathodes. However, low sulfur loading in all those cases made them impractical for the industry. Here, we came up with a novel idea to produce high sulfur loading freestanding cathodes that can be easily integrated into present technology practiced by industry. In the present approach, various  $MnO_x$  deposited carbon structures will be investigated to achieve sulfur loading around  $5 \text{ mg cm}^{-2}$  with good electrochemical performance. This will not only allow to get rid of inactive mass arising from the Al current collector but also reduce the preparation steps.

### 3.2.1 Development of $MnO_x$ deposited CF freestanding sulfur cathode

Electrochemical depositions of  $MnO_2$  is widely employed on various substrates to realize pseudocapacitive behavior in supercapacitors [189, 190]. It is also a well-

known fact that annealing of electrodeposited manganese hydroxide films at different temperature and environment results in manganese oxide films with various oxidation states [191, 192]. This perspective has been exploited to realize freestanding sulfur cathodes using  $\text{MnO}_x$  deposited carbon structures. This also provides an opportunity to reach the right oxidation state of Mn in the form of oxide to efficiently trap LiPS to realize long life Li/S batteries.

### Production of CF cloth and electrochemical deposition of $\text{MnO}_x$

Two different assemblies of carbon materials have been selected to construct freestanding sulfur cathodes. Cellulose carbon cloth (CCC) was produced by carbonization of cotton fabric. For the purpose, cotton cloth was rinsed with acetone to remove residual fats and wax. Then cotton cloth was carbonized at 1000 °C for 1 h with a heating rate 5 °C  $\text{min}^{-1}$ . Electrochemical deposition of  $\text{MnO}_x$  was carried out through anodic chronopotentiometry. The deposition bath was comprised of 0.1 M  $\text{Mn}(\text{CH}_3\text{COO})_2$  and 0.1 M  $\text{Na}_2\text{SO}_4$ . The deposition was performed at a current density of 0.05  $\text{mA cm}^{-2}$ .

Commercial carbon fiber paper (known as a gas diffusion layer, GDL) was also used as a carbon substrate to prepare high sulfur loaded freestanding sulfur cathodes. Electrochemical deposition of  $\text{MnO}_x$  was carried out through anodic chronopotentiometry (figure 3.10). The deposition bath consisted of 0.1 M  $\text{Mn}(\text{CH}_3\text{COO})_2$  and 0.1 M  $\text{Na}_2\text{SO}_4$  solutions. The deposition was performed at a current density of 0.03  $\text{mA cm}^{-2}$ .

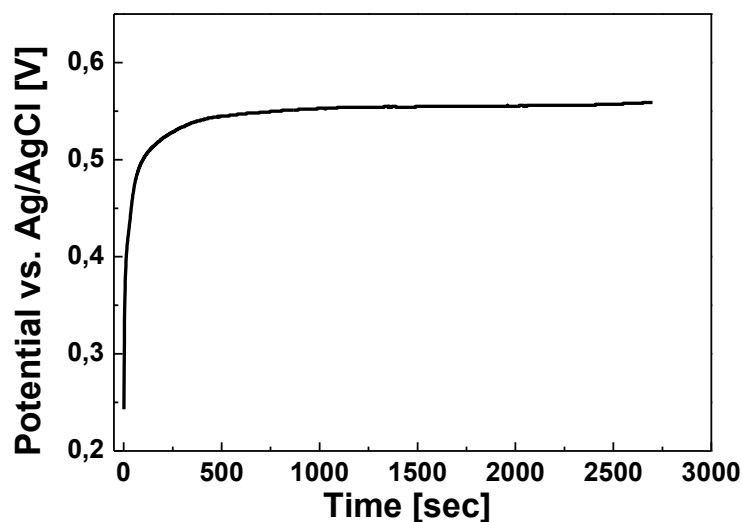


**Figure 3. 10:** Typical Voltage-time profile for electrochemical deposition of  $\text{MnOOH}$  through anodic chronopotentiometry

Activated carbon nanofibers (CNF-Act) sheets were produced by electrospinning, followed by  $\text{CO}_2$  thermal activation and carbonization. Electrospinning baths were prepared by dispersing 10% by weight polyacrylonitrile (PAN) (MW 150000, Sigma Aldrich) in dimethylformamide (DMF). The electrospinning was performed on a high voltage (29.9 kV) three syringes electrospinning setup (MECC Co. LTD., model NF-103) at flow rate 2-3  $\text{ml h}^{-1}$  with a needle to collector distance of 17 cm

and collector cylinder rotating at speed of 300 rpm. The relative humidity was maintained at 65% with a temperature around 25 °C. Thermal annealing of as-spun mats was carried out in two steps; stabilization and activation/carbonization. In stabilization step, the mat was subjected to 280 °C for 5 h in air at a heating rate 1 °C min<sup>-1</sup>. Then a second heating and activation step was conducted at 950 °C with a dwelling time of 1 h and a heating rate of 5 °C min<sup>-1</sup> under CO<sub>2</sub> flux. Electrochemical deposition of MnO<sub>x</sub> was carried out through anodic chronopotentiometry. The deposition bath was comprised of 0.1 M Mn(CH<sub>3</sub>COO)<sub>2</sub> and 0.1 M Na<sub>2</sub>SO<sub>4</sub>. The deposition was performed at a current density of 0.03 mA cm<sup>-2</sup>. To realize different oxidation states of Mn, the as-deposited were subjected to 100 °C, 300 °C, 400 °C and 450 °C under air and 400 °C under argon.

### Construction of freestanding high loading sulfur cathodes and cells

For the preparation of freestanding carbon structures sulfur cathodes, 15 mm diameter discs were punched out of deposited carbon substrates. Then sulfur was dissolved in CS<sub>2</sub>, and then the obtained solution was added dropwise on punched cathodes to reach required loading. The impregnated sulfur cathodes were subjected to 80 °C to remove residual moisture and CS<sub>2</sub> on glass slides. It is worth noting that CCC and GDL substrates have kept intact their structural stability. But, CNF-act has gone brittle and fragile. In most of the cases, cathodes get adhered to glass surfaces and it becomes critical to remove them for further investigations. So, it is decided to drop CNF-act substrate as a possible structure for freestanding cathodes irrespective of high surface areal property. The as-prepared cathodes were assembled against lithium foil with E/S ratio around 7-8 μL/mg of S. As prepared cells were charged and discharged between 1.8 and 2.6 V at 0.05C for the 1<sup>st</sup> cycle and then onward cycling was performed at 0.2C.

#### 3.2.2 Physicochemical Characterization

FESEM of as electrochemically deposited MnO<sub>x</sub> films has revealed dendritic growth of nanoflakes like sea urchin (Figure 3.11). The films are highly porous and uniformly distributed all over the surface of CCC. This morphology not only imparts the spaces to accommodate sulfur and LiPS but also provide a very high surface area to interact with LiPS. Here, it important to mention that almost all the films showed similar morphologies but high charging effects during FESEM imaging capturing does not let all the morphologies to picture. The morphology is in accordance with our understanding of the overpotential (current density) in the course of an electrochemical deposition that strongly influences the nucleation. As per Faraday's law, the rate of electrochemical reaction at the electrode is proportional to the extent of electric charge. Hence, the deposition rates can be predicted for different current densities by following relation [189].

$$V = i_k \eta_k E / \rho$$

where  $V$  is deposition rate,  $i_k$  is current density,  $\eta_k$  is current efficiency,  $E$  is the electrochemical equivalent for Mn ( $0.29282 \text{ g (Ah)}^{-1}$ ) and  $\rho$  is the density of Mn ( $7.21 \text{ g cm}^{-3}$ ). This reveals that the deposition rate has a strong correlation with current density and current efficiency.

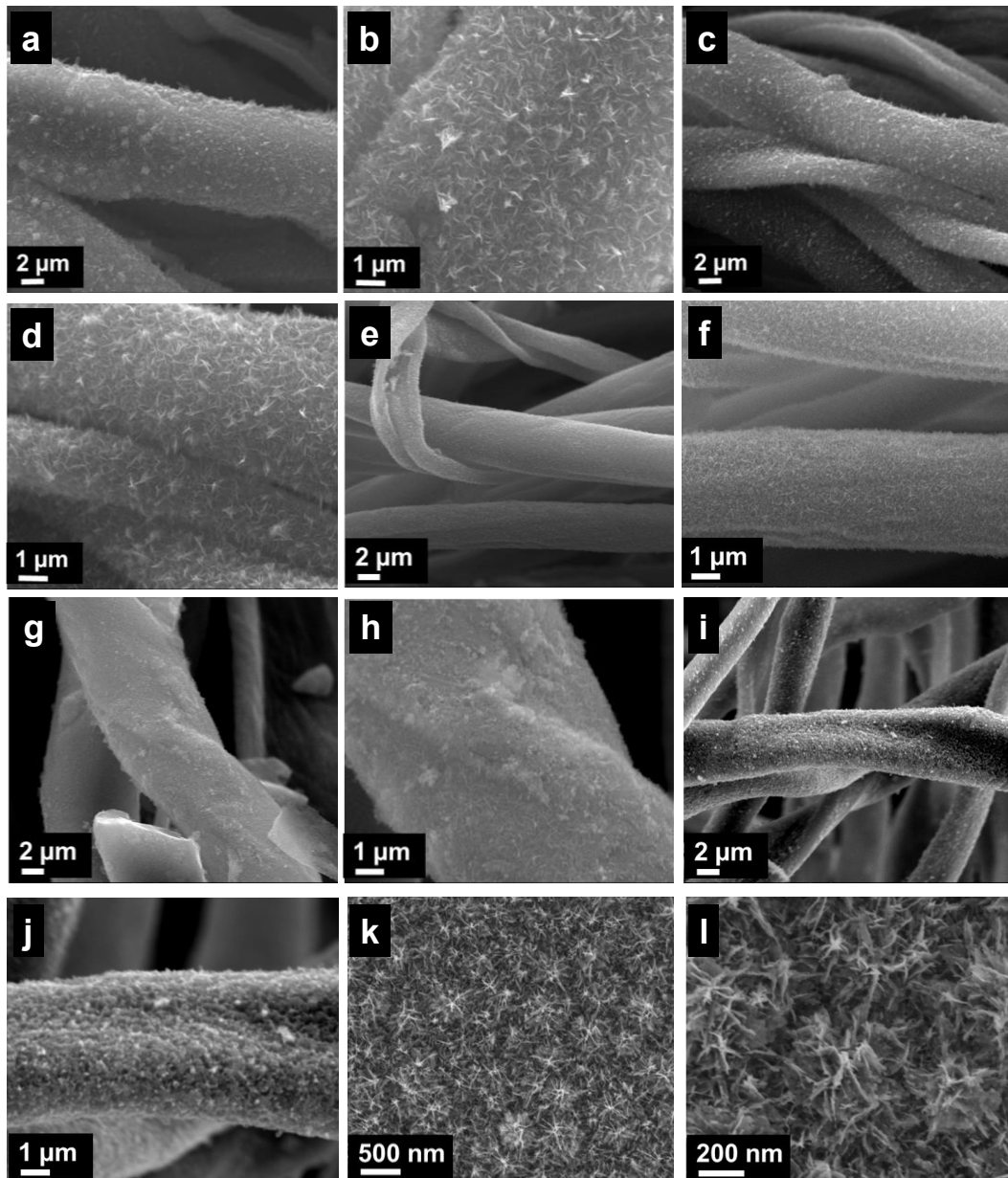


**Figure 3. 11:** SEM images of electrodeposited MnO<sub>x</sub> films on CCC treated at various temperatures and atmospheric conditions; a,b) 100 °C in air, c,d) 300 °C in air, e,f) 400 °C in air, g,h) 400 °C in argon i, j) 450 °C in air k,l) FESEM 300 °C in air

TEM analysis also revealed the similar flake morphologies in case of 100 °C air-dried sample but in other cases in which calcination was performed at high temperature (figure 3.12). The films lose their deposited morphologies during the sample preparation due to the crushing of samples to particulate the sample. However, TEM reveals the scale of morphological elements to a few nm that is indirect evidence of high surface to realize effective interaction among MnO<sub>x</sub> elements and LiPS.

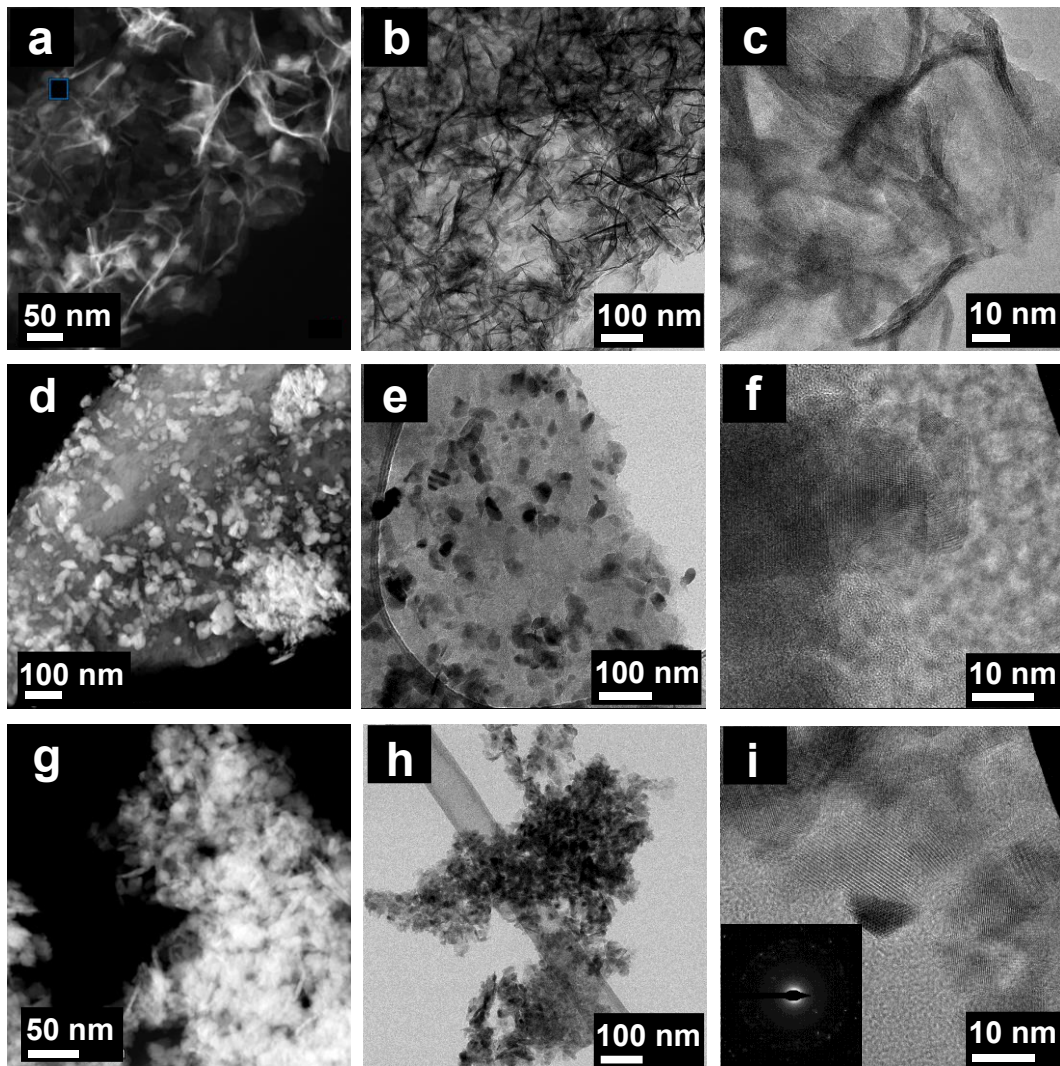


**Figure 3. 12:** HRTEM images of various deposited MnO<sub>x</sub> films; a,b,c) 100 °C air d,e,f) 400 °C air g,h,i) 400 °C argon

XRD analysis has revealed the existence of various phases of MnO<sub>x</sub> on diverse heat treatments [193, 194]. The different phases can be identified in figure 3.13 for all deposited films that are exactly in a match with XNEAS analysis. X-ray absorption near-edge structure (XANES) spectroscopy has been carried out to track the oxidation state of Mn in deposited films. Figure 3.14 shows the measured spectra for the references compounds (Mn, MnO, MnO<sub>2</sub>, Mn<sub>2</sub>O<sub>3</sub>) and samples of Mn oxides named MnO<sub>x</sub>-100C-Air, MnO<sub>x</sub>-300C-Air, MnO<sub>x</sub>-400C-Air, and MnO<sub>x</sub>-400C-Ar. All measurements were performed on X-Ray Absorption Spectrometer R-XAS from Rigaku and the obtained absorption spectra were treated by standard methods using Athena software. Valence states of Mn in the mixed-valence layer and tunnel structure manganese dioxides (MnO<sub>x</sub>), usually referred to as phyllo-manganates and tecto-manganates, can be estimated by X-ray absorption near-edge structure (XANES) spectroscopy. By the use of Mn oxide standards with known oxidation states and performing a calibration curve between the valence band and, for example, edge energy shift. In the present case, we use the method described by

Manceau et al. to estimate the valence state of four  $\text{MnO}_x$  samples (figure 3.15) [193, 195].

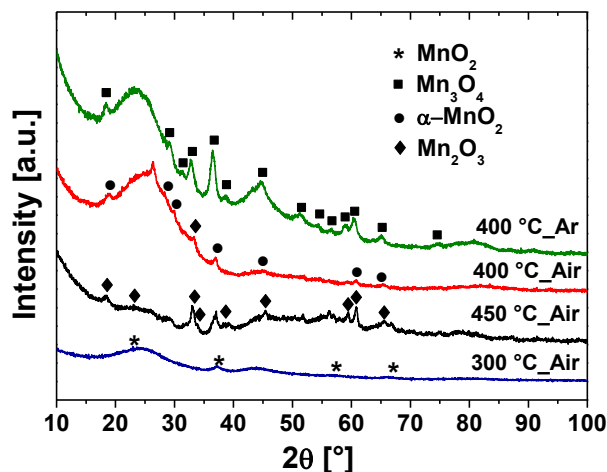


**Figure 3. 13:** XRD diffraction patterns of various as-deposited  $\text{MnO}_x$  films

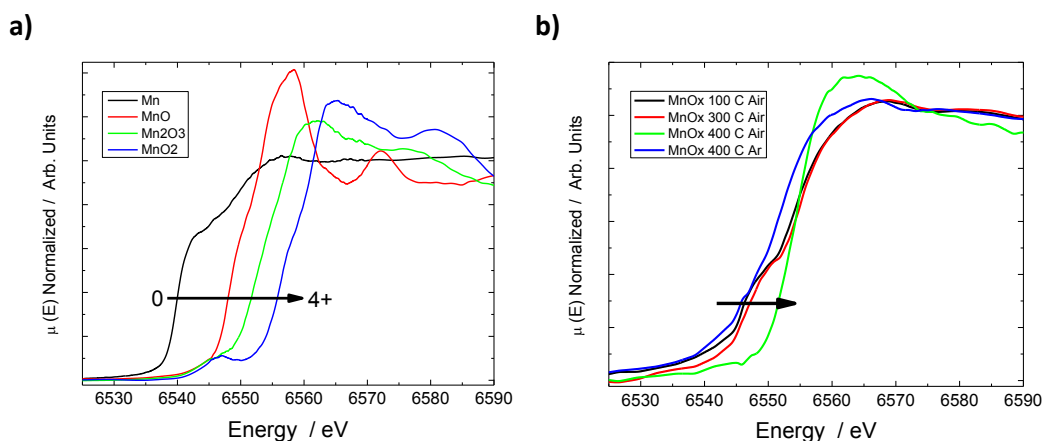


**Figure 3. 14:** a) Mn K edge XANES spectra for Mn reference compounds, energy edge position change with increasing valence value. b) Mn K edge XANES spectra for measured samples.

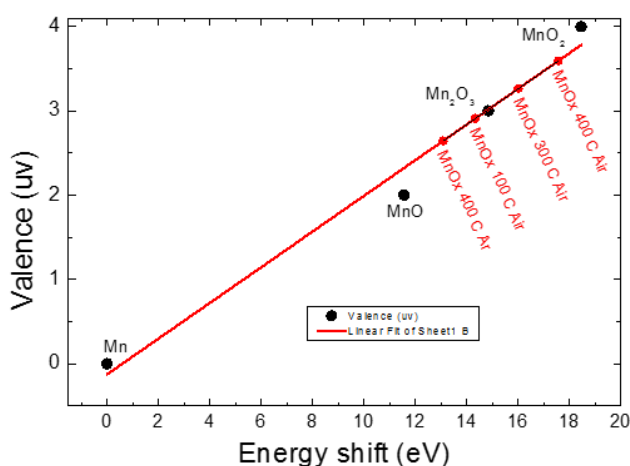


**Figure 3. 15:** The calibration curve and the obtained valence state for the four measured samples.

XPS spectra were measured using as source an Al anode (1486.61 eV), a power of 100 W and a potential difference of 10 kV. The C1s signal equal to 285 eV was

taken as internal calibration. The MnCO<sub>3</sub> sample had to be measured using the load compensation source (Flood Gun). The analysis was carried out using the CASA XPS software. The spectra of Mn2p (633 eV-662 eV) and O1s (538 eV -523 eV) were measured. Additionally, the Mn3s signal (94 eV-76 eV) was measured. Deconvolutions were carried out in order to identify and quantify the species. The survey spectra of the samples showed Mn, O, C as the major surface elements. Figure 3.16 shows the XPS spectra corresponding to Mn2p<sub>3/2</sub> with the deconvolutions corresponding to each species of Mn. In all cases, the binding energy values for each component are contained by the ranges reported in the literature [194, 196].

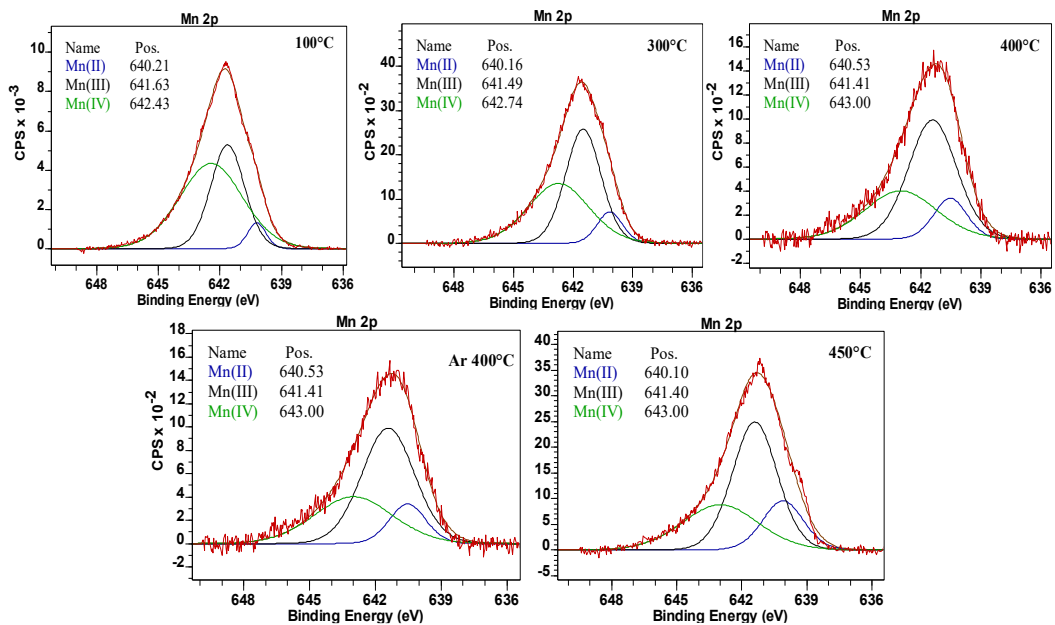


Figure 3. 16: XPS spectra Mn 2p<sub>3/2</sub> of MnO<sub>x</sub> samples.

Figure 3.17 shows the Mn 3p<sub>3/2</sub> spectra measured for the MnO<sub>x</sub> samples that received different thermal treatments in the air. In them, the width values are reported at the average height of the different components (FWHM). It is observed that as the temperature of the heat treatment increases, the widths of the peaks progressively increase [193, 194].

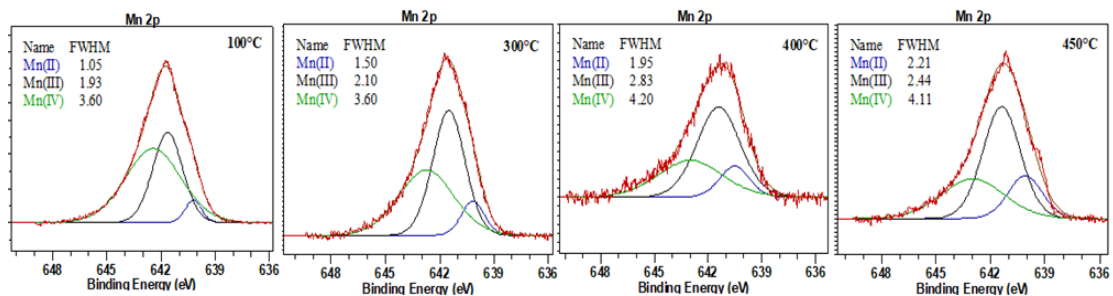


Figure 3. 17: XPS spectra Mn 2p<sub>3/2</sub> of MnO<sub>x</sub> samples that had different thermal treatments in the air.

The relative percentages of each of the Mn species present, calculated according to the relative areas of each peak, are listed in Table 3.1. Comparing the samples treated in air, it is observed that increasing the temperature of the treatment increases the % of Mn (II) (starting reagent of the synthesis process) and decreases the % of Mn (IV) present. Regarding the sample that during the heat treatment was kept under Ar atmosphere, a higher percentage of Mn (IV) is observed compared with the sample subjected to the same temperature but in the air.

**Table 3. 1:** Relative percentage of each of the Mn species present in the samples

Sample	Mn2p <sub>3/2</sub>		
	Mn(II) (%)	Mn(III) (%)	Mn(IV) (%)
100°C air	5,08	37,54	57,38
300°C air	9,38	47,77	42,85
400°C air	12,87	54,36	32,77
450°C air	17,96	51,37	30,67
400°C Ar	10,99	53,02	36,00

Additionally, the corresponding Mn3s orbital signal was studied since it is also useful to estimate the oxidation state of Mn. The separation between the peaks corresponding to internal electrons originates due to the interaction of them with unpaired electrons of the valence band.

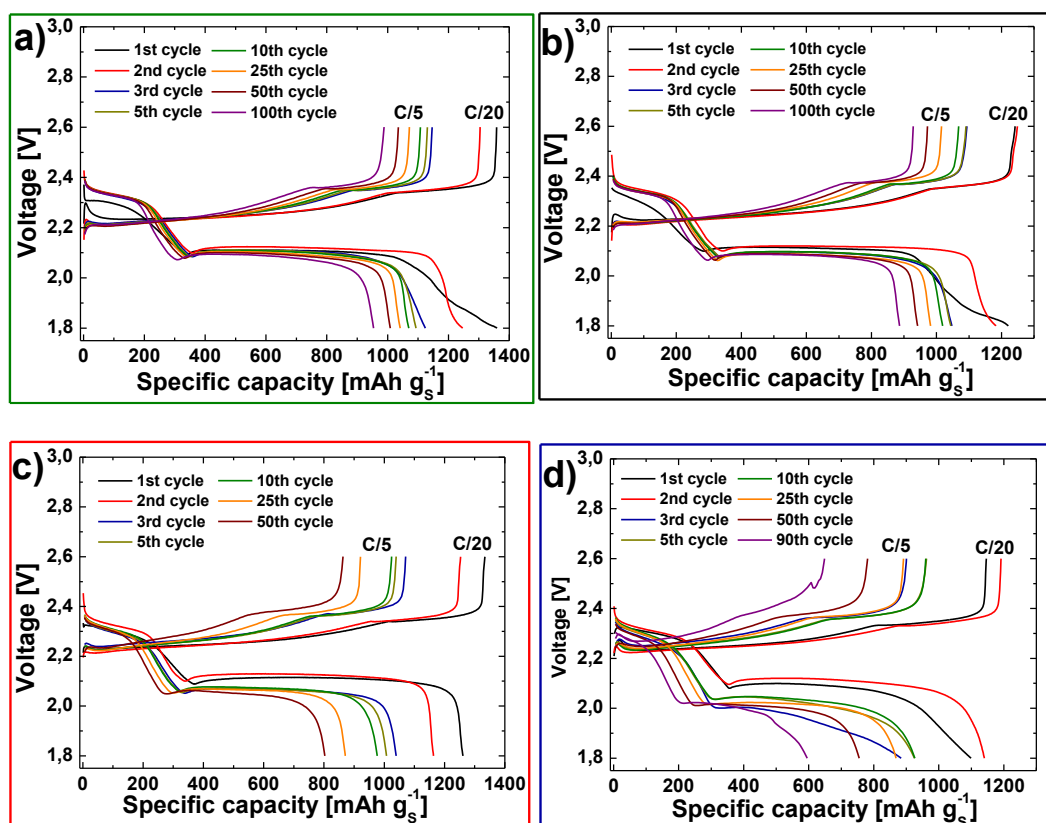
**Table 3. 2:** Results of XPS of Binding Energy and energy separations for the 3s orbital of Mn.

Sample	Mn3s			Average oxidation state*
	peak 1/eV	peak 2/eV	$\Delta E/eV$	
100°C air	89,00	83,94	5,06	3,31
300°C air	88,89	83,76	5,13	3,20
400°C air	88,75	83,23	5,52	2,81
450°C air	88,79	83,20	5,59	2,72
400°C Ar	88,89	83,42	5,47	2,67
MnO <sub>2</sub> (control)	89,30	84,63	4,67	4
MnCO <sub>3</sub> (control)	89,42	83,20	6,22	2

This process takes place after irradiating the sample and "plucking" electrons from it. The separation  $\Delta E$  between the peaks Mn3s will be proportional to two factors:

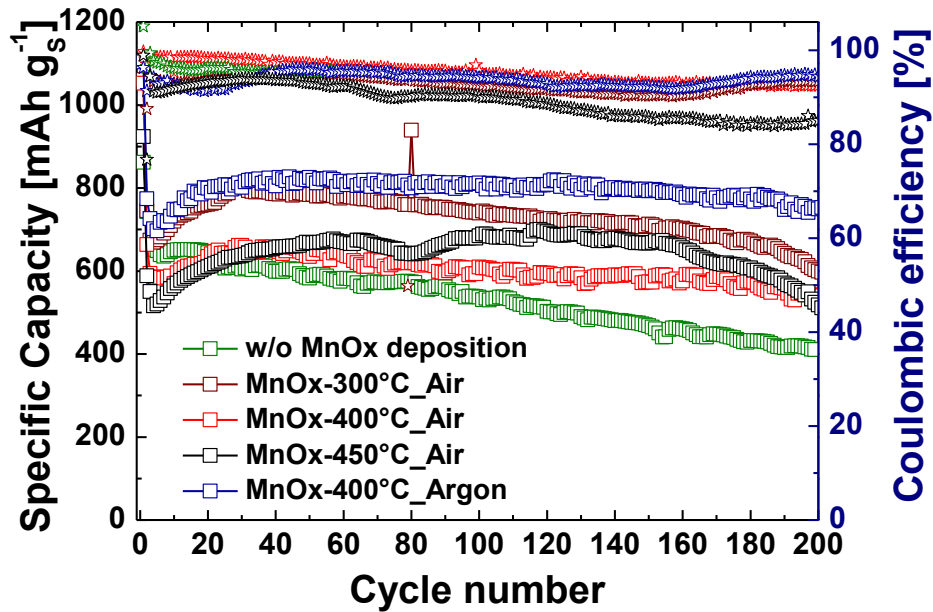


But, these cathodes showed brown film deposits that are not perfectly adhered, causing a lot of material to peel off without any harsh handling. This results in an uneven deposit on CFP, which is also evident from the fluctuating cycling behavior of cathode. While cathodes treated at 400 °C in air and argon identified as  $\alpha$ -MnO<sub>2</sub> and Mn<sub>3</sub>O<sub>4</sub> exhibited excellent cycling performances. Both cathodes showed stable cycling at such a high loading for 100 cycles around 1000 mAh g<sup>-1</sup> for MnO<sub>2</sub> and 1100 mAh g<sup>-1</sup> for Mn<sub>3</sub>O<sub>4</sub>. This performance also points out that the Mn<sub>3</sub>O<sub>4</sub> can interact even better with LiPS than that of MnO<sub>2</sub>. Corresponding voltage capacity profiles have been demonstrated in figure 3.19. All four cathodes exhibited typical plateaus for oxidation and reduction of sulfur. It can be observed that MnO<sub>x</sub> films obtained at 400 °C in air and argon showed minimal overpotential and stable capacity retention. MnO<sub>x</sub> calcined at 300 °C in air showed a higher overpotential and one at 250 °C in H<sub>2</sub>/Ar exhibited the highest of all. In the latter case, such a high overpotential can be due to broken or damaged film as discussed above can be seen in the case of MnO<sub>x</sub>\_250°C\_H<sub>2</sub>+Ar (Fig. 3.19d).



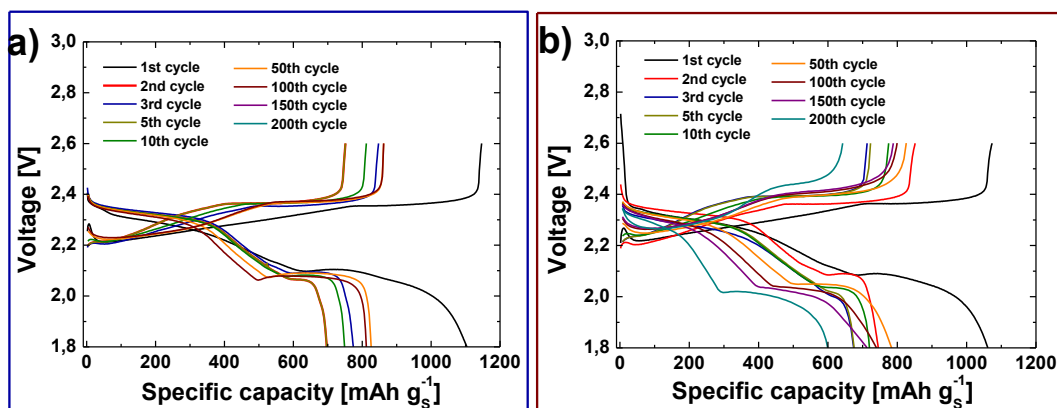
**Figure 3. 19:** Charge and discharge profiles of various synthesized freestanding MnO<sub>x</sub> deposited carbon fiber paper as a sulfur cathode a) MnO<sub>x</sub>\_400°C\_Ar b) MnO<sub>x</sub>\_400°C\_Air c) MnO<sub>x</sub>\_300°C\_Air d) MnO<sub>x</sub>\_250°C\_H<sub>2</sub>+Ar

MnO<sub>x</sub> on CCC sulfur cathode exhibited much better performance than that of MnO<sub>x</sub> on CFP. The better performance from these electrodes could be either related to the flexibility of the carbon matrix or higher surface area and porosity.



**Figure 3. 20:** Long-term Galvanostatic charge-discharge cycling performance of freestanding MnO<sub>x</sub> deposited carbonized cellulose cloth as a sulfur cathode

Here, MnO<sub>x</sub> calcined at 400 °C in argon showed the best performance (Figure 3.20, blue curve). So, it can be inferred that Mn<sub>3</sub>O<sub>4</sub> may strongly interact with LiPS than that of other oxide forms. Initially, all cathodes exhibited lower capacity followed by an increase and stabilization. This could be related to saturating of the matrix and formation of effective SEI layer formation that causes an increase in capacity and stabilization. All other cathodes showed more or less comparable electrochemical performances with a little variation in attained specific capacities. However, the cathode without MnO<sub>x</sub> deposition showed a very lower specific capacity and rapid capacity degradation (figure 3.20, green curve). It can also be observed from figure 3.21e that overpotential is quite high, which kept on increasing with the passage of every cycle. This increase in overpotential could be due to surface deposition of Li<sub>2</sub>S that imparts resistivity on interfaces.



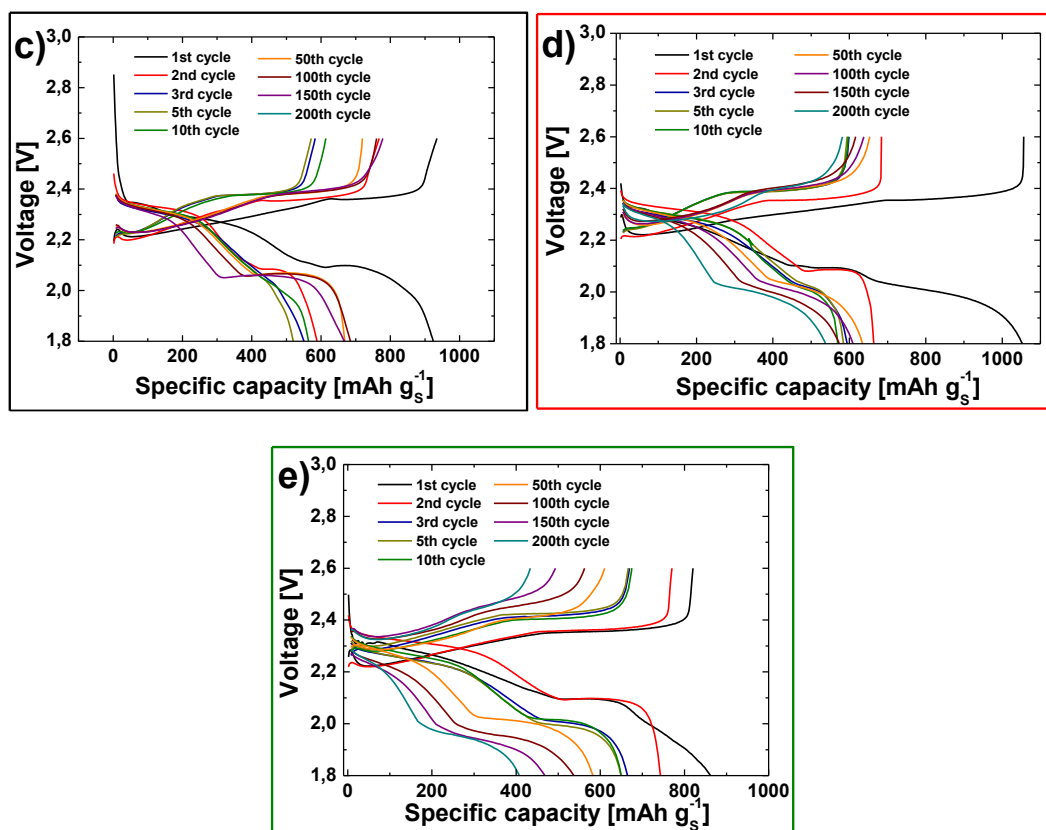


**Figure 3. 21:** Charge and discharge profiles of various synthesized freestanding  $\text{MnO}_x$  deposited carbonized cellulose cloth as a sulfur cathode a)  $\text{MnO}_x$ -400°C\_Ar b)  $\text{MnO}_x$ -300°C\_Air c)  $\text{MnO}_x$ -450°C\_Air d)  $\text{MnO}_x$ -400°C\_Air e) w/o  $\text{MnO}_x$  deposition

### 3.3 Vanadium Nitride (VN) decorated Nitrogen-doped carbon-graphene/ Sulfur Cathodes

It has already been discussed in the literature that nitrides can also be prospective candidates as inorganic moieties that can interact with LiPS to extend the cycle life of Li/S cells. But, preparation of nitrides is mostly a complex and hazardous process because of the involvement of ammonia to carry out a nitridation process. Although very few reports have shown some remarkable performances using nitrides as LiPS host, complex synthesis and special precursors make them really limited to be opted by industry [197, 198]. In this subject, a novel and hassle-free approach have been acquired to reach vanadium nitride using commercial  $\text{V}_2\text{O}_5$  powder as a precursor.

#### 3.3.1 Development of VN decorated N-doped carbon-rGO / sulfur composite cathode

In order to acquire VN decorated on carbon matrices, simultaneous in-situ ammonization and carbonization have been aimed. For this purpose, commercial  $\text{V}_2\text{O}_5$  powder has been mixed with hydrogen peroxide ( $\text{H}_2\text{O}_2$ ) solution followed by mixing of graphene oxide solution to attain a gel. The gel was dried and reduced under argon at 700 °C to achieve rGO and  $\text{VO}_x$  ( $\text{V}_2\text{O}_5$  reduced state). This mixture was blended with dicyanamide to carry out in-situ ammonization followed by

carbonization. The final mixture was subjected to 550 °C under argon to release ammonia for reaction with  $\text{VO}_x$  and  $\text{C}_3\text{N}_4$  structure. On raising the temperature to 800 °C, the carbonization was realized with a significant amount of nitrogen doping along with VN.

### **Synthesis of Vanadium Nitride (VN) decorated Nitrogen-doped carbon-graphene**

0.5 g of vanadium pentoxide ( $\text{V}_2\text{O}_5$ , Sigma Aldrich) was dispersed in 5 mL deionized water (DI, 18 M $\Omega$  at 25 °C). The mixture was added to 25 mL graphene oxide aqueous dispersion (4 mg/mL) from Graphenea to attain homogeneous mixture. 20 ml of  $\text{H}_2\text{O}_2$  solution (50 % v/v, Sigma Aldrich) was introduced in  $\text{V}_2\text{O}_5/\text{GO}$  mixture dropwise at 0 °C under vigorous stirring. The reaction was carried out for 6 h upholding the temperature around 0 °C to achieve hydrogel. This ensures the separation of  $\text{V}_2\text{O}_5$  sheets and insertion of GO sheets among them.  $\text{V}_2\text{O}_5$  on reacting with  $\text{H}_2\text{O}_2$  turns into hydrogen diperoxodioxovanadate (III)  $\text{H}_3[\text{VO}_2(\text{O}_2)_2]$ . The hydrogel was dried out at 90 °C to obtain xerogel weighing 0.68 g. The increase in weight than the sum of individual weights of precursors points to the occurrence of the reaction. As-obtained xerogel was subjected to reduction at 700 °C for 2 h under 3%  $\text{H}_2/\text{Ar}$  gas mixture with heating rate 5 °C/min. On reduction, the mixture weight was reduced to 0.467 g that corresponds to the conversion of GO to rGO and reduction of  $\text{H}_3[\text{VO}_2(\text{O}_2)_2]$  to  $\text{VO}_x$ .

5 g of dicyandiamide (Sigma Aldrich) was dissolved in 25 ml DI water under continuous stirring and heating, then 0.233 g of the as-synthesized reduced mixture was added to the solution. The dried gray colored mixture was reached by heating mixture at 90 °C. The gray mass was heated first at 550 °C at a heating rate of 2.5 °C/min for 1 h under nitrogen flux. Then, the temperature was raised to 800 °C at 1 °C/min for 2 h to get a black mass. The weight of the obtained composite was around 0.255 g. The reaction involves the in-situ ammonization and carbonization. The heating of dicyandiamide to 550 °C involves a solid condensation reaction to  $\text{C}_3\text{N}_4$  with the intermittent release of ammonia. Further, raise in temperature causes the synergetic release of nascent nitrogen species from  $\text{C}_3\text{N}_4$  and reduction of  $\text{VO}_x$  to realize VN decorated N-doped carbon composite. The as-synthesized VN/N-doped carbon composite is labeled as VNNC.

### **Construction of Vanadium Nitride (VN) decorated Nitrogen-doped carbon-graphene sulfur cathodes and cells**

Sulfur infiltrated VNNC composite was prepared in a weight ratio of 70:30. For the purpose, 140 mg of sulfur was dissolved in 1 mL of  $\text{CS}_2$ . Then, 60 mg of VNNC composite was added into the solution and was stirred to homogenize it. The mixture was dried under ambient condition and mortared to further homogenize the mixture. This mixture was transferred to heat furnace to reach melt infused composite. The mixture was heated at 155 °C for 10 h at heating rate 1 °C/min under argon flow. The final weight of sulfur-infused VNNC composite was around

180 mg and labeled as VNNC/S. The slurry was prepared by mixing, 80% VNNC/S, 10% carbon black (TIMICAL Super C65) and 10% PVDF in NMP using mixer mill (MM400, Retsch) at 20 Hz for 20 min. The sulfur loading was around  $1.2\text{--}1.5\text{ mg cm}^{-2}$ . 15 mm discs were cut out for coin cell assembling and dried at  $50\text{ }^{\circ}\text{C}$  for 4 h under vacuum. The coin cells 2032 were assembled using as-prepared cathodes versus metallic lithium anode using EH2010 (PP/PE/PP) separator with E/S ratio  $10\text{ }\mu\text{L mg}^{-1}$ . The electrolyte composition was as usual DME: DIOX (1:1, v/v) with 1 M LiTFSI and 0.25 M  $\text{LiNO}_3$ .

### 3.3.2 Physicochemical Characterization

Morphological characterization of VNNC and VNNC/S has been carried out on FESEM, JEOL-JSM-6700F. It can be observed that nitrogen-doped carbon exists in the form of aerogel with VN particles at the nano dimension dispersed across the matrix (figure 3.22). However, some lumps of VN can be observed due to aggregation. VNNC/S composite also exhibited a similar morphology with a stuffing effect that is due to the presence of sulfur melt infused into the structure of VNNC aerogel.

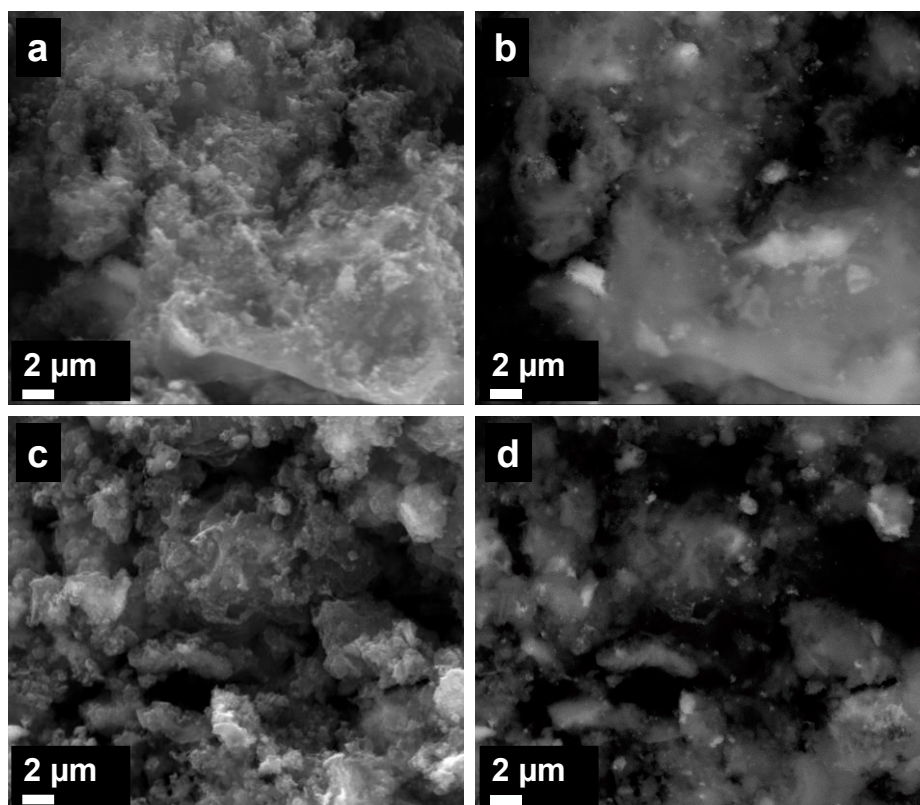


**Figure 3. 22:** a,b) SEM images of VN/N doped carbon-graphene matrix; c,d) sulfur-infused VN/N doped carbon-graphene composite.

TGA analysis of VNNC/S was performed on Mettler Toledo instrument from 0 to  $800\text{ }^{\circ}\text{C}$  in an argon atmosphere at a heating rate of  $10\text{ }^{\circ}\text{C min}^{-1}$ . VNNC/S material exhibited a mass loss around  $300\text{ }^{\circ}\text{C}$  that corresponds to evaporation of sulfur.

There is a 67% loss in mass that equals the mass of sulfur in the composite as indicated in figure 3.23a.

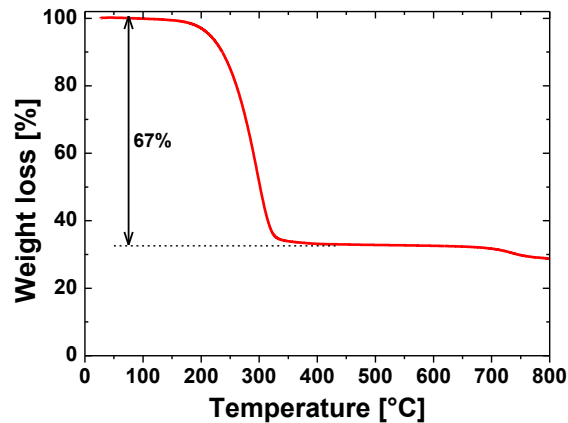


**Figure 3. 23:** a) Thermogravimetric analysis of as prepared sulfur-infused VN/N doped carbon-graphene matrix

XRD analysis of commercial  $V_2O_5$ ,  $V_xO_y/rGO$  intermediate and VNNC were performed on a Panalytical X'Pert PRO diffractometer with a PIXcel detector, using Cu  $K\alpha$  radiation, under the conditions of  $2\theta = 10-100^\circ$  and  $2\theta$  step size = 0.03. Commercial  $V_2O_5$  from Sigma Aldrich exhibited a typical pattern of crystalline  $V_2O_5$ . While intermediate  $V_xO_y/rGO$  composite showed a typical pattern of  $V_2O_3$  on rGO. The peak pattern exactly matches to JCPDS index 98-000-1870 that stands for Kareljanite ( $V_2O_3$ ). The hump around  $24^\circ$  can be clearly observed that represents rGO in the composite. The XRD pattern of VNNC showed typical 5 diffraction peaks that relate to cubic VN (1/1) on JCPDS index 98-002-2321. The XRD confirmed the presence of pure VN in composite without any residue from vanadium oxide precursor, which confirms the complete in-situ ammonization of  $VO_x$  precursor (figure 3.24).

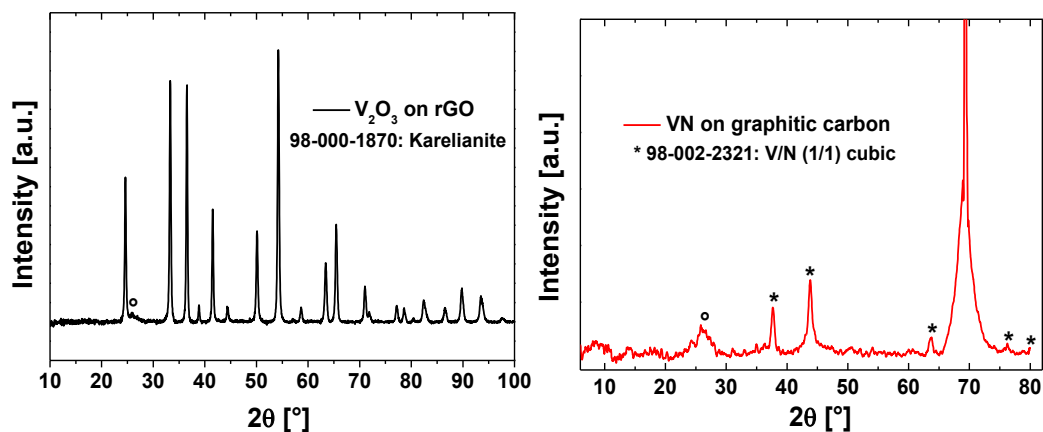


**Figure 3. 24:** a) XRD pattern of intermediate  $VO_x/rGO$  complex, VN/N doped carbon-graphene matrix, sulfur-infused VN/N doped carbon-graphene composite b) Raman spectroscopy of VN/N doped carbon-graphene matrix, sulfur-infused VN/N doped carbon-graphene composite

The visual assessment test was performed to observe the LiPS and VNNC interaction. For the purpose, 8 mg of solid  $\text{Li}_2\text{S}_6$  (prepared by mixing commercial  $\text{Li}_2\text{S}$  and  $\text{S}_8$  in THF in required molar ratio) was dissolved in 20 mL of electrolyte. Then the colored solution was split into two different bottles (Figure 3.25). One was kept for control, and in another bottle, 10 mg of VNNC was introduced. The mixture was mixed for approximately 1 h, and then it was left static for 16 h. After 16 h, the bottle with VNNC was literally faded in color to virtually transparent. Moreover, the mixture was really without any indication of LiPS after 48 h of rest. This speaks about the strong interaction of LiPS with VN. To understand better the interaction, the electronic and atomic environment has been probed through XPS. For this purpose, XPS of pristine VNNC and VNNC interacted with LiPS has been carried out on a Physical Electronics PHI5800 (USA) multi-technique ESCA system, with a monochromatic  $\text{Al K}\alpha$  X-ray radiation. For testing, the samples were placed in an ultrahigh vacuum chamber at  $2 \times 10^{-10}$  Torr. From XPS spectra of VNNC, a 2p doublet can be observed for vanadium with three distinctive peaks of  $\text{V}^{3+}$ ,  $\text{V}^{4+}$ , and  $\text{V}^{5+}$  for V-N, V-N-O, and V-O respectively. While in the case of VNNC/ $\text{Li}_2\text{S}_6$ , two additional peaks can be resolved at 515.25 eV in  $\text{V}2\text{p}^{3/2}$  band and 521.33 eV for  $\text{V}2\text{p}^{1/2}$ , those correspond to V-S binding [199-201]. Moreover, for  $\text{S}2\text{p}$  in addition to bridging and terminal sulfur peaks coming from LiPS, two other additional peaks at 168.2 eV and 159.88 eV can be observed. These two peaks correspond to the oxidized form of sulfur (polythionate) due to interaction with polysulfide [202] and V-S peak arising from LiPS direct interaction with VN.

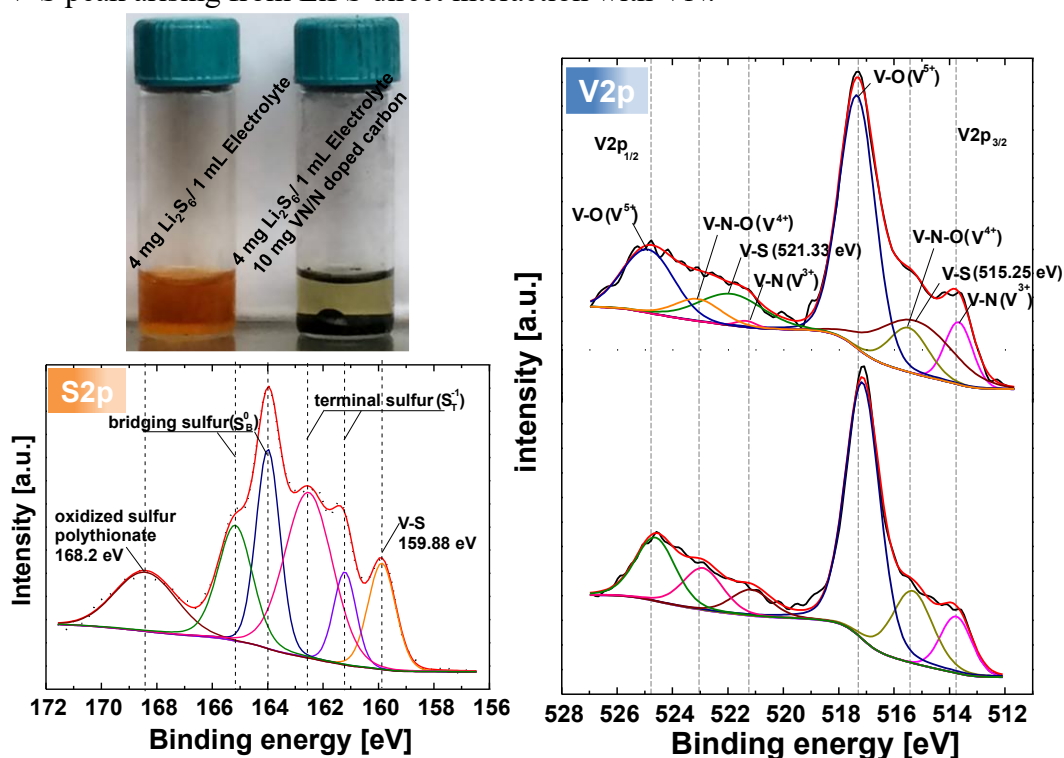


**Figure 3. 25:** a) Experimental demonstration of LiPS adsorption capability of VN-N doped carbon composite b) XPS analysis of VN/N doped carbon-graphene matrix and LiPS adsorbed VN/N doped carbon-graphene matrix.

### 3.3.3 Electrochemical Testing

As prepared VNNC/S cathodes were evaluated for their electrochemical performance vs. metallic lithium anode. The VNNC/S cells were subjected to Galvanostatic charging and discharging at various C-rates. Each cell was subjected to the first cycle between 1.8 and 2.6 V before at 0.1C and then subsequent long cycling was carried out between 1.8 and 2.6 V at various C-rates to investigate the stability of as prepared VNNC/S cathodes. It can be observed that for the first cycle at 0.1C, VNNC/S cathode has delivered the specific capacity around  $1300 \text{ mAh g}^{-1}$  in both cases as depicted in figure 3.26a. Then, one cell that has been cycled at 0.2C, showed the first cycle capacity about  $1013 \text{ mAh g}^{-1}$ . Even after 200 cycles, the capacity retention was 64 % that is  $630 \text{ mAh g}^{-1}$ . In the second case, when the cell was subjected to 0.5C C-rate, the first cycle capacity was  $814 \text{ mAh g}^{-1}$ . On further cycling, the retained capacity was  $503 \text{ mAh g}^{-1}$  after 200 cycles that is 62% of initial capacity at 0.5C. At 0.5C, the capacity retention was about 50% of initial capacity even after 500 cycles of charging and discharging with Coulombic efficiency of 98.5%.

From the voltage profile, typical behavior of sulfur cathodes can be depicted. There exist two distinct plateau at 2.3 and 2.1 V for discharging curves, while during charge the major plateau appears at 2.4 V. The existence of typical plateaus points out the conductivity and suitability of the chosen morphology or architecture. To further evaluate the rate capability performance of the VNNC/S cathode, the cells were exposed to various C-rates ranging from 0.05C to 2C. The values of specific capacity have been recorded approximately as  $1400 \text{ mAh g}^{-1}$  at 0.05C,  $1000 \text{ mAh g}^{-1}$  at 0.1C,  $800 \text{ mAh g}^{-1}$  at 0.2C,  $700 \text{ mAh g}^{-1}$  at 0.5C,  $600 \text{ mAh g}^{-1}$  at 1C and  $500 \text{ mAh g}^{-1}$  at 2C (figure 3.26d). The cell exhibited appreciable recovery when subjected back to lower C-rate after 10 cycles charging and discharging at 2C as shown in the figure 3.26c. This indicates the material responsiveness in term of its capability to function as an efficient host material for sulfur and LiPS. A little polarization can be observed as a little increase in overpotential at high C-rates (2C). This behavior is comprehensible when the insulating sulfur loading is about 70% of the matrix. However, even at 2C cathode material continued to exhibit typical plateaus, although they exist at wider voltage.

To examine VNNC/S cathodes' electrochemical behavior, cyclic voltammetry (CV) has been performed. Three CV cycles have been performed between 1.5 and 3 V at  $0.01 \text{ mV sec}^{-1}$ . During sweep from 3 to 1.5 V, two sulfur reduction peaks can be observed at 2.3 and 1.9 V. One peak at 1.9 V is a broader one with a little shoulder around 2V, but for two subsequent cycles it shifts 2 V and becomes symmetric. While during the sweep from 1.5 to 3 V, a strong oxidation peak pivot around 2.5 V with a strong shoulder peak around 2.6-2.7 V. This shoulder also narrow down for the next two cycles around 2.6 V (figure 3.27). CV of VNNC/S points out some contributions from irreversible reactions during first cycle, which

can be correlated to SEI layer formation. This exactly corresponds to first cycle Galvanostatic charging-discharging where VNNC/S cathode always exhibits a much greater capacity value than that of succeeding cycles. Consistency among the CVs of 2nd and 3rd cycles also demonstrates the stabilization of the system.

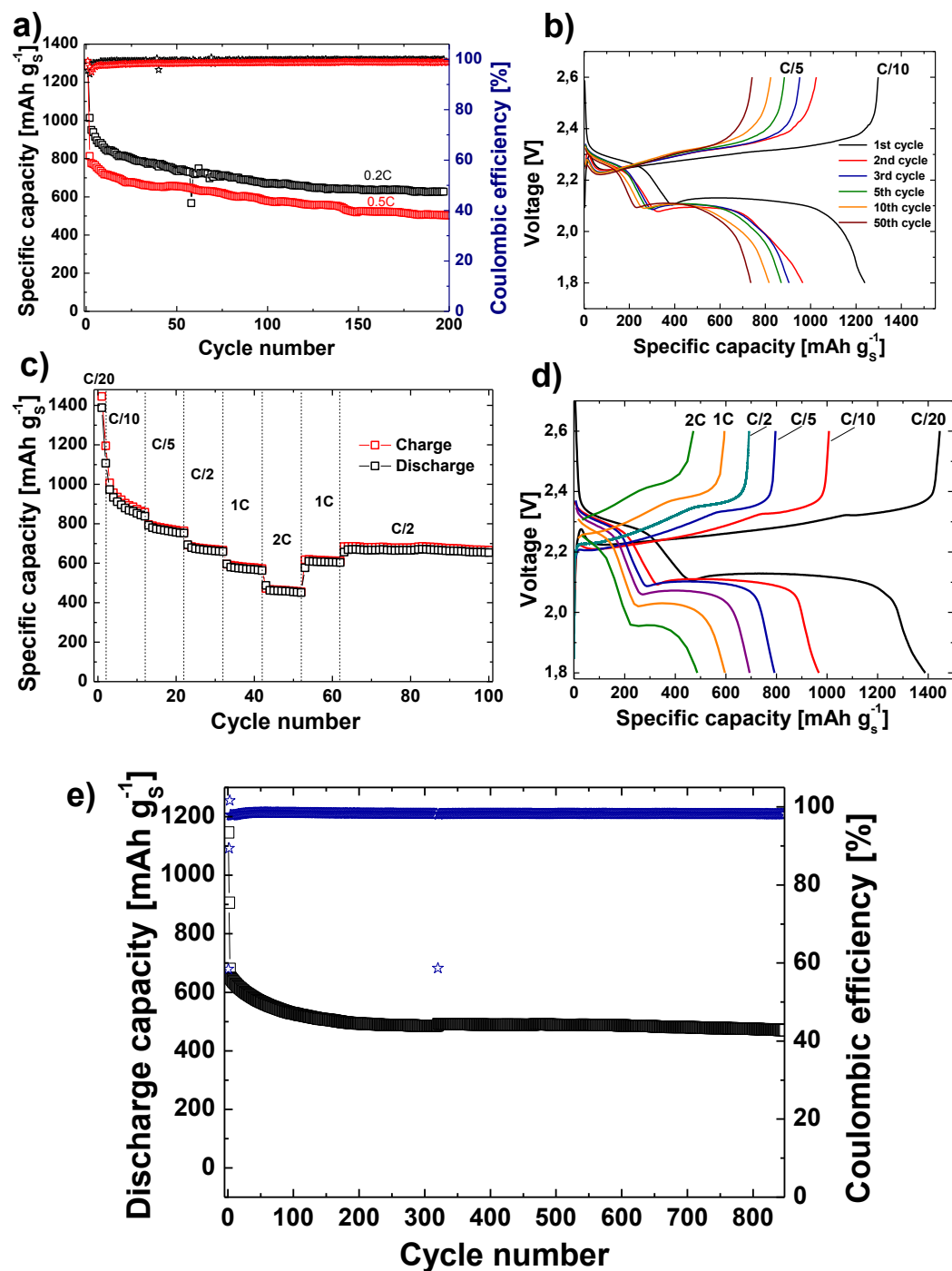


**Figure 3. 26:** (a) Cycling performance of VNNC/S composite Li-S cathode electrodes at C-rates from 0.2 C to 1 C. (b) Corresponding discharge-charge profiles at 0.2 C up to 500 cycles. (c) Rate response of the VNNC/S composite at 0.1C, 0.2, 1C and 2C. (d) Corresponding discharge-charge profiles for each C-rate test. and (e) Long term cycling behavior at a high C-rate of 1 C for 850 cycles with Coulombic efficiency.

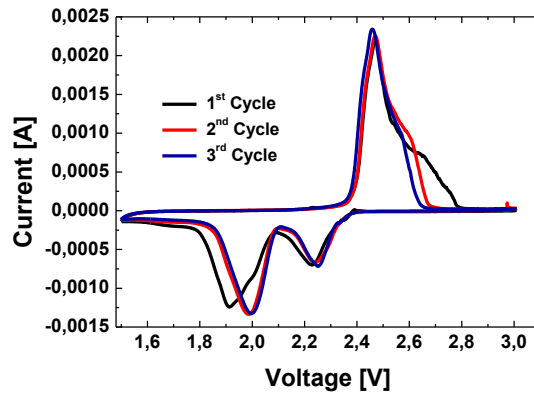


**Figure 3. 27:** First 3 cycles by the CV of VNNC/S cathode.

### 3.4 Conclusion

In summary, a facile production strategy has proposed to synthesize Magnéli Phases  $\text{TiO}_2$  nanoparticles loaded carbon matrices as an efficient sulfur host material. As synthesized host material can effectively limit the dissolution and shuttling of LiPS by synergetic entrapment of carbon matrix and  $\text{Ti}_n\text{O}_{2n-1}$  nanoparticles to achieve extended cycling life. The porous carbon matrix serves to physically entrap sulfur and LiPS, while Magnéli Phases  $\text{TiO}_2$  nanoparticles assist to chemically bind LiPS on their surface. The novel architecture of host material offers better capacity retention (i.e.) 65% and 54% at 0.2C and 1C for more than 500 and 1000 cycles respectively. Moreover, the intensive characterization of the synthesized host material and aged cathodes provides an insight that sulfur species are adsorbed by the surface of  $\text{Ti}_n\text{O}_{2n-1}$  nanoparticles along with conventional physical entrapment by carbon. The current strategy offers a facile and scalable manufacturing process to design an efficient host material for high-performance Li/S batteries.

In the second approach, various electrochemically deposited  $\text{MnO}_x$  carbon structures have been explored as high sulfur loaded freestanding cathodes. It has been successfully demonstrated that achieving the right phase of  $\text{MnO}_x$ , which can interact with LiPS. It is possible to achieve high performing stable electrochemical performance even at high loading of sulfur. The role of carbon substrate is twofold; first, it is acting as a support to carry sulfur and  $\text{MnO}_x$  deposits, secondly, it acts as a matrix that physically traps LiPS. It has been established that the  $\text{Mn}_3\text{O}_4$  phase can better interact with LiPS, thus showed higher specific capacity values and better stabilities.

In the third strategy, vanadium nitride in nitrogen-doped carbon matrix has been produced via in-situ ammonization and carbonization. VNNC showed very strong interaction with the LiPS. High rate capability is reported for sulfur cathodes assembled with this VNNC. Very stable performance has been recorded for hundreds of cycles at various C rates. Both nitrogen-doped carbon and VN has imparted conductivity and ability to interact with LiPS. Cells assembled with VNNC/S cathode has been cycled at 0.2C showed first cycle capacity about 1013

mAh g<sup>-1</sup>. Even after 200 cycles, the capacity retention was 64 % that is 630 mAh g<sup>-1</sup>. Interestingly at higher C-rates, VNNC/S cathodes exhibited even better stabilities.

## Chapter 4

# Development of functional polymers coated sulfur cathodes

In literature, different functional polymers have been addressed as either coating materials or binders to enhance the performance of sulfur cathodes [114, 117]. Functional polymers are macromolecules with unique characteristics. These distinctive characteristics mainly attributed to the presence of chemical functional groups that are different from backbone chains. Such chemical diversity imparts high reactivity and peculiar interactions. Such polymers also bear self-assembling phenomena that greatly contributes towards the supramolecular and order structures. Polymers with functional or interactive groups can greatly improve the performance of sulfur cathode as well as can contain soluble LiPS to the electrode surface. Conductive polymers – a class of functional polymers - can be either electron conducting, proton conducting or ion conducting. Conductivity to such polymeric systems has been imparted by conjugating bonds and/or ionic functional groups. As they contribute towards conductivity and can interact with LiPS, so they can be architecture to design active materials for the sulfur cathode. Conductive polymers likewise are flexible, so they can withstand with volume changes and greatly moderates the pulverization of cathode materials. As discussed previously that simple porous carbon matrices do not interact with sulfur and its species; these can be easily isolated from the conductive surface of carbon and then no more available for further reactions. On another hand, conductive polymers with a proper architecture such as core-shell or yolk-shell can ensure intimate contact. This, in turn, increases the sulfur utilization and promise much better life cycle performances. Lastly, most of the conductive polymers bear functional groups and polar linkages that can recover the evaded LiPS back to electrodes to keep alive their contribution [51, 53, 58].

## 4.1 Formate-ion doped Polyaniline (PANi-COOH) enveloped mesoporous Carbon/Sulfur Composite

Various conductive polymers such as polyaniline, polypyrrole, polythiophene, and PEDOT:PSS have been previously reported as discussed in the review section. Interestingly, a number of research reports have indicated the use of HCl doped PANi as an active material to construct sulfur cathodes [52, 61, 203, 204]. Before conceiving the inadequacy of the said reports, it is important to address the chemistry of PANi and Al foils. PANi is a conductive polymer, typically obtained by oxidative polymerization of aniline. It can exist in three different forms, depends upon the oxidation states. Those states are leucoemeraldine (white/colorless), emeraldine (blue: undoped/ green: doped in form of salt) and pernigraniline (blue/violet), in which leucoemeraldine is fully reduced form and pernigraniline is fully oxidized form as indicated in **Figure 4.1**. Doped emeraldine form, also termed as emeraldine salt, is the most conductive form and achieved by coupling with protonated acids. HCl is the most widely employed acid to target emeraldine salt [205].

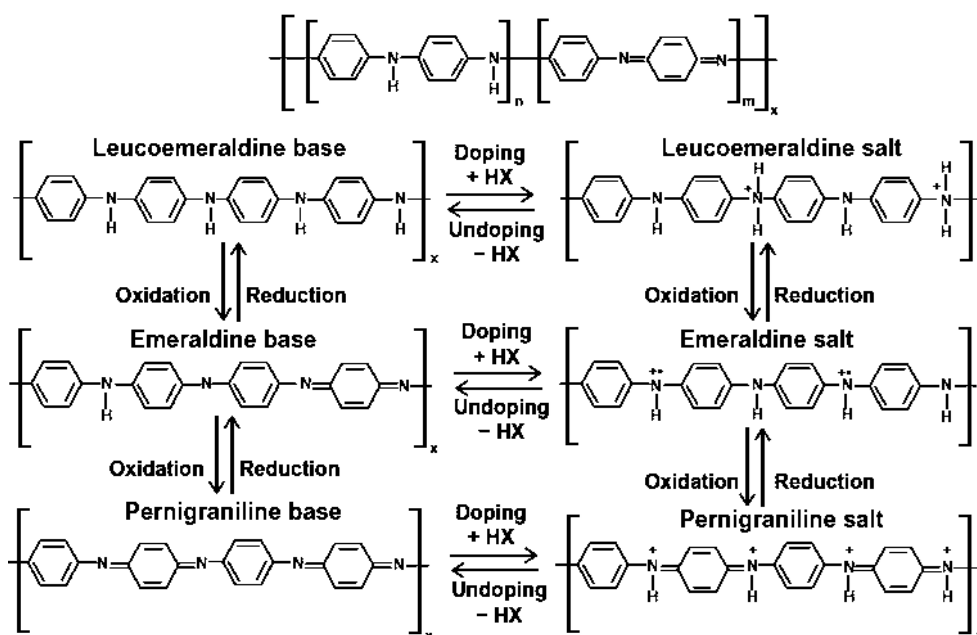


**Figure 4. 1:** Chemical structures of different redox forms of polyaniline [206]

Aluminum metal is highly reactive and prone to corrosion. But the formation of oxide layer passivates the metal for further reactions. There already exist a number of reports; those ascribe the fact that aggressive anions such as chloride ( $\text{Cl}^-$ ) ions can induce the pitting corrosion in aluminum. In the presence of  $\text{Cl}^-$ , the passive oxide film becomes unstable and disintegrates locally causing oxide film breakdown and pitting corrosion [207]. We also observed that chloride ion persists in PANi coatings obtained through HCl doping and causes the pitting corrosion of Al current collector as shown in Figure 4.2. Even on repeated washing of chloride ion doped PANi with deionized water, the pitting corrosion phenomena continues,

although there is a little degree of reduction in the level of corrosion. Very few reports smartly avoided this problem either using carbon paper as a current collector or shaping freestanding cathodes [208]. But, the use of carbon paper demands the high use of electrolyte to realize better electrochemical performances. In order to address this shortcoming of previous reports, formic acid (HCOOH) has been chosen to dope PANi instead of HCl. Formate ion doped PANi also allows the casting of composite on Al foil using conventional methods. Compared with its KJBC/S composite counterpart, the formate ion doped PANi wrapped KJBC/S composite delivered much improved cyclability owing to the presence of internal void space inside the polymer shell to accommodate the volume expansion of sulfur during lithiation.



**Figure 4. 2:** Backside of HCl doped PANi@C/S composite coated Aluminum foils a) 3 times DI water and 3 times alcohol washed b) extensively washed with the bulk of DI water

#### 4.1.1 Development of Formate-ion doped PANi enveloped C/S composite and cathodes

A cost-effective, facile and scalable approach is opted to synthesize PANi wrapped carbon-sulfur (C/S) composite. Commercial Ketjen Black Carbon (KJBC) particles are the core structure of the composite positive electrode material in which sulfur is confined by melt infusion process. Conductive polyaniline (doped PANi) was synthesized by a chemical method through in situ low-temperature oxidative polymerization of aniline on KJBC/S composite particles using formic acid as a dopant. PANi synthesized in formic acid medium demonstrated higher electrical conductivity ( $7.5 \text{ S cm}^{-1}$ ) than the polyaniline synthesized in of hydrochloric acid medium ( $0.143 \text{ S cm}^{-1}$ ) as well as greater doping degree [205].

### In-situ synthesis of PANi to wrap C/S composite by oxidative polymerization

Sulfur (Sigma Aldrich) and Ketjen black EC-300J (KJBC, AkzoNobel) were mixed in the ratio of 80:20 in CS<sub>2</sub> (Sigma Alrich) to obtain a homogenous mixture. The mixture was then heated to 155 °C at 1 °C min<sup>-1</sup> for 12 h to achieve the infusion of sulfur. For comparison, another batch of KJBC/S composite was prepared in the ratio of 70:30. The melt infused C/S composite was crushed into powder using pestle and mortar as cathode and core material for the next set of experiments.

1 g of KJBC/S (80:20) composite was poured into 12.5 ml formic acid solution (> 95%) under vigorous stirring. Then, 0.5 ml aniline (Sigma Aldrich, purity 99.5 %) was added into the mixture. After 12 h stirring, the mixture was subjected to 10 min sonication to disaggregate the composite particles. The temperature of the mixture was maintained to 2 °C using an ice bath. 1.22 g of ammonium persulfate (APS, (NH<sub>4</sub>)<sub>2</sub>SO<sub>4</sub>) was dissolved separately in 17.5 ml of formic acid solution. APS solution was added into the former mixture dropwise in 30 min. The reaction was carried out for 2 h under vigorous stirring about 2 °C. The solid mixture was separated by centrifuge. Then, washed with DI water and absolute alcohol three times each. After that mixture was dried at 50 °C to remove residual solvents. The weight of dried composite labeled as PANi@KJBC/S was around 1.3 g.

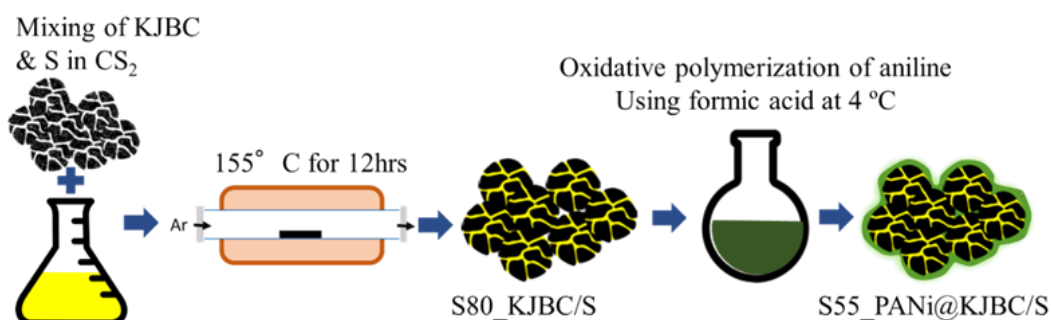


**Figure 4. 3:** Scheme for the preparation of PANi wrapped KJBC/S composite

### Construction of PANi wrapped carbon /sulfur cathodes and cells

KJBC/S and PANi@KJBC/S were prepared on bare aluminum foil. For the purpose, all composites (80%) were mixed with 10 % carbon black (TIMCAL Super C45) and 10 % PVDF in NMP. The slurry was prepared by mixing the mixture on mixer mill (MM400, Retsch) at 20 Hz for 20 min. All slurries were cast on Al foil using a doctor blade with clearance around 200 μm on automatic film applicator. The slurries were ambiently dried and 15 mm diameter cathodes were punched out. The cathodes were shifted to argon glove box after 4 h drying at 50 °C under vacuum. The sulfur loading for as-prepared series of cathodes was around 1.5 mg cm<sup>-2</sup>. The coin cells 2032 were assembled in the argon-filled glove box using EH 2010 microporous separator. The lithium foil was used as counter electrode and E/S ratio was maintained around 7 μL mg<sup>-1</sup>. The electrolyte composition was as usual DME: DIOX (1:1, v/v) with 1 M LiTFSI and 0.25 M LiNO<sub>3</sub>.

### 4.1.2 Physicochemical Characterization

As mentioned formerly, HCl doped polyaniline (PANi-HCl) theoretically is not appropriate to be used in the conventional Al foil coating process. This also has been demonstrated by coating Al foil with PANi-HCl coated KJBC/S composite. Al foil is severely corroded after the coating using normally five times washed composite with DI water and absolute alcohol; even the intensively washed PANi-HCl coated KJBC/S sample has shown the pitting corrosion of the foil under ambient conditions. To achieve PANi-HCl wrapped KJBC/S composite, in-situ oxidative polymerization of aniline has been carried out using the IUPAC recommended procedure [209]. While PANi-HCOOH wrapped KJBC/S has been achieved the above-mentioned protocol. After coating the Al foil with as prepared composite has shown no corrosion at all. So, PANi-HCOOH wrapped KJBC/S can be easily opted by industry using the established battery electrodes manufacturing processes. After in-situ oxidative polymerization of aniline around KJBC/S particles, there is approximately 30% increase in the weight of composite that can be directly linked to the weight of PANi-HCOOH. In parallel, PANi-HCCOH has also been polymerized without KJBC/S composite to estimate yield, conductivity, and other parameters.

From the morphological analysis of the KJBC/S and PANi@KJBC/S under FESEM, it can be inferred that KJBC/S is well wrapped with plastic like material. In figure 4.4a, c, particulate morphology of KJBC/S composite can be observed. While, figure 4.4b, d reflects the coating of KJBC/S aggregates with some polymeric material that is PANi-HCOOH in the present case. These aggregates arise from the wrapping of various chain length PANi macromolecules. But, in nanoscale, it can be observed that KJBC/S particles are individually covered by PANi and then aggregates to a micron in size because of chain growth.

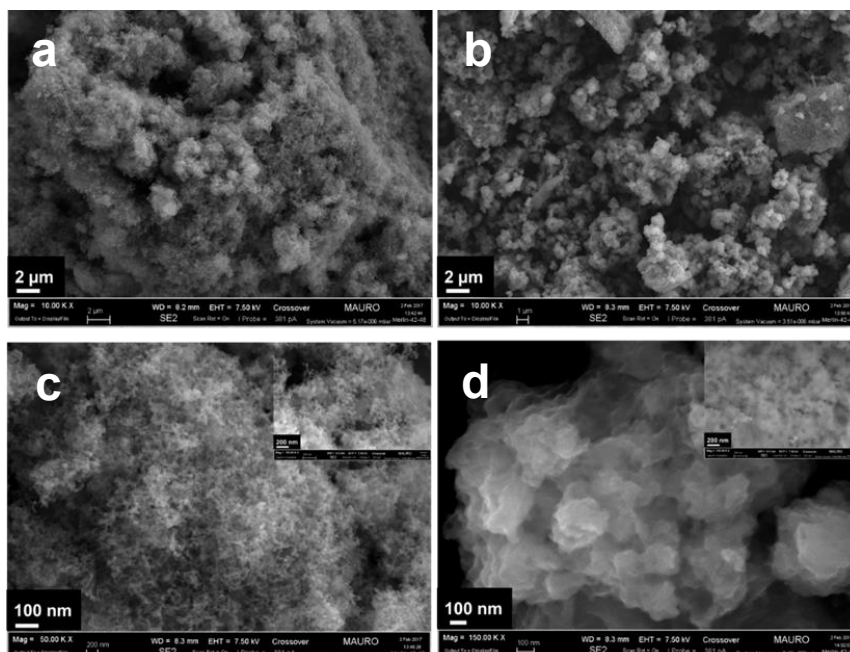


**Figure 4. 4:** FESEM micrographs of a, c) KJBC/S b, d) PANi@KJBC/S

TGA of the KJBC/S and PANi@KJBC/S has been carried out under argon flow from room temperature to 800 °C to assess the amount of sulfur (figure 4.5). After melt infusion, KJBC/S composite has shown the presence of 75% sulfur. While PANi@KJBC/S has exhibited 56% presence that also complements to the theoretical weight calculation after a 30% increase in the weight of the composite.

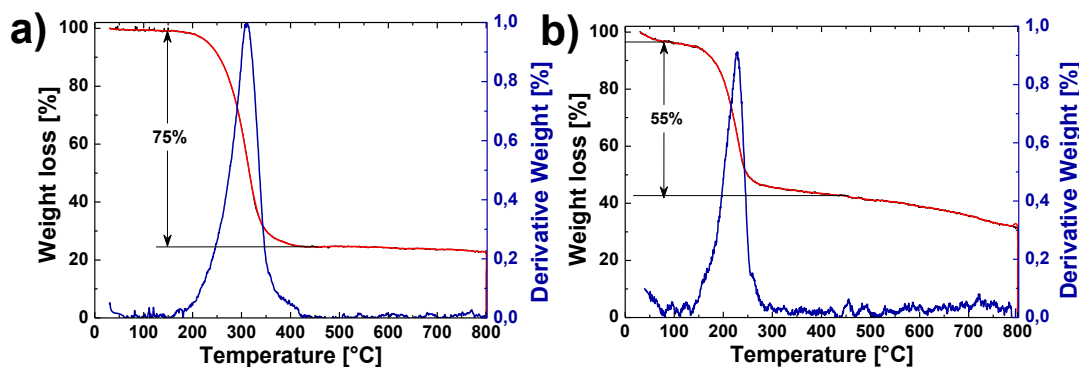


**Figure 4. 5:** TGA and DTG of a) KJBC/S composite, b) PANi@KJBC/S composite

XRD analysis of KJBC, PANi-HCOOH, KJBC/S and PANi@KJBC/S has been carried out as shown in figure 4.6. KJBC has given usual diffraction halo around 24° and 44° (2 $\theta$ ). PANi-HCOOH exhibited the presence of crystalline phase with three peaks at 15, 20, 25° that revealing of ordered structures. While KJBC/S and PANi@KJBC/S composites exhibited the peaks arising from crystalline sulfur (S<sub>8</sub>).

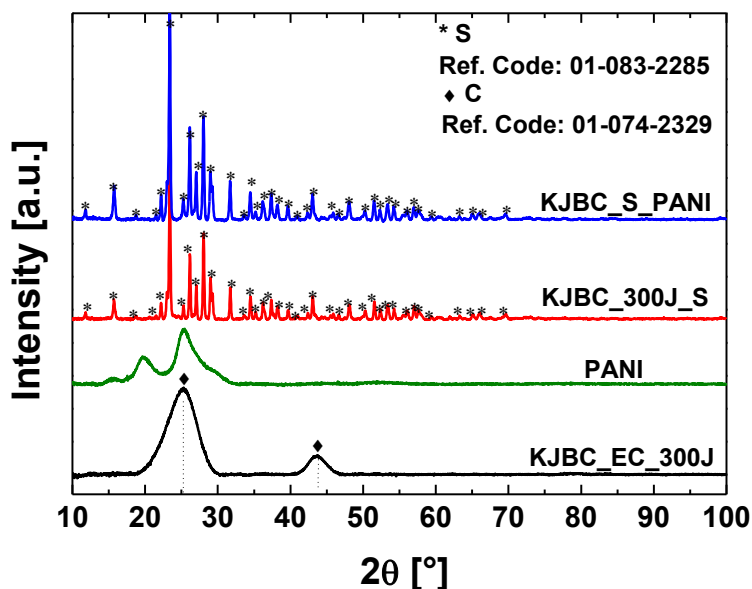


**Figure 4. 6:** X-ray diffraction patterns of Ketjen Black Carbon (KJBC), Formate-ion doped PANi, KJBC/S composite, and PANi@KJBC/S composite

XPS analysis has been carried out for corroded Al coated with PANi-Cl composite, PANi-HCOOH composite, and of PANi-HCOOH KJBC/S electrode both in charged and discharged states (figure 4.7). For XPS survey of corroded Al a significant amount of residual atomic chlorine in the form of chloride ion can be

observed. The level of pit corrosion is so aggressive that the signal went across the Al foil provided us with carbon, sulfur and nitrogen signals from the composite. Oxygen signals are too high that 48% of oxygen has been observed for Al foil. From XPS survey spectra of PANi-HCOOH@KJBC/S composite, as expected nitrogen, carbon, oxygen and sulfur signals can be observed. Sulfur just is giving 4.1% based on atomic wt%, which indicates that sulfur is either existing inside carbon pores or protected underneath polyaniline.

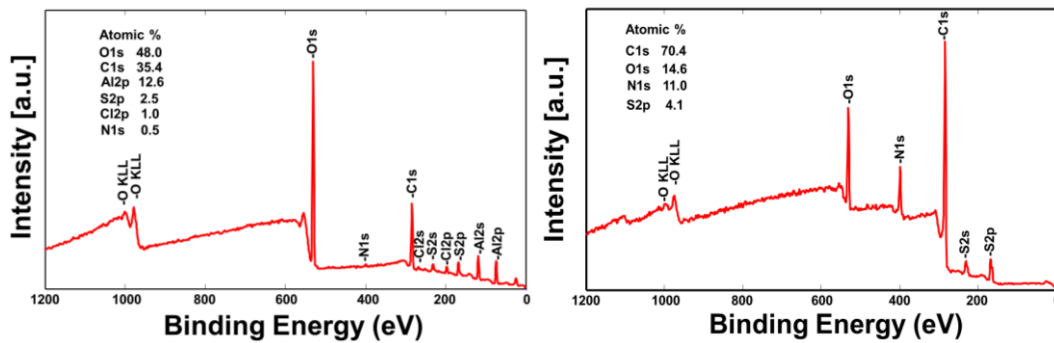


**Figure 4. 7:** XPS spectra of corroded Al coated with PANi-Cl composite and PANi-HCOOH composite

### 4.1.3 Electrochemical Testing

To test the as-prepared cathodes, they were subjected to Galvanostatic charging and discharging between 1.8 and 2.6 V. First cycle was performed at either 0.05C or 0.01C and onward cycling was performed at 0.2C. PANi@KJBC/S cathodes showed initial discharge capacity about 1400 mAhg<sup>-1</sup> at 0.05C for the first cycle. At 0.2C, it showed the specific capacity of 810 mAhg<sup>-1</sup> that depreciates to 750 mAh g<sup>-1</sup> after 300 cycles and 705 mAh g<sup>-1</sup> after 500 cycles (Figure 4.8). While S80/KJBC composite showed an initial discharge capacity of 778 mAh g<sup>-1</sup> that degrades to 570 mAh g<sup>-1</sup> after 300 cycles of charge and discharge at C/5. S70/KJBC composite cathode exhibited high initial discharge capacity of 896 mAh g<sup>-1</sup> that downgrades to 655 mAh g<sup>-1</sup> after 300 cycles. The capacity degradation per cycle for PANi@KJBC/S, S80/KJBC and S70/KJBC can be calculated as 0.024%, 0.09% and 0.09% at 0.2C respectively. It can be deduced that KJBC/S composites exhibit relatively lower specific capacities and higher degradation rates owing to escape of LiPS into the electrolyte. Higher the sulfur loading, lower the specific capacities were observed. But, in the case of PANi@KJBC/S composite, the degradation rate is 4-5 times lower because of polymer shell protection that encloses the LiPS in a closed cell and limits the discharge of LiPS. The reduction of LiPS dissolution in bulk electrolyte arises from both physical barrier and chemical interactions due to the presence of a polar bond in PANi.

From the discharge profiles of all three different cathodes, two distinguishable plateaus; the small one is occurring between 2.2 to 2.3 V and the large plateau is appearing around 2 V (Figure 4.9). It can be observed from figure 4.9a that

S80/KJBC exhibited the highest level of overpotential and lowest specific capacity mainly due to the presence of a higher proportion of insulating sulfur than that of S70/KJBC composite. While PANi@KJBC/S composite showed a reduction in polarization and then stabilization. This phenomenon repeatedly reported in the literature for very few initial cycles because of incomplete wetting of electrode elements. The stabilization of the system is realized by protecting the SEI layer that is achieved in initial cycling. Polyaniline coating allows the buffering of volume changes to protect the SEI layer from disruption. This also allows these cathodes to last longer.

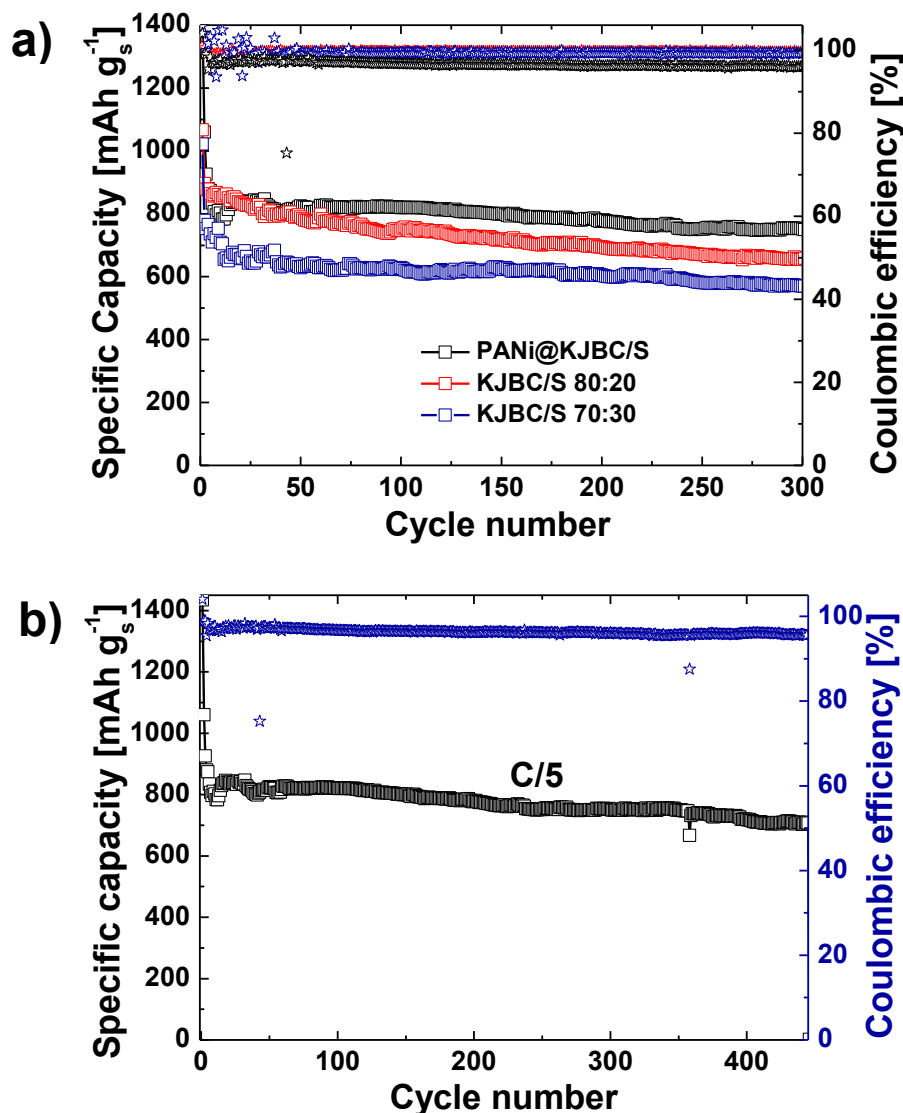


**Figure 4. 8:** Long-term Galvanostatic cycling performance (squares: specific capacity, stars: Coulombic efficiency) a) comparison of cycling performances of PANi@KJBC/S, S80/KJBC and S70/KJBC for 300 cycles, b) cycling performance of PANi@KJBC/S cathodes for 500 cycles

Rate capability tests were carried out on PANi@KJBC/S and S70/KJBC cathodes (Figure 4.10). A similar trend has been observed for low C-rate C/20, C/10, and C/5. But at higher C-rate, even at C/2, S70/KJBC cathodes have delivered the capacity value of 150  $\text{mAh g}^{-1}$ . In contrast, PANi@KJBC/S cathodes exhibited the

specific capacity of 600 mAh g<sup>-1</sup> at C/2 and 350 mAh g<sup>-1</sup> at 1C. The high C-rate capability of PANi@KJBC/S cathode could be attributed to higher conductivity of PANi that enable the lower polarization resistance and better electrochemical performance.

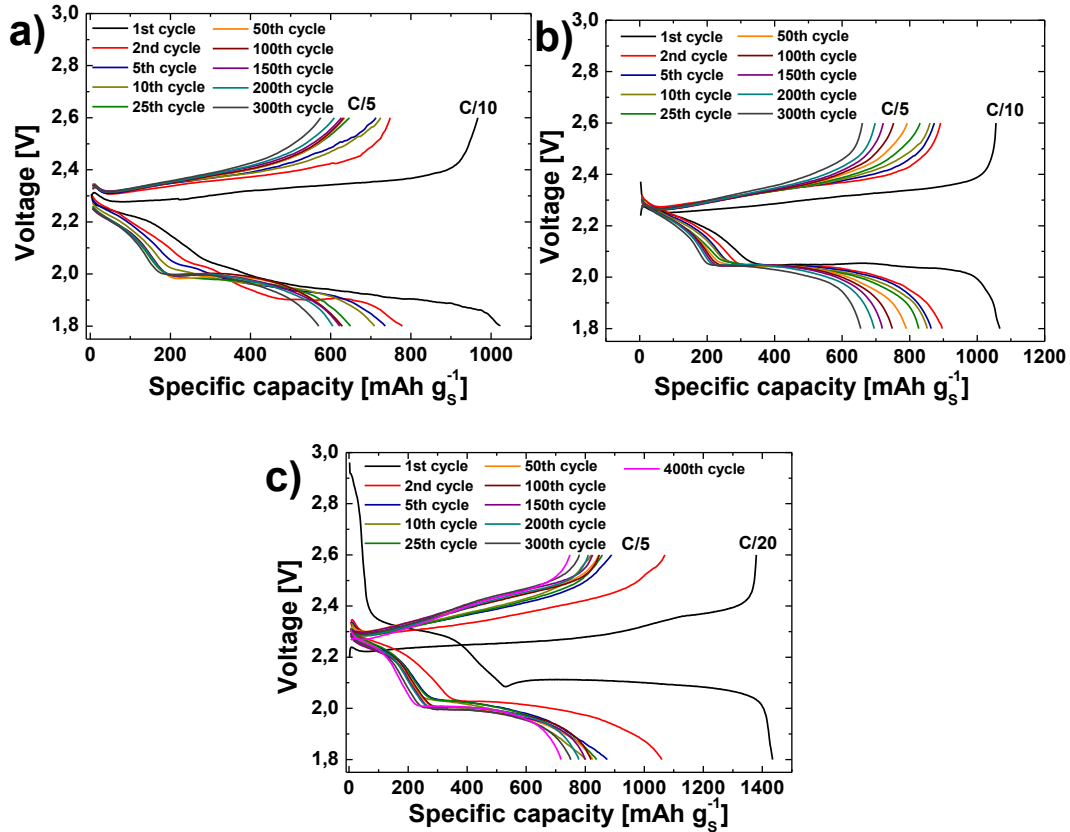


**Figure 4. 9:** Voltage capacity profiles of all three electrodes during long-term cycling test a) S80/KJBC b) S70/KJBC and c) PANi@KJBC/S

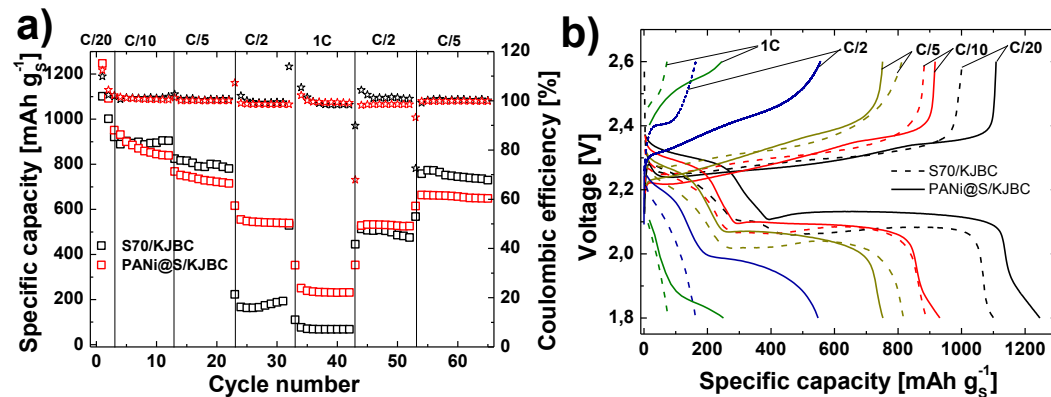


**Figure 4. 10:** C-rate capability test of S70/KJBC and PANi@KJBC/S composites a) Galvanostatic cycling performance and corresponding Coulombic efficiency at various current rates b) Voltage capacity profiles of charge and discharge at various currents

The CV has been performed on PANi@KJBC/S cathodes (Figure 4.11). It can be observed that in cyclic voltammetry typical oxidation and reduction peaks were appeared. Reduction of sulfur cathode gave two peaks at 2.25 and 1.95 V, whereas

oxidation of sulfur provided with an oxidation peak around 2.4 V with a shoulder around 2.5 V.

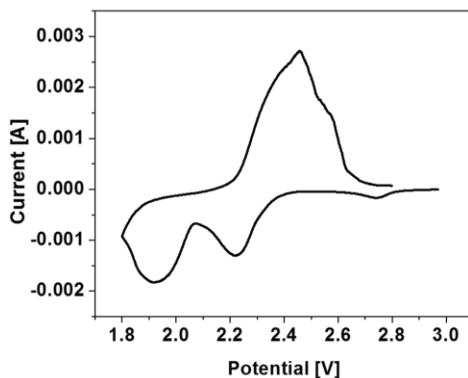


**Figure 4. 11:** first cycle of PANi@KJBC/S composite cathode by CV

## 4.2 Conclusion

In this section, a practical inadequacy of previous reports has been addressed where chloride-ion doped polyaniline had been proposed to limit LiPS solubility. We offered an alternative and better solution by accomplishing formate-ion doped polyaniline wrapped carbon/sulfur composite by in-situ oxidative polymerization. The as-prepared cathodes exhibited very stable performance around 800 mAh g<sup>-1</sup> for more than 500 cycles at 0.2C with capacity fading rate around 0.024%. Rate capability performance of the PANi wrapped C/S composite is remarkably better than that of the bare composite.

## Chapter 5

# Development of Si-based anodes for Li/S batteries

In the review section, it has been demonstrated how the use of metallic lithium shortens battery life. Li anode deters the cell life either by continuously consuming electrolyte due to exposure of highly reactive surface or by the formation of Li dendrites. Formation of dendrites can easily shorten the two electrodes and results in an unexpected event such as an explosion or fire. Hence, the use of metallic Li in batteries is a big safety hazard [13]. This provides a great motivation to design safer Li-ion/sulfur batteries, by switching metallic Li anode with other insertion or alloying type negative electrodes. Choice of the negative electrode for Li/S could be Si, tin (Sn) or graphite. Undoubtedly, Si stands out among the choices mainly because of its highest specific capacity [14]. Secondly, Si anode can be cycled in the ether-based electrolyte as preferred for sulfur-based cathodes. Carbonate-based electrolytes are reactive towards LiPS as discussed previously, so they cannot be utilized either in Li-ion/sulfur system.

Lithium free full cell can be approached either by using lithium sulfide ( $\text{Li}_2\text{S}$ ) vs. a Si anode or by choosing pre-lithiated anode vs. sulfur  $\text{S}_8$  cathode. In the former solution, we have to deal with highly reactive and unstable  $\text{Li}_2\text{S}$  to synthesize sulfur cathode. In the later one, Si anode should be pre-lithiated either chemically or electrochemically before pairing it to  $\text{S}_8$  cathode. Before realizing a full cell, one should have to be focused on fabricating stable Si anodes. Si anodes itself come up with huge volume variations and short cycle life. In the first part of the chapter, we have presented two possible solutions to realize stable anodes. In the first part of the chapter, we reported Si nanoparticle anodes fabricated with an all-designs integrated strategy. SiNP incorporated carbon nanofibers anodes with void spaces have been reported that can be effectively cycled at double capacity than alone carbon anodes. In addition to novel material architecture, a special binder system has been opted to attain stability. In the second part, a very simple approach has

been put forth using commercially available conductive polymer PEDOT:PSS as a binder and a conductive additive. It has been demonstrated that how conductive polymer and other conductive additives contributes towards Si electrode stability.

## **5.1 Silicon nanoparticles (SiNP) incorporated carbon nanofibers (CNF) based anodes**

Electrospinning provides an opportunity to synthesize nanofibers lodged with various nanoparticles in bulk. Various researchers opted the similar strategy to produce nanofibers loaded with Si nanoparticles with some appreciating results [210, 211]. Nevertheless, their performance is limited as is the case with other core-shell structures [137, 210]. Contrary, various researchers have revealed that architectures with free volume or void structures greatly contribute towards the stability of Si anode by standing with the volume changes [140]. This strategy also safeguards the stable SEI on carbon shell, thus also contributes towards low electrolyte depletion. Various approaches have been proposed to achieve these void structures at lab scale. These approaches come with their intrinsic limitations to scalability because of complex nanoscale synthesis and reproducibility. Secondly, HF washing of as produced particulate nanostructures is a quite challenging task to remove sacrificial SiO<sub>2</sub>. Additionally, binders play a critical role here to achieve better electrochemical performance by keeping the structure intact both mechanically and electrically [144]. Various binders have been proposed to target stable electrochemical performances, however, this binder-particle interaction alone is not enough to stand with these volume changes because of phase separation.

### **5.1.1 Development of SiNP@SiO<sub>2</sub>@CNF and SiNP@void@CNF composite materials and anodes**

To structure stable Si anodes, all designs integrated strategy has opted. As pointed earlier that Si anode with void spaces offer better performances, so for the purpose, Si nanoparticles with SiO<sub>2</sub> shell were electrospun with polyacrylonitrile (PAN) solution. As obtained electrospun nSi@SiO<sub>2</sub>@PAN nanofiber sheet was stabilized by oxidation at 280°C followed carbonization at 1000 °C. Carbonized nanofiber sheets embedded with nSi were conveniently washed with HF solution to realize void configuration like that of yolk-shell as demonstrated in **Figure 5.1**. To achieve stable and interactive binding system, alginate was preferred over a series of binders. The binder system used to study are alginates, gelatine, chitosan, PAA, and PVDF. Alginate binding matrix was further stabilized using citric acid as a crosslinking agent. Three-dimensional crosslinking networks was obtained by treating anode spread at 150 °C under high vacuum condition.

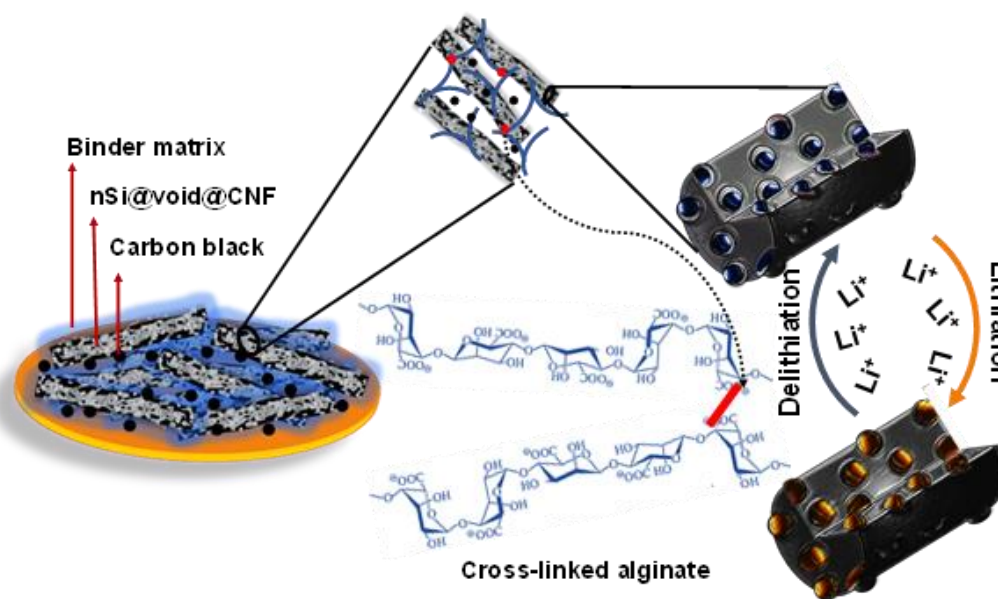


**Figure 5. 1:** Schematic representation of as-configured Si anodes with all designs integrated strategy (i.e. Si nanoparticles with void spaces in CNF (SVCNF) and cross-linked alginate binder) and proposed a functioning mechanism

### Electrospinning and carbonization of Polyacrylonitrile (PAN) and SiNP composites

For the preparation of electrospinning baths, polyacrylonitrile (PAN) (MW 150000, Sigma Aldrich) 10% by weight was dispersed in dimethylformamide (DMF). Additionally, nano silicon (<100nm, Sigma Aldrich) was added 15% on the weight of PAN to the mixture labeled as SSCNF. In a typical procedure, 8 g of PAN was dissolved in 70 g DMF by mechanical stirring 12 h at 60°C. In other 10 g of DMF, 1.2 g of nano-Si particles were dispersed by sonicating for 30 min. Then two solutions were mixed under continuous stirrings for another 12 h to obtain a homogenous mixture. The mixture was again subjected to 30 min sonication just before the start of the spinning process. The electrospinning was carried out on a high voltage (29.9 kV) three syringes electrospinning setup (MECC Co. LTD., model NF-103) at flow rate 2-2.2 ml h<sup>-1</sup>. The relative humidity was maintained at 65% with a temperature around 25 °C. The needle to collector distance was kept at 17 cm, and the collector cylinder was rotating at a speed of 300 rpm. Thermal treatment of as-spun mats was carried out in two steps; stabilization and carbonization. In stabilization step, the mat was subjected to 280 °C for 5 h in air at a heating rate 1 °C min<sup>-1</sup>. This step also contributes to achieving a thick SiO<sub>2</sub> shell around Si nanoparticles. In the second step, carbonization was performed at 1000 °C for 1 h at a heating rate 5 °C min<sup>-1</sup>. In the same way, carbon nanofibers (CNF) mat was produced without Si to estimate the carbon contribution in electrochemical performance. To exhaust the thick silica shell around the silicon particles, nSi@CNF mats were immersed for 30 sec in 10% HF solution. After dipping in HF solution, the sheet of nSi@void@CNF was simply washed with an excess of deionized (DI) water. The as-obtained sheets were labeled as SVCNF.

## Construction of SiNP@SiO<sub>2</sub>@CNF and SiNP@void@CNF anodes

SSCNF and SVCNF anodes were constructed using mortared active material 85% along with 8% carbon black (TIMICAL Super C65) and 7% alginate/citric acid (7:3) mixture (Sigma Aldrich). The slurry was prepared by mixing all the constituents in water using a mixer mill (MM400, Retsch) at 20 Hz for 30 min. The slurry was cast on copper foil using doctor blade thickness 200  $\mu\text{m}$  with automated film applicator. The spread was dried for 12 h at ambient conditions and then was annealed at 150  $^{\circ}\text{C}$  for 2 h under strong vacuum. The loading was around 2.8  $\text{mg cm}^{-2}$  with a thickness of about 80  $\mu\text{m}$ . Similarly, pristine CNF anodes were prepared by mixing 80% grounded CNF, 10% carbon black and 10% alginate. Silicon anodes were also prepared by mixing 30% nano-Si, 60% carbon black and 10% alginate. For CNF and nSi anodes, no curing treatment was performed. The electrodes with a diameter of 15 mm were cut out from casted foil and dried at 80  $^{\circ}\text{C}$  for 6 h before transferring to the glove box for assembling the coin cells.

### 5.1.2 Physicochemical characterization

The morphology of SSCNF and SVCNF was examined using field-emission scanning electron microscopy (FESEM, JEOL-JSM-6700F). Morphological characterization of as-spun carbonized SSCNF sheet through FESEM imaging reveals the uniform distribution of SiNP along CNF structure. It can also be observed that nano-Si is also well confined in carbon structure with minimal agglomeration and surface adhered SiNP (Figure 5.2). On washing SSCNF with HF solution by simple immersion and drying technique, there is no unexpected change in the morphological structure of as-obtained SVCNF structures. Apparently, the SVCNF exhibited the same external morphology as that of SSCNF. However, on higher magnification, the SVCNF showed some hollow three-dimensional structures as highlighted in Figure 5.2d. This apparent change in structure could be a signal to void structures.

To further explore the internal morphological elements, TEM imaging and EDS mapping of SSCNF and SVCNF were carried out. The TEM analysis of SSCNF and SVCNF was conducted using a JEOL JEM-2100 TEM. EDS analysis of SSCNF and SVCNF was conducted on JEOL JEM-2100 TEM. Figure 5.3a-c shows the TEM images of SSCNF, it can be observed that SiNP are well embedded in CNF carbon structure like that of core-shell structures. However, amorphous SiO<sub>2</sub> can be detected between the carbon shell and the Si core (Figure 5.3c). This observation was also established by performing the EDS mapping of the selected zones (Figure 5.4). Zone 1 showed merely carbon signals, while zone 2 exhibited a strong oxygen signal along with weak Si signal and zone 3 exhibited the opposite trend strong Si signals with weak oxygen one. In the third zone appearance of the oxygen signal is because of the core-shell architecture of SiO<sub>2</sub> shell. TEM images of SVCNF have demonstrated the presence of void structure around the SiNP like that of yolk-shell structures (Figure 5.3d-f). On HF washing, SiO<sub>2</sub> shell was washed

away leaving elemental SiNP. This observation can be deduced firstly by witnessing the reduction in diameter of SiNP. Secondly, the absence of oxygen signal also established the argument, as EDS mapping of SiNP just provided with C and Si signals (Figure 5.5).

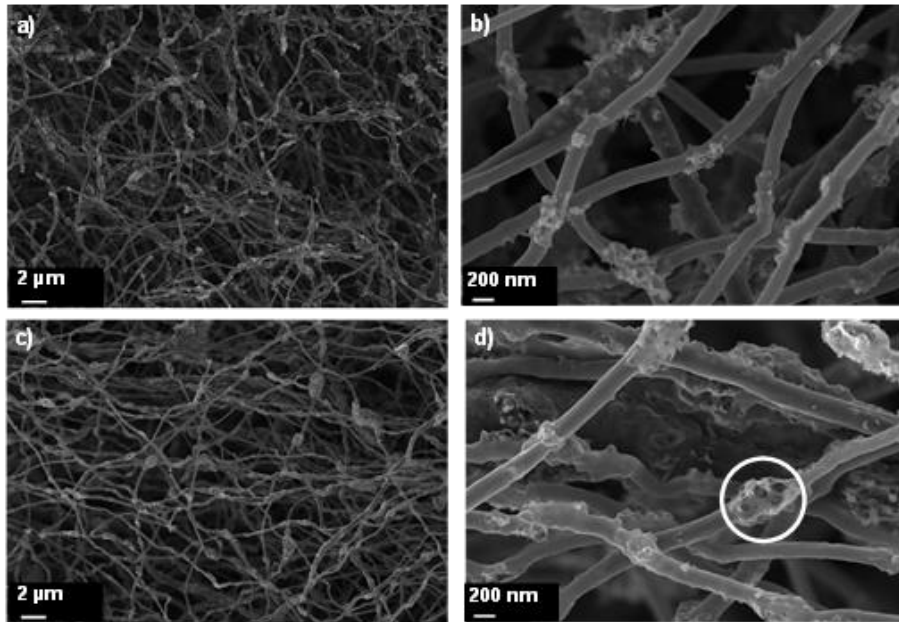


**Figure 5. 2:** FESEM images of as-spun SSCNF anode sheet (a,b) and just washed SVCNF anode composite (c,d)

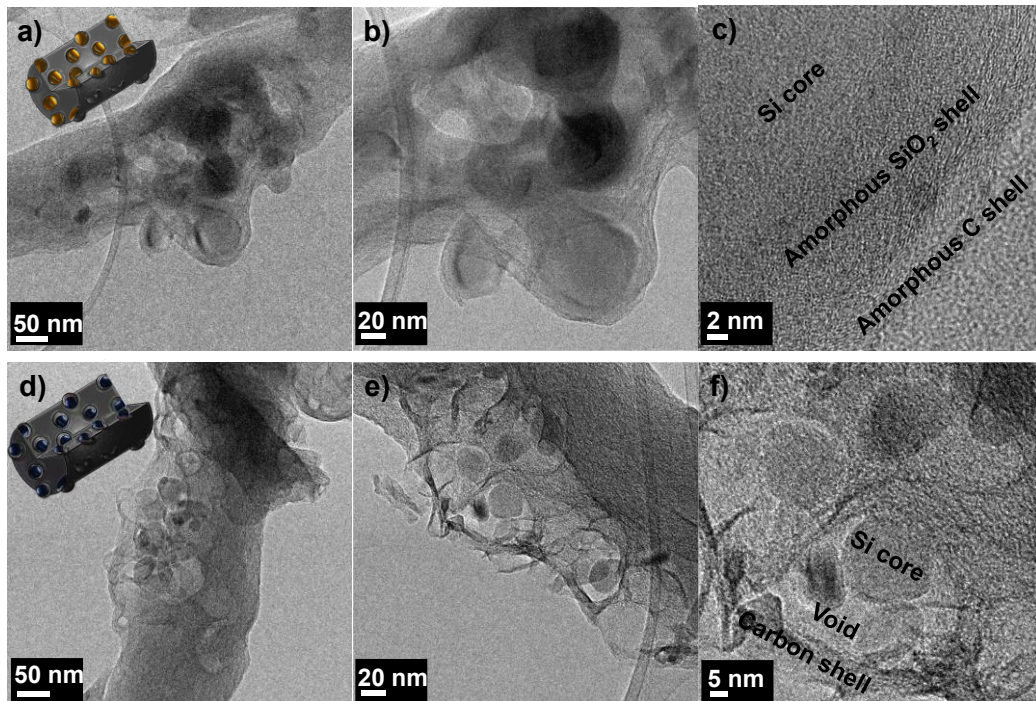


**Figure 5. 3:** TEM imaging of SSCNF (a,b,c) and SVCNF (d,e,f) revealing the structural and morphological elements of the Si anode composites

Silicon and silica content of the composite was evaluated by carrying out TGA and ICP analysis of the composites. Thermogravimetric analyses of SSCNF and SVCNF were carried out on a Mettler Toledo TGA/SDTA 851 instrument by heating the composite at  $10\text{ }^{\circ}\text{C min}^{-1}$  from room temperature to  $800\text{ }^{\circ}\text{C}$  under air (Figure 5.6a). Inductive coupled plasma mass spectrometry of SSCNF was performed on ICP-MS 7500cx, Agilent Technologies to precisely estimate the silicon and silica content. The oxidation of CNF around  $600\text{ }^{\circ}\text{C}$  results in solid content around 36% that is comprised of both  $\text{SiO}_2$  shell and metallic Si core. While the combustion of SVCNF results in the solid content of around 18% that is metallic Si. Rising the temperature beyond  $700\text{ }^{\circ}\text{C}$  in both cases comes up with the rise in solid content that is linked to the oxidation of Si to  $\text{SiO}_2$ . From TGA analysis, it has been deduced that SSCNF has a total solid content of 36% in which 18% is metallic Si and the remaining 18% is  $\text{SiO}_2$ . These outcomes were further established by performing ICP analysis of SSCNF. By ICP measurement, it is detected that 35.93%  $\text{SiO}_2$  matrix in SSCNF comprised of 16.80% metallic Si (Table 5.1). FTIR-ATR measurements of pure alginate and CA crosslinked alginate are performed on the FTIR instrument to investigate new bonds formation. FTIR-ATR of sodium alginate (heat-treated at  $150\text{ }^{\circ}\text{C}$ ) has shown peaks around  $3266$ ,  $1598$  and  $1012\text{ cm}^{-1}$  those can be attributed to OH, C–O–O–, C–O–C groups respectively. FTIR of citric acid crosslinked alginate confirms the esterification mechanism by demonstrating additional bands around  $1710$  and  $1213\text{ cm}^{-1}$  (Figure 5.6b). The appearance of peaks at  $1710\text{ cm}^{-1}$  typically reveals the formation of ester carbonyl groups and at  $1213\text{ cm}^{-1}$  associated with C-O-C stretch. After citric acid modification, broad peak OH peaks around  $3340\text{ cm}^{-1}$  has slightly suppressed, which indicates the esterification of OH groups.

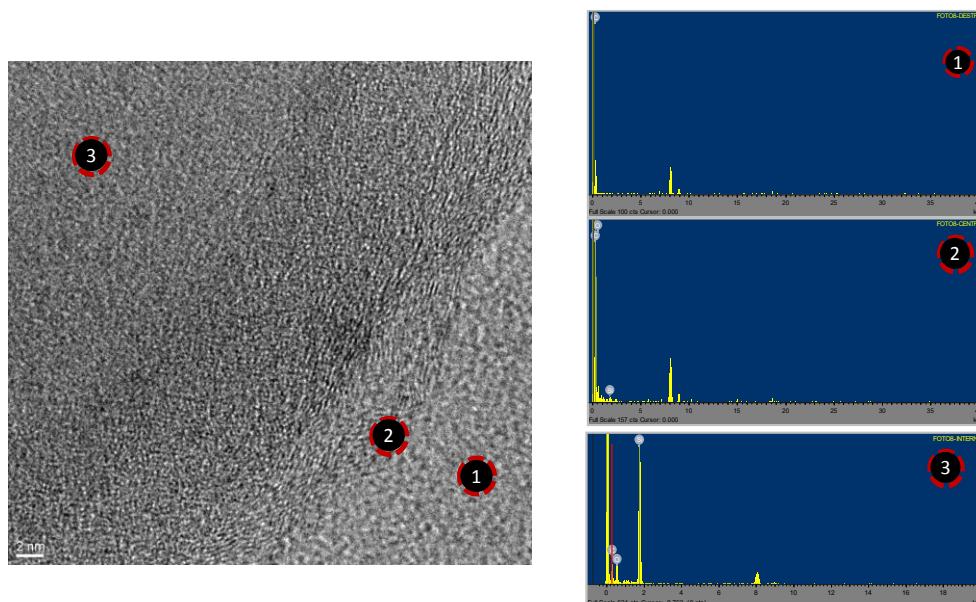


**Figure 5. 4:** EDS mapping of SSCNF material to identify the composition of various localities in composite

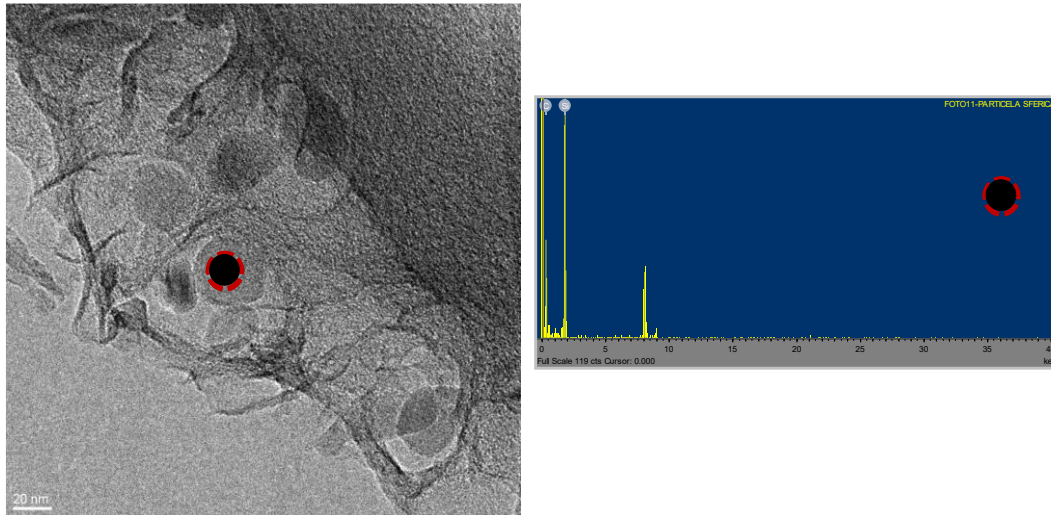


Figure 5. 5: EDS mapping of SVCNF to confirm the presence of pure Si hosted in the void

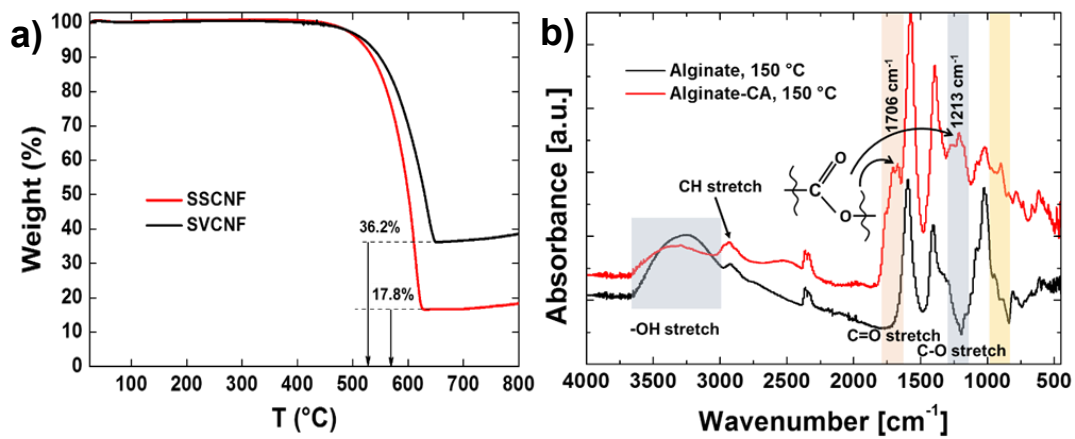


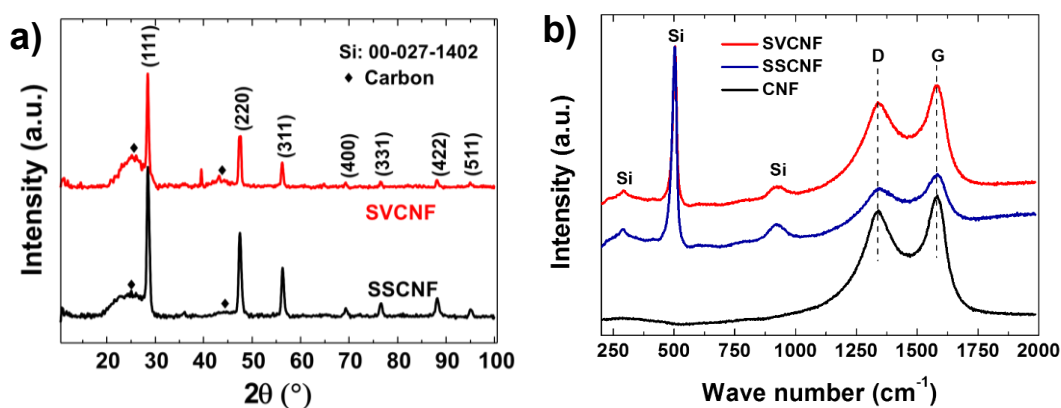
Figure 5. 6: a) TGA analysis of SSCNF and SVSNF composites b) FTIR spectra of pristine alginate and CA crosslinked alginate

Table 5. 1: ICP analysis of SSCNF

Composite Material	% Si p/p	% SiO <sub>2</sub> p/p
SSCNF	16.80	35.93

To observe the phase characteristics of SiNP and that of CNF, XRD analysis and Raman spectroscopy of the composites was performed. The XRD patterns of SSCNF and SVCNF were recorded on a Panalytical X'Pert PRO diffractometer with a PIXcel detector, using Cu K $\alpha$  radiation, under the conditions of  $2\theta = 10-100^\circ$  and  $2\theta$  step size = 0.03, to observe the presence of crystalline Si in the composite structure. XRD analysis of SSCNF showed all three contributions arising from graphitic carbon, amorphous SiO<sub>2</sub>, and crystalline Si, whilst XRD pattern of SVCNF exhibiting contributions coming from graphitic carbon and crystalline Si. Typical diffraction pattern arising from a cubic crystal structure of silicon can be

observed in Figure 5.7a for both SSCNF and SVCNF. XRD pattern of SSCNF has exhibited a broader halo because of the contribution both from SiO<sub>2</sub> (i.e. 2 $\theta$ ~22°) and carbon (i.e. 2 $\theta$ ~24°). XRD pattern of SVCNF instead has a narrower halo about 24° that is characteristic of carbon. Raman spectroscopy of all SSCNF, SVCNF, and CNF has provided two carbon characteristic Lorentzian peaks, one is around 1340 cm<sup>-1</sup> disorder “D” band and other is around 1580 cm<sup>-1</sup> graphitic “G” band (Figure 5.7b). ID/IG ratios of all matrices were estimated by fitting the spectra with Lorentz function to assess the degree of graphitization [212]. This confirms the induction of small order graphitic structures into the CNF. ID/IG value of SSCNF and CVCNF is fractionally greater than that of CNF. A little higher degree of defects in SSCNF and SVCNF could be induced by metallic particles. Raman spectra of both SSCNF and SVCNF showed a strong Si characteristic peaks around 520 cm<sup>-1</sup>, along with two weaker Si peaks about 300 cm<sup>-1</sup> and 970 cm<sup>-1</sup>.



**Figure 5. 7:** a) XRD pattern of SSCNF and SVCNF b) Raman spectra of CNF, SSCNF, and SVSNF

### 5.1.3 Electrochemical Testing

For the half-cell testing of bare nSi, SSCNF, and SVCNF, coin cells (CR2032 type) were assembled in Ar-filled dry glove box (Mbraun Labstar with O<sub>2</sub> and H<sub>2</sub>O < 0.1 ppm) using lithium metal as the anode. The geometric area of the electrodes was 1.76 cm<sup>2</sup>. A lithium disc (16 × 0.2 mm, Chemetall s.r.l.) was used as the anode. A Celgard EH2010 (trilayer PP/PE/PP) 20 mm × 25 μm soaked with the electrolyte was used as the separator. The electrolyte consisted of 1,2-dimethoxyethane (DME) and 1,3-dioxolane (DIOX) 1:1 (v/v) with 1 M LiTFSI and 0.25 M LiNO<sub>3</sub>. Each cell contains no more than 20 μL of the electrolyte. Cells were galvanostatically discharged to 10 mV and charged to 2 V. First cycle was performed at 180 mA g<sup>-1</sup> (0.05C) and subsequent cycling was carried out at current rate 716 mA g<sup>-1</sup> (0.2C) based on Si. For Si anodes, C-rates are calculated using a theoretical capacity of silicon corresponds to Li<sub>15</sub>Si<sub>4</sub> (i.e.) 3579 mAh g<sup>-1</sup>. Initially, all Si anodes including SVCNF, SSCNF, and bare nSi exhibited very high first cycle discharge capacities at a current density of 178 mA g<sup>-1</sup>. In the case of SVCNF and SSCNF, first cycle discharge capacities are more than theoretical values of Si with the coulombic efficiency (CE) of ~60%. The additional contributions for the first cycles of both cathodes are coming from irreversible SEI layer formation and electrolyte

decomposition that can be witnessed from voltage profiles of first cycles (Figure 5.8c, d). While bare nSi anode delivers the discharge value of  $3445 \text{ mAh g}^{-1}$  for the first cycle with CE around 65%. For the second cycle, there is a sharp decrease in specific capacity value of SSCNF cathode to  $2600 \text{ mAh g}^{-1}$  while SVCNF anode showed a marginal decrease with a specific capacity value of  $3800 \text{ mAh g}^{-1}$  both with CE of about 91%. The sharp decrement in specific capacity value can be attributed to silica shell in SSCNF, which got irreversible lithiated in the first cycle. Contrary, SVCNF anodes with pure Si particles housing in void structures maintain their characteristic electrochemical behavior.

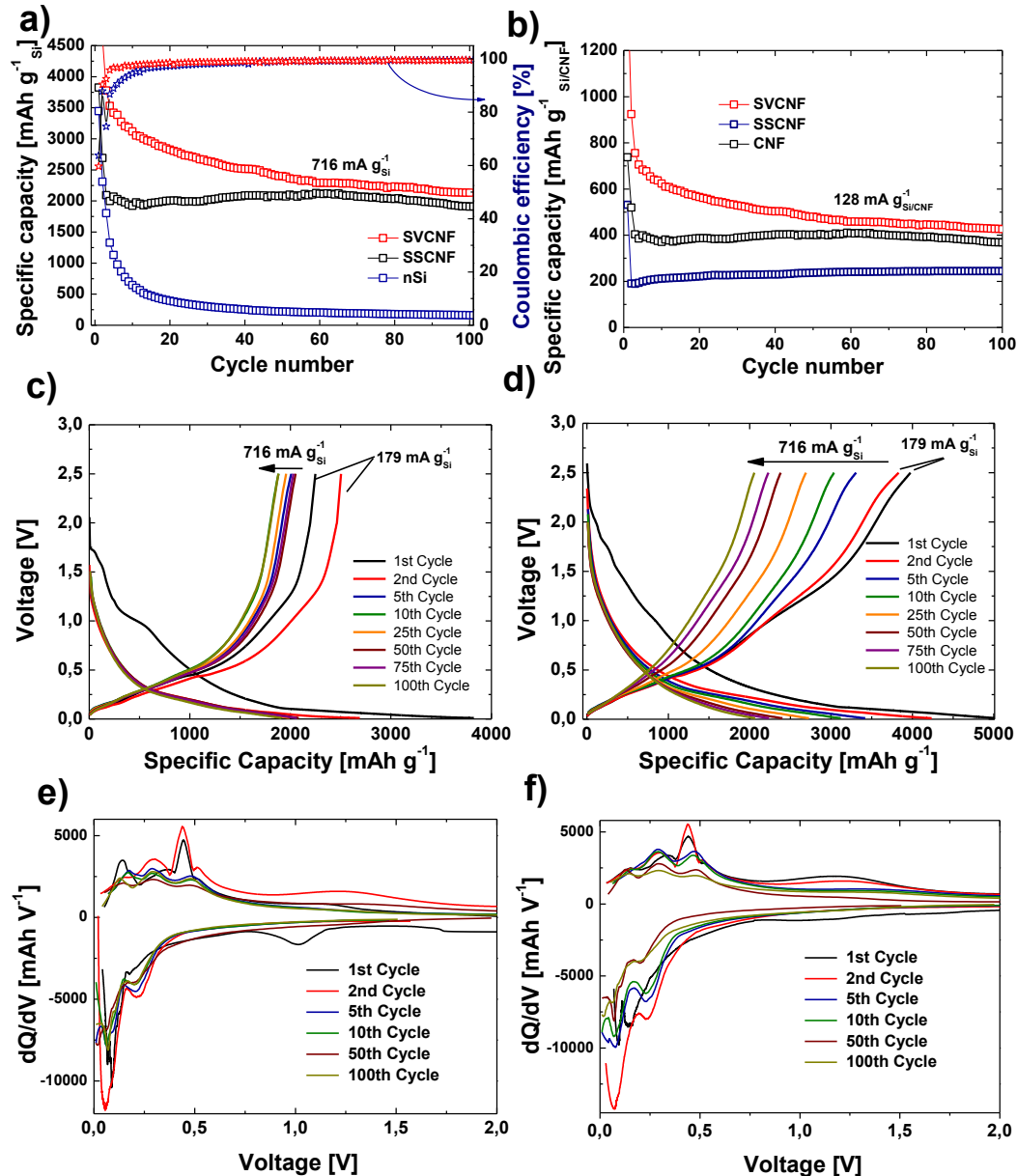


**Figure 5. 8:** a) Cyclic performance (squares: specific capacity, stars: Coulombic efficiency) of nSi, SSCNF, and SVCNF anodes vs. lithium foil on basis of silicon contribution, b) half-cell performance of CNF, SSCNF, and SVCNF on the basis active material loading, voltage profile of c) SSCNF anode, d) SVCNF anode with nominal contribution of first cycle SEI formation

From the second cycle onwards, all Si anodes were subjected to a current density of  $716 \text{ mA g}^{-1}$ . The coulombic efficiency for both SSCNF and SVCNF improved over the span of 10 to 15 cycles and reached to  $\sim 99\%$ . For the third cycle, at high current density, SSCNF and SVCNF showed the specific capacity of  $2092$  and  $3529 \text{ mAh g}^{-1}$  respectively. On long term cycling SSCNF after attaining a peak value of capacity (i.e.  $2130 \text{ mAh g}^{-1}$ ) around the 60th cycle, there is again downgrading behavior (Figure 5.8a). This performance was recorded in a repeated set of measurements more or less with the same values. This phenomenal behavior can be explained based on morphological elements of SSCNF anodes. Initially, thick silica shell gets lithiated and causing the  $\text{SiO}_2$  to pulverize into particles to expose the Si core. Lithiation of Si core causes a rise in the specific capacity value and more vivid Si lithiation peaks in  $dQ/dV$  plots (Figure 5.8e). But the confined architecture of SSCNF anodes cannot withstand with volume changes and the active material start disintegrating that causes a gradual loss in capacity. On another hand, SVCNF showed a steady loss in capacity over a span of 40 to 50 cycles, from which onwards it is stabilized with the specific capacity value of  $2200 \text{ mAh g}^{-1}$ . The initial gradual loss in capacity can be designated to loss of active material that is not flawlessly trapped during the electrospinning process. Once SVCNF anode loses their improperly confined active material, there is no more sweeping change in specific capacity values.  $dQ/dV$  plot for SVCNF showed well-defined lithiation peaks at  $0.24 \text{ V}$  and  $0.09 \text{ V}$  and delithiation peaks at  $0.25 \text{ V}$  and  $0.5 \text{ V}$ . Although SSCNF also showed more or less similar peaks but there are disparities that could arise from structural disintegration of materials. Pure nSi anode, rapidly depletes their capacity within first 20 cycles from  $2309 \text{ mAh g}^{-1}$  to  $394 \text{ mAh g}^{-1}$  with very low CE values. The specific capacity values were calculated for both SSCNF and SVCNF anode based on active material loading considering the  $18\%$  Si contribution in both cases, overlooking the contribution of silica in case of SSCNF. In parallel, pure CNF anodes were also galvanostatically cycled to find the contribution of carbon in overall composite. It can be observed that CNF anodes themselves contribute the specific capacity value of  $220 \text{ mAh g}^{-1}$  at maximum. While SVCNF and SSCNF showed specific capacity values of  $450 \text{ mAh g}^{-1}$  and  $390 \text{ mAh g}^{-1}$  on the basis of active mass (Si/CNF) even after 100 cycles of charging and discharging. SVCNF anodes with pristine alginate polymer as binder also exhibited comparable electrochemical performance (Figure 5.9a) because of material architecture to adsorb the volume changes but relatively with lower capacity and variability in cycling behavior. But, the stable performance of SVCNF with CA crosslinked alginate binder can be associated with better electronic contact and higher mechanical stability of the matrix to the current collector. Further, SVCNF anodes built with CA crosslinked alginate also exhibited the stable charging and discharging behavior at a high current rate of  $1.8 \text{ A g}^{-1}$  with capacity retention about  $1800 \text{ mAh g}^{-1}$  for more than 200 cycles (Figure 5.9b).

EIS of SSCNF and SVCNF anodes against Li has been measured using both LP30 electrolyte and ALISE electrolyte. It can be observed that charge transfer resistance for both type of anodes with ALISE electrolyte is almost half to that of LP30

electrolyte based cells. Interestingly, Warburg resistance is greater for SSCNF anodes to that of SVCNF anodes for both types of the electrolyte.

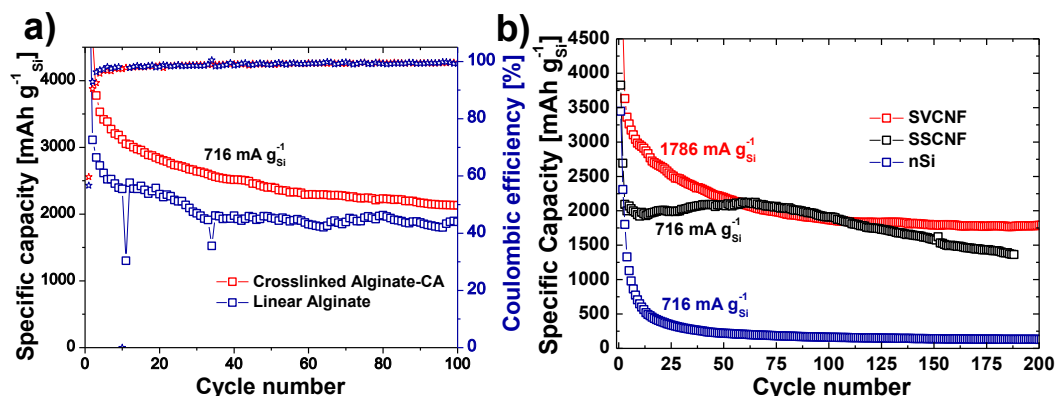


**Figure 5. 9:** a) a comparison of Galvanostatic performance of SVCNF anodes constructed using pristine alginate and CA crosslinked alginate b) long term cycling performance of SVCNF anode at current rate 1786 mA g<sup>-1</sup> in comparison to cycling performance SSCNF and nSi anode at current rate 716 mA g<sup>-1</sup>

## 5.2 Electroactive polymers based Si/CNT and Si/rGO anodes

Most of the previous work on silicon anodes involve complex syntheses and unusual electrode preparations. Pulverization of Si anode is largely sorted out using the nanostructured form of Si active materials such as nanoparticles, nanowires, nanoporous hollow Si. By opting the proper binding system, Si lithiation and delithiation can be realized even without opting the complicated architectures. Research work on binders mostly involves the preparation of 3D crosslinked network that can withstand mechanical stresses [144]. Moreover, the binding system should be physically and chemically compatible with the manufacturing process, active materials, conductive additives, and electrolyte. For example, minimal swelling of binders in the electrolyte and enough interaction among binder and other components to ensure proper adhesion and conductive pathways. A range of polymers has been investigated as a possible binding matrix to meet the aforementioned requirements. A variety of synthetic polymers such Nafion, polyacrylic acid (PAA), styrene butadiene (SBR) and polyamide-imide; various biopolymers such as alginate, carboxymethylcellulose (CMC) and cyclodextrins; or a combination of them such as CMC/SBR have been successfully demonstrated [145]. These binding systems have effectively imparted the elasticity to the matrix without compromising structural integration of the matrix. These binders are usually electronically inert, thus contribute towards inactive mass loading. So, replacing these binders with the electroactive binding system can greatly suppress the physical separation between various components of anodes. The accomplishment of a continuously conductive phase can significantly help in minimizing the capacity loss due to pulverization. A number of studies have already

been reported using conductive polymers such as polyaniline, polypyrrole, PEDOT:PSS as a binding network to achieve Si anodes [135, 136].

### 5.2.1 Development of Si anodes using PEDOT:PSS as a binder with various carbon additives

Poly(3,4-ethylenedioxythiophene)/poly-(styrene-4-sulfonate) PEDOT:PSS has been chosen as a binding matrix owing to its excellent adhesive properties [213]. Additionally, it is a good conductor particularly when a higher degree of doping has been reached. It exhibits good chemical stability towards a range of electrolyte systems, and electrochemical stability in a potential range of Si and S electrodes.

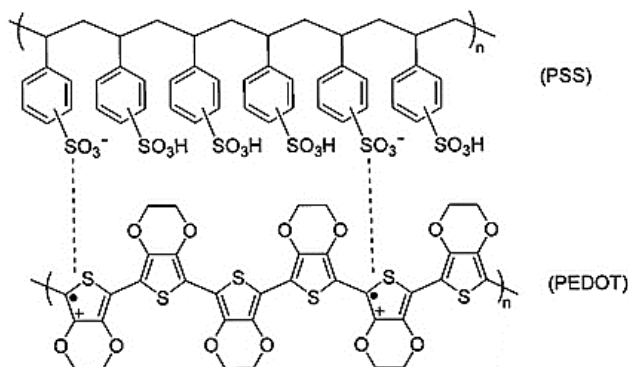


**Figure 5. 10:** Molecular structure of PEDOT:PSS

### Construction of PEDOT:PSS based tri-component Si anodes

To construct Si anode, Clevis PH 1000 (an aqueous based 1.1% w/v PEDOT:PSS solution) from Heraeus was used. SiNP in powder form was acquired from Tekna Advanced Materials; Inc (mean diameter: <100 nm, plasma synthesized) with oxygen content < 3 %. Graphene oxide dispersion was purchased from Graphenea and reduced to rGO at 700 °C for 2 h under 3 % H<sub>2</sub>/Ar. Multiwalled carbon nanotubes (MWCNT, 95 % purity) were acquired from Nanocyl while formic acid (FA, 95 %) as a secondary dopant for PEDOT was acquired from Sigma-Aldrich. In the case of nSi/rGO/PEDOT:PSS and nSi/CNT/PEDOT:PSS tri-component composites, first conductive additive rGO or CNT was mortar mixed with silicon nanoparticles to attain homogeneous mixture. The slurry was prepared by mixing as mortared mixtures or Si nanopowder in PEDOT:PSS solution with FA 50 μL using mixer mill (MM400, Retesch) at 20 Hz for 60 min. The compositions of mixtures were maintained as described in Table 5.2. The viscosity of the slurry was adjusted using DI water in required quantity. The resulting slurries were cast into films on Cu foils using a doctor blade apparatus on automated film applicator. The doctor blade clearance was altered from 25 to 100 μm to change the thickness and loading of casted films. The casted films were dried at 80 °C for 6 h and 15 mm diameter electrodes were punched out for coin cell testing. Electrodes were then heated at 110 °C under vacuum for 3-4 h to evaporate spare FA and

residual water. Here, it is mentioned worthy that FA boils at 100.8 °C at standard pressure.

**Table 5. 2:** Various compositions and thicknesses of nSi and PEDOT:PSS with and without conductive agents

	Composition	Thickness ( $\mu\text{m}$ )
<b>nSi/PEDOT:PSS</b>	80:20	25, 50
<b>nSi/rGO/PEDOT:PSS</b>	50:30:20	25, 50
<b>nSi/CNT/PEDOT:PSS</b>	50:30:20	25, 50

For the testing of as prepared anodes, three different electrolytes have been selected. a) Conventional Li-ion electrolyte (LP30) with the composition of ethylene carbonate (EC) and dimethyl carbonate (DMC) mixed in ratio 1:1 by volume with 1 M LiPF<sub>6</sub> and 1% vinylene carbonate (VC). b) Typical Li/S cell electrolyte (ALISE) with the composition of dimethoxymethane (DME) and dioxolane (DIOX) mixed in a ratio of 1:1 by volume with 1 M LiTFSI and 0.25 M LiNO<sub>3</sub>. c) An ionic liquid based electrolyte (ILS) with 1.2 M LiTFSI in 1-Methyl-1-propylpiperidinium bis(trifluoromethylsulfonyl)imide (PIP13TFSI) and diethylene glycol butyl ether (DEGBEE) with 4% fluoroethylene carbonate (FEC).

### 5.2.2 Physiochemical characterization

A well-spread slurry coating was acquired for all nSi/PEDOT: PSS compositions and coating thicknesses without flaws. Figure 5.11 depicts the electrodes coated with 50  $\mu\text{m}$  doctor blade clearance for nSi/PEDOT:PSS, nSi/rGO/PEDOT:PSS and nSi/CNT/PEDOT:PSS slurries. FESEM analysis of coated electrodes was performed on FESEM instrument to evaluate the morphological elements such as the degree of aggregation, distribution of various constituents (figure 5.12).

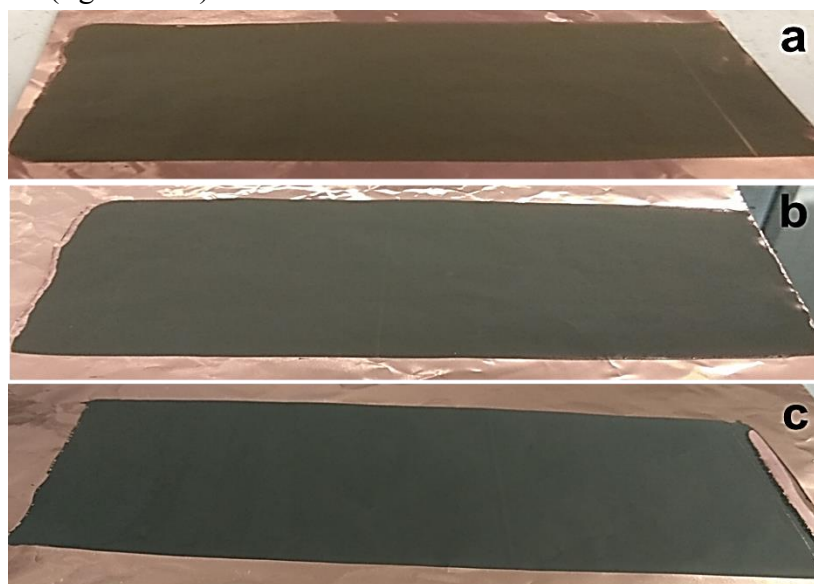


**Figure 5. 11:** Snapshots of the anodes acquired by doctor blade coating with 50  $\mu\text{m}$  clearance on Cu foils for a) nSi/PEDOT:PSS b) nSi/rGO/PEDOT:PSS c) nSi/CNT/PEDOT:PSS

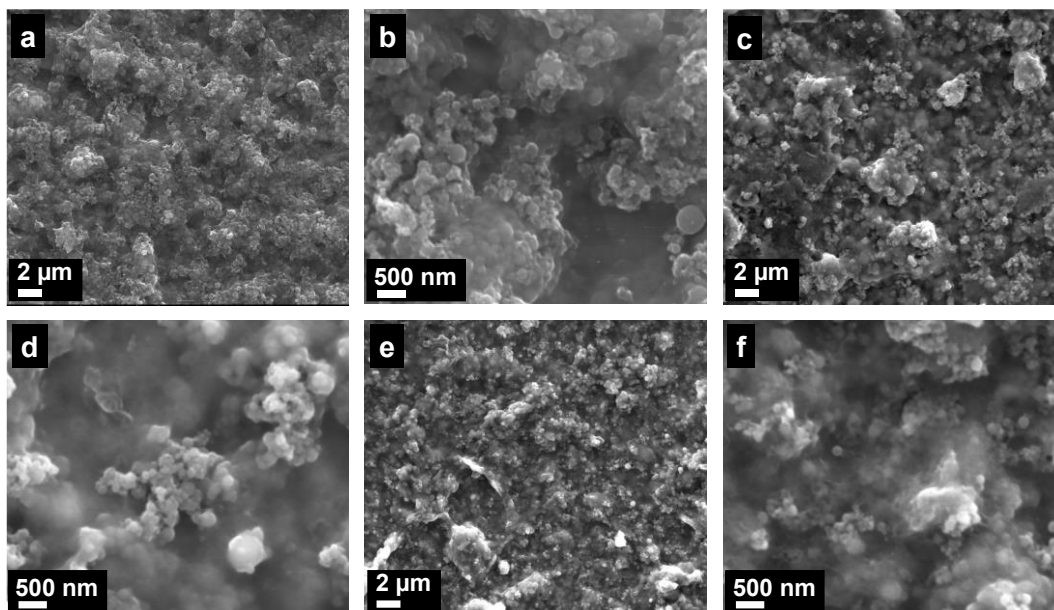


**Figure 5. 12:** SEM images of various as prepared Si anode a,b) nSi/PEDOT:PSS; c,d) nSi/rGO/PEDOT:PSS; e,f) nSi/CNT/PEDOT:PSS

### 5.2.3 Electrochemical Testing

Electrochemical characterization of as produced Si anodes has been carried out against Li metal counter electrodes. Half-cell Galvanostatic cycling was performed in coin cell configuration under varied conditions to arrive the stable electrode performance. In the first set of experiments, nSi/PEDOT:PSS, nSi/CNT/PEDOT:PSS and nSi/rGO/PEDOT:PSS anodes produced with 50  $\mu\text{m}$  doctor blade clearance were subjected to long term cycling using ALISE electrolyte and an EH2010 polymer separator. It can be observed that nSi/CNT/PEDOT:PSS exhibited a relatively stable performance than the other two configurations. nSi/CNT/PEDOT:PSS showed an initial discharge capacity of 3600  $\text{mAh g}^{-1}$  at C/10 that drop down to 2700  $\text{mAh g}^{-1}$  for the next four cycles (figure 5.13a). At C/5, nSi/CNT/PEDOT:PSS exhibited capacity around 2300  $\text{mAh g}^{-1}$  that drops down to 1250  $\text{mAh g}^{-1}$  at 70<sup>th</sup> cycle. While nSi/PEDOT:PSS also exhibited the initial capacity of 3600  $\text{mAh g}^{-1}$  at C/10 that is drop down to 1200  $\text{mAh g}^{-1}$  just after the next four cycles at C/10. At C/5, nSi/PEDOT:PSS anode showed the 650  $\text{mAh g}^{-1}$  that drops down to <200  $\text{mAh g}^{-1}$  within next 15 cycles. On another hand, nSi/rGO/PEDOT:PSS anode presented the relatively higher specific capacity value about 4000  $\text{mAh g}^{-1}$  that is dropped gradually to 2500  $\text{mAh g}^{-1}$ . At C/5, nSi/rGO/PEDOT:PSS anodes gave the specific capacity value of 2200  $\text{mAh g}^{-1}$  that downgrades to 400  $\text{mAh g}^{-1}$  within 50 cycles. Hence, nSi/CNT/PEDOT:PSS has only been chosen for the next electrochemical performance investigation. From figure 5.13b, it can be deduced that nSi/CNT/PEDOT:PSS anodes produced with different doctor blade clearance demonstrated a little different electrochemical

performance. Both anodes with different thicknesses exhibited almost similar capacity fade performances but anode with lower loading gave higher specific capacity values.

Electrochemical performance of nSi/CNT/PEDOT:PSS varied on the change of separator. In the presence of glass fiber separator, nSi/CNT/PEDOT:PSS showed relatively higher specific capacity values and more stable performance for the initial 60 to 70 cycles and then performance degrades quickly. While, in the case of polymer EH2010 separator, nSi/CNT/PEDOT:PSS anodes exhibit gradual degradation throughout the cycle life. This can be attributed to the presence of more electrolyte in case glass fiber separator, as glass fiber separator can hold a higher quantity of electrolyte than thin microporous polypropylene separator,

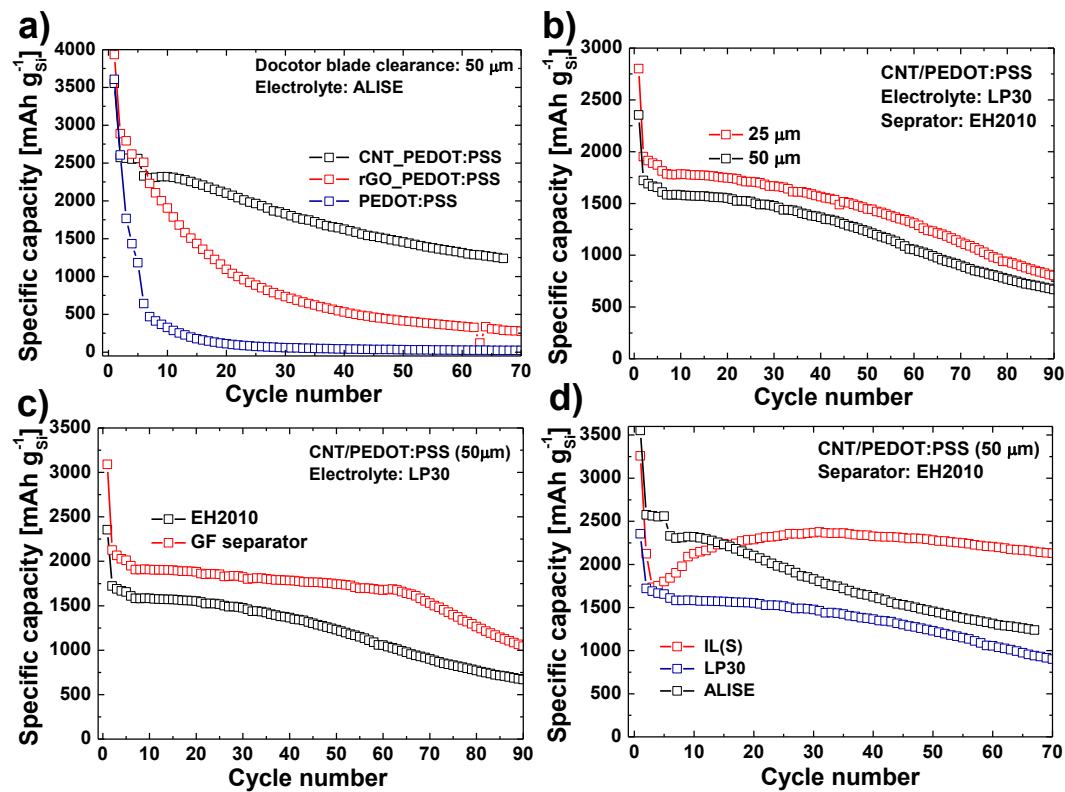


**Figure 5. 13:** Galvanostatic cycling performance of nSi/PEDOT:PSS anodes a) effect of conductive additives b) effect of coating thickness using various doctor blade clearances c) effect of separator d) effect of electrolyte on cycling performance

Figure 5.14a exhibits long-term cycling performance of nSi/CNT/PEDOT:PSS electrodes in ALISE and ILS electrolyte at 0.2C. It can be observed that Si anode in ether-based electrolyte showed initial discharge value around 1500 mAh g<sup>-1</sup> and quickly raise to a maximum value of 1800 mA g<sup>-1</sup> within 10 cycles. Then it degraded to 1000 mAh g<sup>-1</sup> after 120 cycles. The strong degradation can be attributed to the incapability of the ether-based electrolyte component to form a stable SEI layer. As it has previously observed that continuous SEI disruption causes the loss of active material and electrolyte depletion, so causes the hasty anode material degradation. While in the presence of ILS electrolyte, Si anode initially exhibited a lower discharge capacity around 1000 mAh g<sup>-1</sup> but then it raised to 1600 mAh g<sup>-1</sup> after 40 cycles of charge and discharge. Ionic liquids based electrolyte because of

their high density takes longer to impregnate properly the electrode material and their activation. Afterward, anode material starts gradually degrading at a slow rate of 0.23% per cycle for more than 90 cycles. The better performance in the presence of ILS can be linked both to ionic liquid and to FEC. FEC contribute greatly towards better SEI layer formation [214] and the ionic liquid can assist by desirable structural modification of the active material upon repetitive lithium alloying/dealloying [215]. CV curves of Si anodes exhibited the typical alloying and dealloying peaks with the first cycle of SEI layer formation (Figure 5.14b, c). In both cases, the peaks are getting sharper and intense that is exactly in accordance with the gradual activation of the active material during initial cycles.

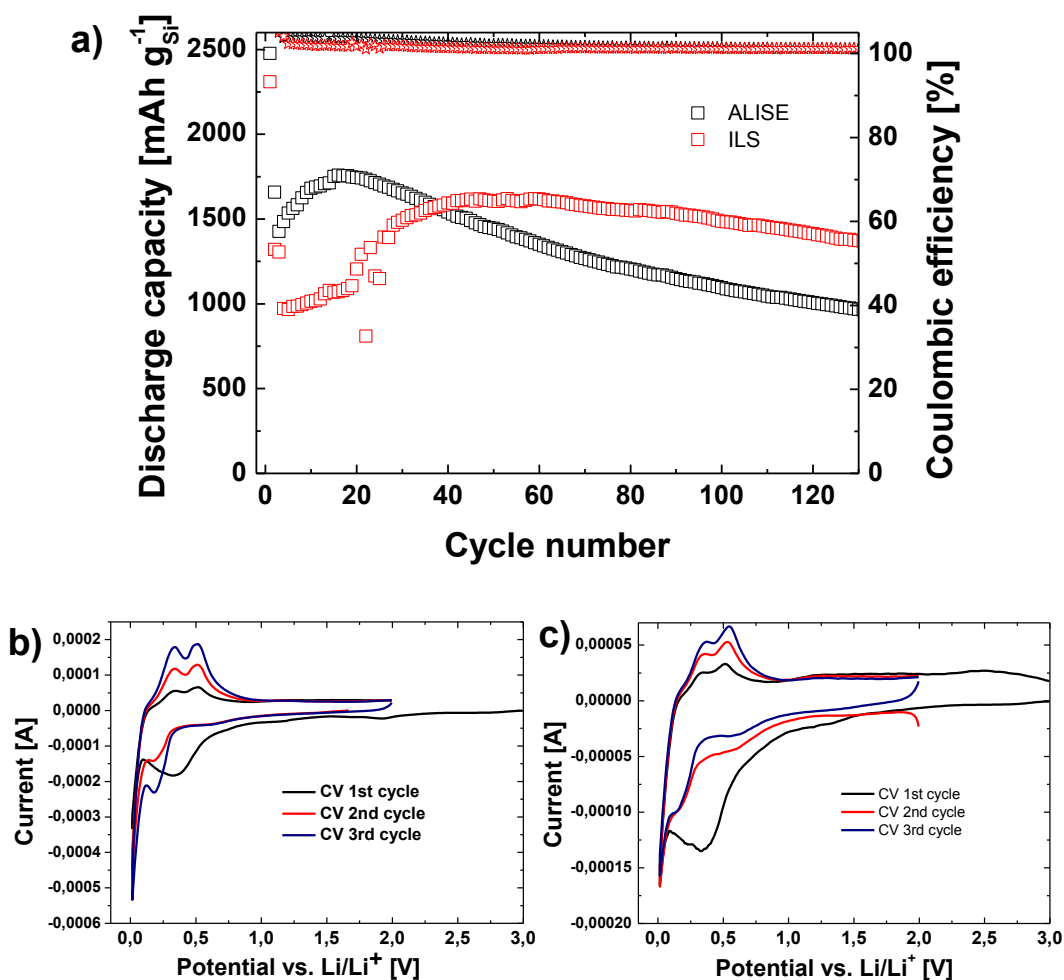


**Figure 5. 14:** a) Long-term cycling performance of nSi/CNT/PEDOT:PSS electrodes; b) CV of nSi/CNT/PEDOT:PSS anodes using ALISE electrolyte; c) CV of nSi/CNT/PEDOT:PSS anodes using ILS electrolyte

### 5.3 Conclusion

In this chapter, two altogether different approaches have been presented to realize stable silicon anodes. In the first strategy, electrospun silicon nanoparticles loaded carbon nanofibers have been produced via electrospinning and carbonization process. Simple HF washing of Si nanoparticle loaded CNF mats has induced void structures to accommodate the volume changes during lithiation and delithiation

process. A novel binder system (CA crosslinked alginate network) has been achieved by iteration of various binder systems. As prepared anodes showed stable electrochemical performances in the ether-based electrolyte. nSi@void@CNF anodes have delivered specific capacity value close to the theoretical value of Si and even after 100 cycle anodes exhibited a stable capacity of 2500 mAh g<sup>-1</sup> basis on Si. While based on the mass of total composite the stabilized capacity value was around 500 mAh g<sup>-1</sup> after 100 cycles at 0.2C. So, all-design integrated strategy enables to realize such a remarkable performance from Si anodes.

While in the second strategy, a simple approach is opted to reach well performing Si anodes. All in shelves chemicals have been integrated into working Si anodes. Commercial nano-Si has been mixed with commercially available PEDOT:PSS electroactive polymer suspensions both as conductive and binding network with or without other conductive additives like CNT and rGO. With different types of electrolyte systems, as-prepared anodes exhibited some promising electrochemical performances. Si anode with CNT and PEDOT:PSS exhibited specific 2500 mAh g<sup>-1</sup> at 0.1C and around 2000 mAh g<sup>-1</sup> at 0.2C in ether-based electrolyte system with 50% Si on the basis of spread material. After 100 cycles of charge and discharge, as-obtained anodes showed more than 70% capacity retention of the initial. It is determined that conductive additive, separator, electrolyte, and mass loading have a nominal effect on capacity and cycling stability. These anodes have been incorporated in full cell configuration to study Li/S full cell.



## Chapter 6

# Towards Li metal free sulfur batteries

As pointed out earlier that either silicon anode or sulfur cathode have to be lithiated before using in full cell configuration. Sulfur cathodes can be built using  $\text{Li}_2\text{S}$  to originate both sulfur and lithium source. But, preparation of  $\text{Li}_2\text{S}$  based cathode is relatively challenging, so the lithiation of Si anode is relatively more opted than former to achieve full cell [132, 216].

### 6.1 All carbon-based Lithiated Silicon Sulfur full cell

In this work, a lithiated silicon sulfur full cell is realized by opting the most appropriate architecture of carbon matrices for both silicon anode and sulfur cathode. For the purpose, the all-designs integrated strategy has opted for both electrodes. Electrospun nano-silicon@void@carbon nanofibers (SVCNF) cross-linked with alginate-citric acid binder network were utilized as silicon anode and heteroatom doped high surface area hierarchical porous carbons were chosen as a host matrix for the sulfur cathode. Herein, to produce anode material, nano silicon particles with a certain thickness  $\text{SiO}_2$  shell were electrospun with polyacrylonitrile as a carbon source for CNF. Carbonization of the as-obtained matrix has provided with  $\text{SiO}_2$ @silicon loaded CNF (SSCNF) sheets.  $\text{SiO}_2$  was removed by simple dipping SSCNF sheet in HF solution in contrast to tedious washing required by particulate structures as demonstrated previously. This simple washing step provides with SVCNF sheet that is mortared to achieve silicon anode using alginate as a binder. To date, carbons with high surface area and hierarchical porous structures can efficiently host sulfur via physical confinement. Moreover, the carbon bearing heteroatoms exhibit polar structures to chemically interact with the LiPS. In order to achieve a well-performing cathode material for the full cell, all-design characteristics have been integrated in present carbon matrices. For the purpose, ultra-porous hierarchical carbons with nitrogen and sulfur doping have

been synthesized via combining KOH activation and carbonization using polypyrrole and polythiophene. Sulfur has been infused into the carbon structure via melt infusion at 155°C. As synthesized carbon exhibited remarkably stable performance vs Li foil.

### 6.1.1 Balancing of anode and cathode

After realizing stable performances for both electrodes in half-cell configuration, it has been decided to replace metallic lithium with lithiated silicon anode to realize SLS full cell. For the purpose, both cathode and anode should be balanced in terms of areal capacities practically accomplished in half-cell testing. In full cell configuration, delithiation of Si anode is closely related to lithiation of sulfur cathodes. In other words, discharging of the sulfur cathode will follow the potential and capacity profile of Si anodes delithiation. Figure 6.1a,b show a comparison of SVCNF anode delithiation vs. PThio\_C/S & PPyr\_C/S cathodes discharging curves. Here, it is important to mention that anode is slightly overbalanced over sulfur cathodes because of initial irreversible loss of lithium owing to SEI formation. SVCNF anodes were electrochemically lithiated using EL-cell setup.

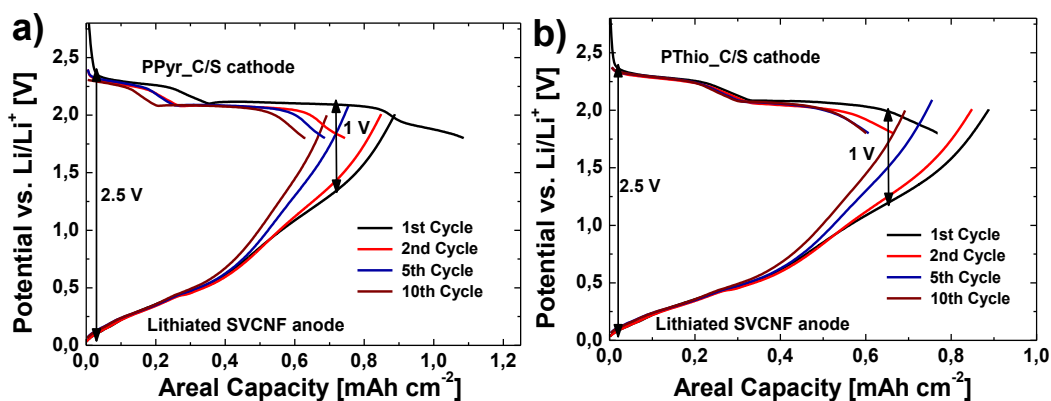


**Figure 6. 1:** Balancing of lithiated SVCNF anodes vs. PPyr\_C/S and PThio\_C/S cathodes in terms of areal capacity and estimation of cut-off voltage for full cells

### 6.1.2 Electrochemical Performance

For the purpose of lithiation of Si anodes, an ECC-STD electrochemical cell configuration (EL-Cell, GmbH) was employed. Lithiation of Si was carried out using a constant current-constant voltage (CCCV) protocol. Discharging of half-cell was carried out at 0.05C followed by holding voltage at 10 mV, then charging was performed at 0.05C till 2V and then 2nd and last discharging were carried out in a similar fashion as first. The  $\text{Li}_x\text{Si}$  anode was reclaimed from an EL cell set up in the glove box and used to assemble full cell against sulfur cathodes in coin cell configuration. The same electrolyte was employed in full cell around 20  $\mu\text{L}$  to ensure the wetting of all three components (i.e. sulfur cathode, Si anodes, and

separator). The full cells subjected to charge and discharge between 1.1 and 2.5 V at a current rate of  $225 \text{ mA g}^{-1}$  based on the mass of sulfur in cathodes. The full cell is balanced in order to have an additional  $\sim 20 \%$  extra areal capacity for the anode, which is far less than the excess of metal Li normally used to assemble Li/S cells. SLS full cell configuration (Figure 6.2a, b) clearly shows the improved cyclability and higher capacity for the PPy<sub>r</sub>\_C/S vs. PThio\_C/S, due to its higher conductivity and better capability to keep LiPS, as previously discussed. After 100 cycles, the cell still provides a specific charge capacity of  $390 \text{ mAh g}^{-1}$  that is almost 50 % of the initial charge capacity with CE of about 98 %. In both cells, the initial drop of CE can be related to imperfect passivation of the SEI layer on the Si anode in the standard electrolyte of Li/S cell [217]. As clearly seen (Figure 6.2c), the Si-C/S full cells display two discharge voltage plateaus at around 2.0 V and 1.7 V, in which the slope is rigorously related to the changes in the voltage profile of the Si anode (Figure 6.1a). With respect to Li-S/C half-cell, such shift of the discharge plateaus towards lower potentials is linked to the kinetics of delithiation at the Si anode. The initial discharge capacity of SLS cell ( $1000 \text{ mAh g}^{-1}$ ) is lower compared to the Li-S/C half-cell counterpart ( $1440 \text{ mAh g}^{-1}$ ) and from the 2nd to 100th cycle, the capacity retention is about 47.5% for SLS full cell against 63.5% of the half cell.

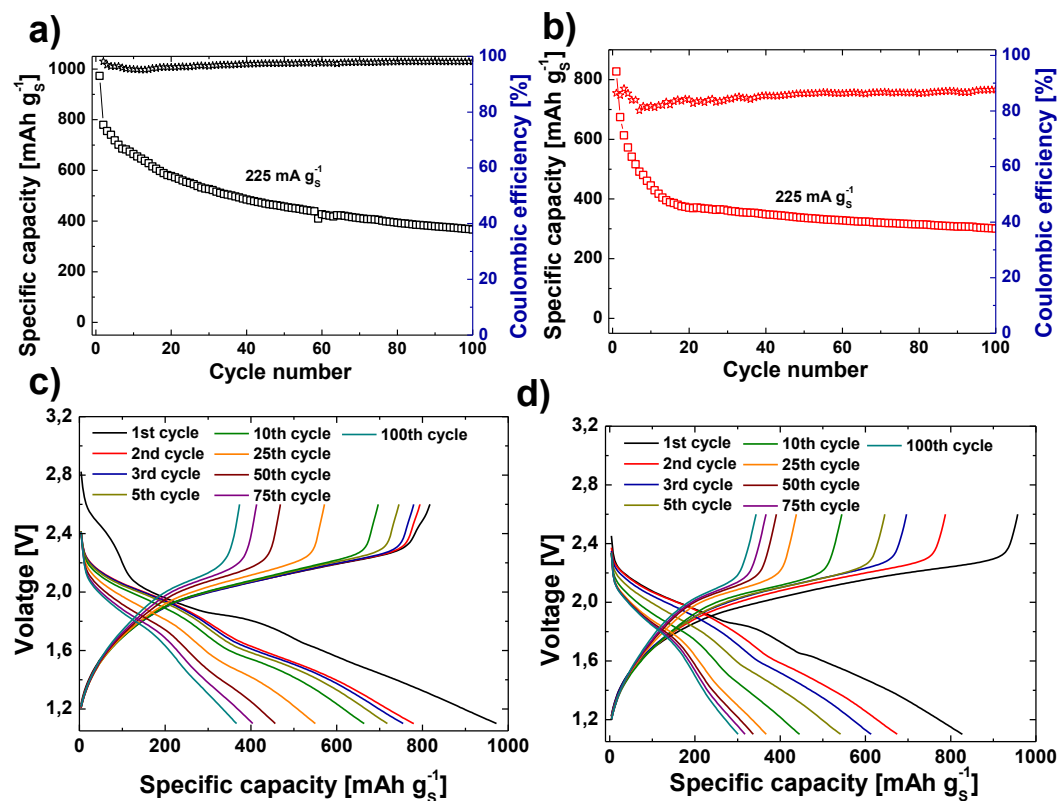


**Figure 6. 2:** a, c) Galvanostatic cycling performance and voltage vs. capacity profile of PPy<sub>r</sub>\_C/S cathode against lithiated SVCNF anode, b, d) Galvanostatic cycling performance and voltage vs. capacity profile of PThio\_C/S cathode against lithiated SVCNF anode

Such a setback in the electrochemical performance that is usually observed in Si-S full cells, must not be traced back to degradation phenomena of the electrodes. On the contrary, this mostly occurs because of the incomplete delithiation of Si anode that never reaches its fully delithiated state ( $\sim 1.0$  V vs.  $\text{Li/Li}^+$ ) in SLS full cells [218]. Till  $\sim 20$ th cycle executed at  $225 \text{ mA g}^{-1}$ , both cells exhibit a descent in specific capacities to  $550 \text{ mAh g}^{-1}$  in case of SVCNF\_PPy\_C/S and to  $380 \text{ mAh g}^{-1}$  for SVCNF\_PThio\_C/S. The electrolyte used for full cell study is not as appropriate as for Li/C-S cells. Presence of  $\text{LiNO}_3$  could initially augment the side reactions and let the LiPS to shuttle. This means that a portion of Li has been left inactive in form of side products by polysulfide oxidation, being the later reactions faster on higher surface area Si anode than on lithium [218, 219]. From that onwards, both cathodes reach stabilized performance, with CE approaching 99% in case of SVCNF\_PPy\_C/S. Such results validate our understanding that integration of PPy\_C/S with nitrogen polar groups can effectually relieve LiPS shuttling at the Si anode, enabling the cell to achieve stable cycling. Relying on these considerations and based on the excellent electrochemical performances of nano-Si/CNF anode vs. N/S doped C/S cathode, SLS full cell is able to deliver specific capacities not less than that of Si/S cells using structured elements prepared by more expensive and less scalable routes to date.

## 6.2 Conclusion

It has been demonstrated that lithiated silicon sulfur cell can be realized by choosing the rational design of electrodes architectures. We have architecture elemental doped hierarchical porous carbon as already presented in chapter 2 and Si nanoparticles comprised carbon nanofiber with void spaces as demonstrated in chapter 5. Then two electrodes were balanced in terms of areal capacity. Si anodes were lithiated and test against sulfur cathode. It is shown that these approaches can deliver very high specific capacity around  $800 \text{ mAh g}^{-1}$  with 50% capacity retention for more than 100 cycles of Galvanostatic charge and discharge. The whole system needs to be optimized for better electrolyte system for full cell configuration. However, it has been successfully demonstrated that lithiated silicon sulfur full cells can be realized by opting rational design of carbon matrices with high energy density and improved safety.

## Chapter 7

# Conclusion and Prospects

This dissertation initially speaks a comprehensive state of research in Li/S electrochemical system. The contributions of the scientific community and the dilemma still linked to Li/S technology has been discussed to balance our approach towards this line of research. Later on, we have presented a broad spectrum of experimental work to realize diverse sulfur host materials. All the approaches opted for this research work can be scaled up feasibly, and manufacturable. The stable silicon anodes have also been realized to reach Li metal free full Li/S cell. The whole system needs to be optimized for better electrolyte system for full cell configuration. However, it has been successfully demonstrated that lithiated silicon sulfur full cells can be realized with high energy density and improved safety. Established processes, those already been practiced by industry, have been exploited to produce effective cathode and anode materials and electrodes.

Two different kinds of carbon host materials have been synthesized. Microporous carbons have been produced from bio-based material to host sulfur for Li-S battery application. For the first time, it was successfully demonstrated that microporous carbons can be obtained from pyrolysis of polymer  $\beta$ -cyclodextrin and exhibited a spongy structure that makes them absorptive for sulfur. We have demonstrated that to make S and  $\text{Li}_2\text{S}$  available for the electrochemical process, it is necessary to provide a suitable conductive network by rGO wrapping the C/S composite. By using the proposed strategy, we are able to reach  $1108 \text{ mAh g}^{-1}$  at 0.01C and  $626 \text{ mAh g}^{-1}$  at 0.2C with a capacity loss of 0.11 % per cycle for more than 100 cycles. In another cell configuration using carbon paper as an interlayer, discharge capacity raised to  $850 \text{ mA h g}^{-1}$  at 0.2 C and maintained it for 100 cycles with excellent rate capability and high Coulombic efficiency. Dual layer cathode protection strategy could prove a step forward towards commercial Li/S batteries for EVs using MPCs.

In another strategy, elemental doped high surface area hierarchical porous carbons have been synthesized by the activation of polymers. As-prepared carbon with twice amount of infused sulfur exhibited remarkable electrochemical performance.

Nitrogen-doped hierarchical porous carbon from polypyrrole showed the specific capacity of  $990 \text{ mAh g}^{-1}$  with capacity decay rate about 0.07% for more than 300 cycles at 0.2C. Whereas, sulfur-doped hierarchical porous carbon demonstrated the specific capacity of around  $800 \text{ mAh g}^{-1}$  with capacity decay rate 0.09% for more than 300 cycles at 0.02C. Such a high capacity stable cathodes were realized because of high surface area, hierarchical porosity, and elemental doping. Elemental doping provides enough polarity to the matrix to interact with LiPS.

Three different approaches have been presented to prepare the inorganic metal compound incorporated carbon matrices. In the first approach, a facile production strategy has proposed to synthesize Magneli Phases  $\text{TiO}_2$  nanoparticles loaded carbon matrices as an efficient sulfur host material. As synthesized host material can effectively limit the dissolution and shuttling of LiPS by synergetic entrapment of carbon matrix and  $\text{Ti}_n\text{O}_{2n-1}$  nanoparticles to achieve extended cycling life. The porous carbon matrix serves to physically entrap sulfur and LiPS, while Magneli Phases  $\text{TiO}_2$  nanoparticles assist to chemically bind LiPS on their surface. The novel architecture of host material offers better capacity retention (i.e.) 65% and 54% at 0.2C and 1C for more than 500 and 1000 cycles respectively. Moreover, the intensive characterization of the synthesized host material and aged cathodes provides an insight that sulfur species are adsorbed by the surface of  $\text{Ti}_n\text{O}_{2n-1}$  nanoparticles along with conventional physical entrapment by carbon. The current strategy offers a facile and scalable manufacturing process to design an efficient host material for high-performance Li/S batteries.

In the second approach, various electrochemically deposited  $\text{MnO}_x$  carbon structures have been explored as high sulfur loaded freestanding cathodes. It has been successfully demonstrated that achieving the right phase of  $\text{MnO}_x$ , which can interact with LiPS. It is possible to achieve high performing stable electrochemical performance even at high loading of sulfur. The role of carbon substrate is twofold; first, it is acting as a support to carry sulfur and  $\text{MnO}_x$  deposits, secondly, it acts as a matrix that physically traps LiPS. It has been established that the  $\text{Mn}_3\text{O}_4$  phase can better interact with LiPS, thus showed higher specific capacity values and better stabilities.

In the third strategy, vanadium nitride in nitrogen-doped carbon matrix has been produced via in-situ ammonization and carbonization. VNNC showed very strong interaction with the LiPS. High rate capability is reported for sulfur cathodes assembled with this VNNC. Very stable performance has been recorded for hundreds of cycles at various C rates. Both nitrogen-doped carbon and VN has imparted conductivity and ability to interact with LiPS. Cells assembled with VNNC/S cathode has been cycled at 0.2C showed first cycle capacity about  $1013 \text{ mAh g}^{-1}$ . Even after 200 cycles, the capacity retention was 64 % that is  $630 \text{ mAh g}^{-1}$ . Interestingly at higher C-rates, VNNC/S cathodes exhibited even better stabilities.

In chapter 4, a practical inadequacy of previous reports has been addressed where chloride-ion doped polyaniline had been proposed to limit LiPS solubility. We

offered an alternative and better solution by accomplishing formate-ion doped polyaniline wrapped carbon/sulfur composite by in-situ oxidative polymerization. The as-prepared cathodes exhibited very stable performance around 800 mAh g<sup>-1</sup> for more than 500 cycles at 0.2C with capacity fading rate around 0.024%. Rate capability performance of the PANi wrapped C/S composite is remarkably better than that of the bare composite.

In chapter 5, two altogether different approaches have been presented to realize stable silicon anodes. In the first strategy, electrospun silicon nanoparticles loaded carbon nanofibers have been produced via electrospinning and carbonization process. Simple HF washing of Si nanoparticle loaded CNF mats has induced void structures to accommodate the volume changes during lithiation and delithiation process. A novel binder system (CA crosslinked alginate network) has been achieved by iteration of various binder systems. As prepared anodes showed stable electrochemical performances in the ether-based electrolyte. nSi@void@CNF anodes have delivered specific capacity value close to the theoretical value of Si and even after 100 cycle anodes exhibited a stable capacity of 2500 mAh g<sup>-1</sup> basis on Si. While based on the mass of total composite the stabilized capacity value was around 500 mAh g<sup>-1</sup> after 100 cycles at 0.2C. So, all-design integrated strategy enables to realize such a remarkable performance from Si anodes.

While in the second strategy, a simple approach is opted to reach well performing Si anodes. All in shelves chemicals have been integrated into working Si anodes. Commercial nano-Si has been mixed with commercially available PEDOT:PSS electroactive polymer suspensions both as conductive and binding network with or without other conductive additives like CNT and rGO. With different types of electrolyte systems, as-prepared anodes exhibited some promising electrochemical performances. Si anode with CNT and PEDOT:PSS exhibited specific 2500 mAh g<sup>-1</sup> at 0.1C and around 2000 mAh g<sup>-1</sup> at 0.2C in ether-based electrolyte system with 50% Si on the basis of spread material. After 100 cycles of charge and discharge, as-obtained anodes showed more than 70% capacity retention of the initial. It is determined that conductive additive, separator, electrolyte, and mass loading have a nominal effect on capacity and cycling stability. These anodes have to be incorporated in full cell configuration to study Li/S full cell.

In the last chapter, it has been demonstrated that lithiated silicon sulfur cell can be realized by choosing the rational design of electrodes architectures. We have architecture elemental doped hierarchical porous carbon as already presented in chapter 2 and Si nanoparticles comprised carbon nanofiber with void spaces as demonstrated in chapter 5. Then two electrodes were balanced in terms of areal capacity. Si anode was lithiated and test against sulfur cathode. It is shown that these approaches can deliver very high specific capacity around 800 mAh g<sup>-1</sup> with 50% capacity retention for more than 100 cycles of Galvanostatic charge and discharge tests. In short, the following three tables present the performance matrices of the electrode materials prepared during the Ph.D. research of this dissertation.

**Table 7. 1:** Performance matrix of as-prepared S cathodes architecture, sulfur content and loading, and cycling performance

Category	Cathode materials	Sulfur content (wt%) / sulfur loading	Electrolyte to sulfur ratio	Electrochemical performance [initial/final (mAh g <sup>-1</sup> s) (C-rate, cycles)]
Carbon	Microporous carbons form $\beta$ -cyclodextrin nanosponges	60/2 mg cm <sup>-2</sup>	15 $\mu$ L/mg <sub>s</sub>	1103/ 483 (0.2C, 100) GF 1108/ 723 (0.2C, 100) CFP
	Hierarchical porous nitrogen/ sulfur doped carbons	66/1.5-2.2 mg cm <sup>-2</sup>	10 $\mu$ L/mg <sub>s</sub>	1100/ 762 (0.2C, 250) N-doped C 800/ 631 (0.2C, 250) S-doped C
Inorganics	Magnèli phase Ti <sub>n</sub> O <sub>2n-1</sub> incorporated carbon matrix	60/ 2-2.3 mg cm <sup>-2</sup>	6-7 $\mu$ L/mg <sub>s</sub>	1100/ 550 (0.2C, 500) 700/ 318 (1C, 1000)
	Vanadium nitride decorated nitrogen doped carbon	70/ 1.5 mg cm <sup>-2</sup>	10 $\mu$ L/mg <sub>s</sub>	1013/ 630 (0.2C, 200) 814/ 530 (0.5C, 1200)
	Electrochemically MnO <sub>x</sub> deposited carbon structures	50/ 5 mg cm <sup>-2</sup>	8 $\mu$ L/mg <sub>s</sub>	800/ 770 (0.2C, 200) 750/ 660 (0.2C, 200)
Polymer	Formate-ion doped polyaniline wrapped carbon/sulfur	55/ 2 mg cm <sup>-2</sup>	7-8 $\mu$ L/mg <sub>s</sub>	896/ 655 (0.2C, 500)

**Table 7. 2:** Performance matrix of as-prepared Si anodes architecture, sulfur content and loading, and cycling performance

	Anode materials	Si content (wt%) / Si loading	Electrochemical performance [initial/final (mAh g <sup>-1</sup> ) (C-rate, cycles)]
Carbon	SiNP hosted in carbon nanofibers with void structures	18/ 0.4 mg cm <sup>-2</sup>	3800/ 2200 (0.2C, 100) on Si wt% 3600/ 2000 (0.5C, 200) on Si wt%
Polymer	nSi/CNT/PEDOT:PSS composite anodes	50/ 0.2-0.8 mg cm <sup>-2</sup>	2300/ 1500 (0.2C, 100) on Si wt%

**Table 7. 3:** Performance matrix of Li metal free full cell realized using carbon matrices

	Cathode materials	Anode materials	Electrochemical performance [initial/final (mAh g <sup>-1</sup> s) (C-rate, cycles)]
Carbon	Hierarchical porous nitrogen/ sulfur doped carbons	SiNP hosted in carbon nanofibers with void structures	800/ 410 (0.2C, 100)

# References

1. Dunn, B., H. Kamath, and J.-M. Tarascon, *Electrical Energy Storage for the Grid: A Battery of Choices*. Science, 2011. **334**(6058): p. 928-935.
2. Tian, H., et al., *High capacity group-IV elements (Si, Ge, Sn) based anodes for lithium-ion batteries*. Journal of Materiomics, 2015. **1**(3): p. 153-169.
3. Ohzuku, T., A. Ueda, and N. Yamamoto, *Zero-Strain Insertion Material of  $\text{Li}[\text{Li}1/3\text{Ti}5/3]\text{O}_4$  for Rechargeable Lithium Cells*. Journal of The Electrochemical Society, 1995. **142**(5): p. 1431-1435.
4. Tarascon, J.M. and M. Armand, *Issues and challenges facing rechargeable lithium batteries*. Nature, 2001. **414**: p. 359.
5. Laure Monconduit, L.C., Rémi Dedryvère, *Electrodes for Li-ion Batteries: Materials, Mechanisms and Performance*. 2015, Wiley-ISTE. p. 100.
6. Wu, Y., *Lithium-Ion Batteries: Fundamentals and Applications*. Electrochemical Energy Storage and Conversion. 2015: CRC Press.
7. Bruce, P.G., et al., *Li-O<sub>2</sub> and Li-S batteries with high energy storage*. Nature Materials, 2011. **11**: p. 19.
8. Nam-Soon, C., et al., *Challenges Facing Lithium Batteries and Electrical Double-Layer Capacitors*. Angewandte Chemie International Edition, 2012. **51**(40): p. 9994-10024.
9. Ji, X., et al., *Stabilizing lithium-sulphur cathodes using polysulphide reservoirs*. Nature Communications, 2011. **2**: p. 325.
10. Manthiram, A., et al., *Rechargeable Lithium-Sulfur Batteries*. Chemical Reviews, 2014. **114**(23): p. 11751-11787.
11. Busche, M.R., et al., *Systematical electrochemical study on the parasitic shuttle-effect in lithium-sulfur-cells at different temperatures and different rates*. Journal of Power Sources, 2014. **259**: p. 289-299.
12. Kim, H., et al., *Metallic anodes for next generation secondary batteries*. Chem Soc Rev, 2013. **42**(23): p. 9011-34.
13. Ruiguo, C., et al., *Anodes for Rechargeable Lithium-Sulfur Batteries*. Advanced Energy Materials, 2015. **5**(16): p. 1402273.
14. Ashuri, M., Q. He, and L.L. Shaw, *Silicon as a potential anode material for Li-ion batteries: where size, geometry and structure matter*. Nanoscale, 2016. **8**(1): p. 74-103.
15. Barchasz, C., et al., *Revisiting TEGDME/DIOX Binary Electrolytes for Lithium/Sulfur Batteries: Importance of Solvation Ability and Additives*. Journal of The Electrochemical Society, 2013. **160**(3): p. A430-A436.
16. Choi, J.-W., et al., *Rechargeable lithium/sulfur battery with suitable mixed liquid electrolytes*. Electrochimica Acta, 2007. **52**(5): p. 2075-2082.
17. Barchasz, C., et al., *Electrochemical properties of ether-based electrolytes for lithium/sulfur rechargeable batteries*. Electrochimica Acta, 2013. **89**: p. 737-743.
18. Kolosnitsyn, V.S., et al., *Cycling a Sulfur Electrode in Electrolytes Based on Sulfolane and Linear Ethers (Glymes) in an  $\text{LiCF}_3\text{SO}_3$  Solution*. Russian Journal of Electrochemistry, 2002. **38**(12): p. 1360-1363.
19. Zhang, S.S., *Role of  $\text{LiNO}_3$  in rechargeable lithium/sulfur battery*. Electrochimica Acta, 2012. **70**: p. 344-348.

20. Zhang, S.S., *Effect of Discharge Cutoff Voltage on Reversibility of Lithium/Sulfur Batteries with LiNO<sub>3</sub>-Contained Electrolyte*. Journal of The Electrochemical Society, 2012. **159**(7): p. A920-A923.
21. Diao, Y., et al., *Shuttle phenomenon – The irreversible oxidation mechanism of sulfur active material in Li–S battery*. Journal of Power Sources, 2013. **235**: p. 181-186.
22. Yim, T., et al., *Effect of chemical reactivity of polysulfide toward carbonate-based electrolyte on the electrochemical performance of Li–S batteries*. Electrochimica Acta, 2013. **107**: p. 454-460.
23. Zheng, S., et al., *High performance C/S composite cathodes with conventional carbonate-based electrolytes in Li-S battery*. Sci Rep, 2014. **4**: p. 4842.
24. Kolosnitsyn, V., E. Kuzmina, and E. Karaseva, *Influence of Lithium Salts on Physicochemical Properties of Lithium Polysulphide Solutions in Sulfolane*. ECS Transactions, 2009. **19**(25): p. 25-30.
25. Yamin, H., et al., *Lithium Sulfur Battery: Oxidation/Reduction Mechanisms of Polysulfides in THF Solutions*. Journal of The Electrochemical Society, 1988. **135**(5): p. 1045-1048.
26. Ding, N., et al., *Key parameters in design of lithium sulfur batteries*. Journal of Power Sources, 2014. **269**: p. 111-116.
27. Wang, C., et al., *Slurryless Li<sub>2</sub>S/reduced graphene oxide cathode paper for high-performance lithium sulfur battery*. Nano Lett, 2015. **15**(3): p. 1796-802.
28. Meng, Z., et al., *Graphene-like g-C<sub>3</sub>N<sub>4</sub> nanosheets/sulfur as cathode for lithium–sulfur battery*. Electrochimica Acta, 2016. **210**: p. 829-836.
29. Gu, X. and C. Lai, *Recent development of metal compound applications in lithium–sulphur batteries*. Journal of Materials Research, 2017. **33**(1): p. 16-31.
30. Xiao, L., et al., *Tuning Transition Metal Oxide–Sulfur Interactions for Long Life Lithium Sulfur Batteries: The “Goldilocks” Principle*. Advanced Energy Materials, 2016. **6**(6): p. 1501636.
31. Borchardt, L., M. Oschatz, and S. Kaskel, *Carbon Materials for Lithium Sulfur Batteries-Ten Critical Questions*. Chemistry, 2016. **22**(22): p. 7324-51.
32. Ji, X., K.T. Lee, and L.F. Nazar, *A highly ordered nanostructured carbon–sulphur cathode for lithium–sulphur batteries*. Nature Materials, 2009. **8**: p. 500.
33. Zheng, J., et al., *Revisit Carbon/Sulfur Composite for Li-S Batteries*. Journal of The Electrochemical Society, 2013. **160**(10): p. A1624-A1628.
34. Zhen, L., et al., *Insight into the Electrode Mechanism in Lithium-Sulfur Batteries with Ordered Microporous Carbon Confined Sulfur as the Cathode*. Advanced Energy Materials, 2014. **4**(7): p. 1301473.
35. Bing, D., et al., *Encapsulating Sulfur into Hierarchically Ordered Porous Carbon as a High-Performance Cathode for Lithium–Sulfur Batteries*. Chemistry – A European Journal, 2013. **19**(3): p. 1013-1019.
36. Li, X., et al., *Tailoring interactions of carbon and sulfur in Li-S battery cathodes: significant effects of carbon-heteroatom bonds*. Journal of Materials Chemistry A, 2014. **2**(32): p. 12866-12872.
37. Ji, L., et al., *Porous carbon nanofiber-sulfur composite electrodes for lithium/sulfur cells*. Energy & Environmental Science, 2011. **4**(12): p. 5053-5059.

38. Zheng, G., et al., *Amphiphilic surface modification of hollow carbon nanofibers for improved cycle life of lithium sulfur batteries*. Nano Lett, 2013. **13**(3): p. 1265-70.
39. Lu, S., et al., *Significantly Improved Long-Cycle Stability in High-Rate Li-S Batteries Enabled by Coaxial Graphene Wrapping over Sulfur-Coated Carbon Nanofibers*. Nano Letters, 2013. **13**(6): p. 2485-2489.
40. Dorfler, S., et al., *High capacity vertical aligned carbon nanotube/sulfur composite cathodes for lithium-sulfur batteries*. Chem Commun (Camb), 2012. **48**(34): p. 4097-9.
41. Guo, J., Y. Xu, and C. Wang, *Sulfur-Impregnated Disordered Carbon Nanotubes Cathode for Lithium-Sulfur Batteries*. Nano Letters, 2011. **11**(10): p. 4288-4294.
42. Cheng, X.-B., et al., *Aligned carbon nanotube/sulfur composite cathodes with high sulfur content for lithium-sulfur batteries*. Nano Energy, 2014. **4**: p. 65-72.
43. Xu, H., et al., *Graphene-encapsulated sulfur (GES) composites with a core-shell structure as superior cathode materials for lithium-sulfur batteries*. Journal of Materials Chemistry A, 2013. **1**(47): p. 15142-15149.
44. Rong, J., et al., *Solution Ionic Strength Engineering As a Generic Strategy to Coat Graphene Oxide (GO) on Various Functional Particles and Its Application in High-Performance Lithium-Sulfur (Li-S) Batteries*. Nano Letters, 2014. **14**(2): p. 473-479.
45. Zhao, M.-Q., et al., *Unstacked double-layer templated graphene for high-rate lithium-sulphur batteries*. Nature Communications, 2014. **5**: p. 3410.
46. Qiu, Y., et al., *High-rate, ultralong cycle-life lithium/sulfur batteries enabled by nitrogen-doped graphene*. Nano Lett, 2014. **14**(8): p. 4821-7.
47. Guangjian, H., et al., *3D Graphene-Foam-Reduced-Graphene-Oxide Hybrid Nested Hierarchical Networks for High-Performance Li-S Batteries*. Advanced Materials, 2016. **28**(8): p. 1603-1609.
48. Zhiwei, Z., et al., *3D Interconnected Porous Carbon Aerogels as Sulfur Immobilizers for Sulfur Impregnation for Lithium-Sulfur Batteries with High Rate Capability and Cycling Stability*. Advanced Functional Materials, 2014. **24**(17): p. 2500-2509.
49. Xin, F., et al., *A Cable-Shaped Lithium Sulfur Battery*. Advanced Materials, 2016. **28**(3): p. 491-496.
50. Hong, X., et al., *A rGO-CNT aerogel covalently bonded with a nitrogen-rich polymer as a polysulfide adsorptive cathode for high sulfur loading lithium sulfur batteries*. Journal of Materials Chemistry A, 2017. **5**(28): p. 14775-14782.
51. Li, W., et al., *Understanding the role of different conductive polymers in improving the nanostructured sulfur cathode performance*. Nano Lett, 2013. **13**(11): p. 5534-40.
52. Zhou, W., et al., *Yolk-Shell Structure of Polyaniline-Coated Sulfur for Lithium-Sulfur Batteries*. Journal of the American Chemical Society, 2013. **135**(44): p. 16736-16743.
53. Peiming, X., et al., *Facile Synthesis of Sulfur-Polypyrrole as Cathodes for Lithium-Sulfur Batteries*. ChemElectroChem, 2017. **4**(1): p. 115-121.
54. Ma, G., et al., *Enhanced performance of lithium sulfur battery with polypyrrole warped mesoporous carbon/sulfur composite*. Journal of Power Sources, 2014. **254**: p. 353-359.

55. Fu, Y. and A. Manthiram, *Core-shell structured sulfur-polypyrrole composite cathodes for lithium-sulfur batteries*. RSC Advances, 2012. **2**(14): p. 5927-5929.
56. Yang, Y., et al., *Improving the Performance of Lithium–Sulfur Batteries by Conductive Polymer Coating*. ACS Nano, 2011. **5**(11): p. 9187-9193.
57. Chen, H., et al., *Ultrafine sulfur nanoparticles in conducting polymer shell as cathode materials for high performance lithium/sulfur batteries*. Sci Rep, 2013. **3**: p. 1910.
58. Wu, F., et al., *Sulfur/Polythiophene with a Core/Shell Structure: Synthesis and Electrochemical Properties of the Cathode for Rechargeable Lithium Batteries*. The Journal of Physical Chemistry C, 2011. **115**(13): p. 6057-6063.
59. J., W., et al., *A Novel Conductive Polymer–Sulfur Composite Cathode Material for Rechargeable Lithium Batteries*. Advanced Materials, 2002. **14**(13-14): p. 963-965.
60. Fang, X. and H. Peng, *A revolution in electrodes: recent progress in rechargeable lithium-sulfur batteries*. Small, 2015. **11**(13): p. 1488-511.
61. Ma, G., et al., *Hollow polyaniline sphere@sulfur composites for prolonged cycling stability of lithium-sulfur batteries*. Journal of Materials Chemistry A, 2014. **2**(27): p. 10350-10354.
62. Liang, X., et al., *A highly efficient polysulfide mediator for lithium–sulfur batteries*. Nature Communications, 2015. **6**: p. 5682.
63. Tao, X., et al., *Strong sulfur binding with conducting Magneli-phase  $Ti(n)O_2(n-1)$  nanomaterials for improving lithium-sulfur batteries*. Nano Lett, 2014. **14**(9): p. 5288-94.
64. Xiao, Z., et al., *Highly Conductive Porous Transition Metal Dichalcogenides via Water Steam Etching for High-Performance Lithium-Sulfur Batteries*. ACS Appl Mater Interfaces, 2017. **9**(22): p. 18845-18855.
65. Seh, Z.W., et al., *Two-dimensional layered transition metal disulfides for effective encapsulation of high-capacity lithium sulphide cathodes*. Nat Commun, 2014. **5**: p. 5017.
66. Chen, T., et al., *Metallic and polar  $Co_9S_8$  inlaid carbon hollow nanopolyhedra as efficient polysulfide mediator for lithium–sulfur batteries*. Nano Energy, 2017. **38**: p. 239-248.
67. Lin, H., et al., *Electrocatalysis of polysulfide conversion by sulfur-deficient  $MoS_2$  nanoflakes for lithium-sulfur batteries*. Energy & Environmental Science, 2017. **10**(6): p. 1476-1486.
68. Liang, X., A. Garsuch, and L.F. Nazar, *Sulfur cathodes based on conductive MXene nanosheets for high-performance lithium-sulfur batteries*. Angew Chem Int Ed Engl, 2015. **54**(13): p. 3907-11.
69. Liang, X., et al., *Interwoven MXene Nanosheet/Carbon-Nanotube Composites as Li-S Cathode Hosts*. Adv Mater, 2017. **29**(3).
70. Hao, Z., et al., *TiN as a simple and efficient polysulfide immobilizer for lithium-sulfur batteries*. Journal of Materials Chemistry A, 2016. **4**(45): p. 17711-17717.
71. Sun, Z., et al., *Conductive porous vanadium nitride/graphene composite as chemical anchor of polysulfides for lithium-sulfur batteries*. Nat Commun, 2017. **8**: p. 14627.
72. Yuan, H., et al., *Efficient Activation of  $Li_2S$  by Transition Metal Phosphides Nanoparticles for Highly Stable Lithium–Sulfur Batteries*. ACS Energy Letters, 2017. **2**(7): p. 1711-1719.

73. Zhong, Y., et al., *Surface Chemistry in Cobalt Phosphide-Stabilized Lithium-Sulfur Batteries*. J Am Chem Soc, 2018. **140**(4): p. 1455-1459.
74. Hong, X.J., et al., *Confinement of polysulfides within bi-functional metal-organic frameworks for high performance lithium-sulfur batteries*. Nanoscale, 2018. **10**(6): p. 2774-2780.
75. Ma, G., et al., *Enhanced performance of lithium sulfur battery with self-assembly polypyrrole nanotube film as the functional interlayer*. Journal of Power Sources, 2015. **273**: p. 511-516.
76. Wang, X., et al., *High-Rate and Long-Term Cycle Stability of Li-S Batteries Enabled by Li<sub>2</sub>S/TiO<sub>2</sub>-Impregnated Hollow Carbon Nanofiber Cathodes*. ACS Applied Materials & Interfaces, 2018. **10**(19): p. 16552-16560.
77. Pang, Q., et al., *Surface-enhanced redox chemistry of polysulphides on a metallic and polar host for lithium-sulphur batteries*. Nat Commun, 2014. **5**: p. 4759.
78. Li, Z., J. Zhang, and X.W. Lou, *Hollow Carbon Nanofibers Filled with MnO<sub>2</sub> Nanosheets as Efficient Sulfur Hosts for Lithium-Sulfur Batteries*. Angew Chem Int Ed Engl, 2015. **54**(44): p. 12886-90.
79. Tao, Y., et al., *Kinetically-enhanced polysulfide redox reactions by Nb<sub>2</sub>O<sub>5</sub> nanocrystals for high-rate lithium-sulfur battery*. Energy & Environmental Science, 2016. **9**(10): p. 3230-3239.
80. Tang, R., et al., *An ultrafine V<sub>2</sub>O<sub>3</sub> modified hierarchical porous carbon microsphere as a high performance cathode matrix for lithium-sulfur batteries*. RSC Advances, 2016. **6**(69): p. 65162-65170.
81. Arumugam, M., C. Sheng-Heng, and Z. Chenxi, *Lithium-Sulfur Batteries: Progress and Prospects*. Advanced Materials, 2015. **27**(12): p. 1980-2006.
82. Su, Y.-S. and A. Manthiram, *Lithium-sulphur batteries with a microporous carbon paper as a bifunctional interlayer*. Nature Communications, 2012. **3**: p. 1166.
83. Su, Y.S. and A. Manthiram, *A new approach to improve cycle performance of rechargeable lithium-sulfur batteries by inserting a free-standing MWCNT interlayer*. Chem Commun (Camb), 2012. **48**(70): p. 8817-9.
84. Choi, S., et al., *Multifunctional Free-Standing Gel Polymer Electrolyte with Carbon Nanofiber Interlayers for High-Performance Lithium-Sulfur Batteries*. Chem Asian J, 2017. **12**(13): p. 1470-1474.
85. Zu, C., et al., *Improved lithium-sulfur cells with a treated carbon paper interlayer*. Phys Chem Chem Phys, 2013. **15**(7): p. 2291-7.
86. Huang, J.-Q., et al., *Permselective Graphene Oxide Membrane for Highly Stable and Anti-Self-Discharge Lithium-Sulfur Batteries*. ACS Nano, 2015. **9**(3): p. 3002-3011.
87. Wu, F., et al., *A polypyrrole-supported carbon paper acting as a polysulfide trap for lithium-sulfur batteries*. RSC Advances, 2015. **5**(114): p. 94479-94485.
88. Han, X., et al., *Reactivation of dissolved polysulfides in Li-S batteries based on atomic layer deposition of Al<sub>2</sub>O<sub>3</sub> in nanoporous carbon cloth*. Nano Energy, 2013. **2**(6): p. 1197-1206.
89. Liang, G., et al., *Ultrafine TiO<sub>2</sub> Decorated Carbon Nanofibers as Multifunctional Interlayer for High-Performance Lithium-Sulfur Battery*. ACS Applied Materials & Interfaces, 2016. **8**(35): p. 23105-23113.
90. Yao, H., et al., *Improved lithium-sulfur batteries with a conductive coating on the separator to prevent the accumulation of inactive S-related species*

- at the cathode-separator interface. *Energy & Environmental Science*, 2014. **7**(10): p. 3381-3390.
91. Juan, B., et al., *Functional Mesoporous Carbon-Coated Separator for Long-Life, High-Energy Lithium–Sulfur Batteries*. *Advanced Functional Materials*, 2015. **25**(33): p. 5285-5291.
  92. Gu, X., et al., *A porous nitrogen and phosphorous dual doped graphene blocking layer for high performance Li-S batteries*. *Journal of Materials Chemistry A*, 2015. **3**(32): p. 16670-16678.
  93. Lu, Y., et al., *Sulfonic Groups Originated Dual-Functional Interlayer for High Performance Lithium–Sulfur Battery*. *ACS Applied Materials & Interfaces*, 2017. **9**(17): p. 14878-14888.
  94. Chung, S.H., P. Han, and A. Manthiram, *A Polysulfide-Trapping Interface for Electrochemically Stable Sulfur Cathode Development*. *ACS Appl Mater Interfaces*, 2016. **8**(7): p. 4709-17.
  95. Fan, C.-Y., et al., *The Effective Design of a Polysulfide-Trapped Separator at the Molecular Level for High Energy Density Li–S Batteries*. *ACS Applied Materials & Interfaces*, 2016. **8**(25): p. 16108-16115.
  96. Song, R., et al., *A trilayer separator with dual function for high performance lithium–sulfur batteries*. *Journal of Power Sources*, 2016. **301**: p. 179-186.
  97. Li, W., et al., *V2O5 Polysulfide Anion Barrier for Long-Lived Li–S Batteries*. *Chemistry of Materials*, 2014. **26**(11): p. 3403-3410.
  98. Ye, F., et al., *Functionalized Boron Nitride Nanosheets/Graphene Interlayer for Fast and Long-Life Lithium–Sulfur Batteries*. *Advanced Energy Materials*, 2017. **7**(13): p. 1602380.
  99. Ting-Zhou, Z., et al., *Rational Integration of Polypropylene/Graphene Oxide/Nafion as Ternary-Layered Separator to Retard the Shuttle of Polysulfides for Lithium–Sulfur Batteries*. *Small*, 2016. **12**(3): p. 381-389.
  100. Fan, C.Y., et al., *The Effective Design of a Polysulfide-Trapped Separator at the Molecular Level for High Energy Density Li-S Batteries*. *ACS Appl Mater Interfaces*, 2016. **8**(25): p. 16108-15.
  101. Drvarič Talian, S., et al., *Fluorinated Ether Based Electrolyte for High-Energy Lithium–Sulfur Batteries: Li+ Solvation Role Behind Reduced Polysulfide Solubility*. *Chemistry of Materials*, 2017. **29**(23): p. 10037-10044.
  102. Chen, S., et al., *A Fluorinated Ether Electrolyte Enabled High Performance Prelithiated Graphite/Sulfur Batteries*. *ACS Appl Mater Interfaces*, 2017. **9**(8): p. 6959-6966.
  103. Drvarič Talian, S., M. Bešter-Rogač, and R. Dominko, *The physicochemical properties of a [DEME][TFSI] ionic liquid-based electrolyte and their influence on the performance of lithium–sulfur batteries*. *Electrochimica Acta*, 2017. **252**: p. 147-153.
  104. Junzheng, C., et al., *Restricting the Solubility of Polysulfides in Li-S Batteries Via Electrolyte Salt Selection*. *Advanced Energy Materials*, 2016. **6**(11): p. 1600160.
  105. Chen, S., et al., *Exceptional electrochemical performance of rechargeable Li-S batteries with a polysulfide-containing electrolyte*. *RSC Advances*, 2013. **3**(11): p. 3540-3543.
  106. Shuru, C., et al., *Functional Organosulfide Electrolyte Promotes an Alternate Reaction Pathway to Achieve High Performance in Lithium–Sulfur Batteries*. *Angewandte Chemie International Edition*, 2016. **55**(13): p. 4231-4235.

107. Cuisinier, M., et al., *Unique behaviour of nonsolvents for polysulphides in lithium-sulphur batteries*. Energy & Environmental Science, 2014. **7**(8): p. 2697-2705.
108. Lee, C.-W., et al., *Directing the Lithium–Sulfur Reaction Pathway via Sparingly Solvating Electrolytes for High Energy Density Batteries*. ACS Central Science, 2017. **3**(6): p. 605-613.
109. Abhinandan, S., et al., *Inhibiting Polysulfide Shuttle in Lithium–Sulfur Batteries through Low-Ion-Pairing Salts and a Triflamide Solvent*. Angewandte Chemie International Edition, 2017. **56**(22): p. 6192-6197.
110. Nagao, M., A. Hayashi, and M. Tatsumisago, *Sulfur–carbon composite electrode for all-solid-state Li/S battery with Li<sub>2</sub>S–P<sub>2</sub>S<sub>5</sub> solid electrolyte*. Electrochimica Acta, 2011. **56**(17): p. 6055-6059.
111. Xu, R.-c., et al., *All-solid-state lithium-sulfur batteries based on a newly designed Li<sub>7</sub>P<sub>2.9</sub>Mn<sub>0.1</sub>S<sub>10.7</sub>I<sub>0.3</sub> superionic conductor*. Journal of Materials Chemistry A, 2017. **5**(13): p. 6310-6317.
112. Cheon, S.-E., et al., *Structural Factors of Sulfur Cathodes with Poly(ethylene oxide) Binder for Performance of Rechargeable Lithium Sulfur Batteries*. Journal of The Electrochemical Society, 2002. **149**(11): p. A1437-A1441.
113. Zhang, Z., et al., *Water-Soluble Polyacrylic Acid as a Binder for Sulfur Cathode in Lithium-Sulfur Battery*. ECS Electrochemistry Letters, 2012. **1**(2): p. A34-A37.
114. Zhang, L., et al., *Effective electrostatic confinement of polysulfides in lithium/sulfur batteries by a functional binder*. Nano Energy, 2017. **40**: p. 559-565.
115. Wei, C., et al., *A New Hydrophilic Binder Enabling Strongly Anchoring Polysulfides for High-Performance Sulfur Electrodes in Lithium-Sulfur Battery*. Advanced Energy Materials, 2018. **8**(12): p. 1702889.
116. Hwa, Y. and E.J. Cairns, *Polymeric binders for the sulfur electrode compatible with ionic liquid containing electrolytes*. Electrochimica Acta, 2018. **271**: p. 103-109.
117. Li, L., et al., *Molecular understanding of polyelectrolyte binders that actively regulate ion transport in sulfur cathodes*. Nat Commun, 2017. **8**(1): p. 2277.
118. Yang, Z., R. Li, and Z. Deng, *Polyelectrolyte Binder for Sulfur Cathode To Improve the Cycle Performance and Discharge Property of Lithium-Sulfur Battery*. ACS Appl Mater Interfaces, 2018. **10**(16): p. 13519-13527.
119. Zhou, G., et al., *An Aqueous Inorganic Polymer Binder for High Performance Lithium–Sulfur Batteries with Flame-Retardant Properties*. ACS Central Science, 2018: p. Medium: ED; Size: p. 260-267.
120. Li, Y., et al., *Carboxymethyl cellulose binders enable high-rate capability of sulfurized polyacrylonitrile cathodes for Li-S batteries*. Journal of Materials Chemistry A, 2017. **5**(11): p. 5460-5465.
121. Chen, Y., et al., *Chitosan as a functional additive for high-performance lithium-sulfur batteries*. Journal of Materials Chemistry A, 2015. **3**(29): p. 15235-15240.
122. Zhang, W., et al., *Influence of pH of Gelatin Solution on Cycle Performance of the Sulfur Cathode*. Journal of The Electrochemical Society, 2010. **157**(4): p. A443-A446.

123. Bao, W., et al., *Enhanced cyclability of sulfur cathodes in lithium-sulfur batteries with Na-alginate as a binder*. Journal of Energy Chemistry, 2013. **22**(5): p. 790-794.
124. Chen, W., et al., *A New Type of Multifunctional Polar Binder: Toward Practical Application of High Energy Lithium Sulfur Batteries*. Adv Mater, 2017. **29**(12).
125. Ding, F., et al., *Dendrite-Free Lithium Deposition via Self-Healing Electrostatic Shield Mechanism*. Journal of the American Chemical Society, 2013. **135**(11): p. 4450-4456.
126. Yang, C.-P., et al., *Accommodating lithium into 3D current collectors with a submicron skeleton towards long-life lithium metal anodes*. Nature Communications, 2015. **6**: p. 8058.
127. Lin, D., et al., *Layered reduced graphene oxide with nanoscale interlayer gaps as a stable host for lithium metal anodes*. Nature Nanotechnology, 2016. **11**: p. 626.
128. Zhao, J., et al., *Air-stable and freestanding lithium alloy/graphene foil as an alternative to lithium metal anodes*. Nat Nanotechnol, 2017. **12**(10): p. 993-999.
129. Rui, Z., et al., *Conductive Nanostructured Scaffolds Render Low Local Current Density to Inhibit Lithium Dendrite Growth*. Advanced Materials, 2016. **28**(11): p. 2155-2162.
130. Karkar, Z., et al., *Threshold-like dependence of silicon-based electrode performance on active mass loading and nature of carbon conductive additive*. Electrochimica Acta, 2016. **215**: p. 276-288.
131. Zhao, X., et al., *Crosslinked Chitosan Networks as Binders for Silicon/Graphite Composite Electrodes in Li-Ion Batteries*. Journal of The Electrochemical Society, 2018. **165**(5): p. A1110-A1121.
132. Krause, A., et al., *High Area Capacity Lithium-Sulfur Full-cell Battery with Prelithated Silicon Nanowire-Carbon Anodes for Long Cycling Stability*. Sci Rep, 2016. **6**: p. 27982.
133. Jia, H., et al., *A novel approach to synthesize micrometer-sized porous silicon as a high performance anode for lithium-ion batteries*. Nano Energy, 2018. **50**: p. 589-597.
134. Xiao, Q., et al., *Inward lithium-ion breathing of hierarchically porous silicon anodes*. Nature Communications, 2015. **6**: p. 8844.
135. Wu, H., et al., *Stable Li-ion battery anodes by in-situ polymerization of conducting hydrogel to conformally coat silicon nanoparticles*. Nature Communications, 2013. **4**: p. 1943.
136. Higgins, T.M., et al., *A Commercial Conducting Polymer as Both Binder and Conductive Additive for Silicon Nanoparticle-Based Lithium-Ion Battery Negative Electrodes*. ACS Nano, 2016. **10**(3): p. 3702-3713.
137. Hwang, T.H., et al., *Electrospun Core-Shell Fibers for Robust Silicon Nanoparticle-Based Lithium Ion Battery Anodes*. Nano Letters, 2012. **12**(2): p. 802-807.
138. Zhou, R., et al., *Preparation and characterization of core-shell structure Si/C composite with multiple carbon phases as anode materials for lithium ion batteries*. Journal of Alloys and Compounds, 2016. **658**: p. 91-97.
139. Sun, Z., et al., *Controlled synthesis of yolk-mesoporous shell Si@SiO<sub>2</sub> nanohybrid designed for high performance Li ion battery*. RSC Advances, 2014. **4**(40): p. 20814-20820.

140. Yajie, L., et al., *An All-Integrated Anode via Interlinked Chemical Bonding between Double-Shelled–Yolk-Structured Silicon and Binder for Lithium-Ion Batteries*. *Advanced Materials*, 2017. **29**(44): p. 1703028.
141. Liu, N., et al., *A Yolk-Shell Design for Stabilized and Scalable Li-Ion Battery Alloy Anodes*. *Nano Letters*, 2012. **12**(6): p. 3315-3321.
142. Sun, Z., et al., *A Silicon/Double-Shelled Carbon Yolk-Like Nanostructure as High-Performance Anode Materials for Lithium-Ion Battery*. *Journal of The Electrochemical Society*, 2015. **162**(8): p. A1530-A1536.
143. Liu, N., et al., *A pomegranate-inspired nanoscale design for large-volume-change lithium battery anodes*. *Nature Nanotechnology*, 2014. **9**: p. 187.
144. Karkar, Z., et al., *A comparative study of polyacrylic acid (PAA) and carboxymethyl cellulose (CMC) binders for Si-based electrodes*. *Electrochimica Acta*, 2017. **258**: p. 453-466.
145. Choi, N.-S., et al., *Recent Progress on Polymeric Binders for Silicon Anodes in Lithium-Ion Batteries*. *Journal of Electrochemical Science and Technology*, 2015. **6**(2): p. 35–49.
146. Jusef, H. and S. Bruno, *A High-Performance Polymer Tin Sulfur Lithium Ion Battery*. *Angewandte Chemie International Edition*, 2010. **49**(13): p. 2371-2374.
147. Fang, S., et al., *Raspberry-like Nanostructured Silicon Composite Anode for High-Performance Lithium-Ion Batteries*. *ACS Applied Materials & Interfaces*, 2017. **9**(22): p. 18766-18773.
148. McDowell, M.T., et al., *The effect of metallic coatings and crystallinity on the volume expansion of silicon during electrochemical lithiation/delithiation*. *Nano Energy*, 2012. **1**(3): p. 401-410.
149. Yang, J., et al., *Amorphous TiO<sub>2</sub> Shells: A Vital Elastic Buffering Layer on Silicon Nanoparticles for High-Performance and Safe Lithium Storage*. *Advanced Materials*, 2017. **29**(48): p. 1700523.
150. Lee, J., J. Kim, and T. Hyeon, *Recent Progress in the Synthesis of Porous Carbon Materials*. *Advanced Materials*, 2006. **18**(16): p. 2073-2094.
151. ALOthman, Z.A., *A Review: Fundamental Aspects of Silicate Mesoporous Materials*. *Materials* 2012. **5**(12): p. 2874-2902.
152. Zubair, U., et al., *Dual confinement of sulphur with rGO-wrapped microporous carbon from  $\beta$ -cyclodextrin nanosponges as a cathode material for Li–S batteries*. *Journal of Solid State Electrochemistry*, 2017. **21**(12): p. 3411-3420.
153. Zanetti, M., et al., *Micro porous carbon spheres from cyclodextrin nanosponges*. *Microporous and Mesoporous Materials*, 2016. **235**: p. 178-184.
154. Steijns, M. and P. Mars, *The adsorption of sulfur by microporous materials*. *Journal of Colloid and Interface Science*, 1976. **57**(1): p. 175-180.
155. Xin, S., et al., *Smaller Sulfur Molecules Promise Better Lithium–Sulfur Batteries*. *Journal of the American Chemical Society*, 2012. **134**(45): p. 18510-18513.
156. E, T., *A primer on sulfur for the planetary geologist*. 1982: NASA.
157. Konios, D., et al., *Dispersion behaviour of graphene oxide and reduced graphene oxide*. *Journal of Colloid and Interface Science*, 2014. **430**: p. 108-112.
158. Liang, C., N.J. Dudney, and J.Y. Howe, *Hierarchically Structured Sulfur/Carbon Nanocomposite Material for High-Energy Lithium Battery*. *Chemistry of Materials*, 2009. **21**(19): p. 4724-4730.

159. Sevilla, M., A.B. Fuertes, and R. Mokaya, *Preparation and hydrogen storage capacity of highly porous activated carbon materials derived from polythiophene*. International Journal of Hydrogen Energy, 2011. **36**(24): p. 15658-15663.
160. Sevilla, M., R. Mokaya, and A.B. Fuertes, *Ultra-high surface area polypyrrole-based carbons with superior performance for hydrogen storage*. Energy & Environmental Science, 2011. **4**(8): p. 2930-2936.
161. Wu, R., et al., *Hierarchically porous nitrogen-doped carbon as cathode for lithium-sulfur batteries*. Journal of Energy Chemistry, 2018. **27**(6): p. 1661-1667.
162. Liu, Z., P.B. Balbuena, and P.P. Mukherjee, *Revealing Charge Transport Mechanisms in Li<sub>2</sub>S<sub>2</sub> for Li-Sulfur Batteries*. J Phys Chem Lett, 2017. **8**(7): p. 1324-1330.
163. Pang, Q., et al., *Review—The Importance of Chemical Interactions between Sulfur Host Materials and Lithium Polysulfides for Advanced Lithium-Sulfur Batteries*. Journal of The Electrochemical Society, 2015. **162**(14): p. A2567-A2576.
164. Zhang, Z., et al., *Sulfur encapsulated in a TiO<sub>2</sub>-anchored hollow carbon nanofiber hybrid nanostructure for lithium-sulfur batteries*. Chemistry, 2015. **21**(3): p. 1343-9.
165. Evers, S., T. Yim, and L.F. Nazar, *Understanding the Nature of Absorption/Adsorption in Nanoporous Polysulfide Sorbents for the Li-S Battery*. Journal of Physical Chemistry C, 2012. **116**(37): p. 19653-19658.
166. Zhang, Z., et al., *Titanium-dioxide-grafted carbon paper with immobilized sulfur as a flexible free-standing cathode for superior lithium-sulfur batteries*. Journal of Power Sources, 2015. **290**: p. 159-167.
167. Xue, W.J., et al., *Double-oxide sulfur host for advanced lithium-sulfur batteries*. Nano Energy, 2017. **38**: p. 12-18.
168. Regonini, D., et al., *AC electrical properties of TiO<sub>2</sub> and Magnéli phases, TiO<sub>2n-1</sub>*. Solid State Ionics, 2012. **229**(Supplement C): p. 38-44.
169. Chris R. Bowen, V.A., Tony Thomas. *Manufacture of Porous Electrically Conductive Ceramics*. in *International Conference on Mining, Material and Metallurgical Engineering*. 2014. Prague, Czech Republic.
170. Harada, S., K. Tanaka, and H. Inui, *Thermoelectric properties and crystallographic shear structures in titanium oxides of the Magnéli phases*. Journal of Applied Physics, 2010. **108**(8).
171. Zhang, X.Y., et al., *Fabrication and characterization of Magnéli phase Ti<sub>4</sub>O<sub>7</sub> submicron rods*. Journal of Materials Science-Materials in Electronics, 2016. **27**(5): p. 4861-4865.
172. Bharti, B., et al., *Formation of oxygen vacancies and Ti<sup>3+</sup> state in TiO<sub>2</sub> thin film and enhanced optical properties by air plasma treatment*. Scientific Reports, 2016. **6**.
173. Sutomu Ioroi, H.S., Shin-ichi Yamazaki, Zyun Siroma, Naoko Fujiwara, Kazuaki Yasuda, *Stability of corrosion-resistant Magnéli-phase Ti<sub>4</sub>O<sub>7</sub>-supported PEMFC catalysts at high potentials*. Journal of The Electrochemical Society, 2008. **155**(4): p. B321-B326.
174. Toyoda, M., et al., *Preparation of carbon-coated Magnéli phases TiO<sub>2n-1</sub> and their photocatalytic activity under visible light*. Applied Catalysis B-Environmental, 2009. **88**(1-2): p. 160-164.

175. Zhen, M.M., et al., *TiO<sub>2</sub>-B nanorods on reduced graphene oxide as anode materials for Li ion batteries*. Chemical Communications, 2015. **51**(3): p. 507-510.
176. Liang, Z., et al., *Sulfur Cathodes with Hydrogen Reduced Titanium Dioxide Inverse Opal Structure*. Acs Nano, 2014. **8**(5): p. 5249-5256.
177. Tao, X.Y., et al., *Strong Sulfur Binding with Conducting Magneli-Phase TiO<sub>2n-1</sub> Nanomaterials for Improving Lithium-Sulfur Batteries*. Nano Letters, 2014. **14**(9): p. 5288-5294.
178. Yuan, C., et al., *Hierarchical sulfur-impregnated hydrogenated TiO<sub>2</sub> mesoporous spheres comprising anatase nanosheets with highly exposed (001) facets for advanced Li-S batteries*. Nanotechnology, 2016. **27**(4): p. 045403.
179. Pang, Q., et al., *Surface-enhanced redox chemistry of polysulphides on a metallic and polar host for lithium-sulphur batteries*. Nature Communications, 2014. **5**.
180. Arif, A.F., et al., *Highly conductive nano-sized Magneli phases titanium oxide (TiO<sub>x</sub>)*. Sci Rep, 2017. **7**(1): p. 3646.
181. Takeuchi, T., et al., *Synthesis of Ti<sub>4</sub>O<sub>7</sub> Nanoparticles by Carbothermal Reduction Using Microwave Rapid Heating*. Catalysts, 2017. **7**(2).
182. Armstrong, G., et al., *Nanotubes with the TiO<sub>2</sub>-B structure*. Chemical Communications, 2005(19): p. 2454-2456.
183. Zakrzewska, K., *Nonstoichiometry in Studied by Ion Beam Methods and Photoelectron Spectroscopy*. Advances in Materials Science and Engineering, 2012. **2012**: p. 13.
184. Hanawa, T., *A comprehensive review of techniques for biofunctionalization of titanium*. J Periodontal Implant Sci, 2011. **41**(6): p. 263-272.
185. Aurbach, D., et al., *On the Surface Chemical Aspects of Very High Energy Density, Rechargeable Li-Sulfur Batteries*. Journal of The Electrochemical Society, 2009. **156**(8): p. A694-A702.
186. Umebayashi, T., et al., *Band gap narrowing of titanium dioxide by sulfur doping*. Applied Physics Letters, 2002. **81**(3): p. 454-456.
187. Sayago, D.I., et al., *A photoemission study of the SO<sub>2</sub> adsorption on TiO<sub>2</sub> (110) surfaces*. Surface Science, 2001. **482-485**: p. 9-14.
188. Wei, H., et al., *Chemical Bonding and Physical Trapping of Sulfur in Mesoporous Magneli Ti<sub>4</sub>O<sub>7</sub> Microspheres for High- Performance Li-S Battery*. Advanced Energy Materials, 2017. **7**(4).
189. Babakhani, B. and D.G. Ivey, *Effect of electrodeposition conditions on the electrochemical capacitive behavior of synthesized manganese oxide electrodes*. Journal of Power Sources, 2011. **196**(24): p. 10762-10774.
190. Chen, Y.-C., et al., *Highly flexible supercapacitors with manganese oxide nanosheet/carbon cloth electrode*. Electrochimica Acta, 2011. **56**(20): p. 7124-7130.
191. Ramírez, A., et al., *Evaluation of MnO<sub>x</sub>, Mn<sub>2</sub>O<sub>3</sub>, and Mn<sub>3</sub>O<sub>4</sub> Electrodeposited Films for the Oxygen Evolution Reaction of Water*. The Journal of Physical Chemistry C, 2014. **118**(26): p. 14073-14081.
192. Saputra, E., et al., *Manganese oxides at different oxidation states for heterogeneous activation of peroxymonosulfate for phenol degradation in aqueous solutions*. Applied Catalysis B: Environmental, 2013. **142-143**: p. 729-735.

193. Geng, Z., et al.,  *$\delta$ -MnO<sub>2</sub>-Mn<sub>3</sub>O<sub>4</sub> Nanocomposite for Photochemical Water Oxidation: Active Structure Stabilized in the Interface*. ACS Applied Materials & Interfaces, 2016. **8**(41): p. 27825-27831.
194. Le, H.A., et al., *Chemical Vapor Synthesis and Characterization of Manganese Oxides*. Chemical Vapor Deposition, 2011. **17**(7-9): p. 228-234.
195. Manceau, A., A. Marcus Matthew, and S. Grangeon, *Determination of Mn valence states in mixed-valent manganates by XANES spectroscopy*, in *American Mineralogist*. 2012. p. 816.
196. Junta, J.L. and M.F. Hochella, *Manganese (II) oxidation at mineral surfaces: A microscopic and spectroscopic study*. Geochimica et Cosmochimica Acta, 1994. **58**(22): p. 4985-4999.
197. Li, X., et al., *Freestanding carbon encapsulated mesoporous vanadium nitride nanowires enable highly stable sulfur cathodes for lithium-sulfur batteries*. Nano Energy, 2017. **40**: p. 655-662.
198. Song, Y., et al., *Enhanced Sulfur Redox and Polysulfide Regulation via Porous VN-Modified Separator for Li-S Batteries*. ACS Applied Materials & Interfaces, 2019. **11**(6): p. 5687-5694.
199. Masikhwa, T.M., et al., *Asymmetric supercapacitor based on VS<sub>2</sub> nanosheets and activated carbon materials*. RSC Advances, 2016. **6**(45): p. 38990-39000.
200. Rao, Y., et al., *Vanadium sulfides interwoven nanoflowers based on in-situ sulfurization of vanadium oxides octahedron on nickel foam for efficient hydrogen evolution*. Applied Surface Science, 2017. **423**: p. 1090-1096.
201. Zhou, Y., et al., *Vanadium sulfide sub-microspheres: A new near-infrared-driven photocatalyst*. Journal of Colloid and Interface Science, 2017. **498**: p. 442-448.
202. Liang, X., et al., *A highly efficient polysulfide mediator for lithium-sulfur batteries*. Nat Commun, 2015. **6**: p. 5682.
203. Zhao, X., et al., *Polyaniline-Coated Mesoporous Carbon/Sulfur Composites for Advanced Lithium Sulfur Batteries*. The Journal of Physical Chemistry C, 2015. **119**(15): p. 7996-8003.
204. Wang, J., et al., *C-S@PANI composite with a polymer spherical network structure for high performance lithium-sulfur batteries*. Phys Chem Chem Phys, 2016. **18**(1): p. 261-6.
205. E. C. Gomes , M.A.S.O., *Chemical Polymerization of Aniline in Hydrochloric Acid (HCl) and Formic Acid (HCOOH) Media. Differences Between the Two Synthesized Polyanilines*. American Journal of Polymer Science, 2012. **2**(2): p. 5-13.
206. Dhand C, D.N., Mishra S, Solanki P, Mayandi V, Beuerman RW, Ramakrishna S, Lakshminarayanan R, Malhotra B, *Polyaniline-based biosensors*. Nanobiosensors in Disease Diagnosis, 2015. **4**: p. 25-46.
207. Natishan, P.M. and W.E. O'Grady, *Chloride Ion Interactions with Oxide-Covered Aluminum Leading to Pitting Corrosion: A Review*. Journal of The Electrochemical Society, 2014. **161**(9): p. C421-C432.
208. Li, G.-C., et al., *A Polyaniline-Coated Sulfur/Carbon Composite with an Enhanced High-Rate Capability as a Cathode Material for Lithium/Sulfur Batteries*. Advanced Energy Materials, 2012. **2**(10): p. 1238-1245.
209. Stejskal, J. and R.G. Gilbert, *Polyaniline. Preparation of a conducting polymer(IUPAC Technical Report)*, in *Pure and Applied Chemistry*. 2002. p. 857.

- 
210. Ji, L. and X. Zhang, *Electrospun carbon nanofibers containing silicon particles as an energy-storage medium*. Carbon, 2009. **47**(14): p. 3219-3226.
  211. Wang, M.-S., et al., *Highly uniform silicon nanoparticle/porous carbon nanofiber hybrids towards free-standing high-performance anodes for lithium-ion batteries*. Carbon, 2015. **82**: p. 337-345.
  212. Ferrari, A.C. and J. Robertson, *Interpretation of Raman spectra of disordered and amorphous carbon*. Physical Review B, 2000. **61**(20): p. 14095-14107.
  213. Qu, J., et al., *Stiffness, strength and adhesion characterization of electrochemically deposited conjugated polymer films*. Acta Biomaterialia, 2016. **31**: p. 114-121.
  214. Markevich, E., G. Salitra, and D. Aurbach, *Fluoroethylene Carbonate as an Important Component for the Formation of an Effective Solid Electrolyte Interphase on Anodes and Cathodes for Advanced Li-Ion Batteries*. ACS Energy Letters, 2017. **2**(6): p. 1337-1345.
  215. Kim, G.-T., et al., *Behavior of Germanium and Silicon Nanowire Anodes with Ionic Liquid Electrolytes*. ACS Nano, 2017. **11**(6): p. 5933-5943.
  216. Li, B., et al., *A new configured lithiated silicon-sulfur battery built on 3D graphene with superior electrochemical performances*. Energy & Environmental Science, 2016. **9**(6): p. 2025-2030.
  217. Piwko, M., et al., *Hierarchical columnar silicon anode structures for high energy density lithium sulfur batteries*. Journal of Power Sources, 2017. **351**: p. 183-191.
  218. Yan, X., et al., *Insights into cyclable lithium loss as a key factor in accelerated capacity fade of lithiated silicon-sulfur full cells*. ACS Appl Mater Interfaces, 2018.
  219. Shen, C., et al., *Silicon(lithiated)-sulfur full cells with porous silicon anode shielded by Nafion against polysulfides to achieve high capacity and energy density*. Nano Energy, 2016. **19**: p. 68-77.



# Appendix A

## List of Publications

Parts of this dissertation have been acquired from some of the following publications.

1. U. Zubair, A. Anceschi, F. Caldera, M. Alidoost, J. Amici, C. Francia, M. Zanetti, F. Trotta, S. Bodoardo, N. Penazzi “Dual confinement of sulphur with rGO-wrapped microporous carbon from  $\beta$ -cyclodextrin nanosponges as a cathode material for Li–S batteries” *J Solid State Electrochem* (2017) 21: 3411, DOI: 10.1007/s10008-017-3664-6
2. D. Versaci, R. Nasi, U. Zubair, J. Amici, M. Sgroi, M. A. Dumitrescu, C. Francia, S. Bodoardo, N. Penazzi, “New eco-friendly low-cost binders for Li-ion anodes”, *J Solid State Electrochem* (2017) 21: 3429, <https://doi.org/10.1007/s10008-017-3665-5>
3. U, Zubair, J. Amici, C. Francia, D. McNulty, S. Bodoardo, C. O’Dwyer, “Polysulfide Binding to Several Nanoscale Magnàli Phases Synthesized in Carbon for Long-Life Lithium–Sulfur Battery Cathodes”, *ChemSusChem* (2018) 11(11), 1838-1848, DOI: 10.1002/cssc.201800484
4. U, Zubair, J. Amici, C. Francia, D. McNulty, S. Bodoardo, “Rational design of porous carbon matrices to enable efficient Lithiated Silicon Sulfur (SLS) full cell”, *Carbon* (2019) 145, 100-111, DOI: 10.1016/j.carbon.2019.01.005
5. J. Amici, M. Alidoost, F. Caldera, D. Versaci, U. Zubair, F. Trotta, C. Francia, S. Bodoardo “PEEK-WC/Nanosponge Membranes for Lithium-Anode Protection in Rechargeable Li-O<sub>2</sub> Batteries”, (2018) 5(12) *ChemElectroChem*, DOI: 10.1002/celec.201800241
6. S. M. Crespiera, D. Amantia, E. Knipping, C. Aucher, L. Aubouy, J. Amici, J. Zeng, U. Zubair, C. Francia, S. Bodoardo, “Cobalt-doped mesoporous carbon nanofibres as free-standing cathodes for lithium–oxygen batteries”, *J Appl Electrochem* (2017) 47: 497. <https://doi.org/10.1007/s10800-016-1035-0>

## Patent:

S. Bodoardo, U. Zubair, M. Serrapede, J. Amici, P. Zaccagnini, D. Versaci, C. Francia, C. Pirri, A. Lamberti, “Dispositivo elettrochimico a commutazione automatica per l’accumulo ad alta energia e ad alta potenza” Vs.rif.: Polito: 2017-041 Ns.rif.: P2952IT00

## List of conferences

Here is the list of conferences in which I have been able to present my Ph.D. work either through talks or posters.

1. U. Zubair, D. Versaci, J. Amici, C. Francia, S. Bodoardo, N. Penazzi, “Magnéli phase TiOx in carbon as highly efficient sulfur cathodes for lithium-sulfur batteries” Poster in 69th Annual Meeting of the International Society of Electrochemistry, Bologna, Italy, 04/09/2018
2. U. Zubair, J. Amici, C. Francia, S. Bodoardo, N. Penazzi, “Ultra-porous Nitrogen / Sulfur doped activated carbon for high-performance Lithium Sulfur batteries” Poster in Li-SM3 2018 (Lithium Sulfur: Mechanisms, Modelling & Materials), Chicago, USA, 25-26/04/2017
3. U. Zubair, S. Basso, J. Amici, C. Francia, S. Bodoardo, N. Penazzi, “Formate ion doped PANi wrapped Ketjen BlackCarbon/Sulphur composites for Li-S batteries” Talk in 21st International Conference on Solid State Ionics (SSI-21), Padova, Italy, 21/06/2017
4. U. Zubair, M. Serrapede, P. Rivolo, M. Armandi, J. Amici, N. Penazzi, S. Bodoardo, E. Tresso, F. C. Pirri “Mildly reduced graphene oxide aerogels as promising host material for Li/S batteries” Poster in 21st International Conference on Solid State Ionics (SSI-21), Padova, Italy, 20/06/2017
5. U. Zubair, J. Amici, D. Versaci, C. Francia, S. Bodoardo, N. Penazzi, “PANi wrapped Ketjen Black Carbon/Sulphur composites for Li-S batteries” Poster in Li-SM3 2017 (Lithium Sulfur: Mechanisms, Modelling & Materials), London, UK, 26/04/2017
6. U. Zubair, M. Alidoost, J. Amici, C. Francia, S. Bodoardo, N. Penazzi, “rGO wrapped activated microporous carbon from beta-cyclodextrin nanospheres for Li/S batteries” Talk in 20th Topical Meeting of the International Society of Electrochemistry, Buenos Aires, Argentina, 22/03/2017
7. D. Versaci, R. Nasi, U. Zubair, J. Amici, M. Sgroi, A. Dumitrescu, C. Francia, S. Bodoardo, N. Penazzi, “New eco-friendly low-cost binders for Li-ion anodes” Poster in EMRS Fall Meeting 2016, Warsaw, Poland, 20/09/2016
8. U. Zubair, M. Alidoost, J. Amici, C. Francia, S. Bodoardo, N. Penazzi, “Dual layer cathode protection for high- performance Lithium Sulfur (Li/S) batteries” Talk in EMRS Fall Meeting 2016, Warsaw, Poland, 21/09/2016
9. M. Alidoost, U. Zubair, D. Versaci, J. Amici, C. Francia, S. Vankova, S. Bodoardo, N. Penazzi, “A new 3D Silicon/Graphene anode material for Lithium-Sulfur batteries” Poster in EMRS Fall Meeting 2016, Warsaw, Poland, 20/09/2016